AACHENER BEITRÄGE ZUR STRÖMUNGSMECHANIK

Aerodynamisches Institut und
Lehrstuhl für Strömungslehre
der RWTH Aachen

Experimental Analysis of the Two-Phase Flow Field in Internal Combustion Engines

Timo van Overbrüggen

ABS BAND 14

Experimental Analysis of the Two-Phase Flow Field in Internal Combustion Engines

Experimentelle Analyse des zweiphasigen Strömungsfeldes in Verbrennungskraftmaschinen

Von der Fakultät für Maschinenwesen der
Rheinisch-Westfälischen Technischen Hochschule Aachen
zur Erlangung des akademischen Grades
eines Doktors der Ingenieurwissenschaften
genehmigte Dissertation

vorgelegt von

Timo van Overbrüggen

Berichter: Universitätsprofessor Dr.-Ing. Wolfgang Schröder
Universitätsprofessor Dr.-Ing. Reinhold Kneer

Tag der mündlichen Prüfung: 28. April 2016

Diese Dissertation ist auf den Internetseiten der Universitätsbibliothek online verfügbar.

AACHENER BEITRÄGE ZUR STRÖMUNGSMECHANIK

Herausgeber:
Univ.-Prof. Dr.-Ing. Wolfgang Schtröder

Timo van Overbrüggen
Experimental Analysis of the Two-Phase Flow Field in Internal Combustion Engines

ISBN: 978-3-95886-104-6

Bibliografische Information der Deutschen Bibliothek
Die Deutsche Bibliothek verzeichnet diese Publikation in der Deutschen Nationalbibliografie; detaillierte bibliografische Daten sind im Internet über http://dnb.ddb.de abrufbar.

Das Werk einschließlich seiner Teile ist urheberrechtlich geschützt. Jede Verwendung ist ohne die Zustimmung des Herausgebers außerhalb der engen Grenzen des Urhebergesetzes unzulässig und strafbar. Das gilt insbesondere für Vervielfältigungen, Übersetzungen, Mikroverfilmungen und die Einspeicherung und Verarbeitung in elektronischen Systemen.

Vertrieb:

1. Auflage 2016
© Verlagshaus Mainz GmbH Aachen
Süsterfeldstr. 83, 52072 Aachen
Tel. 0241/87 34 34
Fax 0241/87 55 77
www.Verlag-Mainz.de

Herstellung:

Druckerei Mainz GmbH Aachen
Süsterfeldstraße 83
52072 Aachen
Tel. 0241/87 34 34
Fax 0241/87 55 77
www.DruckereiMainz.de

Satz: nach Druckvorlage des Autors
Umschlaggestaltung: Druckerei Mainz

printed in Germany
D 82 (Diss. RWTH Aachen University, 2016)

meiner Familie

Danksagung

Die vorliegende Arbeit entstand während meiner Tätigkeit als Stipendiat des Graduiertenkollegs 'Brennstoffe aus nachwachsenden Rohstoffen (Brenaro)' und meiner Tätigkeit als wissenschaftlicher Mitarbeiter am Aerodynamischen Institut und Lehrstuhl für Strömungsmechanik der Rheinisch-Westfälischen Technischen Hochschule Aachen.

Mein besonderer Dank gilt meinem Doktorvater Prof. Dr.-Ing. Wolfgang Schröder für die Betreuung und das große Interesse an meiner Arbeit. Nicht zuletzt durch die mir von ihm gegebenen Freiheiten und Unterstützung war es möglich während meiner Promotion ein halbes Jahr an der Monash University in Melbourne, Australien zu forschen. Außerdem möchte ich mich für die wertvollen Diskussionen bedanken ohne die meine Dissertation in dieser Form nicht möglich gewesen wäre. Den Herren Prof. Dr.-Ing. Reinhold Kneer, dem Leiter des Lehrstuhls für Wärme- und Stoffübertragung, und Prof. Dr.-Ing. Hubertus Murrenhoff, dem Leiter des Instituts für fluidtechnische Antriebe und Steuerungen, danke ich für die Übernahme des zweiten Gutachtens sowie den Vorsitz meiner mündlichen Prüfung.

Prof. Julio Soria, Ph.D. und seinem ganzen Team an der Monash University, Melbourne, Australien danke ich für die mir entgegengebrachte Gastfreundschaft und die Möglichkeit in Prof. Sorias Labor zu forschen.

Ein großer Dank gilt außerdem der Belegschaft der mechanischen Werkstatt, allen voran Karl-Heinz Radermacher für unzählige Ideen und seine Hilfe, sowie Arthur Biertz, Nick Capellmann, Christian Ostlender, Stefan Sauren und Jürgen Exner für ihre großartige Arbeit.

Großer Dank gilt all meinen Arbeitskollegen am Aerodynamischen Institut. Besonders möchte ich Dr.-Ing. Thomas Soodt danken, der mich ermutigt hat eine Promotion am Aerodynamischen Institut durchzuführen. Er ist über die Jahre zu einem guten Freund geworden. Dr.-Ing. Jan Dannemann danke ich für die Einführung in den Versuchsstand die geduldige Erklärung der holographischen PIV und eine großartige Übergabe während unserer gemeinsamen Zeit. Dr.-Ing. Andreas Henze danke ich dafür, dass er durch wertvolle Tipps und große Erfahrung mein fachliches Wissen gesteigert hat. Bei meinen Bürokollegen aus R128 Dr.-Ing. Kai Pielhop, Dr.-Ing. Axel Hartmann, Dr.-Ing. Franka Schröder, Antje Feldhusen, Alexander Rubbert und Pascal Marquardt, sowie den Kollegen aus dem Nachbarbüro, Dr.-Ing. Andrea Winzen und Dr.-Ing. Bernardo Nottebrock sowie bei Dorothee Roggenkamp bedanke ich mich für die aufschlussreichen fachlichen Diskussionen die mich in meiner Arbeit unterstützt und mein fachliches Wissen bereichert haben. Außerdem bedanke ich mich für viele Stunden außerhalb der Arbeitszeit die meine Zeit am Institut unvergesslich gemacht haben.

Fabian Fibigs, Engin Cekic, Simon Heise, Jan Stodollick und Axel Moll danke ich für ihre langjährige Freundschaft und die Möglichkeit außerhalb der Arbeit abzuschalten.

Ein ganz besonderer Dank geht an meine Eltern Maria und Walter van Overbrüggen, die mein technisches Interesse schon in frühester Kindheit geweckt und gefördert und mich in meinen Entscheidungen immer bestärkt haben.

Zuletzt möchte ich der Liebe meines Lebens, meiner Frau Maren, für ihre unermüdliche Unterstützung und Hilfe danken. Bloße Worte können nicht beschreiben, was sie mir bedeutet. Ohne sie wäre diese Dissertation nicht möglich gewesen. Sie ist die Stütze die ich in meinem Leben brauche, weswegen diese Arbeit ihr und unserem wundervollen Sohn Bennet gewidmet ist.

Aachen, Mai 2016 Timo van Overbrüggen

Abstract

The reduction of green house gases and other pollutant emissions is of highest interest in modern engine development. This can be achieved by increasing the engine efficiency. For this, new combustion processes are needed. Another possibility to decrease green house gas emissions is the combustion of bio-fuels. However, these new methods as well as the efficient combustion of bio-fuels require an understanding of the highly three-dimensional flow field inside the combustion chamber.

In this study the non reacting flow in two different research engines is measured. The measurements in the first research engine focus on the understanding of the highly three-dimensional structure of the flow field inside the combustion chamber. For this, holographic and tomographic particle-image velocimetry (PIV) have been applied to gain information on the intake and compression stroke of the research engine. The holographic PIV measurements show the feasibility of the technique to measure the highly unstable volumetric flow field. The analysis of the tomographic PIV measurements is based on the analysis of the flow field at 80°, 160° , and 240° after top dead center(atdc) such that the velocity distributions at the intake, the end of the intake, and the compression stroke at an engine speed of 1,500 rpm are discussed in detail. Furthermore, the influence of an internal exhaust gas recirculation is analyzed at a crank angle of 240° atdc. The flow fields are analyzed by distributions of the velocity fields, the turbulent kinetic energy, and the Γ_1 vortex identification function. The tomographic measurements enable the instantaneous resolution of the large scale three-dimensional vortical structures of the in-cylinder flow. Through this, the U-shaped structure of the tumble vortex core and the development of an elliptic ring vortex below the pent roof could be confirmed. Furthermore, the spatial distribution of the turbulent kinetic energy with high values below the intake valves could be shown. The analysis of the exhaust gas recirculation shows the tumble vortex to decompose at earlier crank angles. Furthermore, compared to the standard configuration, a higher turbulent kinetic energy could be shown.

After that, the interaction of the liquid phase of ethanol and methyl ethyl ketone (MEK) injected with an A-type fuel injector is investigated in the second engine by means of Mie scattering imaging (MSI). The results show the flow field to strongly influence the spray behavior. Especially for late injection during the compression phase a strong interaction of tumble vortex and spray is visible. Compared to ethanol, MEK shows lower piston and liner wetting effects and a reduced influence of the flow field on the injection behavior.

Finally, time-resolved stereoscopic PIV measurements have been performed to investigate the influence of ethanol fuel injection on the flow field behavior at an engine speed of 1,500 and 2,000 rpm. For this, ensemble averaged velocity fields, turbulent kinetic energy, and the Γ_1 vortex identification criterion are used. Through the Γ_1 vortex identification criterion, a change in the propagation of the tumble vortex core could be shown. Furthermore, a reduction of spatial mean vorticity is evident. Additionally, the turbulent kinetic energy is reduced by the injection process. Finally, a stabilizing impact of higher engine speed is evident.

Zusammenfassung

Der Fokus moderner Motorenentwicklung liegt auf der Verringerung von Treibhaus- und anderen Abgasen. Treibhausgase können durch eine Effizienzsteigerung der Verbrennungsprozesse reduziert werden wofür neue, moderne Verbrennungsmethoden benötigt werden. Weiterhin verspricht der Fortschritt in der Synthetisierung von Biokraftstoffen eine Reduktion der Treibhausgase. Allerdings ist sowohl für die Entwicklung neuer Verbrennungsmethoden sowie die Verbrennung von Biokraftstoffen ein genaues Verständnis des dreidimensionalen Strömungsfeldes innerhalb des Brennraums nötig.

Die Dissertation beschäftigt sich mit der Vermessung des nichtreaktiven Strömungsfeld in zwei verschiedenen Verbrennungsmotoren. Der Fokus der Messungen im ersten Versuchsmotor liegt auf dem Verständnis der volumetrischen, dreidimensionalen Strömungsstrukturen innerhalb des Brennraums. Hierfür wurden holographische und tomographische particle-image velocimetry (PIV) Messungen durchgeführt. Mit Hilfe der Holographischen Messungen konnte gezeigt werden, dass diese Technik an einem optischen Versuchsmotor anwendbar ist. Die Analyse der tomographischen PIV Messungen basiert auf der Analyse des Strömungsfeldes bei 80°, 160° und 240° nach dem oberen Totpunkt, sodass die Geschwindigkeitsverteilung während des Einlasstakts, am Ende des Einlasstakts und während des Verdichtungstaktes bei einer Motorgeschwindigkeit von 1500 Umdrehungen pro Minute diskutiert wird. Weiterhin wird der Einfluss einer internen Abgasrezirkulation bei einem Kurbelwellenwinkel von 240° nach dem obern Totpunkt untersucht. Die Strömungsfelder werden mit Hilfe der Geschwindigkeitsverteilung, der turbulenten kinetischen Energie und des Γ_1 Wirbeldetektionskriteriums analysiert.

Mit Hilfe der tomographischen PIV-Messungen ist es möglich die räumliche Ausbreitung der großskaligen Wirbelstrukturen innerhalb des Brennraums instantan aufzulösen. Hierdurch kann die U-förmige Struktur des Tumble-Wirbels gezeigt werden. Weiterhin war es möglich die Entstehung eines elliptischen Ringwirbels unterhalb der Ventile zu bestätigen. Durch die räumliche Analyse der turbulenten kinetischen Energie war es zudem möglich ein Gebiet hoher Durchmischung unterhalb der Einlassventile nachzuweisen. Die Analyse der internen Abgasrückführung zeigt erhöhte Werte der turbulenten kinetischen Energie sowie ein früheres Zerfallen des Tumble-Wirbels.

Im zweiten Versuchsmotor wurde die Interaktion von Flüssigphase und Strömungsfeld eines Ethanol Sprays und eines Methyl-Ethyl-Keton (MEK) Sprays aus einer A-Düse mit Hilfe des Mie scattering Imaging (MSI) untersucht. Die Ergebnisse zeigen deutlich den starken Einfluss des Strömungsfelds auf den Sprühkegel. Vor allem für späte Einspritzzeitpunkte während der Kompressionsphase ist eine starke Interaktion von Spray und Tumble-Wirbel sichtbar. Verglichen mit dem Ethanol Spray zeigt das MEK Spray eine Verringerte Benetzung des Kolbens und des Zylinders. Weiterhin zeigt sich ein verringerter Einfluss des Strömungsfeldes auf das MEK Spray verglichen mit dem Ethanol Spray.

Zudem wurde das Mischungsverhalten von Ethanol Spray und Strömungsfeld mit Hilfe der zeitaufgelösten stereoskopischen PIV für eine Drehzahl von 1500 und 2000

Umdrehungen pro Minute vermessen. Die Strömungsfelder werden mit Hilfe der zyklusgemittelten Geschwindigkeitsfelder, der turbulenten kinetischen Energie und des Γ_1 Wirbeldetektionskriteriums analysiert. Letzteres zeigt den Einfluss der Einspritzung auf die zeitliche Trajektorie des Tumble-Wirbels. Zudem konnte eine Verringerung der turbulenten kinetischen Energie durch den Einspritzvorgang festgestellt werden. Zudem zeigt die Analyse höherer Motorgeschwindigkeiten eine Stabilisierung der Strömung und des Tumble-Wirbels.

Contents

Abstract **i**

Zusammenfassung **ii**

Contents **iii**

Nomenclature vii

1 Introduction **1**

2 Internal Combustion Engines **5**

2.1 Introduction 5

2.2 Flow Characteristics 7

2.3 Mathematical Flow Description 8

2.3.1 Primary Breakup of Fuel Sprays 11

3 Optics **15**

3.1 Gemoetrical Optics 15

3.2 Physical Optics 17

3.2.1 Coherence 19

3.2.2 Polarization 21

3.2.3 Interference 22

3.2.4 Diffraction 24

3.3 Holography 25

3.3.1 Basic Principle of Holographic Recording and Reconstruction . . 25

4 Measurement Techniques **31**

4.1 Particle-Image Velocimetry 31

4.1.1 Basic Principles of PIV 31

4.1.2 Stereoscopic PIV 32

4.1.3 Holographic PIV 35

4.1.4 Tomographic PIV 37

4.1.5 Algebraic Reconstruction Technique (ART) 40

4.1.6 Tracer particles 42
4.2 Mie Scattering Imaging 46

5 Test Facilities **47**
5.1 Research Engines 47
5.1.1 SUZI 47
5.1.2 TINA 50
5.2 Test Cases 55
5.3 Holographic Particle-Image Velocimetry System 57
5.3.1 Optical Setup 58
5.3.2 Post-Processing of the Holographic Particle Images 60
5.4 Tomographic Particle-Image Velocimetry System 61
5.5 Stereoscopic Particle-Image Velocimetry System 65
5.6 Mie Scattering Imaging Test Rig 66

6 Results **69**
6.1 Data Validation and Estimation of Measurement Errors. 69
6.1.1 HPIV Error Estimation 70
6.1.2 Tomo-PIV Error Estimation 71
6.1.3 Mie scattering Imaging Error Estimation 74
6.1.4 Stereo-PIV Error Estimation 74
6.2 Engine Measurements 76
6.2.1 HPIV Results 76
6.2.2 Tomo-PIV Results 82
6.2.3 Three-Dimensional Flow Results 83
6.2.4 Three-Dimensional Distribution of the Tumble Vortex 84
6.2.5 Multi-Plane Visualization 85
6.2.6 Influence of Internal Exhaust Gas Recirculation 90
6.2.7 Mie Scattering Analysis of Fuel Injection 99
6.2.8 Stereo-PIV Results 108

7 Conclusion **123**

References **126**

A Hologram development and bleaching **135**

B Test rig for particle analysis **137**

C Author-related pre-published papers and theses **141**

Nomenclature

Roman Symbols

A	area
B	magnetic field intensity
B	bore
B	energy
b	distance
C	reconstruction beam
C_d	discharge coefficient
c	speed of light
c_p	specific heat at constant pressure
c_v	specific heat at constant volume
d	distance
d	diameter
D	diameter
E	electrical field intensity
e	Euler number
f	focal length
f	frequency
f	flow field variable
H	hologram
I	image
I	irradiance
I	intensity
k	turbulent kinetic energy
k	wave number
L	distance
L	integral length scale
L	number
l	distance
M	number
n	number of cycles
N	number
m	natural number
n	refractive index
O	object
O	object beam
Oh	Ohnesorge number
P	Pixel
p	distance
R	distance
R	reference beam

r	compression ratio
r	radius
r	relaxation parameter
r	distance
Re	Reynolds number
S	symmetric component of the velocity gradient tensor
S	distance
S	number of grid points
S	plane
S	stroke
SR$_z$	swirl ratio around z-axis
$\vec{S}$	Poynting vector
r	distance
$\vec{r}$	positioning vector
t	time
T	transmission
TR$_x$	tumble ratio around x-axis
TR$_y$	tumble ratio around y-axis
V_c	clearance volume
V_d	displacement volume
W	weighting matrix
w	weighting coefficient
$\vec{v}$	velocity vector
u, v, w	velocity components in a Cartesian system
x, y, z	Cartesian coordinates
y_p	penetration length

Greek Symbols

α	angle
α	background transmittance
β	angle
β	amplitude transmittance
β	phase response
Γ	auto-correlation function
Γ_1	vortex identification criterion
γ	normalized coherence coefficient
ϵ_0	vacuum permittivity
η	amplitude ratio
η	dynamic viscosity
θ	angle
θ	phase shift
λ	wave length
λ_2	second eigenvalue of $M = S^2 + \Omega^2$

κ	ratio of specific heats
ν	phase velocity of a light wave
ν	kinematic viscosity
π	ratio of a circle's circumference to its diameter
ρ	density
ρ^*	density ratio
σ	surface tension
τ	time difference
τ	degree of transmittance
ϕ	angle
ϕ	phase shift
ω	angular frequency
Ω	asymmetric component of the velocity gradient tensor

Calligraphic Symbols

$\mathcal{O}(\,\cdot\,)$	order of magnitude

Operators and Notations:

Δ	Laplace Operator
∇	Nabla Operator
∂	partial derivative
$\langle\rangle$	time average
cos	cosinus
Im	imaginary part
max	maximum
min	minimum
Re	real part
sin	sinus

Superscripts

$\vec{\ }$	vector
$'$	fluctuation of a quantity
$-$	time-averaged quantity
T	transposed

Subscripts

0	starting value
A	plane averaged
a	ambient
ac	air cycle
Cam	camera
c	cyclic
c	clearance

d	displacement
disp	displacement
max	maximum
e	engine
f	fluid
f	fuel
g	gas
i	injection
l	liquid
los	line of sight
p	particle
p	penetration
ppp	particles per pixel
r	real
sp	spray
t	turbulent
v	virtual
x, y, z,	cartesian coordinates

Acronyms

2C	two-component
2D	two-dimensional
3C	three-component
3D	three-dimensional
AIA	Institute of Aerodynamics
atdc	after top dead center
BBO	Basset-Bousinesq Ossen
bdc	bottom dead center
CAD	crank angle degree
CAI	controlled auto ignition
CO_2	carbon dioxide
CoE	Cluster of Excellence
CCD	charge coupled device
CMOS	complementary metal oxide semiconductor
CV	Control Volume
DAQ	data aquisition
DEHS	Dy-Ethyl-Hexyl-Sebacat
DFG	Deutsche Forschungsgemeinschaft
DISI	direct injection spark ignition
DNS	direct numerical simulation
DOI	duration of injection
EGR	exhaust gas recirculation
FFT	fast-fourier transformation
fig.	figure
HC	hydrocarbon

Holo	Holographic
HPIV	Holographic Particle-Image Velocimetry
IC	Internal Combustion
ILA	Intelligent Laser Applications
LES	large eddy simulation
MEK	methyl ethyl ketone
MS	Microspheres
MSI	Mie Scattering Imaging
NI	National Instruments
NO_x	Nitrogen Oxide
PDF	Probability density function
PIV	Particle-Image Velocimetry
PTU	Programmable Timing Unit
PTV	Particle-Tracking Velocimetry
px	pixel
RANS	Reynolds-averaged Navier-Stokes
RPM	rounds per minute
RWTH	Rheinisch-Westfälische Technische Hochschule
SI	spark ignition
SFB	Sonderforschungsbereich
tab.	table
tdc	top dead center
Tomo	Tomographic
Tomo-PIV	Tomographic Particle-Image Velocimetry
VRPM	emulsion for holographic recordings

1

Introduction

Since the beginning of the 20th century, motored vehicles has become the most important transport option worldwide. They are directly related to wealth, mobility, convenience, and personal freedom. It is assumed that the world will reach about 1.3 billion motored vehicles by 2020 [93]. However, this leads to increased pollutant emissions, which can directly be related to global warming. Furthermore, the emission of nitrogen oxide (NO_x), hydrocarbons (HC), particulate matter, and carbon monoxide leads to health issues especially in urban areas [68]. Additionally, the product of combustion, CO_2, has been identified as a strong green house gas that influences global warming. Global warming itself causes global problems like floods in some parts of the world and droughts in others. Furthermore, motored vehicles, and therefore combustion engines, are dependent on fossil fuels. These resources are not commonly available in all areas of the world, which leads to ever-increasing conflicts and environmental problems like the catastrophic accident of the Deepwater Horizon oil platform. Therefore, the aim of modern engine development is an increase in efficiency, which directly leads to a decreased fuel consumption and pollutant emission, and the use of bio-fuels to make engines more independent from fossil fuels.

One approach for more efficient internal combustion (IC) engines is the development of new, more efficient combustion processes. Especially the so-called Controlled Auto-Ignition (CAI) and the Homogeneous Charge Compression Ignition (HCCI) appear to be promising technologies. Both are characterized by a high homogenization and exhaust gas recirculation (EGR). The former avoids rich combustion such that soot emission decreases, whereas the latter significantly reduces the combustion temperature which, in turn, substantially reduces NO_x emissions. The lower combustion temperatures are achieved through the high thermal heat capacity of the recirculated exhaust gas. Furthermore, fuel consumption is reduced through de-throttling as well as decreased heat release due to the diluted mixture, which leads to lower peak in-cylinder pressures and a higher ratio of specific heats resulting in enhanced engine efficiency and decreased fuel consumption [1]. Lang et al. [54] reported a maximum fuel reduction of 15 % and a reduction of NO_x emissions by up to 90-99 %.

However, CAI as well as HCCI are limited in their operation range due to knocking and misfiring (Bhave et al. [15], Ma et al. [59], Urushihara [102]). What is more, these instabilities cannot be controlled by combustion performance measures, e.g., air-fuel ratio measurements, such that they have to be chemically and physically suppressed. Stapf et al. [95] state that self-ignition highly depends on the stratification of fuel, recirculated exhaust gas, and fresh air. Consequently, the control of the combustion process strongly depends on the thermodynamic conditions of the in-cylinder mixture (Adomeit et al. [4]). These conditions are significantly influenced by the gas flow within the cylinder especially during the intake and compression stroke. Hence, the large and small scale structures within these strokes strongly influence the mixing and as such the combustion process (Heywood [44]) since the point of ignition and the propagation are directly influenced by the flow field. New developments try to control these instabilities through model-based control [6]. These approaches rely on reduced-order models of the underlying combustion process. To generate these models of the flow field a detailed analysis of the temporal and spatial development of the characteristic flow phenomena is essential.

Additionally, new fuels, synthesized from biomass, and the improvement of their combustion process stands in the focus of scientific interest. By reducing the dependence on fossil fuels, the effect of global warming can be reduced. The German Cluster of Excellence (CoE) "Tailor-made Fuels from Biomass" at RWTH Aachen, University tries to design novel fuels from lignocellulosic biomass, a waste product in agriculture and timber industry [96]. The new fuels have to be tested and special new engine concepts have to be designed to increase efficiency and reduce pollutant emissions. The mixture of fuel and internal combustion flow field plays an important role in the optimization of the combustion process. Therefore, the Chair of Fluid Mechanics and Institute of Aerodynamics Aachen (AIA) experimentally investigates the cold mixing process during intake and compression stroke inside an internal combustion engine.

Previous work focused on the investigation of the planar flow field inside different engines. Dannemann et al. [30, 29] performed planar two-component particle-image velocimetry (PIV) measurements for several crank angles and several planes inside the combustion chamber of an unfired four-valve IC engine at 1,500 rpm. They analyzed the three-dimensional structure of the flow field. It was possible to visualize the large scale flow structures, i.e., the tumble vortex and ring vortices below the intake valves. Furthermore, the analysis revealed the highly three-dimensional character of the flow field. Karhoff et al. [48] compared the flow structures of the three-dimensional flow field in two four-valve IC engines with different intake port geometries. The study is based on the analysis and comparison of the temporal development of the mean kinetic energy, the turbulent kinetic energy, and the vorticity. They show a positive effect of a tumble port intake geometry on the mean vorticity of the flow field compared to an engine without tumble port. Furthermore, Karhoff [49] investigated the temporal evolution of the flow field in a driven IC engine by means of high-speed stereoscopic PIV. It was possible to show significant variations in the development of the mean kinetic energy and the turbulent kinetic, which suggests a high cyclic variability of the flow field. This could also be confirmed by investigating the tumble movement of several cycles and comparing it the the mean tumble movement. Bücker et al. [20, 18] performed stereoscopic PIV measurements in a set of planes for several crank angles at 1,500 rpm.

They analyzed the temporal development of the mean kinetic energy in two planes. Furthermore, by analyzing 14 axial planes, a quasi three-dimensional propagation of the large scale vortical structures could be reconstructed. Additionally, Bücker et al. [21] investigated a variable valve timing as an in-cylinder flow control mechanism. It could be shown that turbulent kinetic energy, kinetic energy, and vorticity show a dependency on the intake valve timing. This effect can be used to control the mixture of fuel and air, prevent fuel impingement, and control the combustion rate.

In this study, the three-dimensional volumetric velocity field of an internal combustion engine is investigated by means of laser optical flow measurement techniques to gain information on the large-scale flow structures and the mixture between fuel and flow field. By volumetrically measuring the flow field for different crank angles it is possible to analyze the three-dimensional character of the whole in-cylinder flow field at the SUZI engine operated at 1,500 rpm. Furthermore, the mixture formation of two bio-fuels, i.e., ethanol and methyl ethyl ketone (MEK), is analyzed inside the TINA research engine. This is done by means of planar Mie scattering to investigate the liquid penetration length of both fuels. Furthermore, the interaction of ethanol spray and flow field is directly investigated using planar stereoscopic particle-image velocimetry. This provides an insight in the highly complex mixture process and the interaction of liquid fuel and air inside the combustion chamber of the TINA research engine.

First a review concerning internal combustion engine flows, optics, and optical flow measurement techniques is given. After that, the two test engines, SUZI and TINA, and the test setups for the holographic particle-image velocimetry measurements, the tomographic particle-image velocimetry measurements, the stereoscopic particle-image velocimetry measurements, and the Mie scattering imaging measurement are explained in detail. After that, the results of the experimental volumetric and planar measurements are analyzed at length. This starts with the description of the volumetric flow field propagation. After that the interaction of fuel spray form an A-type hollow cone injector and flow field are analyzed in detail. The thesis finishes with a conclusion and an outlook for future work.

2

Internal Combustion Engines

2.1 Introduction

Internal combustion (IC) engines transfer chemical energy in the form of fossil fuels into mechanic energy by burning fuel and air inside the liner of the engine. IC engines can be divided in rotary engines, reaction engines, and reciprocating engine. In this thesis, the flow field inside two reciprocating four-stroke spark ignition (SI) IC engines is analyzed. The first approach of this type of engine is related to Dr. N. A. Otto who patented a stationary gas engine in 1876 (Heywood, [44]). The idealized energy generating process of this kind of engine can be expressed by a p-V diagram (fig 2.1).

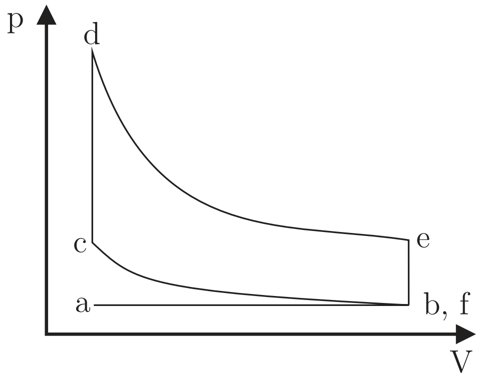

Figure 2.1 – P-V diagram of the ideal Otto cycle.

The corresponding piston movement is shown in figure 2.2. At point "a", the piston is at the top of its movement. This position is commonly referred to as top dead center (tdc). The inlet valves are open, the exhaust valves are closed. From this position, the piston moves downward, drawing in air at ambient pressure. The position "b" is at the bottom of the piston movement. It is called bottom dead center (bdc) and the stroke from tdc to bdc is known as the intake stroke. At bdc, the inlet valves close instantaneously. Mind, that this instantaneous closing of the inlet valves is an idealization, as valves cannot close instantaneously. After reaching bdc, the piston moves upwards and compresses the air. Due to the compression the air is heated but

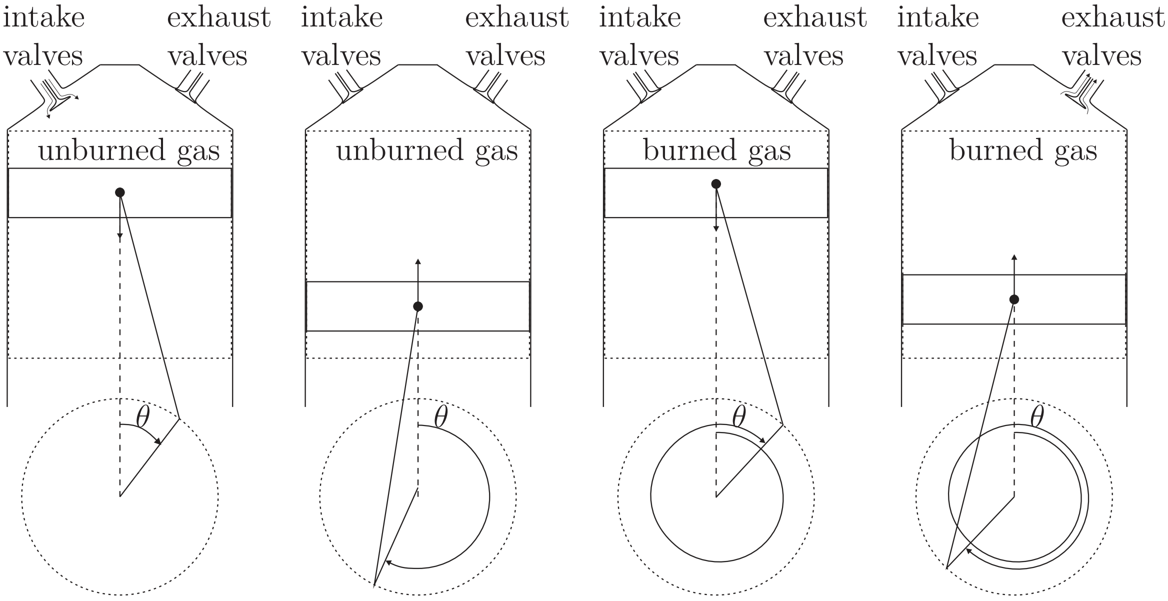

(a) Intake stroke. (b) Compression stroke. (c) Power stroke. (d) Exhaust stroke.

Figure 2.2 – The four cycles of the Otto process.

heat losses through the cylinder wall are neglected so that the process can be assumed to be adiabatic. When the piston reaches point "c" a specific amount of heat is added to the idealized process. This corresponds to heat released by the combustion of gasoline and air. The instantaneous release of heat, resulting in a pressure raise from point "c" to "d" is another idealization as the charge burns gradually in real engines. The crank shaft continues to turn, as the piston is pushed downward by the high pressure inside the cylinder until it reaches point "e" at btc. Here, the exhaust valves open instantaneously and the cylinder pressure drops to atmospheric pressure corresponding to a movment in fig. 2.2 from point "e" to "f". After that, the piston rises to the top to point "a", expelling the gas through the open exhaust valves. The resulting work of an Otto-cycle is equal to the area within the diagram of fig. 2.2. As some of the heat created through combustion is released through the exhaust valves, not all thermic energy is converted to work. An efficiency can be defined, using an isentropic compression from "b" to "c" and an isentropic expansion from "d" to "e" [44]. The resulting efficiency reads:

$$\eta_{ac} = 1 - \left(\frac{1}{r}\right)^{\kappa-1} \quad . \tag{2.1}$$

Here, the subscript "ac" refers to air cycle, as the medium in the idealized Otto cycle is assumed to be air, r is the compression ratio and, κ is the ratio of specific heats, $\kappa = c_p/c_v$, the specific heats at constant pressure and at constant volume. For diatomic gases at normal temperature $\kappa = 1.4$. The compression ratio is defined as

$$r = \frac{V_d + V_c}{V_c} \tag{2.2}$$

and can be in the range of 7 to 24. The quantities V_c and V_d refer to the minimum

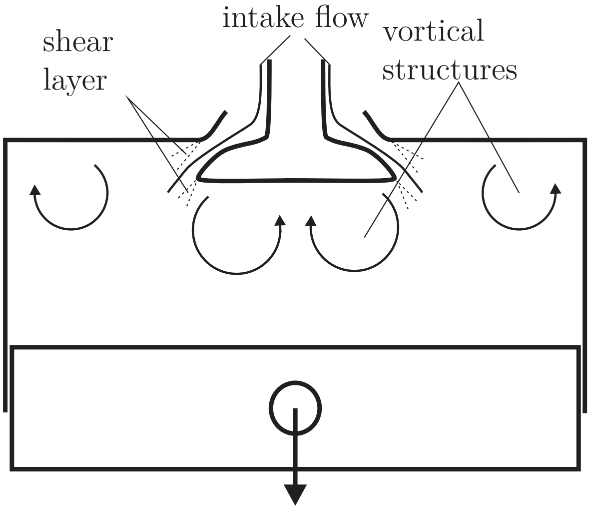

Figure 2.3 – Exemplary intake in cylinder flow field.

volume, or clearance volume, inside the cylinder at tdc and the displacement volume,

$$V_d = \frac{\pi B^2 S}{4} \tag{2.3}$$

with B being the bore and S the stroke of the engine.

2.2 Flow Characteristics

The flow field in internal combustion engines is very complex and consists of several large and small scale vortical structures, shear, and boundary layers. During intake the fluid enters the engine through small gaps between intake valves and pent roof with high velocity. These high speed jets separate from the intake valves and the pent roof. The resulting shear layers create recirculating regions below the intake valves and generate ring-like vortical structures below the valves and in the upper corner of the pent roof, which can be seen in fig. 2.3. However, the high speed jet is used to create either a tumbling or a swirling motion which can be seen in fig. 2.4. These large scale vortical structures are created by intake port geometry as explained by Borée and Miles [16]. Swirl can normally be found in Diesel engines whereas tumbling motion is most common in SI engines. These large scale vortical structures are normally used for crude mixing of fuel and air and to conserve energy during compression. At the end of compression they decompose releasing turbulent kinetic energy and speeding up the combustion process [44].

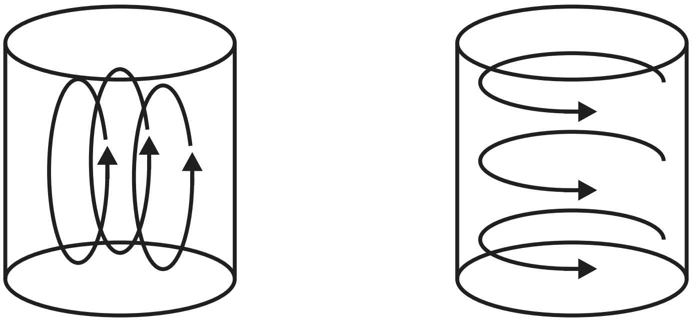

(a) tumble (b) swirl

Figure 2.4 – Large scale flow motions of the in-cylinder flow field.

2.3 Mathematical Flow Description

The flow field in IC engines can be described using an Eulerian approach. With this, the flow field velocity vector $\vec{v}(r,t)$ is defined for a spatial position in time. The spatial vector $\vec{r}$ can be expressed in Cartesian coordinates by:

$$\vec{r} = \begin{pmatrix} x \\ y \\ z \end{pmatrix} \quad . \tag{2.4}$$

With this, the velocity vector is composed of three Cartesian velocity components such that,

$$\vec{v} = \begin{pmatrix} u \\ v \\ w \end{pmatrix} \quad . \tag{2.5}$$

with u, v, and w being the velocity components in x-, y-, and z-direction. In general, Reynolds decomposition can be used to separate turbulent velocity field into their mean velocity and a fluctuating velocity part. Therefore, the velocity $\vec{v}$ can be written as

$$\vec{v} = \overline{v} + v' \tag{2.6}$$

with $\overline{v}$ being the mean velocity and v' the fluctuating velocity. The mean velocity $\overline{v}$ can be calculated by

$$\overline{v} = \lim_{T->\infty} \frac{1}{T} \int_{t_0}^{t_o+T} udt \tag{2.7}$$

with T being the time span and t_0 being the starting time. However, as the flow field in IC engines is not stationary but rather dependent on crank angle, an ensamble averaged velocity is commonly used, which is defined by:

$$\overline{v(\theta)} = \frac{1}{N} \sum_{n=1}^{N} u(\theta, n) \quad . \tag{2.8}$$

Here, θ is the corresponding crank angle and N is the number of cycles used, for calculating the ensemble mean velocity. The fluctuating velocity component v' can further be divided into a cyclic component v'_c and a turbulent component v'_t such that

$$v'(\theta) = v'_c(\theta) + v'_t(\theta) \quad . \tag{2.9}$$

Mind that neither cyclic nor turbulent fluctuations in IC engines are fully understood. It is assumed that the former are low frequency fluctuations caused by large-scale variations in flow structures [16]. These are caused by changing boundary conditions like variations in intake air pressure or temperature gradients. Cyclic variations are assumed to be destructive as they create non-reproducible changes in engine flow and therefore changes in combustion and exhaust gas emissions. Turbulent fluctuations are of high frequency and assumed to be stochastic [81, 99]. The rate of turbulent fluctuations is related to the engine Reynolds number that can be calculated as:

$$Re_{Engine} = \frac{10 \cdot S \cdot n \cdot B}{3 \cdot \nu} \tag{2.10}$$

as introduced by Borée et al. [16] with S, n, and B being the engine stroke, frequency, and bore, respectively. The Reynolds numbers for the investigated engines are $Re_S \approx 48.500$ for the SUZI engine and $Re_T \approx 34.000 - 46.000$ for the TINA engine, depending on the investigated engine rpm.

Therefore, the following statistic quantities are based on u' rather than separating the fluctuation in flow velocities into turbulent and cyclic variability.
Tennekes and Lumley [98], and Heywood [44] define the ensemble averaged variance $\overline{v'^2}$ as

$$\overline{v'^2} = \sigma_v^2 = \frac{1}{N} \sum_{n=1} N (v_n - \overline{v})^2 \tag{2.11}$$

with σ_v being the standard deviation of v. As turbulence plays an important role for IC engines, as it improves mixing and flame propagation, turbulence can be expressed by the mean turbulent kinetic energy k (Tennekes and Lumley [98]) in general:

$$\overline{k(\theta)} = \frac{1}{2} \sqrt{\overline{u'^2} + \overline{v'^2} + \overline{w'^2}} \quad . \tag{2.12}$$

Using the instantaneous fluctuating terms, the instantaneous turbulent kinetic energy reads

$$k(\theta, n) = \frac{1}{2} \sqrt{u'^2 + v'^2 + w'^2} \quad . \tag{2.13}$$

For analysis of temporal resolved data the plane averaged turbulent kinetic energy

$$\overline{k(\theta, n)_A} = \frac{1}{LMN} \sum_{i=1}^{L} \sum_{j=1}^{M} \sum_{k=1}^{N} k(\theta, n)_{i,j,k} \tag{2.14}$$

can be used to gain a general overview about turbulence development during one cycle. The quantities L, M, and N are the number of spatial grid points in x-, y-, and z-direction. Furthermore, the ensemble and plane averaged turbulent kinetic energy is given by

$$\overline{k(\theta)_A} = \frac{1}{LMN} \sum_{i=1}^{L} \sum_{j=1}^{M} \sum_{k=1}^{N} \overline{k(\theta)_{i,j,k}} \quad . \tag{2.15}$$

To analyze the spatial character of the flow the velocity field can most easily be visualized using streamlines. A streamline describes a line that is tangential to the velocity field such that

$$\frac{dx}{u} = \frac{dy}{v} = \frac{dz}{w} \quad . \tag{2.16}$$

Furthermore, the vorticity vector

$$\vec{\omega} = \nabla \times \vec{v} = \begin{pmatrix} \omega_x \\ \omega_y \\ \omega_z \end{pmatrix} = \begin{pmatrix} \frac{\partial w}{\partial y} - \frac{\partial v}{\partial z} \\ \frac{\partial u}{\partial z} - \frac{\partial w}{\partial x} \\ \frac{\partial v}{\partial x} - \frac{\partial u}{\partial y} \end{pmatrix} \tag{2.17}$$

can be used to analyze vortical structures in flow fields. To reduce errors occouring from random errors, Raffel [85] suggests using a least-square approach for calculating differential data like vorticity that is given by

$$\left(\frac{df}{dx}\right)_i \approx \frac{2f_{i+2} + f_{i+1} - f_{i-1} - 2f_{i-2}}{10\Delta X^2} \quad . \tag{2.18}$$

Abdelfattah [2] used an equivalence to streamlines to investigate the spatial distribution of vortices by defining vortex lines by

$$\frac{dx}{\omega_x} = \frac{dy}{\omega_y} = \frac{dz}{\omega_z} \quad . \tag{2.19}$$

Equivalent to a streamline, a vortex line is described by a line that is tangential to the vorticity field. The out of plane component of the absolute mean vorticity vector can be used to determine a vortex core. Vortical structures in flow fields can be identified through different methods. Graftieaux et al. [38] introduced the Γ_1 vortex center criterion. The dimensionless scalar function Γ_1 is defined as follows:

$$\Gamma_1 = \frac{1}{s}\sum_{i=1}^{s} \frac{\vec{r} \times \vec{v}}{||\vec{r}||\,||\vec{v}||} \quad . \tag{2.20}$$

Here, s represents the number of grid points to calculate Γ_1, $\vec{r}$ the radius vector, and $\vec{v}$ the velocity vector at point i, which can also be seen in fig. 2.5. Although this function is, unlike vorticity, not independent of the frame of reference, it can still be used to detect vortex cores in three-dimensional flow fields. For this, the velocity field itself has to be rotated around one axis, which is shown in eq. 2.21 for a rotation around the z-axis.

$$\vec{v}(\alpha) = \begin{bmatrix} \cos\alpha & -\sin\alpha & 0 \\ \sin\alpha & \cos\alpha & 0 \\ 0 & 0 & 1 \end{bmatrix} \cdot \begin{bmatrix} u \\ v \\ w \end{bmatrix} \quad . \tag{2.21}$$

Another approach for vortex identification was introduced by Jeong and Hussain [47]. They defined the λ_2-criterion. The quantity λ_2 is the second largest eigenvalue of the symmetric matrix $M = S^2 + \Omega^2$, with

$$S = \frac{1}{2}((\nabla\vec{v} + \nabla\vec{v}^T) \tag{2.22}$$

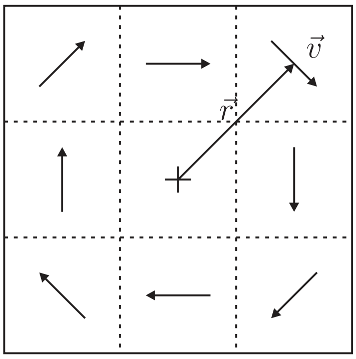

Figure 2.5 – Definitions of the Γ_1 vortex center identifications criterion with S=9 (Stansfield et al. [94] and Graftieaux et al. [38])

and

$$\Omega = \frac{1}{2}((\nabla\vec{v} - \nabla\vec{v}^T) \quad . \tag{2.23}$$

Values of $\lambda_2 < 0$ represent vortex cores. However, one has to keep in mind that PIV is a discrete grid-based method. Therefore, gradient based methods to calculate vortices are prone to truncation errors that increase with increasing grid sizes (Louranco and Krothapalli [57]).
For the analysis of the large scale vortical structures in terms of an absolute value, the tumble and swirl ratios are defined as [58, 46]:

$$TR_x = \frac{\omega_x}{\omega_e} = \frac{\sum_{n=1}^{m}(yw - zv)}{\omega_e \sum_{n=1}^{m}(y^2 + z^2)} \tag{2.24}$$

$$TR_y = \frac{\omega_y}{\omega_e} = \frac{\sum_{n=1}^{m}(zu - xw)}{\omega_e \sum_{n=1}^{m}(x^2 + z^2)} \tag{2.25}$$

$$SR_z = \frac{\omega_z}{\omega_e} = \frac{\sum_{n=1}^{m}(xv - yu)}{\omega_e \sum_{n=1}^{m}(x^2 + y^2)} \tag{2.26}$$

with m being the number of total grid points for discrete measurement date. The ratios describe the angular velocities ω_x, ω_y, and ω_z of the solid body rotations normalized to the angular velocity of the engines crank shaft ω_e. Unfortunately, these quantities do not account for counter rotating flow inside the engine. Therefore, Dannemann [29] introduced the absolute value of the averaged vorticity ω divided by the crank shaft angular speed, ω_e with:

$$\Omega_i = \frac{1}{m\omega_e}\sum_{n=1}^{m}|\omega_i| \quad . \tag{2.27}$$

2.3.1 Primary Breakup of Fuel Sprays

This subsection will give a brief overview about the general classification of the primary breakup. A detailed overview can be found in Mathieu [62] and Reddemann [86]. The

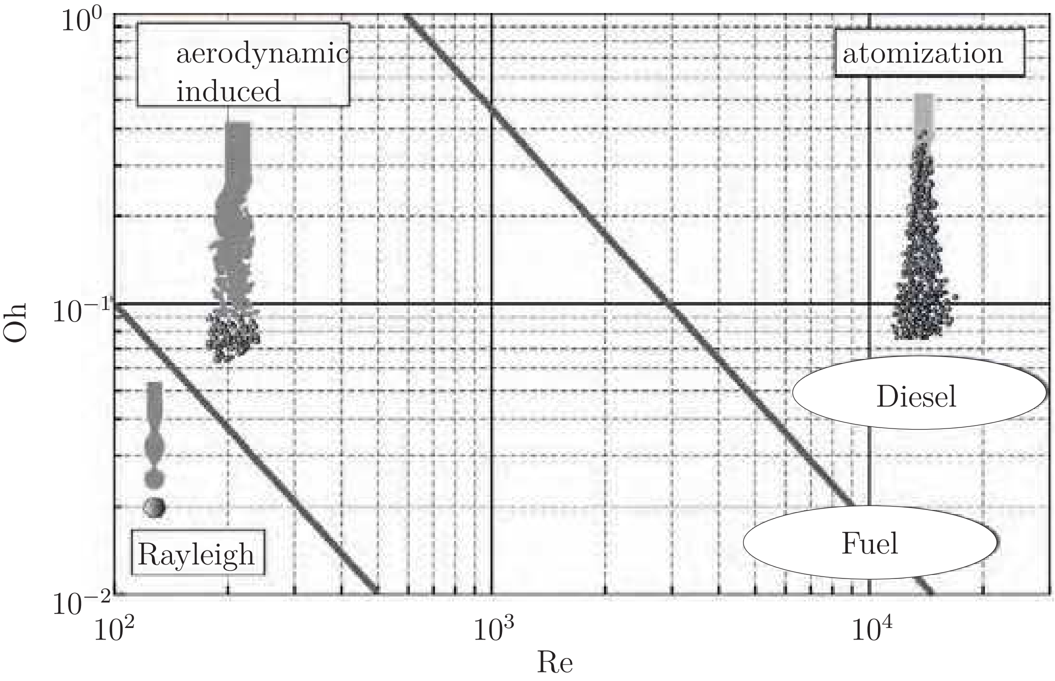

Figure 2.6 – Primary breakup regimes defined Ohnesorge [66] and Leick [56] (from Mathieu [62]).

primary breakup can be classified by three dimensionless numbers. This is the Reynolds number

$$Re = \frac{\rho_l v_{sp} d}{\eta} \quad , \tag{2.28}$$

the Ohnesorge number that relates the viscous forces to inertial and surface tension forces

$$Oh = \frac{\eta}{\sqrt{\rho_l \sigma d}} \quad , \tag{2.29}$$

and the density gradient of fuel and air

$$\rho^* = \frac{\rho_g}{\rho_f} \quad . \tag{2.30}$$

The Reynolds number determines the grade of turbulence for a fuel spray and is calculated using the nozzle exit velocity, v_{sp}, and the nozzle diameter d. The Ohnesorge number is only dependent on the nozzle geometry and fuel properties, that is, the fuel density ρ_f, the fuel surface tension σ and the fuel dynamic viscosity η. It is used to classify the primary breakup into different regimes. Figure 2.6 shows the different regimes defined by Ohnesorge. For very low Reynolds numbers the breakup is induced by inertia and surface tension, which causes amplified oscillations. Through this, the fuel jet is necked until it dissolves into bigger droplets. With higher Reynolds numbers, inertia forces get more important such that the breakup is earlier after injection with smaller droplets. For high Reynolds and Ohnesorge numbers the fuel is atomized into very small droplets shortly after the injector. This is the primary case of application for fuel injection. The two lines in fig. 2.6 are showing the transient area between two different breakup regimes. Furthermore, with increasing density ratio, these regimes shift to smaller Reynolds numbers. Finally, to determine the nozzle Reynolds number, the exit velocity has to be calculated. This is normally done using a Bernoulli approach:

$$v = C_d \sqrt{\frac{2(p_i - p_a)}{\rho_f}} \quad . \tag{2.31}$$

The quantities C_d, p_i, and p_a are a nozzle and fuel dependent discharge coefficient in the range of 0.65 - 0.93 [62]. the injection pressure, and the ambient pressure, respectively.

3

Optics

In the following chapter a short introduction to the fundamental laws of optic that are relevant for the used measurement techniques in this thesis is given. It starts with the description of basic geometric optics. After that, the physical approach, describing light as an electromagnetic function will be explained. Finally, the main aspects of holographic recordings are introduced. A comprehensive treatment of this topic is given by Demptröder [32] and Hecht [40].

3.1 Gemoetrical Optics

In geometric optics, light propagation is described in terms of rays perpendicular to the light's wavefront, neglecting the wave character of light and therefore diffraction. This approximation is valid for for light rays with a diameter D greater than two times its wave length λ. The basic laws are given by the principles of reflection, refraction, and superposition. When a light ray hits a reflective surface, e.g., a mirror, under an angle θ_1 it is reflected and the angle of incidence equals the angle of reflection θ_3, see fig. 3.1:

$$\theta_1 = \theta_3 \qquad . \tag{3.1}$$

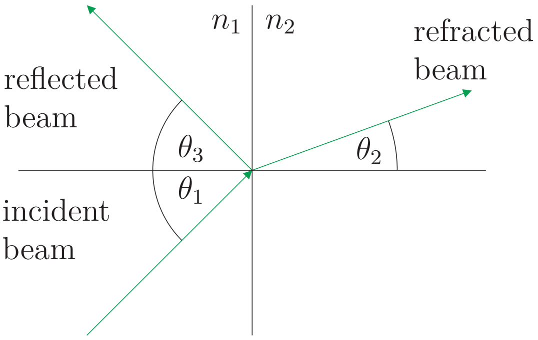

Figure 3.1 – Reflection and refraction of light

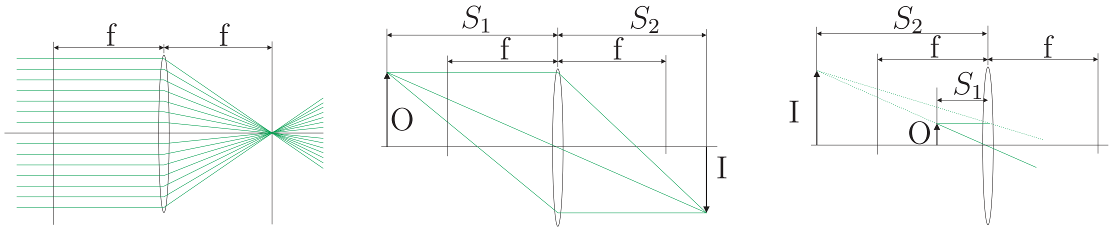

(a) focal length. (b) real image (c) virtual image

Figure 3.2 – Geometric properties of a thin lens as an optical imaging system.

Figure 3.1 also shows refraction which refers to a change in light beam direction due to different optical media. Assuming a light beam crossing the boundary between two media with different refractive indices n_1 and n_2, the refraction angle θ_2 can be determined by Snell's law:

$$n_1 \sin\theta_1 = n_2 \sin\theta_2 \qquad . \tag{3.2}$$

Here, θ_2 is the angle between the surface normal and the refracted beam. Furthermore, the principle of superposition states that there is no interaction with overlapping optical beams.

These basic principles can be used to analyze optical systems. This is of special interest for the analysis of lens systems. In conjunction with the paraxial approximation, that is a small angle approximation, lens systems can be analyzed. Taking into account a lens of negligible thickness a connection between focal length of the lens f, distance between lens and object plane S_1 and image plane S_2 can be estimated:

$$\frac{1}{f} = \frac{1}{S_1} + \frac{1}{S_2} \qquad . \tag{3.3}$$

For a converging lens, the focal length f is the distance from the lens to the point, where a collimated beam will be focused (see fig. 3.2(a)). If an object is placed in the distance S_1 from the lens an image I is created at the distance S_2 if the distance S_1 is larger than f (see fig. 3.2(b)). This image can be seen by placing a screen within the image plane. This image is known as the a real image. If S_1 is smaller than f, a virtual image is created at the same side as the object. This virtual image can be seen by an observer looking through the lens (see fig. 3.2(b)).

The first order and the thin lens approximation normally suffice to describe optical systems. However, for a more detailed description of lens systems, the lens thickness as well as aberrations have to be taken into account.

Aberrations can be divided into chromatic (aberrations due to the frequency of the light wave, see fig. 3.3(a)) and monochromatic aberrations. For chromatic aberrations the focal length depends on the wave length of the light. Monochromatic aberrations are independent from the wave length and can be divided into spherical aberrations, coma, astigmatism, distortion and field curvature. The different types of aberrations can be seen in fig. 3.3. These monochromatic aberrations enlarge or blur the image. Spherical aberrations (fig. 3.3(b)) are created through an increased refraction of light near the edge of a lens. This leads to a blurred image of the point source. Figure 3.3(c) shows a coma. This aberration is created by rays passing a thin lens under an angle to the optical axis creating a comet like image. Figure 3.3(d) refers to astigmatism. This monochromatic aberration is created through different points of focus for two perpendicular planes if the point is away from the optical axis. Figure 3.3(e) refers to Petzval field curvature. This effect causes a flat object normal to the optical axis to be pictured in a spherical image surface. The last monochromatic aberration is distortion (see fig 3.3(f)). This aberration is caused by different focal lengths for different parts of the lens. In the absence of other aberrations distortion can be seen through a deformation of the whole image while every point in the image is sharp.

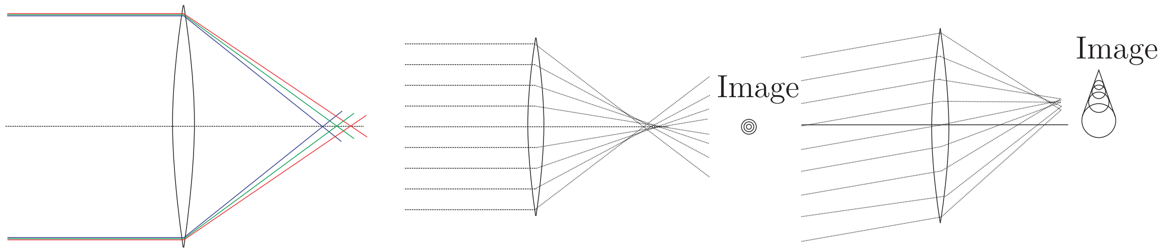

(a) Chromatic abberation (b) spherical aberration (c) Coma

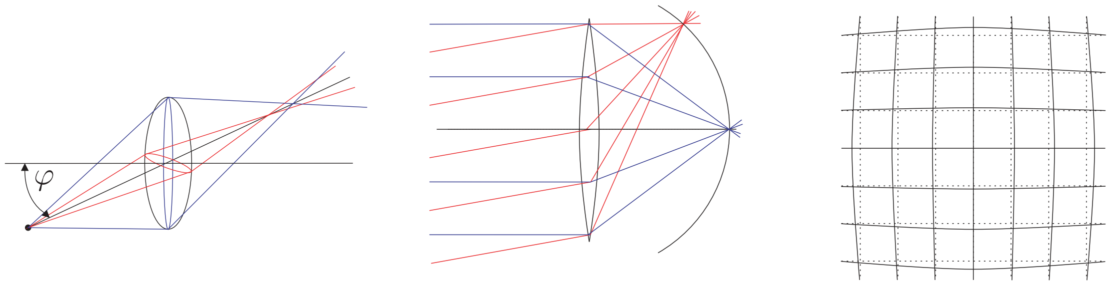

(d) Astigmatism (e) field curvature (f) Distortion

Figure 3.3 – Optical aberrations.

3.2 Physical Optics

The behavior of light can be expressed through the Maxwell equations for a time dependent electromagnetic wave:

$$\Delta\vec{E} - \frac{1}{\nu}\frac{\partial^2\vec{E}}{\partial t^2} = 0 \quad and \tag{3.4}$$

$$\Delta\vec{B} - \frac{1}{\nu}\frac{\partial^2\vec{B}}{\partial t^2} = 0 \qquad , \tag{3.5}$$

with Δ beeing the Laplace operator

$$\Delta = \nabla^2 = \frac{\partial^2}{\partial x^2} + \frac{\partial^2}{\partial y^2} + \frac{\partial^2}{\partial z^2} \quad , \tag{3.6}$$

t the time, and $\vec{E}$ and $\vec{B}$ the electrical and the magnetic field intensity, respectively. The quantity ν describes the phase velocity of the wave with propagation speed c in a given medium with refraction index n:

$$\nu = \frac{c}{n} \qquad . \tag{3.7}$$

The energy flux of an electromagnetic wave can be expressed by the Poynting-vector $\vec{S}$ that has the direction of the propagating wave (Hecht [40]):

$$\vec{S} = c^2 \epsilon_0 \vec{E_0} \times \vec{B_o} \cos^2(\vec{k} \cdot \vec{r} - \omega t) \qquad . \tag{3.8}$$

The quantity ϵ_0 refers to the vacuum permittivity.
As $\vec{B}$ and $\vec{E}$ are perpendicular to each other commonly only the equation for the electrical field is used to describe a light wave. For planar polarized light waves propagating in z-direction ($\vec{E} = (0, 0, E_x)$) in vacuum (n = 1) eq. 3.4 can be simplified to:

$$\frac{\partial^2 E_x}{\partial z^2} - \frac{1}{c^2} \frac{\partial^2 E_x}{\partial t^2} = 0 \qquad . \tag{3.9}$$

Equation 3.9 can be expressed in form of a wave equation:

$$\vec{E_x}(z, t) = E_{0,x} cos(kz - \omega t - \varphi_0) \tag{3.10}$$

with $E_{0,x}$ being the maxium amplitude of E, k the wave number, and ω the angular frequency, respectively:

$$k = \frac{2\pi}{\lambda} \quad and \quad \omega = 2\pi f \qquad . \tag{3.11}$$

Here, f denotes the frequency of the wave, whereas λ is its wavelength. Frequency and wavelength are related by the speed of light:

$$c = f\lambda \qquad . \tag{3.12}$$

The spatially variing term

$$\varphi = -kz - \varphi_0 \tag{3.13}$$

is named phase with φ_0 being a constant phase shift. For visible light, its vacuum wavelength is in the range of 400 nm (violet) to 780 nm (red). This results in a frequency range of $3.8 \cdot 10^{14}$ Hz to $7.5 \cdot 10^{14}$ Hz. As light sensors are not able to resolve such high frequencies, the only measurable quantity is light intensity. As intensity is proportional to the time average of the square of the electrical field, it can be expressed as follows:

$$I = \frac{\epsilon_0 c}{2} \left\langle E_0^2 \right\rangle_t = \epsilon_0 c \lim_{T -> \infty} \frac{1}{2T} \int_{-T}^{T} E^2 dt \qquad . \tag{3.14}$$

Here, $\langle\rangle$ denotes the time average of the light wave.

3.2.1 Coherence

Coherence describes the correlation between individual electromagnetic waves. It can be divided into temporal and spatial coherence. The former describes the correlation between electromagnetic waves observed at different moments in time, whereas the latter describes the correlation between electromagnetic waves at different points in space (Kreis [52]).

Temporal Coherence

As already mentioned, light can be expressed as a sine wave with a given amplitude. However, for real light waves the frequency of the wave is not monochromatic but composed through a frequency band. The superposition of the different frequencies causes spontaneous phase shifts in the electromagnetic wave. The time between these spontaneous phase shifts is called temporal coherence Δt_c, which is directly proportional to the inverse band width $\Delta\nu$ of the electromagnetic wave. The easiest way to visualize temporal coherence is with the aid of a Michelson interferometer, see fig 3.4: At a beam splitter light is divided into two separate beams. One light beam that is called E_1 is reflected at a fixed mirror, whereas the second beam that is called E_2 is reflected by a moveable mirror. Both beams travel back and hit a screen. Due to the movement of the second, moveable mirror, a time shift can be introduced between the different beams. This time shift can be changed, changing the position of the moveable mirror. The relationship between both beams is then given by:

$$E_2(t) = E_1(t+\tau) \tag{3.15}$$

where

$$\tau = \frac{2d}{c} \quad . \tag{3.16}$$

At the screen, a superposition of both beams can be observed with

$$E(t) = E_1(t) + E_2(t) = E_1(t) + E_1(t+\tau) \tag{3.17}$$

and the intensity

$$\begin{aligned} I &= \langle EE^* \rangle \\ &= \langle E_1E_1^* \rangle + \langle E_2E_2^* \rangle + \langle E_2E_1^* \rangle + \langle E_1E_2^* \rangle \\ &= 2I_1 + 2Re(\langle E_1E_2^* \rangle) \end{aligned} \tag{3.18}$$

due to the assumption of equal amplitudes for both waves. Defining a complex self coherence $\Gamma(\tau)$ as

$$\begin{aligned} \Gamma(\tau) &= \langle E_1(t)^* E_1(t+\tau) \rangle \\ &= \lim_{T->\infty} \frac{1}{T} \int_{-T}^{T} E_1^*(t) E_1(t+\tau) dt \quad . \end{aligned} \tag{3.19}$$

This is the auto-correlation function of $E_1(t)$. By defining a normalized quantity

$$\gamma(\tau) = \frac{\Gamma(\tau)}{\Gamma(0)} \tag{3.20}$$

a degree of coherence can be defined.

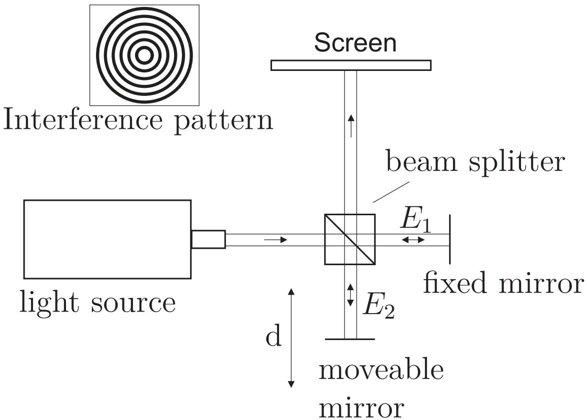

Figure 3.4 – Schematic of a Michelson-Interferometer.

Spatial Coherence

Spatial coherence describes the correlation of different parts of the same electromagnetic wave (Kreis [52]). This can be best described by Young's double slit experiment, which can be seen in fig. 3.5. An opaque wall with two holes or parallel slits with a distance d is illuminated by a light source, which is a distance R away from the wall. On an observation screen at a distance "L" from the wall light passing through the holes or slits forms an interference pattern. The distances between light source and slits are r_1 and r_2 and the distances from the two slits to one observation point are l_1 and l_2. As we can assume that the intensity of both light waves leaving the slits is identical, the intensity at the observation point is defined as

$$I(x,y) = 4I_0(x,y)cos^2(\Delta\varphi(x,y)) \tag{3.21}$$

with $\Delta\varphi(x,y)$ being the half phase difference defined by

$$\Delta\varphi(x,y) = \frac{2\pi\Delta l}{2\lambda} \tag{3.22}$$

whith Δl being the difference in path length of the light from the light source to the observation point $B = (0, y_0, 0)$ defined by

$$\begin{aligned}\Delta l &= r_2 + l_2 - r_1 - l_1 \\ &= \sqrt{R^2 + (d/2 + y_1)^2} + \sqrt{L^2 + (d/2 - y_0)^2} \\ &- \sqrt{R^2 - (d/2 - y_1)^2} - \sqrt{L^2 + (d/2 + y_0)^2} \quad .\end{aligned} \tag{3.23}$$

By assuming that y_0 and d are small compared to L and R, the square roots of the form $\sqrt{1+b}$ can be approximated by $1 + b/2$ such that

$$\Delta l = -d\left(\frac{y_1}{R} + \frac{y_0}{L}\right) \quad . \tag{3.24}$$

This results in an intensity distribution of

$$I = I_0 cos^2\left[\frac{\pi d}{\lambda}\left(\frac{y_1}{R} + \frac{y_0}{L}\right)\right] \tag{3.25}$$

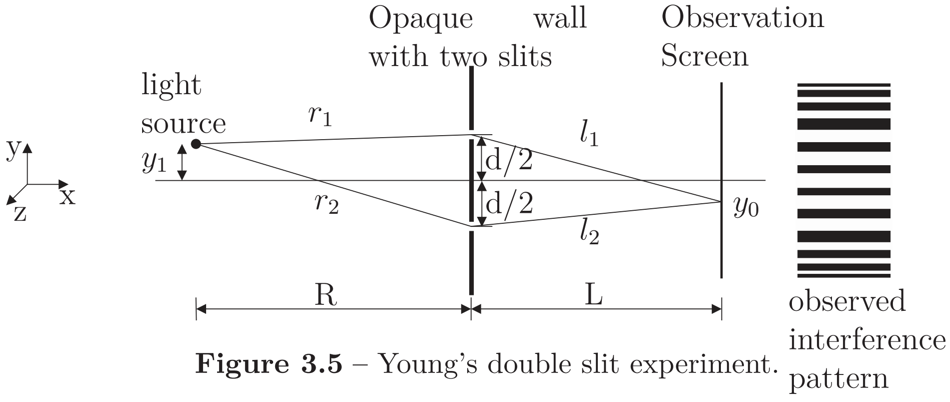

Figure 3.5 – Young's double slit experiment.

which describes a fringe pattern parallel to the x-axis with a spacing of $\lambda L/d$ in y-direction. With this, the spatial coherence for a given time t can be described as:

$$\Gamma_{12}(0) = \langle E_1(-d/2,t)^* E_1(d/2,t)\rangle \tag{3.26}$$

The equations for spatial and temporal coherence can be combined yielding a mutual coherence function. For a general case (see fig. 3.6) this can be defined as:

$$\Gamma_{12}(\tau) = \langle E_1(-d/2,t)^* E_1(d/2,t)\rangle \quad . \tag{3.27}$$

This equation can be normalized, yielding the complex degree of mutual coherence:

$$\gamma_{12}(\tau) = \frac{\Gamma_{12}(\tau)}{\sqrt{\Gamma 11(0)\Gamma 22(0)}} \quad . \tag{3.28}$$

Γ_{11} and Γ_{22} describe the intensities at r_1 and r_2, respectively. With this, the following cases of mutual coherence can occur ($\tau \neq 0, |\gamma_{12}| = 1$):

$$|\gamma_{12}(\tau)| = 1 \qquad \text{total coherence} \tag{3.29}$$

$$0 \leq |\gamma_{12}(\tau)| \leq 1 \qquad \text{partial coherence} \tag{3.30}$$

$$|\gamma_{12}(\tau)| = 0 \qquad \text{no coherence} \tag{3.31}$$

3.2.2 Polarization

Polarization describes the orientation of oscillation of an electromagnetic wave. Until now, light has been described as a planar wave that propagates in z-direction. Equation 3.10 describes a planar wave, propagating in z-direction with an oscillating electromagnetic field in x-direction. This wave is called horizontally polarized. A vertically polarized wave is described by:

$$\vec{E_y}(z,t) = E_{0,y}\cos(kz - \omega t + \varphi) \quad . \tag{3.32}$$

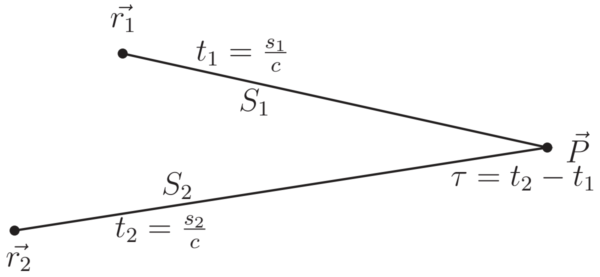

Figure 3.6 – Notation used in the derivation of the mutual coherence function (Lauterborn [55]).

Superposing both waves yields a polarization state depending on the electric field strength of $E_{0,y}$ and $E_{0,z}$ and their phase difference between each other. G.G. Stokes introduced in 1852 four parameters that describe the polarization state of an electromagnetic wave. Assuming the aforementioned superposition these parameters can be defined as:

$$\vec{S} = \begin{pmatrix} S_0 \\ S_1 \\ S_2 \\ S_3 \end{pmatrix} \begin{pmatrix} |E_{0,x}^2| + |E_{0,y}^2| \\ |E_{0,x}^2| - |E_{0,y}^2| \\ 2Re(E_{0,x}^* E_{0,y}) \\ 2Im(E_{0,x}^* E_{0,y}) \end{pmatrix} \quad . \tag{3.33}$$

S_0 defines the general intensity of the wave, whereas S_1, S_2, and S_3 define the polarization state. Positive values of S_1 define a horizontal and negative values of S_1 a vertical polarization state. S_2 defines a rotation of polarization around the z-axis with positive values resulting in a positive rotation. S_3 defines circular polarization with positive values of S_3 resulting in right circular polarization. An overview about different polarization states is given in fig. 3.7 (Hecht, [40]). The oscillating direction of eq. 3.10 and eq. 3.32 is orthogonal to each other.

3.2.3 Interference

Interference describes the change in amplitude for two or more overlapping coherent waves of similar polarization. Assuming two waves E_1 and E_2 with different wave vectors k_1 and k_2, phase differences φ_1 and φ_2, equal angular frequency ω, and equal amplitudes $E_{0,1}$ and $E_{0,2}$ the scalar notation is:

$$E_1(r,t) = E_{0,1}\cos(k_1 r - \omega t + \epsilon_1) \tag{3.34}$$

$$E_2(r,t) = E_{0,2}\cos(k_2 r - \omega t + \epsilon_2) \quad . \tag{3.35}$$

Superimposing both waves results in a new electromagnetic wave:

$$E(r,t) = E_{0,1}\cos(k_1 r - \omega t + \epsilon_1) + E_{0,2}\cos(k_2 r - \omega t + \epsilon_2) \quad . \tag{3.36}$$

With eq. 3.14 and assuming that only relative intensities in the same medium occur the intensity of the resulting wave can be written as;

$$I = \left\langle E^2 \right\rangle \tag{3.37}$$

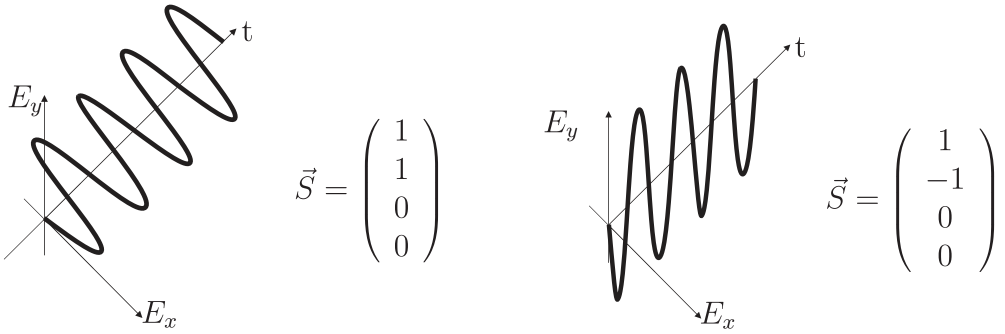

(a) horizontal polarization (b) vertical polarizaton

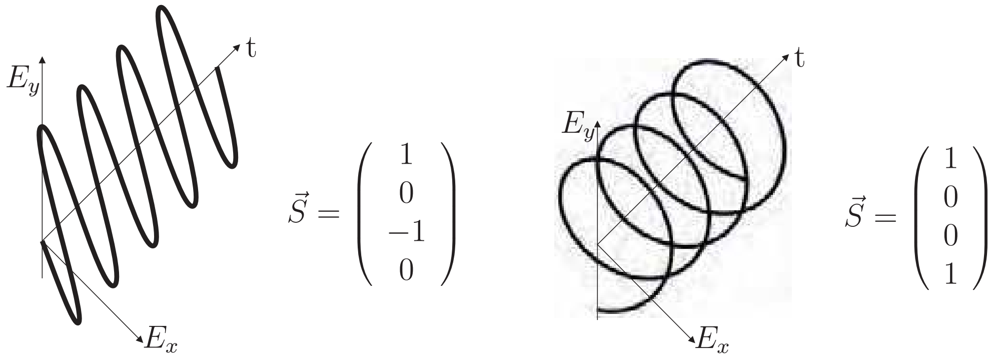

(c) -45° polarization (d) Right-hand circular polarization

Figure 3.7 – Examples of different polarization states.

with E^2 being

$$E^2 = (E_1 + E_2)(E_1 + E_2) = E_1^2 + E_2^2 + 2E_1E_2 \quad . \tag{3.38}$$

By calculating the temporal mean the total intensity is given by

$$I = I_1 + I_2 + I_{1,2} \tag{3.39}$$

with

$$I_1 = \left\langle E_1^2 \right\rangle_T \tag{3.40}$$

$$I_2 = \left\langle E_2^2 \right\rangle_T \tag{3.41}$$

$$I_{1,2} = \langle 2E_1E_2 \rangle_T \quad . \tag{3.42}$$

The quantity $I_{1,2}$ is called interference term (Hecht, [40]). By calculating the temporal mean of eq. 3.42 the interference term can be expressed by:

$$I_{1,2} = E_{0,1}E_{0,2}\cos\delta = 2\sqrt{I_1 I_2}\cos\delta \tag{3.43}$$

with $\delta = k_1 r - k_2 r + \epsilon_1 - \epsilon_2$ being the phase difference between E_1 and E_2 such that the total intensity can be written as:

$$I = I_1 + I_2 + \sqrt{I_1 I_2}\cos\delta \quad . \tag{3.44}$$

Depending on δ and the difference in I_1 and I_2 an increase or decrease in total light intensity is visible. Fig. 3.8 exemplary shows the interference of two coherent planar light waves with the same intensity.

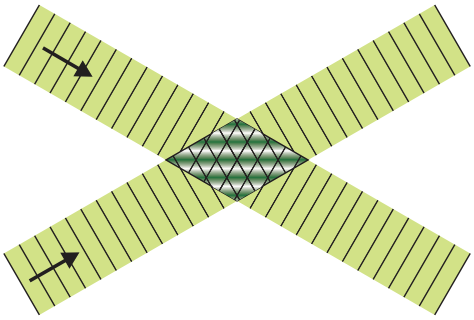

Figure 3.8 – Interference pattern of two planar interfering wave fronts.

3.2.4 Diffraction

Diffraction is the deflection of a wave by interacting with a transparent or opaque obstacle and is strongly related to interference. The Fresnel-Huygens principle states that every unshielded point of an elementary wave can be the source to a secondary elementary wave with the same wavelength. After this, the observerd amplitude is given by the superposition of every secondary elementary wave. This can be seen in fig. 3.9, which shows diffraction at a slit for two different cases. In fig. 3.9 a), the diffraction of a planar light wave at a slit with a width b in the order of the wave length of the light can be seen. The slit acts as a point source such that light waves propagate in concentric cicles. Fig. 3.9 b) the width of the slit b is much bigger than the wave length of the light. Therefore, the light wave downstream of the slit is composed of the superposition of several point sources. A more general explanation can be given observing the diffraction at a diffraction grating. With the Huygens-Fresnel principle,

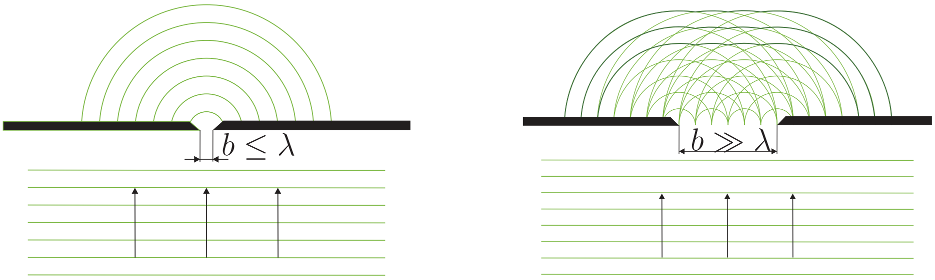

(a) Diffraction for a slit diameter in the order of the wave length.

(b) Diffraction for a slit diameter much bigger than the wave length.

Figure 3.9 – Diffraction pattern at an opaque wall with single slit.

the irradiance after the diffraction grating is given by:

$$I(\theta) = I_s \frac{\sin^2[\pi(b/\lambda)\sin(\theta)]}{[\pi(b/\lambda)\sin(\theta)]^2} \cdot \frac{\sin^2[N\pi(d/\lambda)\sin(\theta)]}{\sin^2[\pi(d/\lambda)\sin(\theta)]} \quad , \tag{3.45}$$

where N is the number of slits, b the width of the slits, d the distance between two slits, I_s the emitted irradiance of a single slit, and θ the angle between direction of propagation before and after the slits. The first factor describes the diffraction for one slit and the second one the interference between N slits. Maxima of $I(\theta)$ can be found for:

$$\sin(\theta) = m\lambda/d \quad m \in \mathbb{N} \quad . \tag{3.46}$$

Therefore, the order of diffraction is given by m. An example for 0th order and 1th order diffraction can be seen in fig. 3.10.

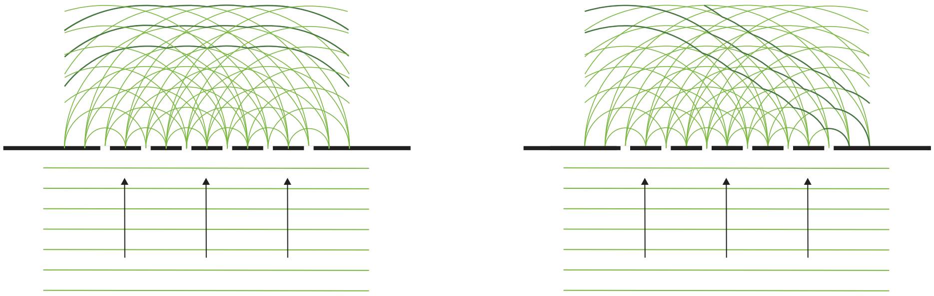

(a) 0th order diffraction.

(b) 1th order diffraction.

Figure 3.10 – Diffraction at a diffraction grating.

3.3 Holography

The word holography refers to the greek word $o\lambda o\varsigma$ (hólos), which means completely, and $\gamma\rho\alpha\varphi\eta$ (grafe) for written. In optics, it is an interference technique to record the wave character of light waves. It is able to not only store the amplitude, but also the phase information of a light wave on a photographic film plate such that a volumetric reconstruction of the image is possible [27]. The technique was invented by Garbor [36] in 1948 to increase the resolution of electron microscopy. However, with the advent of lasers, it became a well known tool for measurements in various applications.

3.3.1 Basic Principle of Holographic Recording and Reconstruction

As mentioned before, a hologram stores the amplitude as well as the phase information of a light wave to enable the reconstruction of the complex optical wave field. The basic principle can be seen in fig. 3.11(a). An object beam illuminates the object to be recorded. The object scatters light from the object beam and redirects it in the direction

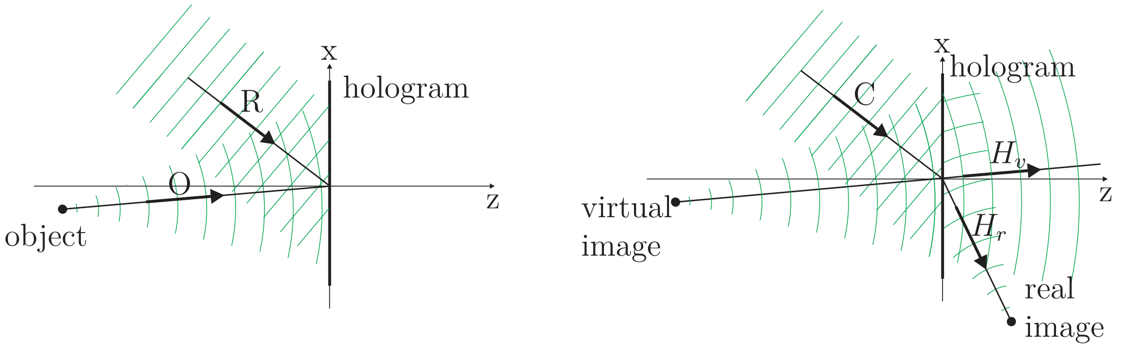

(a) recording (b) reconstruction C=R, $\alpha_C = \alpha_r$

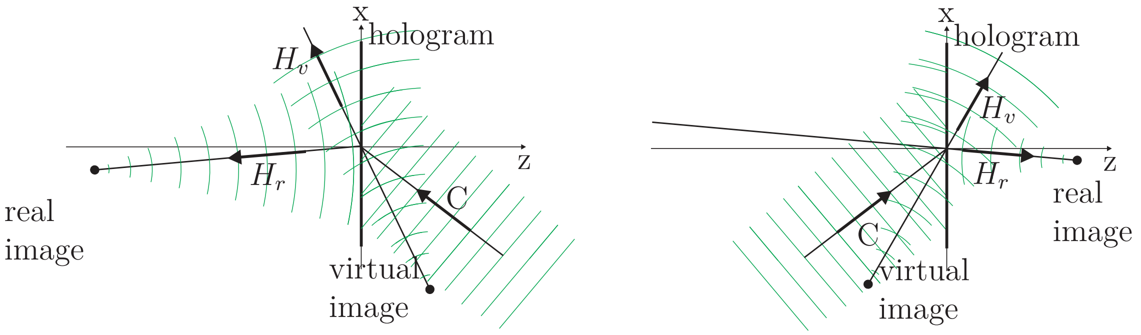

(c) reconstruction $C = R^*$, $\alpha_C = \alpha_r + 180°$ (d) reconstruction $\alpha_C = -\alpha_R$

Figure 3.11 – Holographic off-axis recording and three different reconstruction geometries (Konrath [50] and Dannemann [29])

of the recording medium. At the same time, a reference beam illuminates the recording medium. If both, object and reference beam are coherent, an interference pattern rather than an amplitude distribution is superimposed onto the recording medium. The object wave, reflected at one point P at the object can be described as:

$$E_P = \frac{E_{0,P}}{p} e^{i(kp+\phi)} \tag{3.47}$$

with p being the distance between the point P and one point $Q = (x, y, 0)$ on the recording medium. The reference wave, emitted at a point R can be written as:

$$E_R = \frac{E_{0,R}}{r} e^{i(kr+\psi)} \tag{3.48}$$

with r being the distance between R and Q. The recording medium registers an intensity I of the superimposed waves (Kreis [52]) of:

$$\begin{aligned} I(x,y) &= |E_P + E_R|^2 \\ &= E_P E_P^* + E_R E_R^* + E_P^* E_R + E_P E_R^* \\ &= \frac{E_{0,P}^2}{p} + \frac{E_{0,R}^2}{R} + \frac{2E_{0,P}E_{0,R}}{pr} \cos(k(r-p) + \phi - \psi) \quad . \end{aligned} \tag{3.49}$$

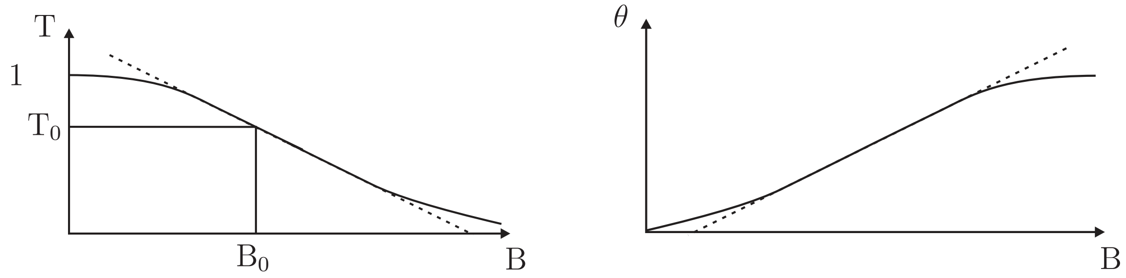

(a) Amplitude hologram (b) Phase hologram

Figure 3.12 – Amplitude transmittance T and phase shift θ as as a function of recieved energy B.

Because of the superposition principle, the same equations are valid for a continuum of object waves.
The received energy on the recording medium is directly related to the intensity I and the recording time t_B:

$$B(x,y) = \int_0^{t_B} I(x,y,t)dt \quad . \tag{3.50}$$

During processing, the energy is translated into a blackening and a change in refractive index of the recording medium that can be expressed through the complex degree of transmission τ as a spatially varying function:

$$\tau(x,y) = T(x,y)e^{i\theta(x,y)} \tag{3.51}$$

with T being the real transmission and θ being the phase shift. Eq. 3.51 contains the real transmission T and phase shift θ that both depend on the received energy B. Depending on the development process, two different kinds of holograms can be processed. These are divided into amplitude and phase holograms. Being processed as amplitude holograms, the degree of transmission, τ, is only dependent on amplitude. For phase holograms, the degree of transmission is only dependent on the phase (see fig 3.12. For both kinds of holograms, the energy has to be within the linear part of the curve.
The linear part of the real transmission for amplitude holograms can be expressed as

$$\begin{aligned} T(x,y) &= \alpha - \beta B \\ &= \alpha - \beta t_B I \end{aligned} \tag{3.52}$$

for I being temporally constant. The values α and β represent a uniform background transmittance and the positive slope of the amplitude transmittance, respectively. The resulting transmittance over energy can be seen in fig. 3.12(a). The points B_0 and T_0 mark the working point for a given energy and the mean transmittance, respectively.

Kreis [52] writes the real amplitude transmittance as:

$$\begin{aligned}T =&\alpha - \beta t_B(E_P E_P^* + E_R E_R^* + E_P^* E_R + E_R^* E_P)\\ =&\alpha - \beta t_B\\ &\cdot\left(\frac{E_{0,P}^2}{p^2} + \frac{E_{0,R}^2}{r^2} + \frac{E_{0,P}E_{0,R}}{pr}e^{i(k(r-p)+\psi-\phi)} + \frac{E_{0,P}E_{0,R}}{pr}e^{-i(k(r-p)+\psi-\phi)}\right)\\ =&T_0 - \frac{\beta t_B E_{0,P}E_{0,R}}{pr}\cos(k(r-p)+\psi-\phi) \quad .\end{aligned} \tag{3.53}$$

For phase holograms, the linear part of the curve describing the effective phase shift θ against exposure, fig 3.12(b), can be described as:

$$\theta = \alpha' + \beta' t_B I \quad . \tag{3.54}$$

The resulting transmittance reads:

$$\tau = Te^{i\theta(I)} \approx T\left((1+i\alpha') + i\beta' t_B(E_P E_P^* + E_R E_R^* + E_P^* E_R + E_P E_R^*)\right) \quad . \tag{3.55}$$

For resolving such a hologram, a given spatial resolution of the recording medium is necessary. By assuming that reference and object wave are both plane waves, the fringe distance of the resulting holographic interference pattern is

$$d = \frac{\lambda}{2\sin(\theta/2)} \tag{3.56}$$

with θ being the angle between reference and object beam [52]. For Nd:Yag lasers, commonly used for flow visualization, with a wave length of $\lambda = 532$ nm and an angle between reference and object beam of about $\theta = 10°$, the resulting fringe spacing is about 3.1 μm. Therefore, a minimum resolution of about 328 LP/mm (line pairs per millimeter) is necessary to resolve the resulting hologram. As state of the art CCD chips achieve a resolution of about 200 LP/mm, only small angles between object and reference beam are possible for digital recording of holograms.

In the following, the reconstruction process for an amplitude hologram will be explained. To reconstruct a recorded hologram, the processed hologram, has to be illuminated with a reference wave of the same conditions than during recording. The hologram acts as a diffraction grating that creates the image wave H (Kreis [52]):

$$\begin{aligned}H =&TE_R\\ =&\alpha C - \beta t_B C(E_P E_P^* + E_R E_R^* + E_P^* E_R + E_P E_R^*)\\ =&(\alpha - \beta t_B(|E_R|^2 + |E_P|^2))C\\ &-\beta t_B C E_R E_P^*\\ &-\beta t_B C E_R^* E_P \quad .\end{aligned} \tag{3.57}$$

The first term refers to 0th order diffraction which is the reference wave multiplied with the mean transmittance. This term is not of interest. The two first order diffraction terms are

$$H_c = -\beta t_B C E_R E_P^* \quad \text{(conjugate image) and} \tag{3.58}$$

$$H_p = -\beta t_B C E_R^* E_P \quad \text{(primary image).} \tag{3.59}$$

By using the same wave fronts for recording and reconstruction (C=R), a virtual primary image and a real conjugate image are created as shown in fig. 3.11(b). By changing the reconstruction wave to a complex conjugated wave (C=R^*) the primary image becomes real and the conjugate image virtual. The easiest way for a complex conjugate reconstruction is to use plane reference and reconstruction waves a with constant amplitude that pass the hologram in opposite directions (fig. 3.11(c)).

Alternatives in Holographic Recording

Until now, holographic recording via off-axis holography has been explained. This concept relies on an angle $\beta > 0$ between reference and object beam. This method is the most universal method of recording holograms. However, for transparent media or measurements of particle laden flows, in-line holography can also be used. With this technique, the object beam becomes the reference beam such that an angle of $\beta = 0°$ is acchieved. With this, CCD or CMOS chips can be used to record holograms digitally rather than analogue. Soria et al. [92] used digital in-line holography to successfully reconstruct volumetric particle positions with minimal errors. However, digital in-line holography is prone to speckle noise as the real and virtual image are created on top of each other. Furthermore, it is restricted to small volumes. Bigger volumes could be recorded on holographic film. This however, restricts the possibility to store several time steps on the same hologram by changing the direction of the reference beam as explained by Konrath [50]. Alternative concepts of recording like a hybrid in-line and off-axis approach by Zhang et al. [110] or a separation of different time steps in off-axis holography by multiplexing and polarization and multiplexing using Bacteriorhodopsin (BR) as holographic recording material [24, 25], are also possible.

Errors in Holographic Imaging

Holographic recording is prone to a wide range of errors. Some of these are correlated to a wrong recording setup like misaligned or uncollimated reference beams that yield aberrations, too low a coherence length of the illuminating laser beam that totally or partially prevents holographic recording or a difference in wave length between recording and reconstruction. Furthermore, shrinkage can occur in the recording emulsion that lead to erroneous reconstruction. Finally, moving objects can also induce errors. A detailed description of errors during holographic recording is given for example in Barnhart et al. [12], Dannemann [29], Herrmann [43], Konrath[50] and Caulfield [23] and is beyond the scope of this thesis.

4

Measurement Techniques

4.1 Particle-Image Velocimetry

Particle-image velocimetry (PIV) is a well established non-intrusive, whole field, optical measurement technique that determines the velocity components of a flow field, based upon the estimated displacement of imaged tracer particles at two or more instances in time. Originally, flow field images have been captured on film and were evaluated using elaborate optical Fourier techniques. Today, it is almost exclusively performed using digital image recording and processing. A detailed report on the history and development of PIV can be found in Adrian [5].

Compared to other flow measurement techniques like hot wire anemometry or the measurement of velocities via pressure tubes, it does not require probes inside the flow field that disturb the flow. Furthermore, it is a whole field measurement technique and therefore capable of resolving the flow field in not only one point, but in an area of the flow. In its most simple arrangement, it is able to resolve two velocity components in one plane of a flow field (2C-2D PIV). More complex test setups enable the measurement of a third velocity component in one plane via stereoscopic PIV (3C-2D PIV or stereo-PIV) or volume, i.e., holographic PIV (holo-PIV) or tomographic PIV (Tomo-PIV). In the following, the basic principles of PIV measurements are described in detail. After that, the three different PIV measurement setups used during this thesis, i.e., stereo-PIV, Holo-PIV, and Tomo-PIV are explained. Furthermore, an in-detail explanation concerning seeding particles and their flow following behavior is given.

4.1.1 Basic Principles of PIV

The most simple PIV setup typically consists of five basic elements. Tracer particles have to be added to the flow. These tracers are illuminated by means of a light source, i.e., a laser in a plane, at least twice within a short time interval. A camera records the scattered light on different frames. Finally, a software calculates the displacement of the particle images between the different light pulses and a post processing is performed to eliminate and replace spurious velocity vectors [85]. To calculate a vector velocity map the images are divided into small subareas, so called "interrogation windows". Cross-

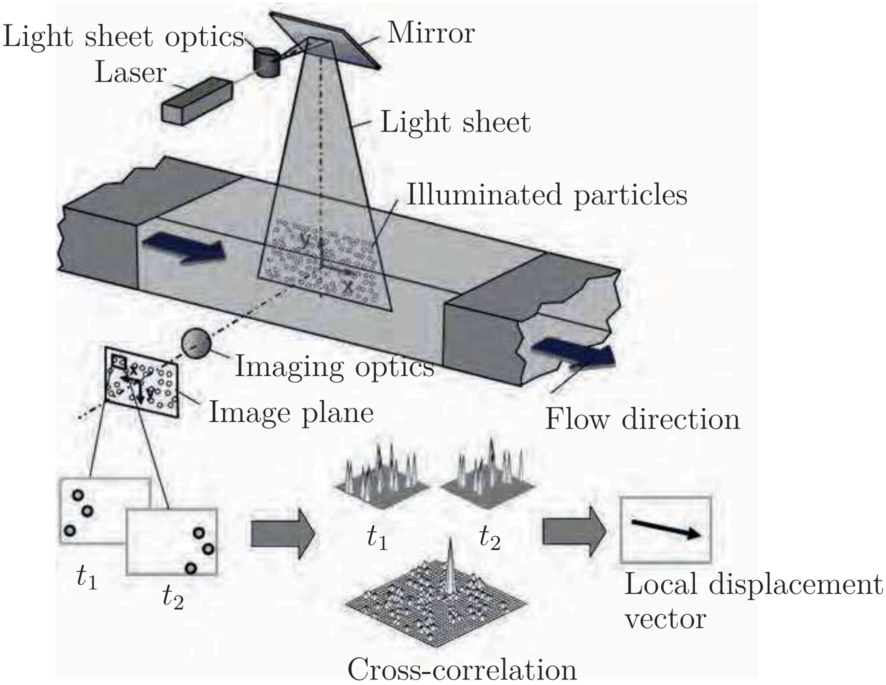

Figure 4.1 – Standard PIV setup at a windtunnel [85]

correlation algorithms are used to calculate the displacement between the different illuminations of the different interrogation windows. The velocity is calculated from the displacement and the time between the different illuminations. A basic PIV-setup in a wind tunnel can be seen in fig. 4.1. Since PIV is an indirect measurement technique, not the velocity of the flow itself but rather the velocity of the tracer particles is measured. Hence, tracer particles, that do not follow the flow perfectly, can disturb the measurement. Therefore, one has to carefully test the particle characteristics whether they fit to the specific flow problem. Moreover, the seeding density has to be adjusted. A flow with not enough particles generates no correlation peaks in some interrogation windows, whereas too many particles lead to ambiguous correlation peaks due to noise.

4.1.2 Stereoscopic PIV

The 2C-2D PIV setup is able to measure the two in plane velocity components of a light sheet plane. The third velocity component however, cannot be resolved. As the light sheet possesses a certain thickness, errors introduced by a flow perpendicular to the light sheet plane may occur as illustrated in fig. 4.2. Here, d is the light sheet thickness, dx the particle displacement in the x-direction, dz the particle displacement in the z-direction, x_1 the measured particle displacement in the x-direction and x_2 the true displacement in the x-direction. This error can be minimized through a large viewing distance with large focal lenses. Nevertheless, the knowledge of the third velocity component is of great importance for a wide field of PIV investigations. To measure the third velocity component (out-of-plane velocity), several investigators used a second camera to get a stereoscopic view of the flow field [7, 28, 37, 83, 84, 91, 34]. Both

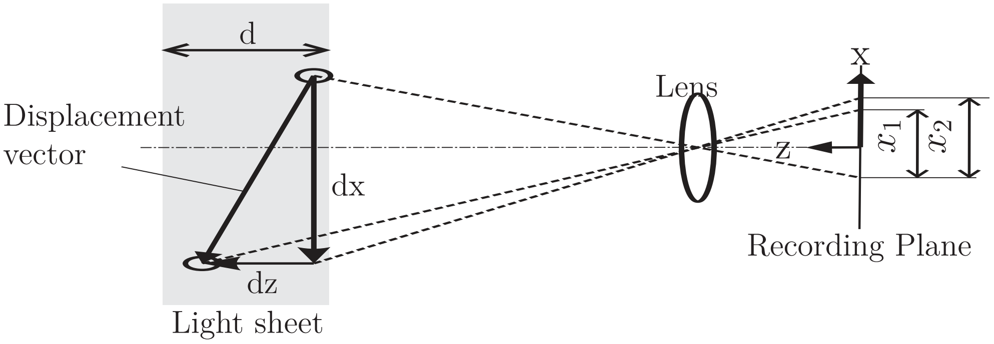

Figure 4.2 – Displacement error through third velocity component in 2C-PIV [85].

cameras are tilted with respect to the measurement plane (Fig. 4.4) and record the same field of view. To achieve a sharp recording of all particles inside the light sheet plane, the Scheimpflug condition has to be fulfilled. This condition states that the image plane, the lens plane, and the object plane of a camera have either to intersect in one point, or to be parallel. For standard PIV measurements the second condition is fulfilled. However, for stereoscopic PIV a Scheimpflug imaging arrangement is necessary. This arrangement is realized by tilting the lens with respect to the camera [85] and can be seen in fig 4.4. The two cameras record a slightly different image of the flow, and therefore a different displacement for the same interrogation windows. The true velocity components are calculated out of the displacements of both cameras. The equations 4.1 - 4.7 calculate the true displacement vector for the single interrogation windows [85] as shown in fig. 4.3

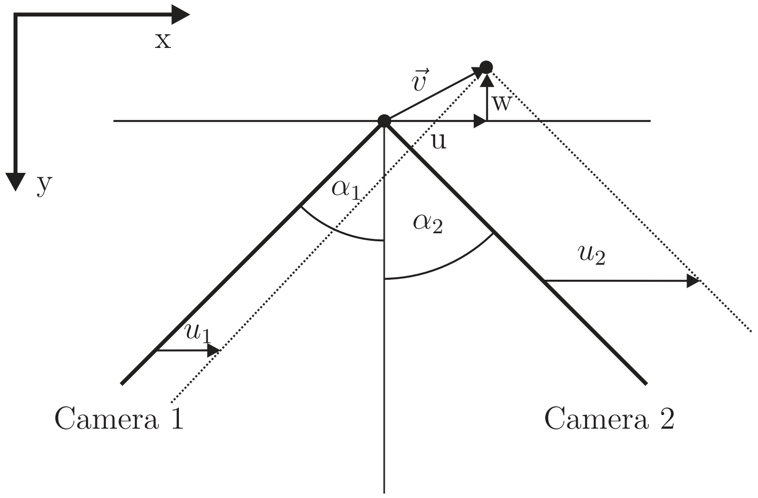

Figure 4.3 – Stereo viewing geometry in the XZ-plane [85].

$$\tan \alpha_i = \frac{x_i(t + \Delta t)}{z_0} \tag{4.1}$$

$$\tan \beta_i = \frac{y_i(t + \Delta t)}{z_0} \tag{4.2}$$

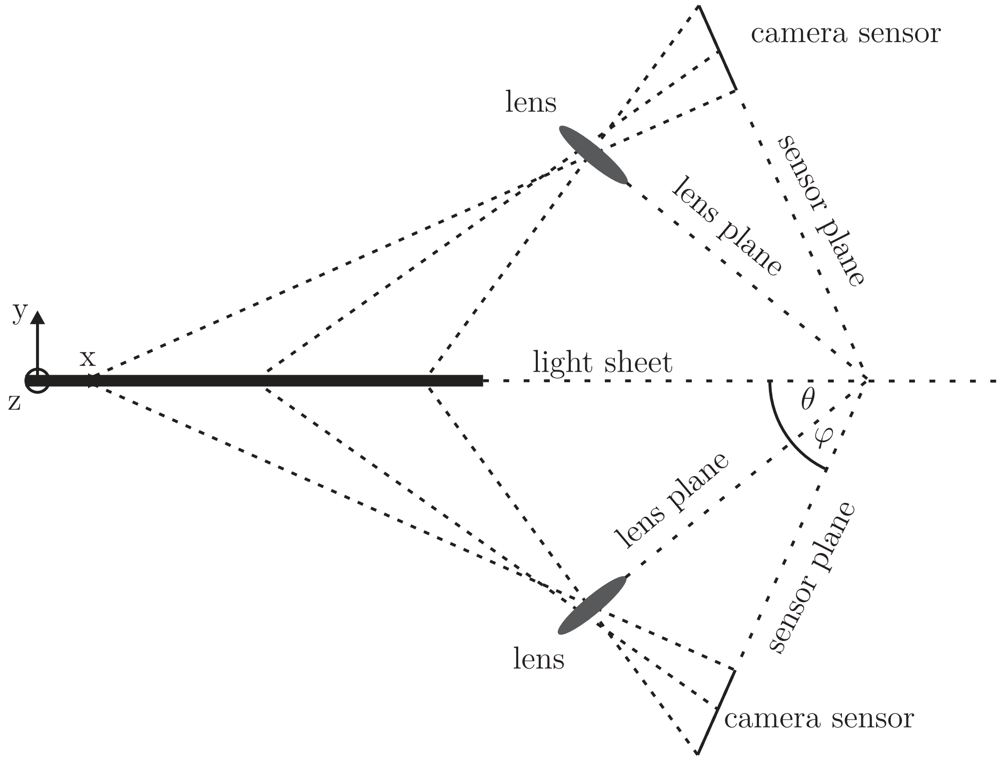

Figure 4.4 – Displacement error through third velocity component in 2C-PIV [85].

$$u_i = \frac{x_i(t+\Delta t) - x_i(t)}{M \cdot \Delta t} \tag{4.3}$$

$$v_i = \frac{y_i(t+\Delta t) - y_i(t)}{M \cdot \Delta t} \tag{4.4}$$

$$u = \frac{u_1 \cdot \tan\alpha_2 + u_2 \cdot \tan\alpha_1}{\tan\alpha_1 + \tan\alpha_2} \tag{4.5}$$

$$v = \frac{v_1 \cdot \tan\beta_2 + v_2 \cdot \tan\beta_1}{\tan\beta_1 + \tan\beta_2} \tag{4.6}$$

$$w = \frac{u_1 - u_2}{\tan\alpha_1 + \tan\alpha_2} \tag{4.7}$$

The quantities α and β are the angles between the z-axis and the ray from the tracer particle through the lens center to the recording plane, whereas α lies inside the XZ-plane and β inside the YZ-Plane. The velocity components u, v and w are in the X-, Y-, and Z-direction, respectively. The quantity M defines the magnification of the used lenses. The variables x_0, x_i, y_0 and y_i define the position of the tracer particle in the X- and Y-direction at time step t and t' respectively. These formulas are usable for any opening angle as long as the viewing axes are not collinear. Before applying eq. 4.1- 4.7, the 2C velocity components for both camera double images have to be calculated using standard cross-correlation algorithms and to be post-processed to acquire two different velocity fields on a rectangular grid. After that, the images of both cameras have to be mapped to the same grid. For this, a calibration target is positioned inside the measurement plane and recorded by both cameras. Finally, the corresponding position of the recorded grid points in the image plane of the two cameras can be calculated using a pinhole model. For this thesis, a Tsai model [101] was used. The two grids have to be mapped on a common grid to calculate the resulting velocity vector. As both rectangular grids are originally not on top of each other, it is necessary to interpolate both grids to a common grid. However, this will introduce spurious vectors. Therefore, the original particle images of both cameras are mapped and dewarped onto the common grid providing the same grid for each camera.

One error in mapping the particle images is introduced by misaligning of light sheet and calibration target. This error cannot fully be avoided. However, by calculating a disparity map and calculating a corresponding correction to the mapping function it can be corrected. This is done by cross-correlating the mapped images of both cameras. The resulting displacement corresponds to the misalignment of light sheet and calibration target. As the light sheet thickness itself introduces an error by calculating the disparity map, the averaged cross correlation peak of several images is used to determine the misalignment error [85].

4.1.3 Holographic PIV

In this section a short introduction into holographic PIV (HPIV) will be given. A detailed analysis of holographic PIV measurement techniques as well as a literature overview about existing HPIV setup can be found in Barnhart [11], Konrath [50] and Dannemann [29].

Holographic PIV is a volumetric measurement technique. In contrast to planar PIV, as described in section 4.1 the particle field recorded holographically (see sect. 3.3). Therefore, not only the intensity but also the phase of the particles scattered light is recorded. This enables the volumetric reconstruction of the particle position in space, and therefore the calculation of the three-dimensional velocity field via volumetric cross-correlation algorithms. A simple holographic PIV setup can be seen in fig. 4.5. The flow field is illuminated by means of a laser two times in a short time interval. The laser beam is divided into an object and a reference beam. The reference beam is expanded and collimated by two lenses and illuminates the hologram plate. The object beam is expanded and illuminates the particles inside the flow field. The scattered light interferes with the reference beam on the hologram plane, which stores the three-dimensional information on the hologram plate. After developing the holographic film the particles field can be reconstructed by illuminating the holographic plate with a collimated reconstruction beam that has the same wave length as the laser used for recording. The resulting real image can be scanned by a digital camera. After that, the data can be evaluated using standard PIV algorithms to calculate the three-dimensional velocity field. Konrath [50] mentions three main problems for holographic PIV systems, Speckle noise, light energy, and velocity limits. Speckle noise is directly related to particle concentration, depth of the measurement field and the optical aperture. Decreasing particle concentration reduces speckle but also reduces spatial resolution of the PIV

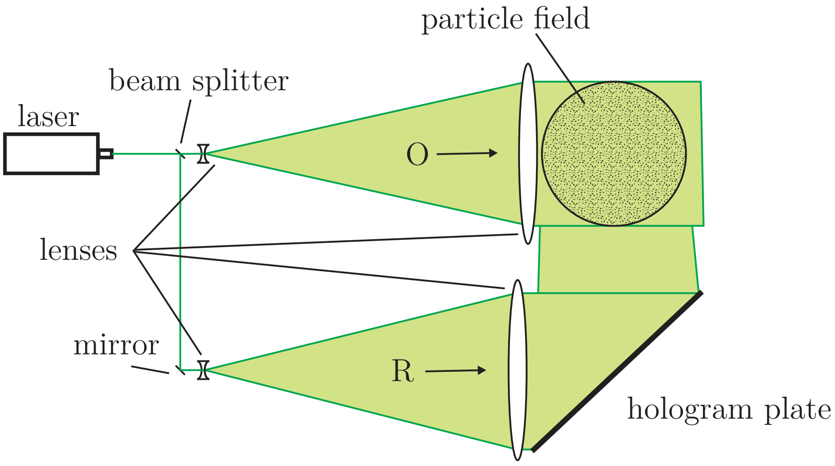

(a) HPIV recording

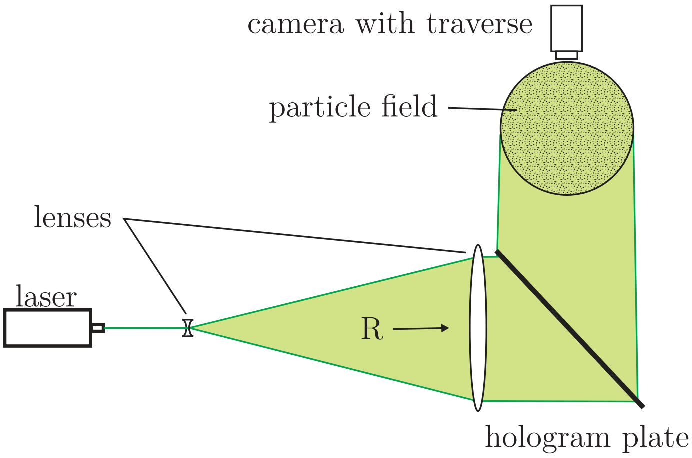

(b) HPIV reconstruction

Figure 4.5 – Typical setup for off axis, phase conjugate holographic particle-image velocimetry [29]

analysis as the mean particle number per interrogation volume decreases. A decreasing depth of field naturally reduces the resolved measurement volume. Furthermore, an increase in optical aperture reduces speckle. Additionally, it also increases the recorded light intensity per particle. Furthermore, it increases the accuracy and spatial resolution of the measurement. Unfortunately, a bigger aperture leads to image aberrations doe to misalignments of the reference beam illuminating the hologram during reconstruction (Herrmann [43]).
Light energy is restricted by particle size and type, measurement volume sensitivity of the holographic film optical aperture and scattering angle of the particles. Larger particles scatter more light. Therefore, the needed light intensity decreases. Larger measurement volumes however, increase the needed light energy. With increasing sensitivity of the holographic film, less light is needed for recording. However, higher intensity is normally coupled to bigger grain sizes in the holographic emulsion, which could restrict the holographic setup to smaller off-axis angles.

The measurable maximum velocity is related to the length of the laser light pulse and the scattering angle of the light. To successfully record a hologram, changes in path length of the object beam have to be avoided. The allowable difference in the optical path length has to be well below the wave length (Vikram [104]). With this, the maximum velocity is given by Konrath [50]:

$$|v_{max}| = \frac{\lambda_R}{4\tau_p|(1-\cos(\phi))\cos(\gamma) - \sin(\phi)\sin(\gamma)|} \tag{4.8}$$

with λ being the laser wave length, ϕ and γ the scattering angles, and τ the laser pulse length.

4.1.4 Tomographic PIV

In the following, the basics of tomographic PIV (Tomo-PIV) are explained. A detailed explanation can be found in Atkinson [8] or Elsinga [35]. Tomographic particle-image velocimetry allows the analysis of three-dimensional flow fields without the need to record the phase and amplitude information of the scattered light wave. It has been introduced by Elsinga et al. [35] and is based on the simultaneous view of illuminated particles in a volumetric flow field with three or more digital cameras placed at several viewing positions such that several observation directions are realized [85]. Rather than detecting individual particles the volumetric field is recorded by three or more cameras and the information is used to reconstruct a discretized 3D light intensity over an array of voxels by using tomographic algorithms that are adopted from medical diagnostics (Oldendorf, [67]) or astronomy (Bracewell [17]). Figure 4.6 shows the principle of tomographic reconstruction for one time step with four cameras. The tracer particles in the flow field are illuminated by means of a pulsed light source within a volumetric region of the flow field. The digital cameras record the scattered light from several viewing positions. It is important that the volume recorded is in focus. Hence, a proper aperture has to be used to achieve a sufficient depth of field. Furthermore, the Scheimpflug condition has to be fulfilled between image plane, lens plane and mid-object plane. With this, a tomographic reconstruction algorithm can calculate the estimated 3D light intensity distribution from its projections on the cameras. Elsinga et al. [35] state that the reconstruction is an inverse problem with a non-straightforward solution as the problem normally is under-determined. The most likely distribution is calculated by means of tomographic algorithms and is the topic of tomography (Hermann and Lent, [42]). As with stereo-PIV, a calibration of the cameras is indispensable. To gain information on the three-dimensionality of the flow field, either a 3D target, a calibration target with more than one plane in z-direction, or several images of a 2D target at two or more different z-positions have to be used. After recording the target with all cameras, either a pinhole fit or a third order polynomial fit can be used to map the volumetric positions to the 2D image coordinates. For a successful tomographic reconstruction Elsinga et al. [35] state that a maximum calibration error of 0.4 pixel (px) is acceptable, which is difficult to achieve from calibration without further improvement due to several errors,

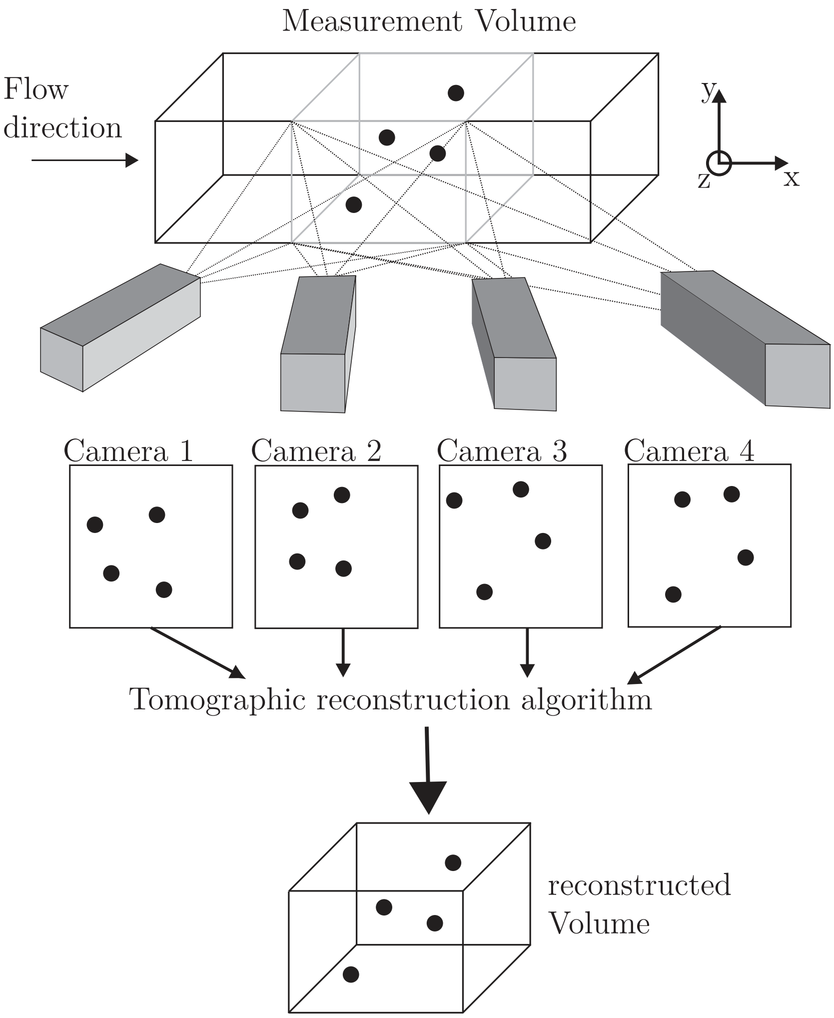

Figure 4.6 – Principle of tomographic reconstruction.

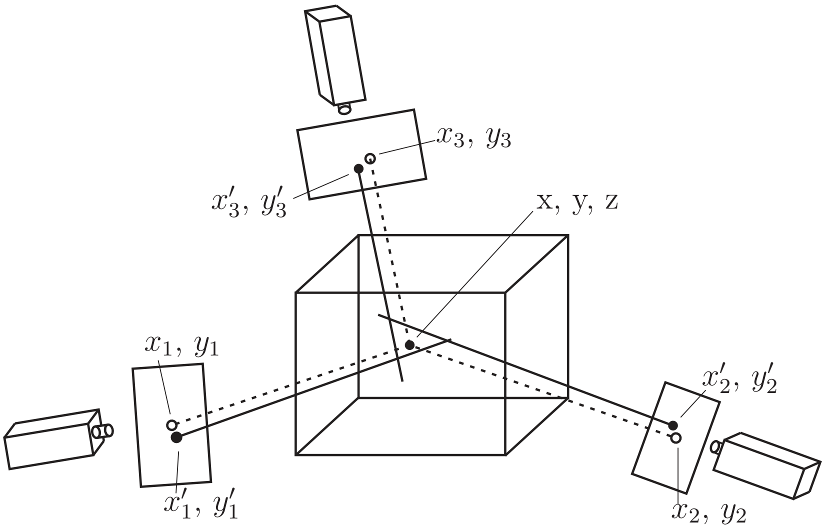

Figure 4.7 – Principle of volume self calibration [108]

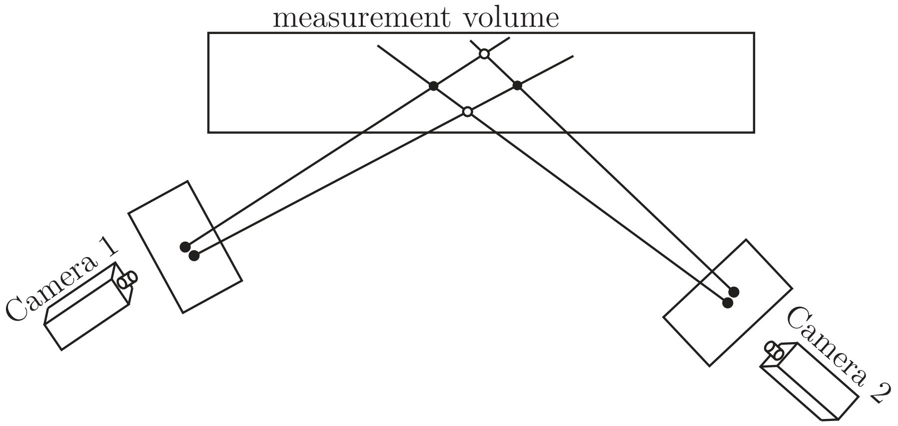

Figure 4.8 – Example of ghost particle generation [8].

i.e., mechanical vibration, inaccurate calibration plate, or optical distortion not covered by the calibration function. Wieneke [108] proposed, based on his work on self calibration for stereo-PIV [107] a volume self calibration algorithm. The alogrithm calculates, based on recorded particle images, a deviation in the mapping function and corrects it accordingly. It is based on volumetric particle tracking velocimetry (PTV) algorithms. Therefore, sparsely seeded volumes should be used for volume self calibration. The recorded sparsely seeded images are used to triangulate the volumetric particle position. This is exemplary shown in fig. 4.7 for a three camera setup. The solid lines show the reconstructed position of one pixel. For a perfectly calibrated setup, all lines would intersect in one single point. In reality, there often is an intersecting area due to small misalignment of the calibration. Hence, the best fitting position for one parameter has to be determined using optimization methods. The optimization algorithms use a maximum allowable error $\epsilon_{disp,max}$ for the triangulation of the particle position x, y, z for the matching of all lines of sight of all cameras. However, a bigger triangulation error increases the creation of so called ghost particles. Ghost particles are created by the intersection of the line-of-sight of all cameras on positions where no particles are present. This can exemplary be seen in fig. 4.8 for a two camera setup. Two particles (solid circles) create a signal in the image of each camera. As the cameras only see the projected line-of-sight, in summation four cross-sections of both lines-of-sight are created in the measurement volume. The resulting two particles (empty circles) are so called ghost particles that are only created through the under-determined solution of the volumetric reconstruction. By increasing the maximum allowable error in the volume self calibration, naturally more intersections at points, where no real particles are present, can be found. Wieneke [108] found that the ratio of ghost particles (G) and real particles is strongly dependent on the maximal allowable error and the number of particles per pixel, N_{ppp}:

$$G = 8 l_{los} \epsilon_{disp,max}^{5} N_{ppp} \tag{4.9}$$

with l_{los} being the the length of the line-of-sight inside the measurement volume. Elsinga [35] showed that a seeding density of $0.025 \leq N_{ppp} \leq 0.05$ yields acceptable results. Furthermore, these ghost particles tend to be slightly elongated since cameras normally share a similar depth of field [92]. However, algebraic reconstruction methods spread the intensity across these location. Hence, ghost particles tend to have lower intensity than true particles (Atkinson and Soria [9], Elsinga et al. [35]).

4.1.4.1 Tomographic Volume Reconstruction Methods

The reconstruction of particle positions in 3D space from a restricted number of viewing positions (typically 3 to 6 cameras) is a challenging task. From the two-dimensional information of the cameras, the camera pixel intensity can be expressed as

$$P_i = \int_{-\infty}^{\infty} I(x, y, z) ds_i \tag{4.10}$$

where I(x,y,z) represents the unknown intensity distribution inside the volume. To reconstruct the particle intensity inside the voxel volume, the integal has to be inverted. This can either be done by algebraic methods or by analytical reconstruction methods like Fourier or back-projection(Verhoeven [103]). However, due to the limited viewing positions, algebraic reconstruction methods are the most promissing for reconstructing the particle position in 3D space. For this reason, only algebraic reconstruction methods are described.

The algebraic reconstruction approach is based on the iterative solution of a set of linear equations modeling the imaging system. The volume is divided into a 3D grid of voxel elements. The original intensity of each camera pixel P_i can be expressed by

$$P_i = \sum_j W_{i,j} I_j \tag{4.11}$$

where I_j is a vector representing the intensity of each voxel. $W_{i,j}$ is a weighting matrix, which represent the contribution of each voxel to a pixel value (Atkinson [8]). Note, that $W_{i,j}$ is assumed to be very sparse since a line-of-sight of each camera intersects only with a small part of the total measurement volume. In the following, several approaches to solve the eq. 4.11 iteratively are presented.

4.1.5 Algebraic Reconstruction Technique (ART)

The iterative ART algorithm is implemented as through:

$$I(x_j, y_j, z_j)^{k+1} = I(x_j, y_j, z_j)^k + r \frac{I(x_i, y_i) - \sum_{j \in N_i} w_{i,j} I^k(x_j, y_j, z_j)}{\sum_{j \in N_i} w_{i,j}^2} w_{i,j} \quad . \tag{4.12}$$

The iteration-loop is performed for each pixel in each camera i and in a second loop for each voxel j. The quantity r is a relaxation parameter whose value is betwen 0 and 2. The starting condition $I(x_j, y_j, z_j)^0$ is normally set to a uniform value of 0. Elsinga et al. [35] showed that the ART algorithm is prone to artefacts that are unacceptable for PIV cross correlation algorithms which can be seen in fig. 4.9.

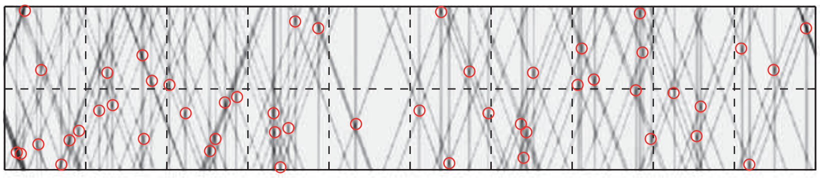

Figure 4.9 – Reconstruction of a two dimensional volume using the ART algorithm [35].

Multiplicative Algebraic Reconstruction Technique (MART)

The MART algorithm uses a different iterative reconstruction approach. Rather than using a summation, a multiplication is used for the iterative reconstruction, which is normally initialized with $I^0(x_j, y_j, z_j) = 1$:

$$I(x_j, y_j, z_j)^{k+1} = I(x_j, y_j, z_j)^k \left(\frac{I(x_i, y_i)}{\sum_{j \in N_i} w_{i,j} I(x_j, y_j, z_j)^k} \right)^{r w_{i,j}} \quad . \tag{4.13}$$

Here, the fraction represents the comparison between the two dimensional projection of the intensity distribution for the kth iteration and the recorded intensity distribution. It is used to correct the kth intensity distribution using a relaxation parameter r with $r \leq 1$ and the weighting coeffient w. This ensures that only affected elements are updated in $I(x_j, y_j, z_j)^{k+1}$. Compared to ART, the MART reconstruction yields acceptable particle reconstructions, which could be shown by Elsinga et al. [35] and can be seen in fig. 4.10. One disadvantage of the MART algorithm is the long time for the solution to converge.

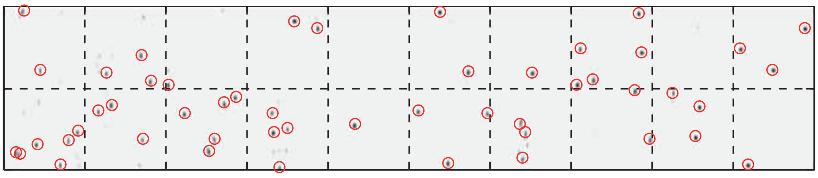

Figure 4.10 – Reconstruction of a two dimensional volume using the MART algorithm [35].

This is mostly due to the low relaxation factor that typically is in the range of $r = 0.2$ (Elsinga et al [35]). Other solutions for the Multiplicative algebraic reconstruction, which seem to improve computation time, can be found in Mishra et al. [65].

Multiplicative line-of-sight (MLOS) and Minimum Line-of-Sight (MinLOS)

The Multiplicative line-of-sight approach uses the calibration mapping to consider the intensity of each pixel for an estimation of the location of non-zero voxels [9]. All pixels whose line-of-sight intersect with a given voxel are multiplied. As a result, non-zero voxels are created for the intersection of non-zero pixels from all cameras. As mentioned earlier, ghost particles can be created as more intersections of the line-of-sight are present than real particles. Furthermore, an intensity correction has to be performed as the multiplication of the intensity of several cameras raises the reconstructed voxel

intensity above the actual level. The correction is performed with a power of $1/n_{Cam}$. Compared to MART, the ghost level is not significantly reduced but MART yields about 50% lower light intensities for ghost particles after five iterations [9].
A similar approach using the line-of-sight from the mapping function is given by the Minimum line-of-sight (MinLOS) or minstore algebraic reconstruction technique (MinART) method introduced by Maas et al. [60]. In literature, it is commonly refered to MinLos as proposed by Michaelis et al. [64]. In general, it uses the same approach as MLOS but rather than multiplying all pixels for one voxel the voxel value is set to the minimum pixel value.

Simultaneous Algebraic Reconstruction Technique (SART) and Simultaneous Multiplicative Algebraic Reconstruction Technique (SMART)

To overcome the time consuming process of multiple ART or MART iterations, Atkinson and Soria [9] introduced the so called SART and SMART algorithms. These are based on an initial MLOS step to identify non-zero voxels. The result from this first step is used as initialization field for the following iterative calculation of the voxel intensities. This reduces processor time and memory usage as only non-zero voxels have to be stored for the initial light intensity distribution $I^0(x, y, z)$. Furthermore, the weighting coefficients only need to be calculated for the remaining voxels. The iterative update to the SART method slightly differs from the ART iteration:

$$I(x_j, y_j, z_j)^{k+1} = I(x_j, y_j, z_j)^k + r \frac{\sum_{i \in N_i} \left(\frac{I(x_i, y_i) - \sum_{n \in N_i} w_{i,n} I^k(x_n, y_n, z_n)}{\sum_{n \in N_i} w_{i,n}} \right)}{\sum_{i \in N_i} w_{i,j}} w_{i,j} \tag{4.14}$$

with $\sum_{n \in N_i} w_{i,n} I^k(x_n, y_n, z_n)$ representing the projection of all voxels to a pixel. The SMART iteration has been changed to:

$$I(x_j, y_j, z_j)^{k+1} = I(x_j, y_j, z_j)^k \prod_{i}^{N_i} \left[\left(\frac{I(x_i, y_i)}{\sum_{n \in N_i} I^k(x_n, y_n, z_n)} \right)^{r w_{i,j}} \right]^{\frac{1}{} N_i} . \tag{4.15}$$

For both equations, N_i and r are defined similar to the standard ART and MART algorithms.
Atkinson and Sorio [9] showed, that the total number of iterations needed for SART are $N_{it,SART} = (24 N_{cam} + 4) N_{nonzero}$ and for SMART $N_{it,SART} = (24 N_{cam} + 3) N_{nonzero}$ with $N_{nonzero}$ being the total number of non-zero voxels in the volume. Therefore, the theoretical estimated processing time for SMART is slightly faster compared to ART.

4.1.6 Tracer particles

One main issue in setting up a (PIV) experiment is the correct choice of seeding particles. The flow following capability of a particle depends on its size as well as the density difference between particle and fluid [45, 88]. Due to decreasing inertia, the smaller the particle, the better the flow following behavior. Unfortunately, light scattering dramatically increases with bigger particle sizes. Assuming spherical particles, the amount of

scattered light is a function of particle diameter, ratio of refractive index, observation angle, and laser polarization [85]. Therefore, a tradeoff between light intensity and flow following behavior has to be made.
The Stokes number provides an easy way to assess the uncertainty resulting from particle size. The Stokes number reads:

$$St_1 = \frac{\tau_p}{\tau_f} \tag{4.16}$$

where τ_p is the particle relaxation time and τ_f is the characteristic time scale of the fluid. The particle relaxation is defined by

$$\tau_p = \frac{\rho_p d_p^2}{18 \rho_f \nu_f} \tag{4.17}$$

with ρ_p being the particle density, d_p the particle diameter, ρ_f the fluid density, and ν the fluid kinematic viscosity. For a Stokes number of 0, particles follow the flow field perfectly, whereas high Stokes numbers indicate a particle movement nearly independent of the fluid. Several researchers stated different Stokes numbers to be feasible for flow measurements. Tropea et al. [100] state that the condition $St \leq 0.1$ yields an acceptable flow tracing accuracy with errors below 1%. Ruck [88] performed LDA measurements for different Stokes numbers in the flow of a backward facing step and defined a relationship between Stokes number and measurement error of the volumetric flow rate. They found that Stokes numbers as small as 1 generate a maximum measurement error of about 18%. Unfortunately, no direct comparison between flow field and particle trajectory has been made. Kulick et al. [53] investigated the effect of measured turbulence in a fully developed channel flow for three different Stokes numbers ($St = 0.57$, 1.4, and 3.0). By using flow tracers with a diameter of $d_p = 1\mu m$ and larger tracer particles they were able to measure the velocity of the flow field and the tracer particles at the same time. Their findings show decreasing turbulence for particles with larger Stokes numbers. Melling [63] presents a general overview over feasible particles for PIV experiments. Furthermore, he discusses the analytic approaches of Hjelmfelt and Mockros [45], Haertig [39], and Chao [26] for the solution of the Basset-Bousinesq-Oseen (BBO) equation [13, 97].The BBO-equation describes the unsteady motion of a suspended sphere within a turbulent neglection all external forces.

$$\begin{aligned}
\frac{\pi d_p^3}{6}\rho_p \frac{du_p}{dt} = & -3\pi\eta d_p(u_p - u_f) && \text{acceleration force and viscous resistance} \\
& + \frac{\pi d_p^3}{6}\rho_f \frac{du_f}{dt} && \text{pressure force} \\
& - \frac{\pi d_p^3}{12}\rho_f \frac{d(u_p - u_f)}{dt} && \text{inertial force} \\
& - \frac{3}{2} d_p^2 \sqrt{\pi\eta\rho_f} \int_{t_0}^{t} \frac{d(u_p - u_f)}{d\xi} \frac{d\xi}{\sqrt{t-\xi}} && \text{Basset history integral} \quad .
\end{aligned} \tag{4.18}$$

The first two terms are the acceleration force and the viscous resistance according to Stokes' law. The third term defines the force due to pressure gradients. The resistance of an invicid fluid to the acceleration is defined by the fourth term. The last term is the "Basset history" integral, which defines the resistance due to unsteadiness in the flow field. An analytic solution of this equation is given by Hjelmfelt and Mockros [45]. They define an amplitude ratio η and a phase shift β between fluid velocity and particle velocity by

$$\eta = \sqrt{(1+f_1)^2 + f_2^2} \tag{4.19}$$

and

$$\beta = \tan^{-1}\left(\frac{f_2}{1+f_1}\right) \quad . \tag{4.20}$$

with the dimensionless parameters f_1 and f_2 given by

$$f_1 = \frac{\left(1+\frac{9N_s}{\sqrt{2}(s+0.5)}\right)\left(\frac{1-s}{s+0.5}\right)}{\frac{81}{(s+0.5)^2}\left(2N_s^2+\frac{N_s}{\sqrt{2}}\right)^2 + \left(1+\frac{9N_s}{\sqrt{2}(s+0.5)}\right)^2} \tag{4.21}$$

and

$$f_2 = \frac{\frac{9(1-s)}{(s+0.5)^2}\left(2N_s^2+\frac{N_s}{\sqrt{2}}\right)}{\frac{81}{(s+0.5)^2}\left(2N_s^2+\frac{N_s}{\sqrt{2}}\right)^2 + \left(1+\frac{9N_s}{\sqrt{2}(s+0.5)}\right)^2} \tag{4.22}$$

In eqs. 4.21 and 4.22, s represents the particle-to-fluid density ratio and N_s the inverse of the Stokes number defined by

$$s = \frac{\rho_p}{\rho_f} \tag{4.23}$$

and

$$N_s = \sqrt{\frac{\nu_f}{\omega d_p^2}} \quad . \tag{4.24}$$

This solution applies for particles in homogeneous, stationary turbulence with particles smaller than the smallest turbulence eddies. Furthermore, particle interaction is not considered such that the particle concentration has to be low. Finally, the particle Reynolds number Re_p has to be smaller than about unity. Experiments have been conducted to verify the analytic solution for PIV. The experimental setup can be seen in appendix B. The results show a good agreement of analytic result and experimental data. The whole analysis is beyond the scope of this thesis and can be found in [76].

Table 4.1 – Tracer particle properties

particle	d_p [μm]	ρ [kg/m^3]	τ_p [ms]	St
DEHS	1	914	0.003	0.004
EM 461 DET40 d25	40	25	0.12	0.682

All researchers recommend a particle size as small as possible to assure a nearly perfect flow following behavior. However, the volumetric measurement techniques performed in this thesis require high light scattering behavior. As normal tracer particles, i.e., DEHS droplets with a mean diameter of 1 μm, do not scatter enough light, other options for tracer particles have been investigated. The most promising particles are

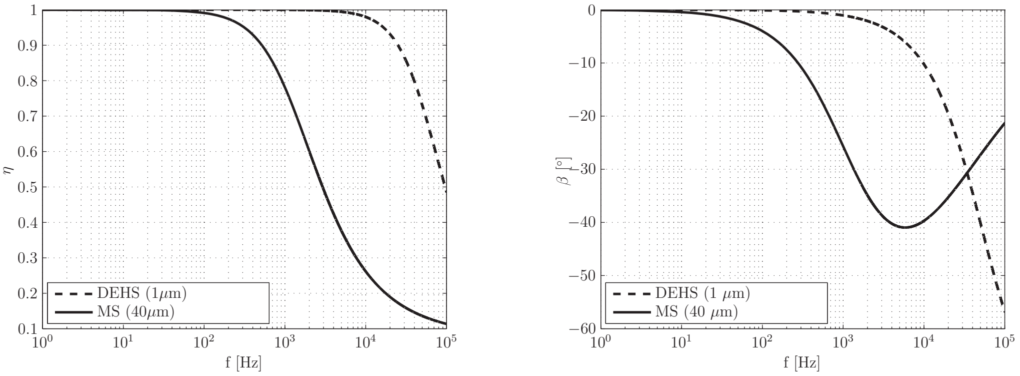

(a) amplitude ratio

(b) phase shift

Figure 4.11 – Amplitude ratio (a) and phase shift (b) for DEHS and Microspheres.

Expancel® microspheres EM 461 DET40 d25 (MS). The bigger diameter of about 40 μm ensures a high light scattering intensity, whereas the density of about 25 kg/m^3 provides good flow tracking capabilities. Tab. 4.1 lists the basic properties compared to DEHS, used for the planar PIV measurements. The Stokes number has been calculated, using the a maximum flow velocity about 20 m/s [29] and an integral length scale of about 3.5 mm [79]. The phase lag and amplitude ratio for DEHS and MS for a turbulence frequency of up to 100 kHz can be seen in fig. 4.11. One can see that phase and amplitude lag are higher for MS compared to DEHS. However, low frequency phenomena can be resolved. Moreover, two component PIV measurements with MS and DEHS were performed to analyze the flow-following behavior in more detail. The measured crank angle was 180° atdc. The resolution was 16x16 px (1.4 mm^2) with a final interrogation window size of 16x16 px and an overlap of 50% for Microspheres and 8x8 px (0.7 mm 2) with an overlap of 50% for DEHS. The velocity fields were used to calculate the energy spectra as explained by Petersen and Ghandhi[79] for both measurements at a given point ([x,z] = (0 mm, 50 mm)). Fig. 5 shows that for both particles the spectrum of the inertial subrange is well captured. Furthermore, both energy spectra show good agreement such that sufficient flow following capabilities of

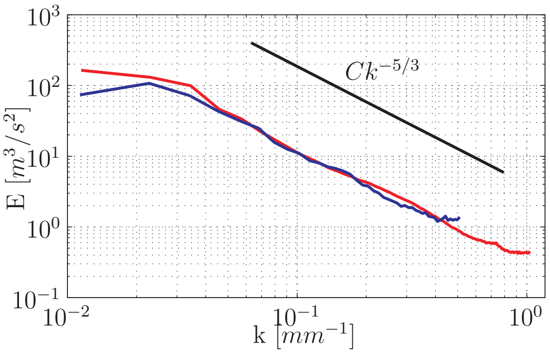

Figure 4.12 – Energy spectra at a crank angle of 160° atdc obtained from 2C-PIV measurements with DEHS (red) and MS (blue).

MS can be assumed.

4.2 Mie Scattering Imaging

Mie scattering Imaging (MSI) is a simple visualization technique for solid particles or liquid droplets in the micrometer regime. It is based on the reflection and light scattering properties of the recorded media. For the investigation of fuel sprays MSI is a common tool that has been applied by several researchers to investigate the liquid penetration length of a fuel spray [10, 62, 80, 86, 90].
In general, a light source is used to illuminate the fuel spray that is recorded by a CCD or CMOS camera. To avoid blurring of the image, either a light source with a short pulse length or a short shutter time in the nanosecond regime is used. To focus on the center of the spray, it is common to illuminate the spray via a light sheet but other illuminations are also possible [10]. In this thesis, fuel spray analysis is based on a light sheet illumination with a laser with a short pulse length. Through this, the propagation of the spray can be seen. After recording, custom made algorithms combined with calibration algorithms known from planar measurement techniques, i.e., PIV, calculate the spray position.

5

Test Facilities

To investigate the three-dimensional unsteady flow field within the cylinder of a four stroke four valve single cylinder internal combustion engine several measurement techniques have been applied to the two optical research engines of the Institute of Aerodynamics. Based on the work of Dannemann et al. [29, 30] holographic particle-image velocimetry (holo-PIV) measurements have been performed and compared to 2C-2D PIV measurements by Dannemann et al. [30] for one crank angle at the SUZI research engine to validate the holographic PIV system. Afterwards, Tomographic PIV (Tomo-Piv) has been applied to the SUZI research engine to perform a more thorough analysis of the large scale flow structures during intake and compression stroke and to perform an analysis of the influence of two different cam shaft geometries. Finally, the interaction of fuel injection and flow field for a hollow cone injector has been measured using Mie-scattering for the visualization of the liquid fuel and stereoscopic PIV for the investigation of the flow field at the TINA research engine. The latter have been compared to data by Karhoff [49] to analyze the difference between the flow field with and without injection. In the following chapter the two research engines and the four different measurement systems are introduced and described in detail.

5.1 Research Engines

5.1.1 SUZI

The optical research engine SUZI has been designed and constructed for the collaborative research center SFB 224 "Motorische Verbrennung" of the Deutsche Forschungsgemeinschaft (DFG) by Ortmann [69]. The research engine is based on a Suzuki DR750 motorcycle four-stroke four valve single-cylinder internal combustion engine. The engine is driven by an electrical 55 kW engine, i.e., the engine is not fired. The bore of the engine is B = 105 mm and the stroke is S = 85 mm. This results in a cylinder displacement of V = 728 cm^3. The valves are driven by a single overhead camshaft. The parameters of the engine are listed in tab. 5.1. All measurements in this thesis performed at this engine were conducted at a mean engine speed of 1,500 RPM without fuel injection and combustion. The typical progression of the engine

Table 5.1 – Parameters of the original Suzuki DR750 motorcycle engine and the modified research engine.

	Original	Modified
Number of Valves	4	4
Bore	105 mm	105.32 mm
Stroke [mm]	84 mm	84 mm
Displacement Volume	727 cm^3	727 cm^3
compression chamber	86 cm^3	90 cm^3
Compression ratio	9.5:1	9:1
Output (at 6800 rpm)	37 kW	-
Torque (at 5600 rpm)	55 Nm	-

speed, the valve lift curves, the intake pressure, and the cylinder pressure can be seen in fig. 5.1. To accomplish full optical access, the original cylinder of the Suzuki engine has been replaced by a transparent Perspex liner that is placed between the original cylinder head of pent roof geometry and an elongated lower liner that keeps the piston properly aligned. As the original liner and the thread rods were removed, a mounting frame was designed by Dannemann [29] that fixes the cylinder head to the liner. The piston rings are located in the lower iron liner. The clearance between the piston and the Perspex liner of 0.16 mm is sufficient to ensure a free piston movement within the optical liner. Due to the larger top-land crevice volume, the compression rate of the modified engine is reduced from 9.5 to 9. To further enhance radial optical access, the camshaft drive chain was displaced by means of an elongated camshaft and an elongated crankshaft. This is of special interest for tomographic PIV to guarantee a wide range of viewing angles. As the supporting frame is needed to support the cylinder head, it is the only part blocking optical access. The improvement in optical access can be seen in fig. 5.2. Axial optical access is achieved by a Perspex piston crown and a 45° mirror inside the elongated piston. The modified engine can be seen in fig. 5.3.

Both, the perspex liner as well as the perspex piston crown, restrict the maximum cylinder pressure to values well below the pressure levels achieved in a fired engine. Furthermore, the heat development of combustion would damage the perspex. For this reason, it is not possible to run the engine in fired condition. However, as the aim of the performed measurements is the analysis of intake and compression stroke, the constriction has no negative effect on the conducted measurements.

Two flaps, located between seeding reservoir and intake valves allow fast switching between unseeded and seeded air. This reduces the contamination of the liner with seeding particles during engine start. The seeding reservoir has a volume of about 20l. This is enough for about 28 consecutive engine cycles. To record more than 28 consecutive cycles, the seeding reservoir can either be connected to the exhaust of the engine or be refilled with particles during measurement. A baffle plate in the middle of the seeding reservoir avoids unwanted turbocharging due to the seeding generator or exhaust gas recirculation.

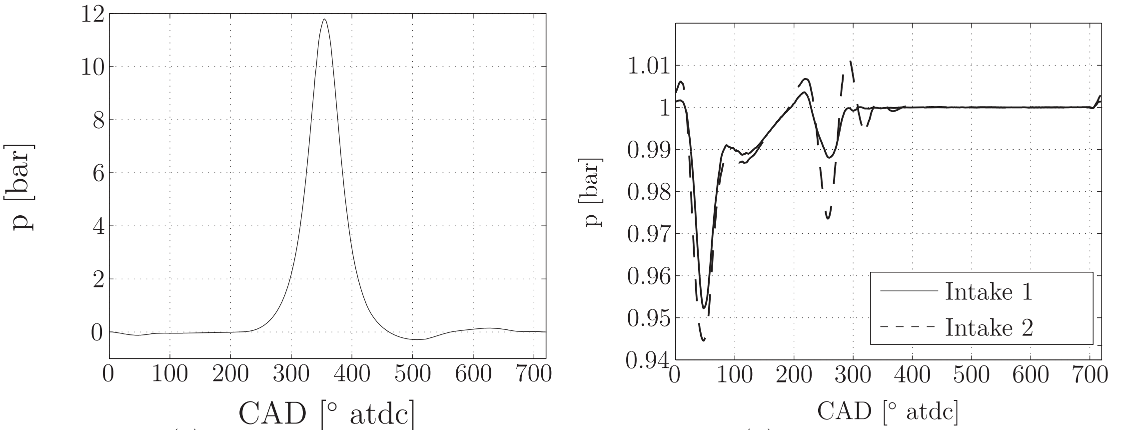

(a) cylinder pressure (b) Intake pressure

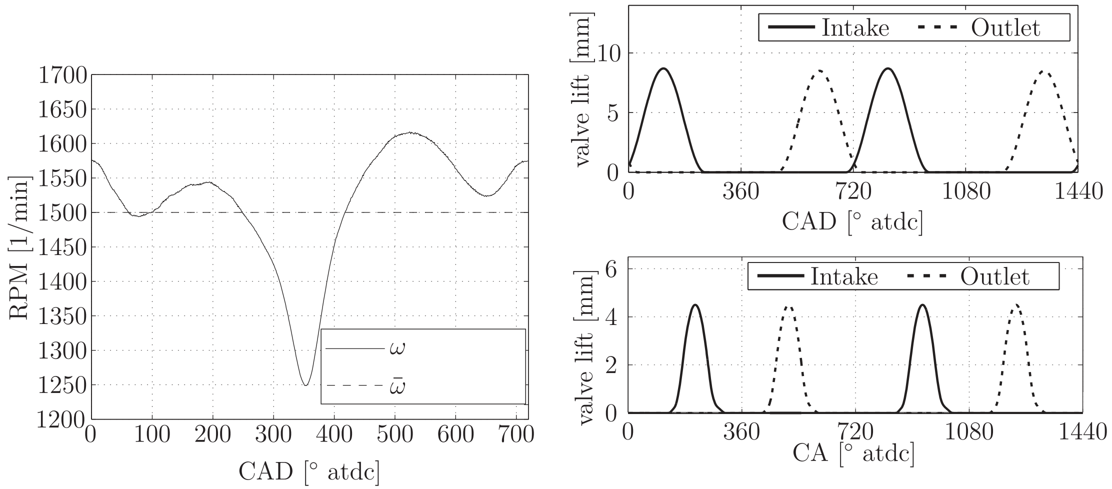

(c) Engine speed (d) Valve movement

Figure 5.1 – Cylinder pressure (a), intake pressure (b), progression of engine speed (c), and investigated valve timings (d) for the SUZI engine.

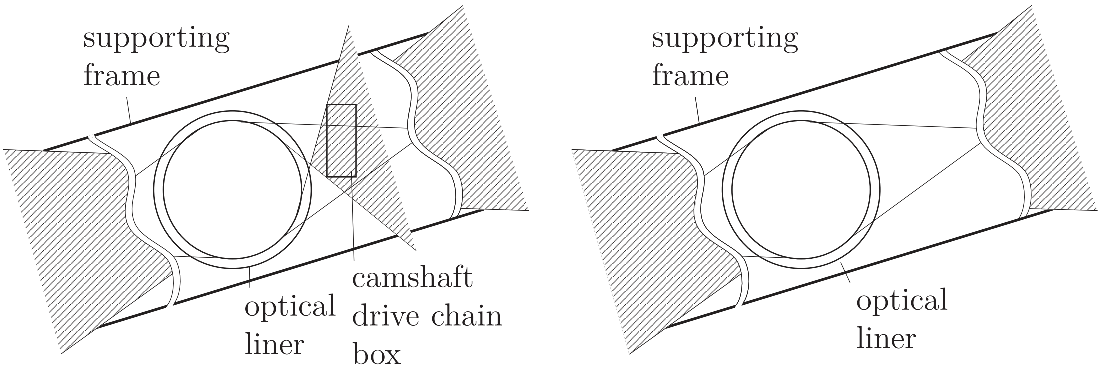

(a) cylinder pressure (b) Intake pressure

Figure 5.2 – Optical access with and without camshaft drive chain box. Dashed areas show restrictions in optical acces.

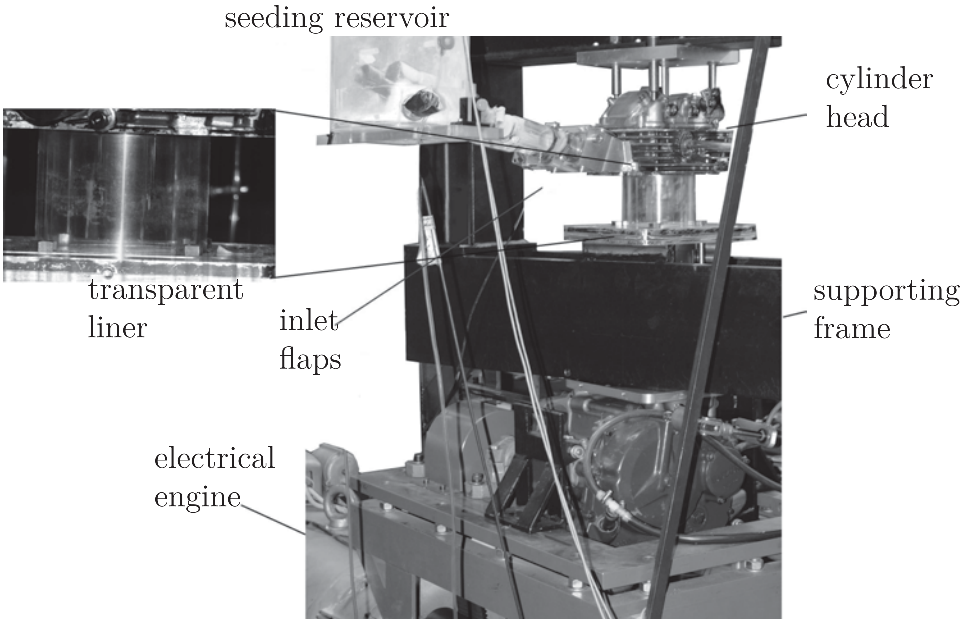

Figure 5.3 – SUZI research engine.

As seeding particles contaminate the liner, the engine has to be disassembled from time to time. This is easily achieved by loosening the bolts, fixing the cylinder head to its position. After that, the optical liner can be removed for easy cleaning. The complete disassembly and reassembly process takes about 10 minutes.

The engine is equipped with an incremental shaft encoder by Heidenheim with a resolution of 0.25° crank angle to measure engine speed and actual crank angle. The actual position is determined by quadrature pulsing and a zero index pulse. To distinguish between intake and compression stroke, and power and exhaust stroke, a reflective sensor scans a coding disc mounted to the cam shaft.

5.1.2 TINA

The four valve research engine TINA is a motored model of a direct injection spark-ignition (DISI) engine made by FEV Motorentechnik GmbH. The basic design and geometric parameters were predefined by the thermodynamic research engine "TINE", which is used by the Institute of Combustion Engines (Lehrstuhl für Verbrennungskraftmaschinen, VKA) of RWTH Aachen University. This was done to achieve comparability between measurements performed at the different institutes, as both engines are used in the Cluster of Excellence "Tailor made Fuel from Biomass" (TMFB). It is equipped with a tumble port, a pent roof combustion chamber and a flat piston crown. The tumble ports ensure a tumble number of about 5 to 10 depending on crank angle [19]. A flow coefficient of 0.11 has been measured by Adomeit et al. [3]. The bore of the engine is D = 75 mm and the stroke is S = 82.5 mm. This results in a cylinder displacement of V = 364 cm^3. A quartz glass liner and quartz glass piston crown grant optical access

Table 5.2 – Parameters of the TINA research engine. TDC denotes the gas exchange top dead center.

Bore	75 mm
Stroke	82.5 mm
Displacement Volume	364 cm^3
Compression ratio	7.4:1
Number of valves	4
Valve lift	9 mm
Valve diameter intake/exhaust	27.1 mm / 23 mm
Exhaust valves open (1 mm lift)	206° before TDC
Exhaust valves close (1 mm lift)	20° before TDC
Intake valves open (1 mm lift)	10 ° after TDC
Intake valves close (1 mm lift)	196° after TDC
Connecting rod length	146 mm
Crank radius	42.2 mm

to the combustion chamber. Free piston movement within the optical liner is ensured by a clearance between piston and liner of 0.4 mm. The piston rings are located in the lower part of the engine, i.e., below the displacement volume in the iron liner section. The optical engine is driven by a 30 kW electrical engine that allows fast accelerating and decelerating of the test engine. This reduces the starting time and prevents unnecessary contamination of the optical parts of the engine. Furthermore, a mass balancing, which meets reciprocating forces of all orders, and a flight wheel, connected to the crank shaft, limits the deviation in engine speed due to varying cylinder pressures during compression and power stroke to about 1.5% of the actual engine speed. The crank shaft is equipped with a shaft encoder with 3600 pulses per revolution. An additional pulse at top dead center combustion is measured to distinguish between top dead center gas exchange and top dead center combustion. The progression of engine speed, intake pressure, and cylinder pressure can be found in fig. 5.5. The engine is equipped with an oil lubrication system to lubricate all essential engine parts. This system is also used to control the engine temperature. A custom made oil conditioning system ensures oil temperatures between 60 and 70 °C. A detailed description of the system can be found in Karhoff [49]. The intake pressure is monitored with a Kistler 4005BA5FA0 piezo-pressure transducer and the combustion chamber pressure with a Kistler 6045A piezo-pressure transducer. The main characteristics of the engine are listed in tab. 5.2. An image of the TINA engine during measurement can be seen in fig. 5.4. A laser light sheet is introduced laterally onto the 45° mirror positioned below the piston crown. The light sheet is directed by the mirror through the flat quartz glass piston crown inside the combustion chamber. As the light sheet does not pass the quartz glass liner, reflection can be avoided. The quartz glass piston crown is fixed onto the piston by a metal union nut with an inner diameter of 58.5 mm. For this reason, the illumination of the combustion chamber is restricted to its inner part. However, Ruess et al. [87] suggest that the uncertainty in detecting particles in the outer part of

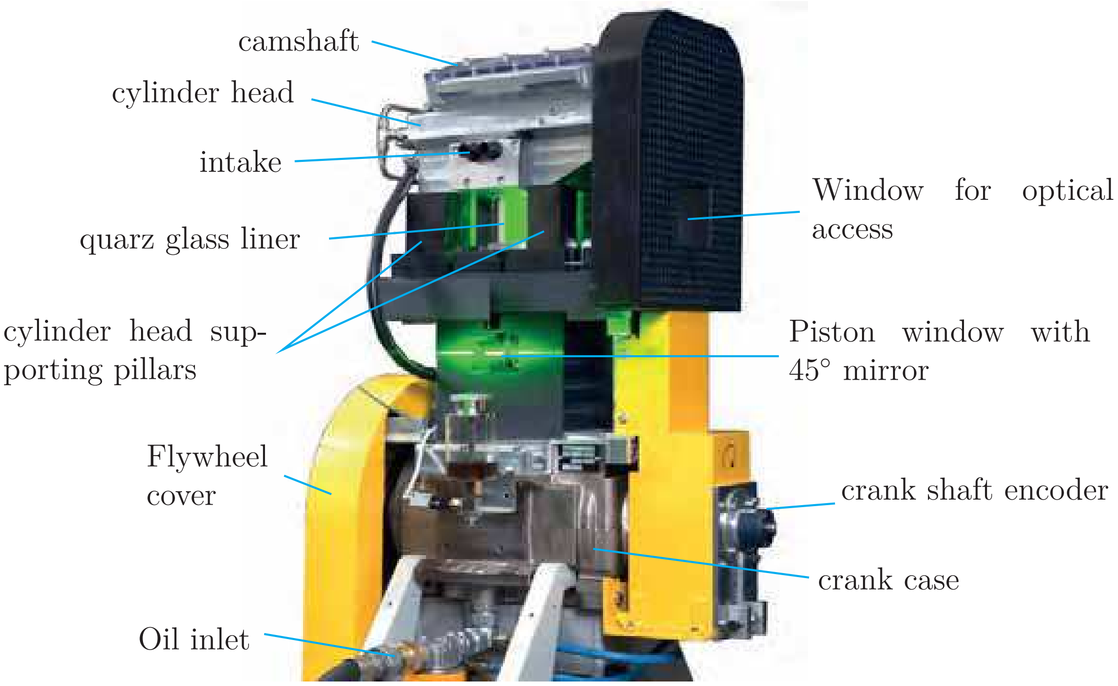

Figure 5.4 – TINA engine with introduced light sheet [49].

a cylinder increase. They suggest to restrict the field of view to the inner 76% of the cylinder, which still can be achieved.

As the cylinder head has to be supported, the radial optical access is restricted. However, depending on the measurement technique, the engine can be equipped with two different supporting pillar layouts to achieve sufficient optical access. For 2C-2D measurements, i.e., Mie scattering, the engine can be equipped with a four pillar setup, whereas a three pillar setup can be used for stereoscopic PIV. Fig. 5.6 shows a schematic of the two different pillar configurations and the imposed restrictions in the radial field of view.

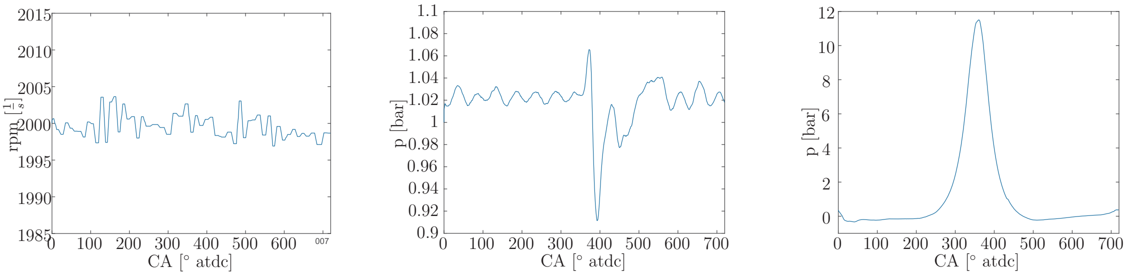

(a) engine speed (b) intake pressure (c) cylinder pressure

Figure 5.5 – Progression of the engine speed (a), intake pressure (b), and cylinder pressure (c) for the TINA engine.

Fuel injection and seeding for PIV measurements contaminates the optical piston crown and liner. Therefore, the optical parts have to be cleaned between measurements.

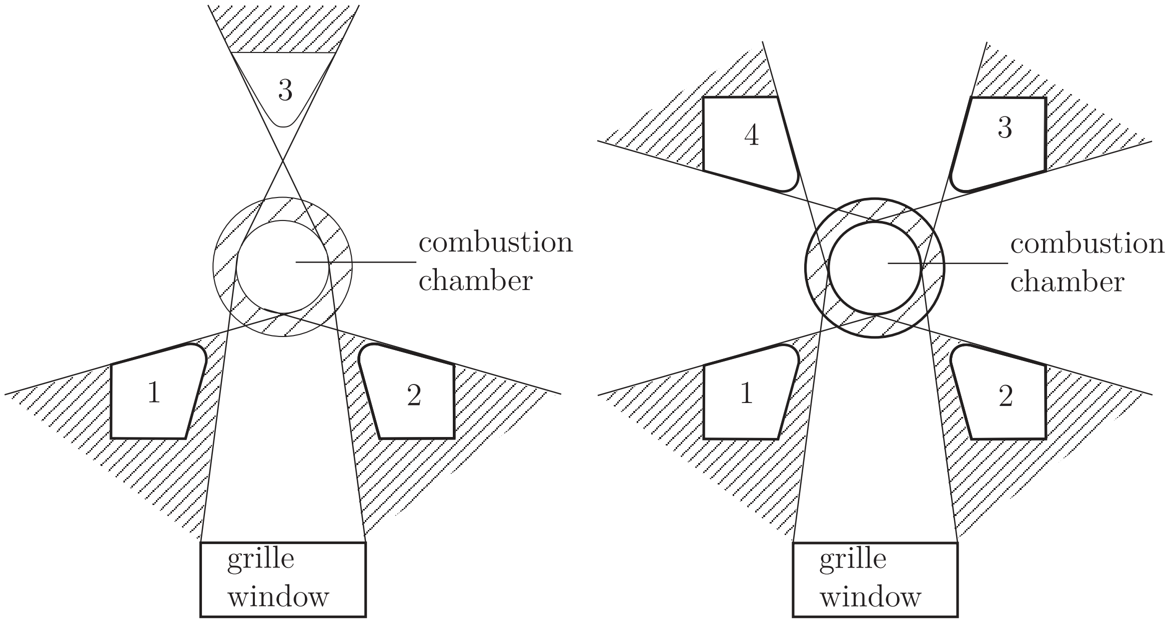

(a) three-pillar configuartion (b) four-pillar configuration

Figure 5.6 – TINA engine with introduced light sheet [49].

For this reason, the pillar connection between iron liner section and cylinder head is mounted on a platform. This platform, including pillars and cylinder head, can be lifted about 7 mm using two hand operated levers. With this, the quartz glass liner can be removed without disassembling the complete upper part of the engine.

For the fuel injection measurements, the engine is equipped with a piezo-electric hollow cone A-type fuel injector (Siemens VDO 104480-501). The half-cone angle of the injector is 47°, the maximum needle lift is 35 μm. A detailed description of the injector can be found in Mathieu [62]. The injector is driven by a VAPA piezo power amplifier (Vemac GmbH). The piezo power amplifier can be controlled by a TTL signal from the engine control software. The injection pressure is controlled by a custom made hydraulic injection system by FEV Motorentechnik GmbH. The system consists of a pressure vessel that separates fuel and N_2 via a float lever. Due to safety reasons, the maximum injection pressure is restricted to 200 bar. The fuel is pressurized by an external pressure source, i.e., a N_2 pressure bottle. A high pressure hose connects the pressure vessel and the fuel injector. A schematic of the hydraulic injection system can be seen in fig. 5.7. Apart from this, the engine has been equipped with an intake air conditioning system that enables the control of intake air pressure in the range of 0.7 - 1.5 bar. The intake pressure is measured by the intake air pressure transducer. This signal is used to control air mass flow into the pressure reservoir via two magnetic valves through a PI control mechanism implemented in Labview. A schematic of the intake pressure conditioning system can be seen in fig. 5.8.

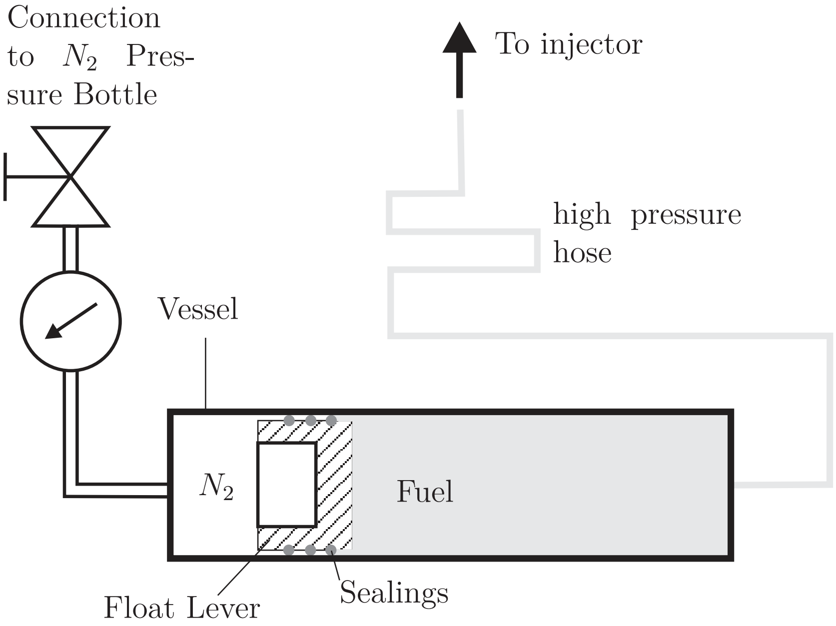

Figure 5.7 – Schematic of the pressure vessel for fuel injection.

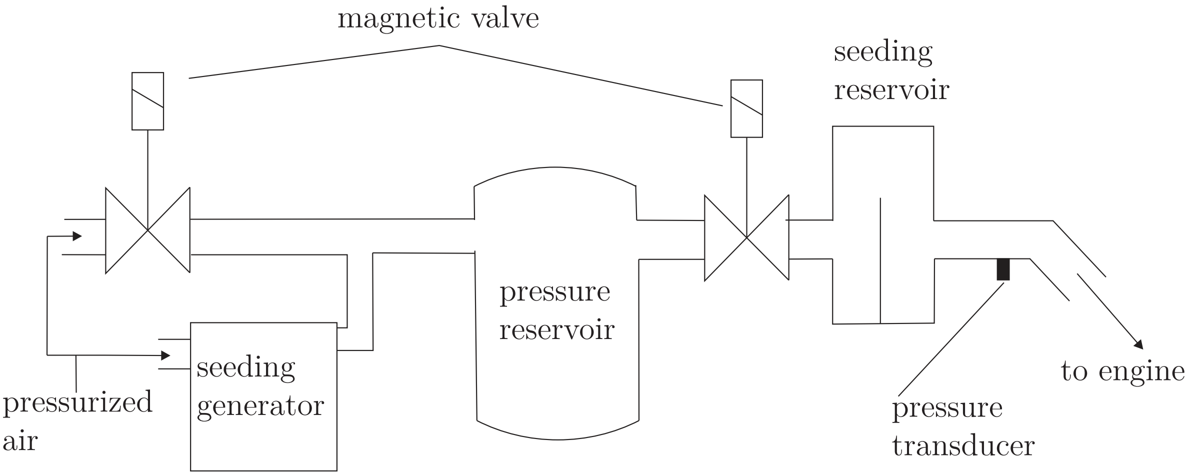

Figure 5.8 – Intake air conditioning system

5.2 Test Cases

Several optical measurement techniques have been applied to the in-cylinder flow field to yield spatial information on the flow field of an internal combustion engine, to investigate the influence of different valve timings, and the influence of fuel injection on the in-cylinder flow. At first, two different volumetric measurement techniques have been conducted at the SUZI engine. The first was a feasibility study for holo-PIV. Three independent holograms have been recorded at a crank angle of 160° atdc and 1500 RPM.

To gain a deeper understanding of the large scale flow structures, Tomo-PIV measurements have been performed for 80°, 160°, and 240° atdc and 1500 RPM. To yield ensemble-averaged data, about 300 double images have been recorded for each measurement volume. Furthermore, Tomo-PIV measurements have been performed for another valve timing with internal EGR at 240° atdc at 1500 RPM. About 300 double images have been recorded to gain statistically relevant data.

Furthermore, the influence of fuel injection on large scale flow structures has been analyzed using planar measurement techniques. Mie scattering Imaging (MSI) has been conducted to visualize the interaction of liquid ethanol fuel and the in-cylinder flow field for four different injection pressures (50, 100, 150, and 200 bar) and three different injection durations (0.5 ms, 1 ms, and 2 ms). Furthermore, three different starting times

Table 5.3 – Measurements performed during this thesis at the research engines SUZI and TINA.

Name	Holo 3D	Tomo 3D	Stereo-PIV	Mie scattering
Engine	SUZI	SUZI	TINA	TINA
Method	HPIV	Tomo-PIV	Stereo-PIV	Mie Scattering
Position	complete Volume	60 x 60 x h mm^3	y = 0 mm plane	y = 0 mm plane
RPM	1500 1/min	1500 1/min	1500, 2000 1/min	1500, 2000 1/min
Start of Injection	-	-	60, 277, 297° atdc	60, 277, 297° atdc
Injection Pressure	-	-	50, 100, 150, 200 bar	50, 100, 150, 200 bar
Injection Duration	-	-	500, 1000 μs	500, 1000, 2000 μs
Fuel	-	-	Ethanol	ethanol, methyl ethyl ketone (MEK)
Valve Timing	standard	standard and internal EGR	standard	standard
Crank angles	160° atdc	80°, 160°, 240° atdc	100, 104, 108, ..., 320° atdc	60, 61, 62,..., 337° atdc

Table 5.4 – Reynolds and Ohnesorge number for isooctane, ethanol, and MEK for a fuel temperature of 60°C before injection for different injection pressures and a cylinder pressure of 1 bar.

Fuel	Re / Oh (10^{-}2)			
	50 bar	100 bar	150 bar	200 bar
Isooctane	9,691 / 1.1219	14,156 / 1.1167	17,671 / 1.1092	20,706 / 1.1021
Ethanol	7,235 / 1.6657	10,707 / 1.6416	13,397 / 1.6277	15,717 / 1.6208
MEK	13,767 / 0.8969	20,016 / 0.8958	24,4857 / 0.8941	28,8998 / 0.8920

of injection have been analyzed, namely 60°, 277°, and 297° atdc corresponding to an in cylinder pressure of 1, 2, and 3 bar. The measurements have been performed with a temporal resolution of 1° CA. Furthermore, the interaction of methyl ethyl ketone (MEK) has also been investigated for the aforementioned injection pressures and starting points of injection for an injection duration of 0.5 ms. To yield ensemble-averaged data, 100 images have been recorded. Furthermore, separate stereo-PIV measurements for the same injection parameters have been conducted to investigate the influence of fuel injection on the large scale flow structures. Again, 100 double images have been recorded to calculate ensemble-averaged flow fields. The temporal resolution is 4° CA. Both, MSI and Stereo-PIV measurements have been conducted at an engine operational speed of 1,500 and 2,000 RPM. Table 5.3 shows an overview of all performed measurements.

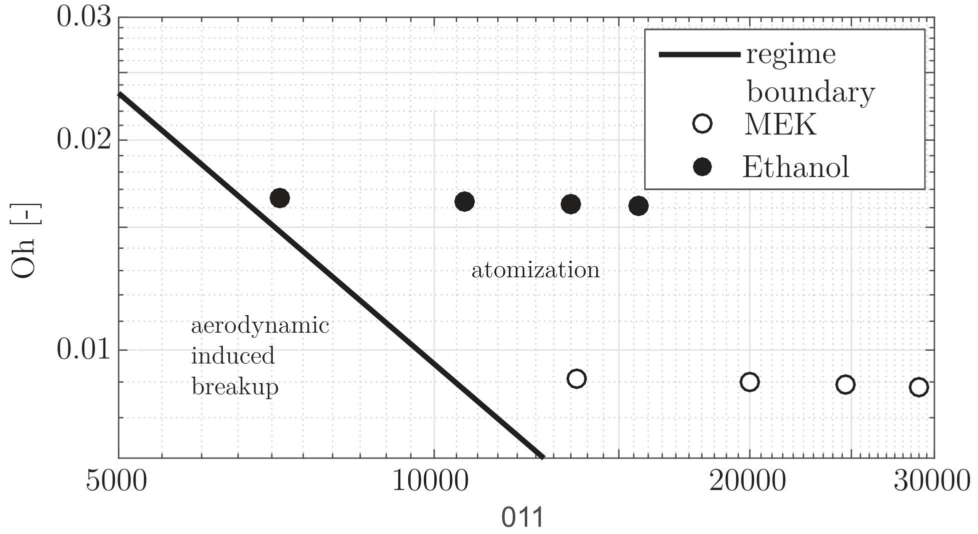

Figure 5.9 – Ohnesorge Reynolds diagram with qualitative classification of the measurement points.

Furthermore, tab. 5.4 shows the Reynolds- and Ohnesorge-number for the ethanol and MEK spray at 60 °C fuel temperature before injection, different injection pressures, and an ambient pressure of 1 bar. Additionally, the Reynolds and Ohnesorge numbers for an isooctane spray at the same conditions has been added for reference. To calculate

Table 5.5 – Physical properties of isooctane, ethanol, and MEK at 298 K and an ambient pressure of 1 bar. All values except research octane number from Daubert and Danner [31].

	unit	isooctane	ethanol	MEK
empirical formula	-	C_8H_{18}	C_2H_6O	C_4H_8O
oxygen content	mass-%	<0.5	34.7	22.2
density	Kg/m^3	699	787	799
dynamic viscosity	mPas	0.467	1.073	0.396
surface tension	mN/m	18.3	22.1	23.9
boiling temperature	K	372.15	351.15	353.15
vapor pressure	kPa	5.3	5.8	10.8
lower heating value	MJ/Kg	44.34	26.84	31.45
octane number	-	100	109	117

Table 5.6 – Mass of injected fuel.

	p	0.5 ms	1 ms	2 ms
Ethanol	50 bar	7.7 mg	15.7 mg	32.7 mg
	100 bar	10.2 mg	20.7 mg	42.5 mg
	150 bar	10.6 mg	21.8 mg	43.8 mg
	200 bar	10.9 mg	22.7 mg	44.5 mg
MEK	50 bar	8.3 mg		
	100 bar	10.3 mg		
	150 bar	10.6 mg		
	200 bar	10.9 mg		

both dimensionless numbers, the approach described in Mathieu [62] has been used. Figure 5.9 shows the Ohnesorge-Reynolds diagram for the performed measurements. The black bar shows the boundary between aerodynamic induced primary breakup and primary breakup with an atomization of the spray. It can clearly be seen that the injection is mostly performed in the atomization regime. Only the ethanol injection with 50 bar shows values near the boundary. Table 5.5 gives an overview of the fuel properties of ethanol, MEK, and isooctane at standard conditions. Table 5.6 shows the mass of injected fuel for all measured parameters. It is evident the injected mass increases for both fuels with increasing injection pressure and injection duration. However, only small differences between ethanol and MEK concerning the injected fuel mass are visible.

5.3 Holographic Particle-Image Velocimetry System

The holographic Particle-Image Velocimetry system is based on a holographic off-axis design by Konrath [51] and has been improved by Dannemann [29]. In the following section the measurement setup will be described. A detailed description of the basic system is given by Konrath [51] and a description of the improvements can be found at Dannemann [29].

5.3.1 Optical Setup

The system mainly consists of three optical components: the relay lens module containing the holographic film plate, the reference beam module, and the flow field illumination module. A schematic of the HPIV system is shown in fig. 5.10. In the following, the basic features and some modifications of the HPIV system are explained.
Two single cavity Spitlight600 Nd:YAG lasers with a total laser pulse energy of approximately 2 x 400 mJ are used to record the holograms. Since holographic PIV recordings require a high coherence length to achieve a sufficiently large contrast within the hologram plane, both lasers are seeded using an injection seeder which leads to a coherence length of approximately 1.5 m. To separate the two laser pulses in the reference module, the pulses are slightly shifted, such that both beams have a distance of 7 mm at the separation mirror. This technique avoids the deployment of a pockels cell and thus reduces the complexity of the HPIV system. A beam splitter divides the beams in a low-power reference beam and a high-power object beam. The path lengths of both beams are carefully aligned to enhance the contrast of the interference pattern. The holograms are recorded on a 127 x 102 mm^2 green sensitive VRPM glass plate by Slavich. The holographic film, rather than digital cameras, is used due to the high resolution of the optical film. As already explained in section 3.3.1 a high spatial resolution of the recording medium is necessary to resolve the interference pattern of object and reference beam for off-axis holography. The VRPM-plates are capable of recording phase- and amplitude holograms and possess a resolution of 3000 lines/mm, which is high enough to record the holographic fringe pattern. The distance between two consecutive fringes d is a function of the off-axis angle θ and the wavelength of the laser light λ:

$$d = \frac{\lambda}{2\sin\theta} \tag{5.1}$$

resulting in a fringe distance of about 0.32 μm. To measure all three velocity components simultaneously, the flow field is recorded from two orthogonal sides. For each direction, two lenses and mirrors are used to relay the particle image in front of a single hologram plate, whereas both optical paths have the same length. The illumination direction of the transmitted particle images are ±15° (horizontal) with respect to the normal of the hologram plate. The relay module is mounted on a 1,200 x 900 mm^2 breadboard and can be rotated by 180° to perform phase conjugate reconstruction. Therefore, the identical geometry during hologram recording and reconstruction is guaranteed and image aberrations due to lens impairments can be neglected. To derive the velocity vectors from the particle images, the particles are illuminated twice within a defined time interval and both images are stored on the same hologram plate. For temporal separation of the single particle images, two reference beams are used. They illuminate the hologram from ±5° vertically and 53° horizontally with respect to the normal of the hologram plane. The maximum numerical aperture is set to 0.094 to avoid overlap of direct and phase conjugate images of one of the four recorded images. For reconstruction, a continuous-wave (cw) Nd:YAG laser with the same wave length as the recording lasers is used. To switch between both reference beams, a laser modulator and a polarizing beam splitter are used. A half-cylinder made from Perspex cancels distortions in radial direction as well as astigmatic aberrations due to the original Perspex liner. The cylinder is placed in the reconstruction setup at the position of the original cylinder. For precise reversal of the reference beam angles, the alignment system described by Heflinger et al. [41] is used. The remaining reference beam aligning error is neglected using the method described by Konrath [50]. The actual measurement volume is shown in fig. 5.11. Due to slightly different beam profiles of the two Spitlight lasers, the sectional plane of the two volumes is not circular. Nevertheless, it was possible to analyze a large area of the flow inside the cylinder.

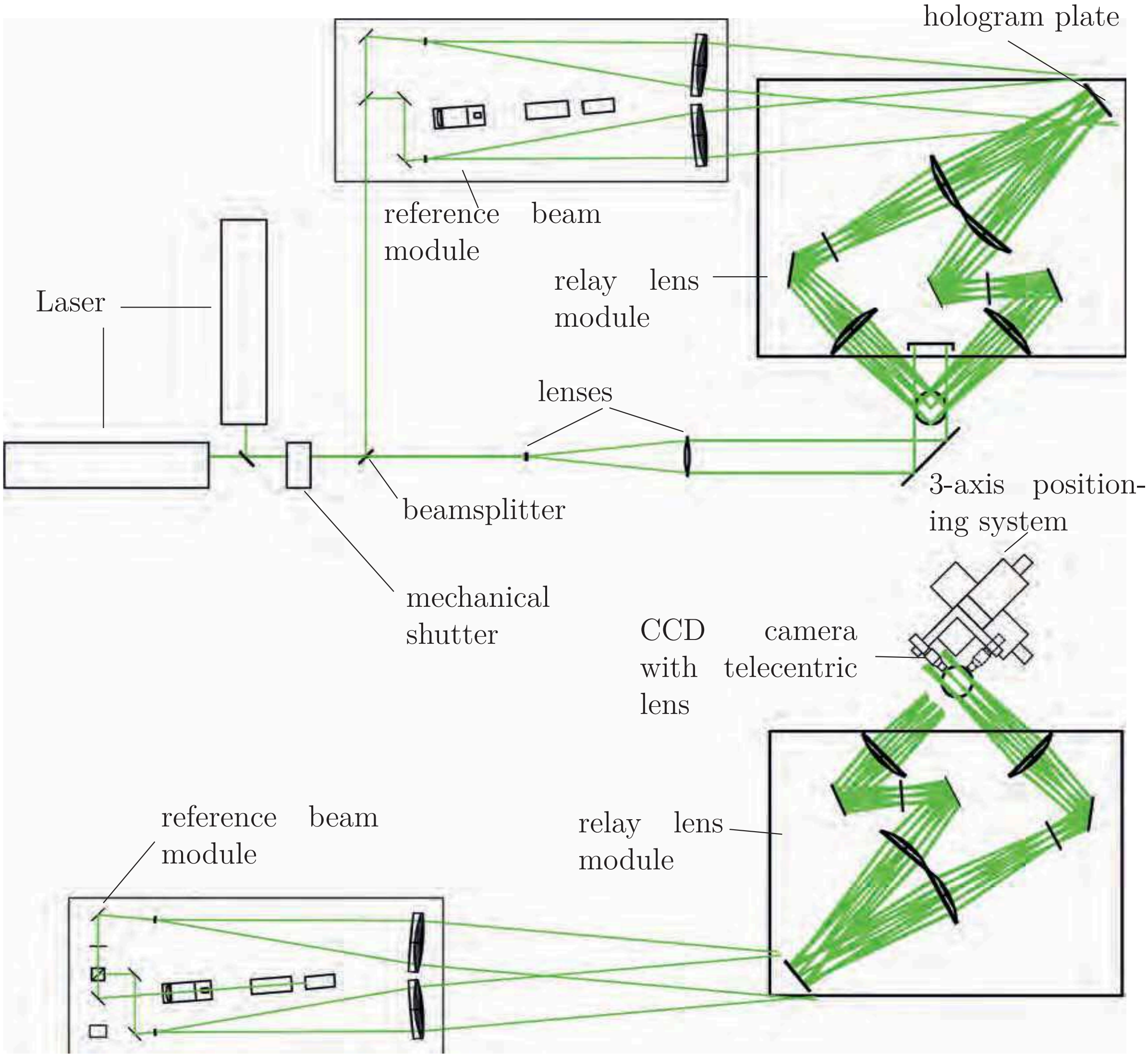

Figure 5.10 – Schematic of the recording (left) and reconstruction (right) setup of the holographic particle-image velocimetry system.

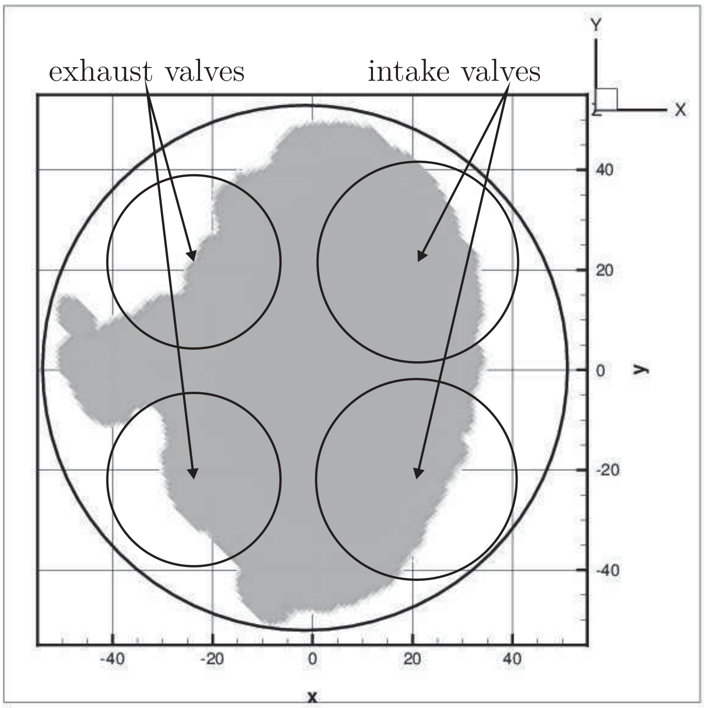

Figure 5.11 – Top view of the illuminated measurement volume for the holographic PIV measurements.

5.3.2 Post-Processing of the Holographic Particle Images

The holographic images are scanned using an AVT Guppy F-146 CCD camera and a telecentric lens (Vision & Control T50/7). The camera chip has a size of 1024 x 1392 pixels with a pixel size of 4.65 μm. The lens has a magnification of M = 0.704 and an aperture of N.A. = 0.12 resulting in a depth of focus of approximately 0.24 mm. Thus, the lens does not degrade the resolution due to an immoderate integration in longitudinal direction. The setup is mounted on a three axis positioning system (OWIS Limes 120). The image post processing is performed using Matlab routines explained by Dannemann [29] in detail. A fully automatic scanning and electronic switching of the laser modulator of each view is realized by LabView. The images are post-processed using adaptive cross-correlation algorithms, linear window deformation techniques, and vector filters like global velocity filters and local median filters. In a first step, the three-dimensional vector matrices are allocated, and split into n two-dimensional vector maps, where n is the total number of double images. The calculation of the cross-correlation is parallelized and performed on a high performance computer cluster due to the large amount of double images (e.g. 51612 double images for the engine measurements). The adaptive cross-correlation starts using an interrogation window of 256 x 256 pixels with 50% overlap. Thus, 7 x 10 velocity vectors are obtained from one double image. For the first iteration, no window shifting and deformation is used. However, the quality of the adaptive cross-correlation increases with each iteration step since window shifting decreases the loss of pairs and the window deformation compensates velocity gradients in the interrogation window. After processing all double images, the 2C/2D vector maps are composed to a three-dimensional vector field using the equations for stereo-PIV reconstruction (eq. 4.1 - 4.7) given by Raffel et al.[85]. Spurious velocity vectors are filtered and interpolated after every iteration step. If subsequent iteration steps are obtained, the velocity map is smoothed to obtain better results from the adaptive cross-correlation algorithm. The final resolution of the vector fields is a direct function of the scanning distance. The aforementioned window size of 256 x 256 pixels leads to a vector spacing in the final three-dimensional vector field of 0.75 mm.

5.4 Tomographic Particle-Image Velocimetry System

The tomographic PIV system consists of two Spitlight 600 single-cavity Nd:YAG lasers with a maximum output power of about 400 mJ per pulse and a wavelength of 532 nm, Expancel® microspheres EM 461 DET40 d25 as seeding material, four sCMOS cameras (PCO edge, 2560 x 2160 pixels, 16-bit, double-frame exposure), and Zeiss lenses with a focal length of 100 mm and f/2.0 (Carl Zeiss 100 mm / F 2,0 Makro-Planar). The cameras were arranged horizontally on a circular arc around the center axis of the cylinder. This ensures a similar distortion for all four cameras. The angle between camera 1 and camera 4 is $\alpha = 75°$, the angle between camera 2 and camera 3 is $\beta = 36°$ (fig. 5.12). Scheimpflug adpaters, an aperture of f/22, and a magnification of $M_0 = 0.163$ were used, providing a depth-of-field of 64 mm. Due to the radial distortion of the PMMA-cylinder, 17 calibration planes were used to calibrate and match the viewing planes for each camera. The software used for evaluation interpolates linearly between the calibration planes. Therefore, a high amount of calibration planes is necessary to cancel

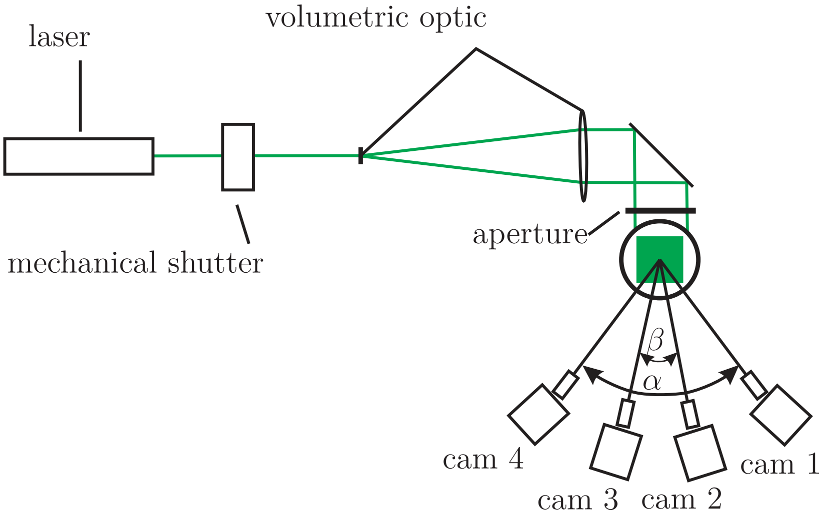

Figure 5.12 – Tomographic PIV setup. Volumetric optic consists of a f =-25 mm expanding lens and a f = 200 mm collimating lens.

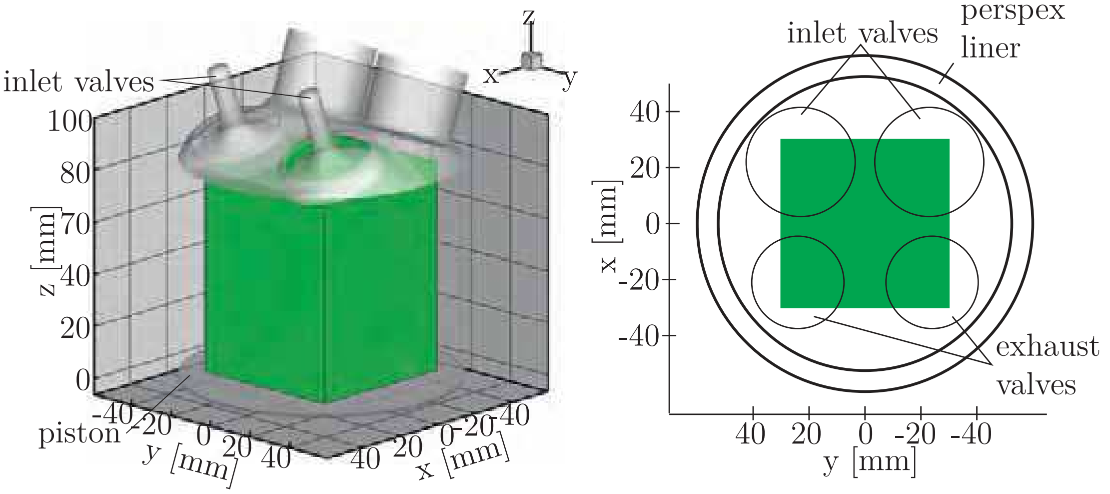

(a) Three-dimensional view of the measurement volume (green).

(b) Top view of the measurement volume.

Figure 5.13 – Top view of the measurement volume (green).

the strong radial distortion produced by the perspex liner. The 17 calibration planes ensure a calibration for the whole volume of the measurement field. The light band was formed by an expanding and collimating lens. A rectangular aperture was used to limit the illuminated volume. The setup leads to a measurement volume with an area of 60 mm x 60 mm and a height depending on the crank angle. Fig. 5.13 illustrates the cubic measurement volume at a crank angle $\theta = 160°$ and a horizontal plane of the measurement volume. A programmable timing unit (PTU, LaVision) was connected to the incremental shaft encoder of the SUZI engine to perform 300 phase locked measurements at three different crank angles. The PTU synchronizes engine, laser pulses and camera trigger accordingly. The commercial software DaVis 8.14 (LaVision) was used to record and process the raw data. Before the volume reconstruction was performed, reflections at the pent roof and the piston were masked out and a 5x5 sliding minimum was subtracted from the raw images to remove background noise. Additionally, a 3x3 Gaussian smoothing was applied to further improve the image quality. A transformation matrix (3^{rd} order polynominal approach) based on the images of the 17 calibration planes was used to match the viewing planes of all four cameras. Subsequently, several volume self-calibration steps were applied for the different measured crank angles to further reduce the deviation of the 3^{rd} order polynominal approach leading to a maximum remaining deviation of less than 0.2 pixels with several planes achieving an error <0.1 pixels. The result of the final volume self-calibration for 160° is illustrated for camera 3 at $x = 4$ mm plane in fig. 5.14.

For tomographic reconstruction a fast MART algorithm implemented in Davis was used. The reconstruction was performed for up to 6 iterative reconstruction steps with a pixel to voxel ratio of 1. The volumes have been initialized with a MinLOS volume reconstruction [64]. After each iteration, a volume enhancement has been applied with a diffusion of 0.5. The resulting three dimensional particle fields are subsequently correlated. For better results, a direct correlation approach has been used. For the first correlation, an interrogation Volume of 192 voxel^3 with a volume binning of 4 voxel^3 and an overlap of 75% has been calculated. In subsequent steps, the correlation volume has been decreased to a final volume of 96 voxel^3 without binning and an overlap of 75%. The resulting vector spacing is 0.85 mm for all three measured crank angles. After each iteration step, the vector fields are post-precessed using an universal outlier detection, interpolating of spurious vectors, and a Gaussian smoothing. After the last iteration step, the Gaussian smoothing has been skipped.

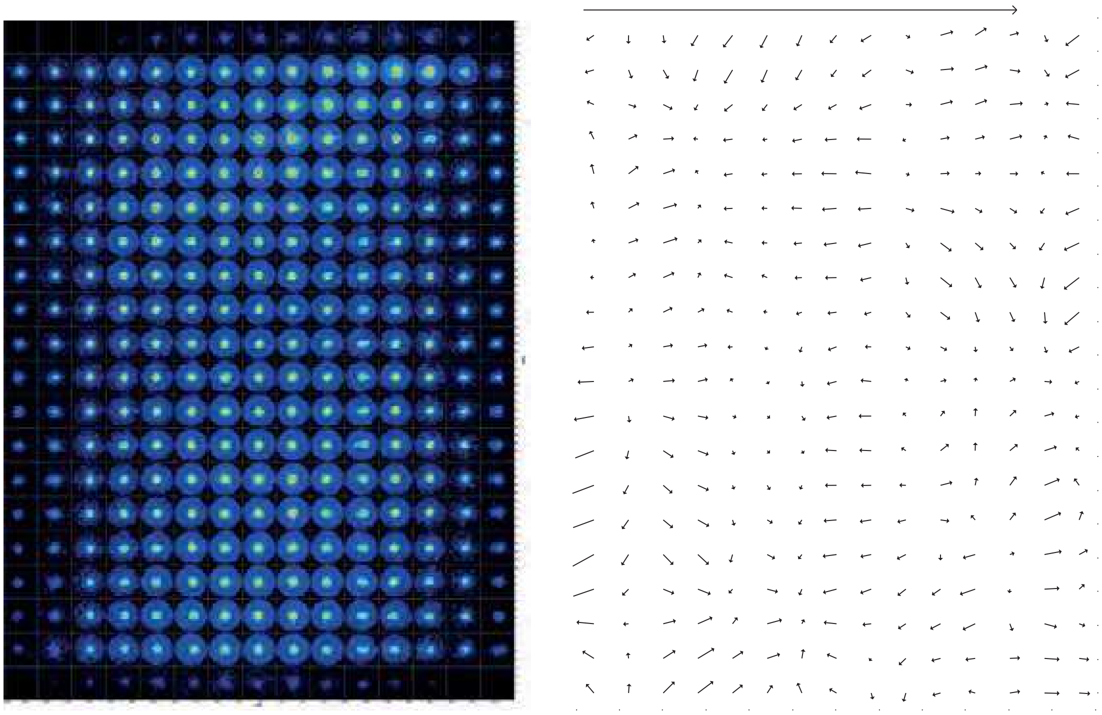
(a) Sum of correlation peaks. (b) Post-processed disparity vector map.

Figure 5.14 – Volume self calibration of one camera.

5.5 Stereoscopic Particle-Image Velocimetry System

Stereo-PIV has been used to investigate the interaction of fuel spray and in-cylinder flow field in higher detail. However, as reflexions from fuel droplets at higher injection durations heavily disturbed the PIV measurements, only measurements at an injection duration of 500 μs have been performed. Furthermore, as an investigation after fuel injection for injections with a late start of injection (SOI = 277° atdc and SOI = 297° atdc) is not possible, the focus is on the interaction of fuel and flow field for early injection at a start of injection of 60° atdc.

A schematic of the experimental setup for the Stereo-PIV measurements is shown in fig. 5.15. The setup consists of a Darvin Duo dual cavity high speed laser, which is pulsed with a frequency of 3000 Hz per cavity and two Photron Fastcam SA5 high-speed cameras with Tamron 180 mm macro lenses. The light sheet is produced using a commercial light sheet optic. The cameras are positioned in an ideal stereoscopic setup [82] with a symmetric angle of 45° with respect to the normal of the light sheet plane. The cameras and lenses were positioned in Scheimpflug condition [85] with custom made Scheimpflug adapters. Reflexions at the quartz glass liner are avoided by introducing the light sheet through the optical piston crown via an elliptical 45° mirror in the elongated slotted piston. the light sheet thickness is about 1 mm. It covers the complete stroke and about 76% of the bore as explained in subsection 5.1.2. The flow field is seeded with Di-Ethyl-Hexyl-Sebacat (DEHS) at a nominal diameter of 0.5 - 1 μm. The seeding is introduced by a seeding generator upstream of the intake valves. This ensures a homogeneous distribution of the seeding particles inside the in-cylinder flow field. The intake pressure was controlled by the intake air control system to be at 1.05 bar for all measurements. The engine temperature was set to 60°C with the oil conditioning system. To calculate ensemble averaged velocity fields, 100 cycles have been recorded. For early injection, the measurements start with start of injection. However, as strong reflections from the liquid fuel restrict the PIV evaluation, the analyzed crank angle regime is between 100° - 320° atdc with a resolution of 4° CA.

After recording, a background subtraction of a minimum image, calculated out of all images, has been used to increase the image quality. Furthermore, a masking algorithm has been applied to mask out reflexions at the piston and the pent roof.

After that the software PivView has been used for the flow field evaluation. Before calculating the vector fields, a calibration has been performed to map pixel coordinates of both cameras to real coordinates. The calibration is based on a 2D target placed inside the cylinder. The target has equally spaced dots with a dot spacing of 5 mm and a dot diameter of 2 mm. An advanced Tsai-model based on a mixture of calibration approaches by Soloff et al. [91] and Tsai [101] is used to calculate the mapping function. Furthermore, the calibration had to be improved as imaging through transparent cylinders leads to non-linear radial distortions [87]. Additionally, errors through small misalignment between laser light sheet and calibration plane, so-called registration errors [109], have to be canceled out. For this, disparity maps out of the recorded

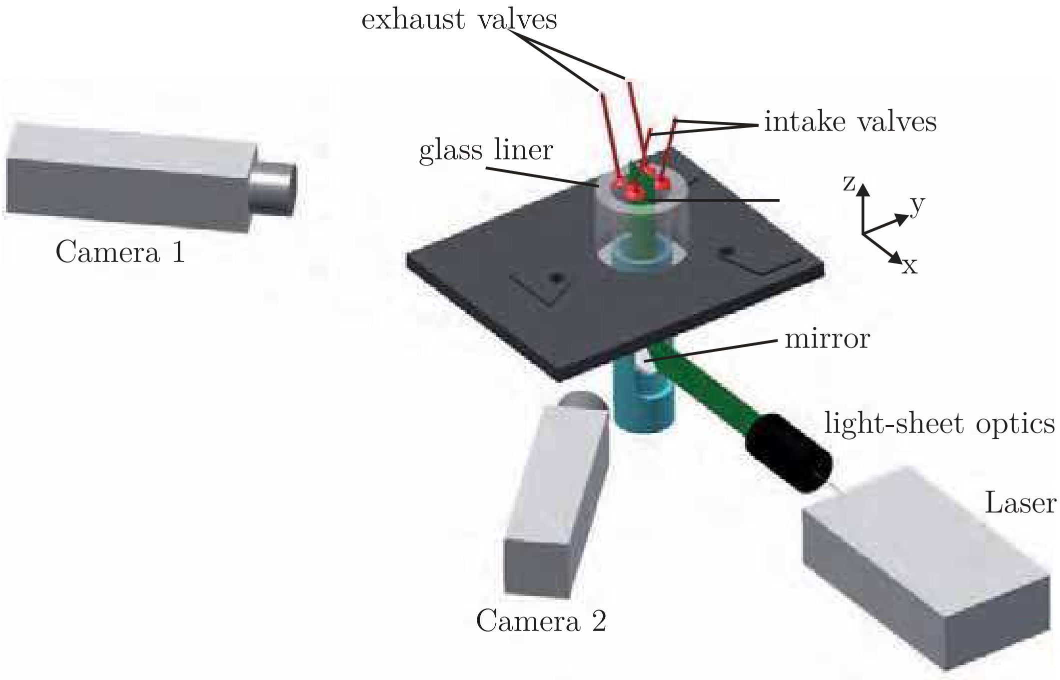

Figure 5.15 – Stereo-PIV test rig.

particle images have been calculated using the approach explained in Raffel [85]. The technique uses the calibration between images from camera 1 and camera 2 at the same time step to calculate the disparity of the views with respect to each other. As both cameras are stationary, ensemble correlation is used to create statistically more reliant disparity maps. After that, the map is used to correct the calibration factors accordingly. After calibration, a multi-grid interrogation algorithm with a starting window size of 96 x 96 px^2 and a final window size of 24 x 24 px^2 with 50% overlap and sub-pixel accuracy has been used to calculate the velocity vectors. Between each correlation step, five validation passes with a normalized median test [106] have been used to determine and filter spurious vectors. The vectors have either been replaced by lower order peaks from the cross correlation or interpolated into the velocity field. This leads to a vector field with over 93% valid vectors in the last pass.

5.6 Mie Scattering Imaging Test Rig

Mie scattering Imaging (MSI) has been used to investigate the interaction of a liquid fuel spray and the air flow field of the TINA engine. The setup can be seen in fig. 5.16. Laser light from a Darvin Duo high-speed laser is used to illuminate the liquid phase of the fuel spray with a frequency of 12.000 Hz. The laser light is expanded using a commercial light sheet optic. The light sheet is redirected by an elliptical 45° mirror and illuminates the fuel spray through the quartz glass piston crown. It covers the complete stroke and about 76% of the bore. The restricted field of view is through the

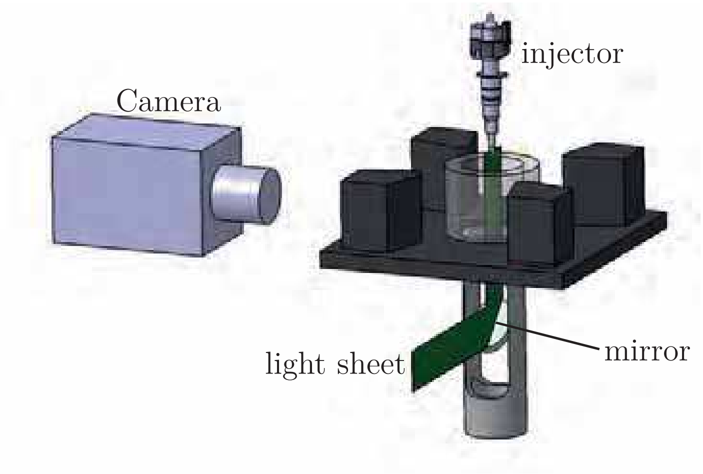

Figure 5.16 – Mie Scattering Imaging test rig.

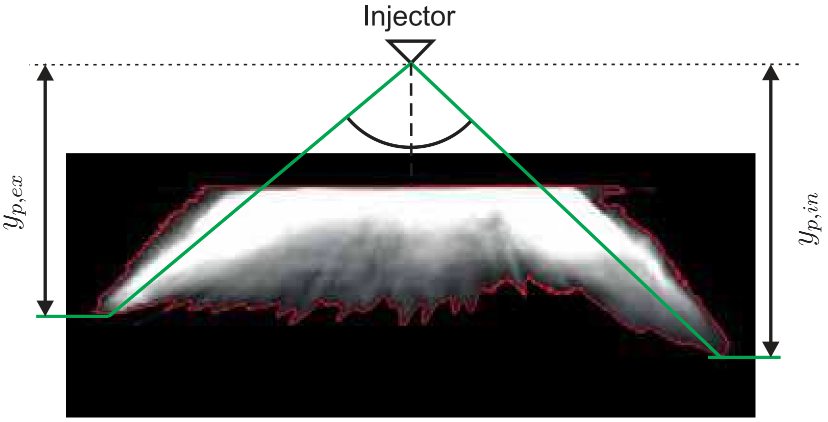

Figure 5.17 – Mie scattering image of the liquid phase. The image shows an extracted contour (red) and the penetration length for intake and exhaust side.

union nut, as explained in subsection 5.1.2. Through this, reflexions at the liner wall are avoided. The intake air pressure has been controlled with the intake air control system to be at 1.05 bar for all measurements. The engine temperature was set to 60°C with the oil conditioning system. A Photron Fastcam SA5 and a Tamron 180 mm macro lens with f/8 were used to record the fuel spray with a temporal resolution of 12.000 Hz. To resolve the entire injection process, the image recording has been started at start of injection. To achieve statistically converged data, 100 cycles have been recorded for each measurement point. The data has been processed using an in-house Matlab code. After recording, a background subtraction was used to reduce noise through reflections at the cylinder head and the cylinder walls. Afterwards, the grayscale images have been binarized using a fixed intensity threshold of 11% of the maximum intensity. Although, literature proposes a threshold of 3% [10, 80] or 13% [78] we found the value to be the most stable concerning for spray boundary detection. After that, a boundary detection algorithm, already implemented in Matlab, was used to detect the boundary of the binarized spray. The boundary contour allows the detection of the penetration length.

For this study, the 2D sheet of the hollow cone spray has been divided into two parts. The first half is below the intake valves whereas the second part is located below the exhaust valves. The penetration length $y_{p,i}$ is defined as the maximum distance between injector and fuel boundary on both sides. Figure 5.17 shows the liquid phase and the detected spray boundary as well as the extracted penetration length for the intake and exhaust side for one exemplary time step.

6

Results

6.1 Data Validation and Estimation of Measurement Errors.

In the following section, an error estimation is done for all measurements. The 3D velocity measurements are validated using the principle of mass conservation:

$$\frac{\partial \rho}{\partial t} + \frac{\partial(\rho u_i)}{\partial x_i} = 0 \quad . \tag{6.1}$$

In the case of the HPIV measurements, it was applied to different control volumes (CV). For the Tomo-PIV measurements, the CV is corresponding to one interrogation volume. Since in the cold flow field the temporal (fig. 6.1) and spatial variation of the density at a given crank angle can be assumed negligible, eq. 6.1 can be simplified to

$$\frac{\partial u_i}{\partial x_i} = 0 \quad . \tag{6.2}$$

At equidistant spacing the divergence of the velocity vector can be approximated by

$$\Delta U = \sum_{i=1}^{3} \frac{\Delta u_i}{\Delta x_i} \tag{6.3}$$

to assess mass conservation, i.e., non-zero values of ΔU indicate an uncertainty of the measurement results. The quantities Δu_i and Δx_i denote the discretized velocity gradient and the equidistant vector spacing. Furthermore, the standard deviation of the normalized velocity flux

$$\sigma = \sqrt{\frac{1}{N-1} \sum_{CV} \left(\frac{\Delta U(CV)}{U_{av}(CV)} - \frac{1}{N} \sum_{CV} \frac{\Delta U(CV)}{U_{av}(CV)} \right)^2} \tag{6.4}$$

was calculated to show the validity of the data. Here, U_{av} is the averaged velocity vector that enters the CV. Additionally, the absolute error within a confidence interval of 95%

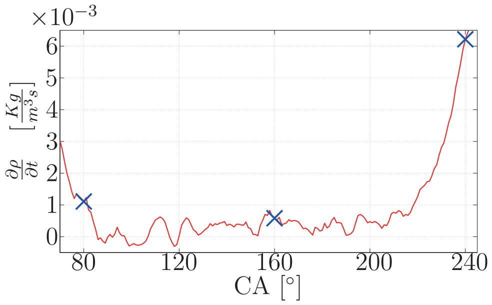

Figure 6.1 – Temporal density gradient in test engine. The crosses mark the measurement timings.

of all three velocity components and the variance of all three velocity components have been calculated. The variance of the mean velocity component $\overline{u}$ is given by

$$var(\overline{u}) = \frac{1}{N}\overline{u'^2} \tag{6.5}$$

and the variance of the fluctuating velocity component u'

$$var(u') = \frac{1}{N}\left(\overline{u'^4} - (\overline{u'^2})^2\right) \tag{6.6}$$

the theoretical errors for a confidence interval of 95% read

$$\Delta\overline{u} = 1.96\sqrt{var(\overline{u})} \tag{6.7}$$

and

$$\Delta u' = 1.96\sqrt{var(u')} \quad . \tag{6.8}$$

6.1.1 HPIV Error Estimation

To assess the quality of the HPIV measurements the mass conservation principle as explained in eq. 6.1 has been applied to different CV's of the unfiltered and low pass filtered velocity field. A CV is defined as $j \cdot W^3$ with $W = 0.75$ mm as the correlation window size and j = 1, 2, 4 and 8. Figure 6.2(a) shows the probability density function (PDF) of the divergence for the unfiltered data for different control volumes. It is obvious that the PDF for small CVs is broadened compared to the PDF for larger CVs. This shows an uncertainty for the mass conservation for small CVs and results from discretization errors. Zhang et al. [110] suggest that the main source of this error is a non-uniform particle distribution in the sample volume as well as a limit in spatial resolution. Figure 6.2(b) shows the PDF of the divergence for the low-pass filtered data for different control volumes. One can see that the PDF possesses higher values at $\Delta U = 0$ and is therefore less broadened.

Furthermore, the standard deviation of the normalized velocity flux as explained in eq. 6.4 was calculated to show the validity of the data. The values for the different CVs for the unfiltered as well as the low-pass filtered velocity data can be seen in table 6.1.

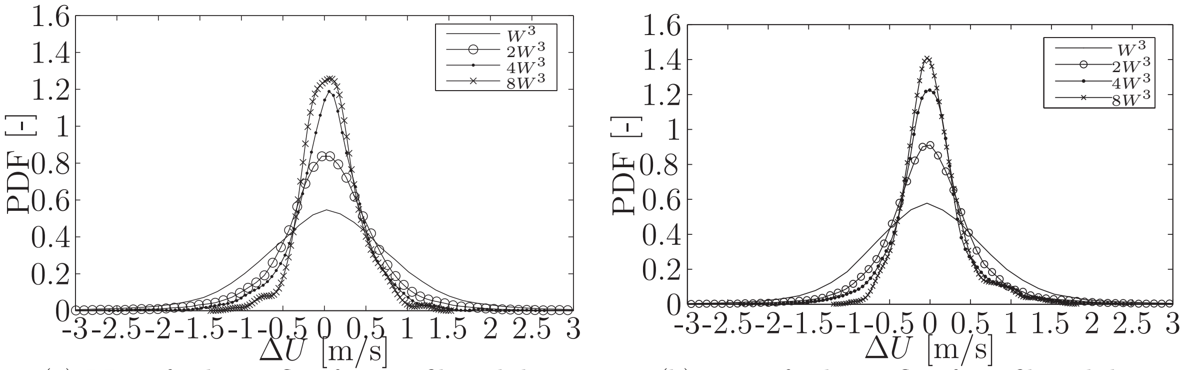

(a) PDF of velocity flux from unfiltered data.

(b) PDF of velocity flux from filtered data.

Figure 6.2 – PDF of velocity flux at different control volumes of the unfiltered (a) and the filtered (b) velocity field.

The uncertainty for the smallest CV (W) is high, but decreases significantly for larger CVs (tab. 6.1). Furthermore, the uncertainty for the filtered data is much lower and in the region of uncertainty of other volumetric measurements (Baum et al. [14], Scarano and Poelma [89], Zhang et al. [110]). Hence, the errors of the current HPIV data are in the same range as those of other experimental data.

Table 6.1 – Standard deviation of the normalized velocity flux for different control volumes (CV) for unfiltered and low-pass filtered (LP) velocity fields.

CV	σ [%]	σ_{LP}[%]
W^3	18.95	12.87
$2W^3$	9.65	5.84
$4W^3$	6.94	4.20
$8W^3$	5.65	3.64

6.1.2 Tomo-PIV Error Estimation

The mass conservation principle has been applied to the Tomo-PIV measurements. Here, a control volume is defined by a $96 \times 96 \times 96$ voxel^3 volume, which is one interrogation box. Figure 6.3 shows the probability density function (PDF) of the divergence of the velocity vector at several crank angles. It is evident that the maximum of the PDF at 80° atdc is slightly shifted to positive $\Delta_G U$ values. The broadening of the PDF is due to the higher overall velocity during the intake. The shifts for 80° and 160° of the peak value and the widening of the distribution express the fact that the spatial resolution of the measurement cannot sufficiently resolve high velocity gradients especially in the upper region of the cylinder. The increasing value of the PDF for 160° atdc and 240° atdc shows the decelerating nature of the flow field and therefore a higher PDF value for zero divergence.

Furthermore, the standard deviation of the normalized velocity flux was calculated to

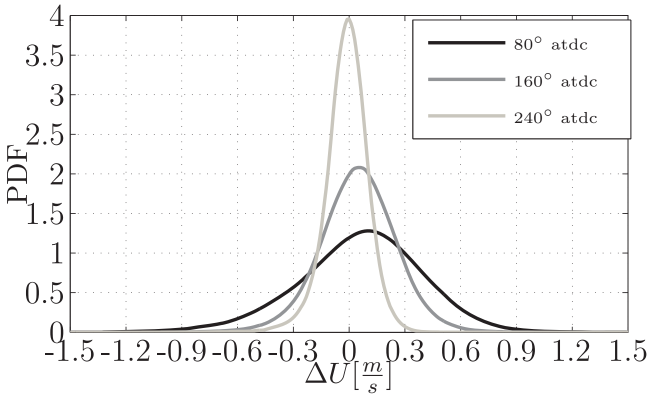

Figure 6.3 – PDF of the divergence of the velocity vector for intake (80° atdc and 160° atdc) and compression (240° atdc).

show the validity of the data. Table 6.2 shows the values for three investigated crank angles. The precision uncertainty for 240° is 8.11 % and increases up to 10.76 % for 80° atdc. Possible reasons for these errors are the inability to resolve the volumetric velocity with ample resolution. Furthermore, the large volume leads to a larger number of ghost particles that also contribute to the error (Elsinga et al. [35]). The error introduced by the perspex liner can be assumed as systematic for all measurements. Nonetheless, a precision within 10 % is in good agreement with other tomographic PIV measurements (Baum et al. [14], Scarano and Poelma [89]). Note that the measurement volume for this analysis is up to 15 times larger than the volumes reported in literature. These larger volumes result in a coarser spatial resolution compared to measurements performed with similar cameras. However, since it is the aim of the Tomo-PIV measurements to resolve the large-scale vortical structures of the mean engine flow, a decreased spatial resolution was acceptable.

Table 6.2 – Standard deviation of the normalized velocity flux for several crank angles

$^\circ atdc$	σ [%]
80	10.76
160	8.80
240	8.11

Additionally, fig. 6.4 shows the development of the mean velocity and the convergence at 80° atdc. At $n > 150$ only small variations in the mean velocity components occur. Therefore, a sample rate of $N = 300$ for all three crank angles was sufficient to calculate a converged ensemble averaged flow field.
Furthermore, the absolute error within a confidence interval of 95%, the maximum error of all three velocity components and the variance of all three velocity components have been calculated.

Using a sample size of $N = 300$ the relative maximum error for all mean velocity measurements is 12.4%. The relative maximum error for all velocity fluctuations is 29.4%. The latter is comparable to stereoscopic PIV-measurements performed by Bücker et

al. [20] whereas the former is somewhat higher. Note that in this study a separation of cyclic and turbulent fluctuations is not possible and therefore, a more thorough error analysis concerning the turbulent fluctuations cannot be given.
Furthermore, the flow field at 160° atdc based on stereoscopic and tomographic PIV measurements are juxtaposed in fig 6.5(a).The position of the tumble-vortex core for both measurements coincide and the distribution of the turbulent kinetic energy are quite similar.
In summary, the error estimate shows the tomographic PIV results to be valid for the analysis of the ensemble averaged large-scale flow structures as well as the mixing process visualized by the turbulent kinetic energy of the in cylinder flow field.

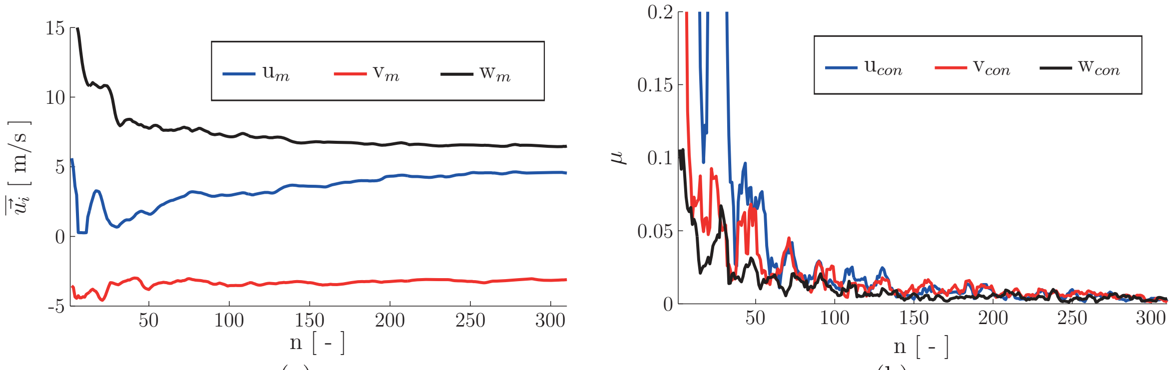

(a) (b)

Figure 6.4 – Mean velocity values (a) and convergence (b) for 80°, atdc (x, y, z) = (-1 mm, -12 mm, 71 mm).

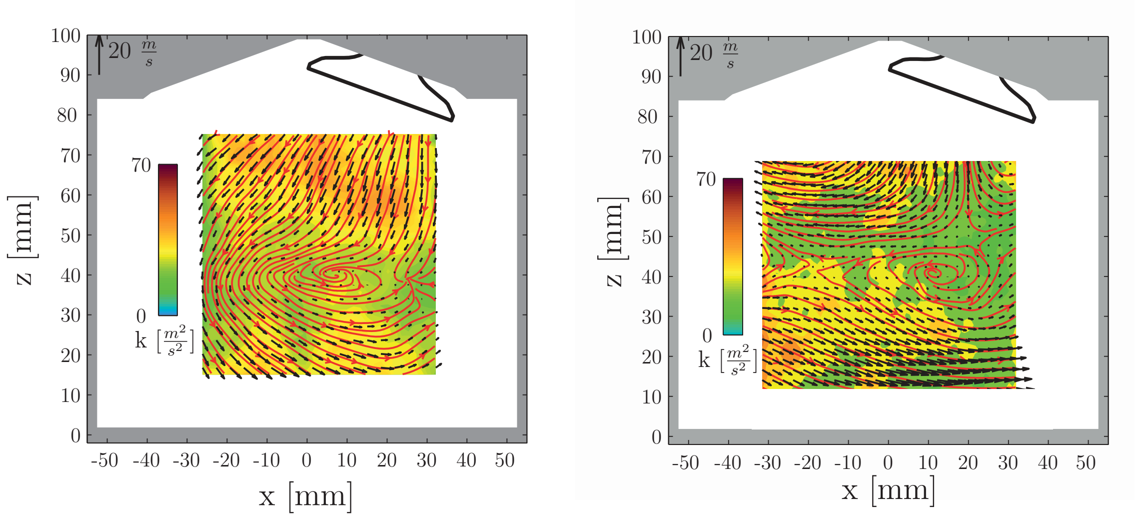

(a) Stereo-PIV (b) Tomo-PIV

Figure 6.5 – Velocity vectors (every 3rd arrow), streamlines (red lines) and turbulent kinetic energy k (color code) measured by stereo-PIV (a) and tomographic PIV (b) at 160° atdc.

6.1.3 Mie scattering Imaging Error Estimation

A convergence check [20] has been used to control whether enough MSI samples have been recorded. Figure 6.6 shows the running mean penetration for two different time steps and the convergence

$$\mu = \frac{||y_{p,n} - y_{p,n-1}||}{||y_{p,n}||} \tag{6.9}$$

with y_p being the penetration. One can see that after the first 20 samples the convergence reaches values below 1%. This suggest that the number of recorded cycles is sufficient for penetration analysis.

Furthermore, using a sample size of $N = 100$ the relative maximum error for all penetrations y_p for a confidence interval of 95% has been calculated. The results show the maximum error for early injection (first two frames) to be lower than 2.5% of the maximum penetration. Later on, the error drops below 1%, which suggest an excellent quality of the measurement data.

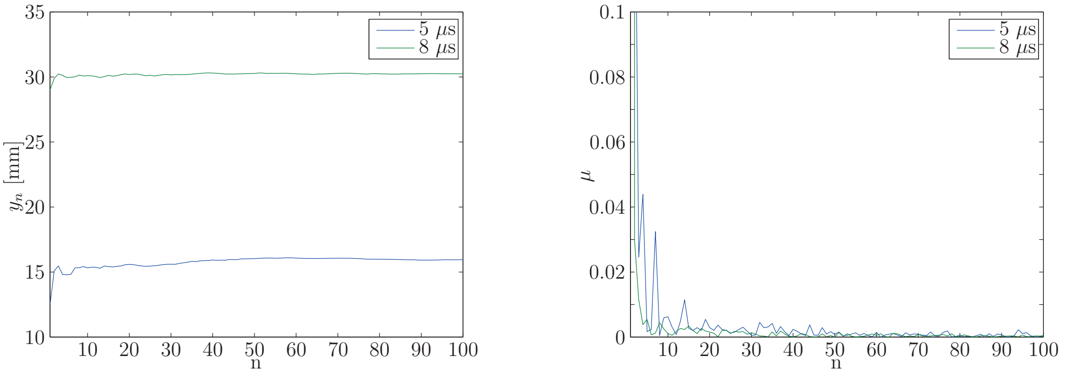

(a) (b)

Figure 6.6 – Ensamble averaged penetration for two time steps(a) and convergence μ for the two time steps at an increasing number of samples (b).

6.1.4 Stereo-PIV Error Estimation

The stereo-PIV measurements have been analyzed concerning the quality of the data. For this, a convergence check has been performed that can be seen in fig. 6.7. Fig. 6.7(a) shows the running mean of all three velocity components at the [x,z] = (0,10). Furthermore, fig. 6.7(b) shows the convergence of all three velocity components. It is evident, that after about 50 measurements, the convergence rate reaches values below 2% for all measured velocity components. After that, the convergence drops to even lower points. Therefore, a sample size of N = 100 was sufficient to calculate a converged ensemble averaged flow field. Furthermore, using a sample size of N = 100, the relative maximum error for all three velocity components for a confidence interval of 95% has been calculated. The results show the maximum theoretical error of the mean velocity to be

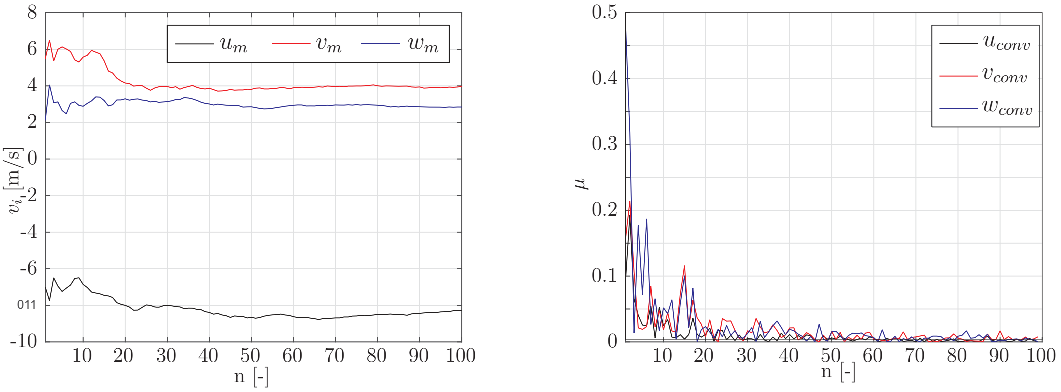

(a) (b)

Figure 6.7 – Ensemble averaged velocity components $\overline{u}$, $\overline{v}$, and $\overline{w}$ for 180° in the center of the tumble plane near the piston (a) and convergence u_{conv}, v_{conv}, and w_{conv} of the aforementioned velocity components (b).

lower than 6%. The maximum theoretical error of the fluctuating velocity components is about 10%.

6.2 Engine Measurements

6.2.1 HPIV Results

In the following, the flow field of the measurements at 160° atdc is described and discussed in detail. At first, the results of the HPIV measurements are compared to 2C-2D-PIV measurements performed by Dannemann et al.[30]. After that, the volumetric results of the measurements are discussed in detail.

Comparison of 3D/3C-HPIV and 2C/2D-PIV data

To analyze the quality of the data derived from the HPIV measurements, the fully three-dimensional velocity fields are compared to corresponding velocity distributions measured by Dannemann et al. [30] using standard 2D-2C PIV. Note that DEHS was used as seeding material in the 2D-2C PIV measurements. Although, as shown in subsection 4.1.6, both tracer particles show a similar flow following behavior for in cylinder flows. The measurement parameters for both measurement techniques are shown in table 6.3.

Table 6.3 – Measurement parameters for HPIV and 2C/2D-PIV

	HPIV	2C/2D-PIV
Resolution of recording material	3000 lines/mm ≙77.72 MPix	1376 x 1040 px
Vector spacing	0.75 mm^3	1.5 mm^2
Overlap	50 %	50 %
Sample size	3	150
Seeding	Microspheres $\bar{d} = 40\mu m$ $\rho_{MS} = 25\ \frac{kg}{m^3}$	DEHS $\bar{d} = 0.5\mu m$ $\rho_{DEHS} = 912\ \frac{kg}{m^3}$

To compare the flow fields, the ensemble averaged velocity fields in three selected measurement planes are juxtaposed as to the general structure of the flow field and the turbulent kinetic energy k. Note that for HPIV three volumetric flow fields, i.e., three hologram plates, were used to calculate the average velocity fields whereas at 2C/2D PIV 150 double images were used. Figure 6.8 shows a comparison of the in-plane velocity fields, the streamlines, and the TKE in two vertical measurement planes at 160° atdc. The two measurement planes are the symmetry plane $y = 0$ mm and a measurement plane beneath the intake valves, i.e., $y = 20$ mm (fig. 5.11). In the symmetry plane, both measurement techniques evidence the existence of the tumble-vortex, whose center can be found at approx. [x,z] = (-10 mm, 50 mm). The vortex rotates counter-clockwise and is the dominating flow structure in this measurement plane.

The turbulent kinetic energy differs between the 2C/2D-PIV and the HPIV measurements. Note that in the HPIV measurements all three velocity components were used to calculate the turbulent kinetic energy, whereas for the 2C/2D-PIV measurements only the in-plane velocity components were used. This fact has to be considered when the turbulent kinetic energy distributions are compared. At this position, the out-of-plane velocity components and their deviations, are high compared to the in-plane velocity due to a meandering of the tumble vortex which was already shown by Buschbeck et al. [22]. Furthermore, the number of HPIV measurements is low, resulting in different and not fully converged values of the turbulent kinetic energy for the HPIV measurements in the center of the tumble vortex. For $y = 20$ mm the center of the tumble vortex is more evident in the HPIV measurements than in the 2C/2D-PIV measurements. This is due to the higher spatial resolution of the HPIV measurements (vector spacing of 0.75 mm^3) compared to the spatial resolution of the 2C/2D PIV measurements (vector spacing of 1.5 mm^2). Its center is located at [x,z] = (0 mm, 52 mm). Furthermore, parts of the vortical structure of the 2C/2D-PIV measurements at [x, z] = (35 mm, 65 mm) are also observed in the HPIV measurements. Unfortunately, not the entire flow field was recorded such that this structure is incomplete. Again, a difference in the turbulent kinetic energy occurs.

Figure 6.9 illustrates the in-plane velocities, the streamlines, and the turbulent kinetic energy for the 2C/2D-PIV measurements and the HPIV measurements in three y-z planes, namely $x = -20$ mm, $x = 0$ mm, i.e., the so-called cross-tumble plane, and $x = 20$ mm (5.11). For both measurement techniques, the measurement plane at x = -20 mm shows a counter-rotating vortex pair beneath the intake valves and a downward directed jet in the gap between the intake valves. For the $x = 0$ mm plane the counter rotating vortex pair directly beneath the intake valves occurs in both images, whereas the general flow pattern further downward is different. The position of the stagnation point, which can be seen in both measurements, is lower for the HPIV measurements compared to the 2C/2D PIV measurements. Again, this can be explained by the low number of recorded holograms in conjunction with the meandering of the tumble vortex. Furthermore, a second counter-rotating vortex pair can be observed in the lower part of the cylinder, which is not visible in the 2C/2D-PIV measurements. A comparison of the HPIV measurement for the $x = 0$ mm plane with the 2C/2D-PIV measurements in the $x = -20$ mm plane shows a comparable vortex pair with similar size and identical sense of rotation. Note that the in-cylinder flow possesses cyclic variations that can explain the displacement of the vortical structures. This displacement can also be seen at the counter-rotating vortex pair below the intake valves for the $x = 20$ mm plane. In the HPIV measurements, the vortices and the stagnation point are slightly shifted to negative y values. The general propagation of the flow is nearly identical in both measurements.

To compare turbulent kinetic energy under the same conditions fig 6.10 shows the velocity and TKE distributions in the tumble plane (y = 0 mm) for the HPIV and the 2C/2D-PIV measurements. Note that for the computation of the turbulent kinetic energy, only the in-plane velocity components were used. Apart from the center of the tumble, whose turbulent kinetic energy is high, regions of high turbulent kinetic energy in both measurements in the upper and right parts of the flow are evident. The high value of turbulent kinetic energy in the vortex center results from the meandering of

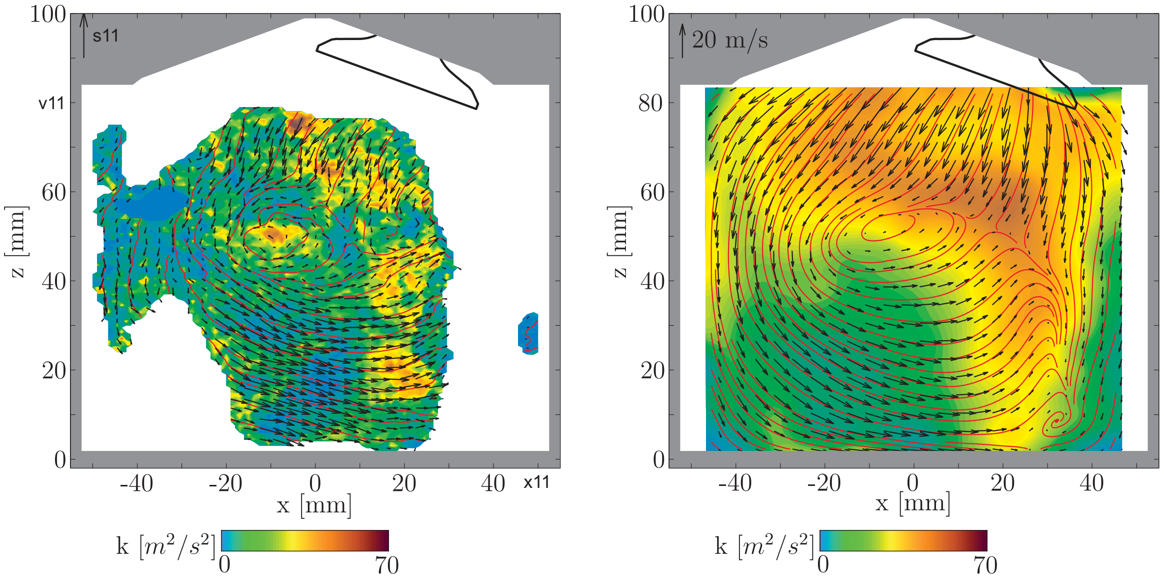

(a) y = 0 mm, HPIV

(b) y = 0 mm, 2C/2D-PIV

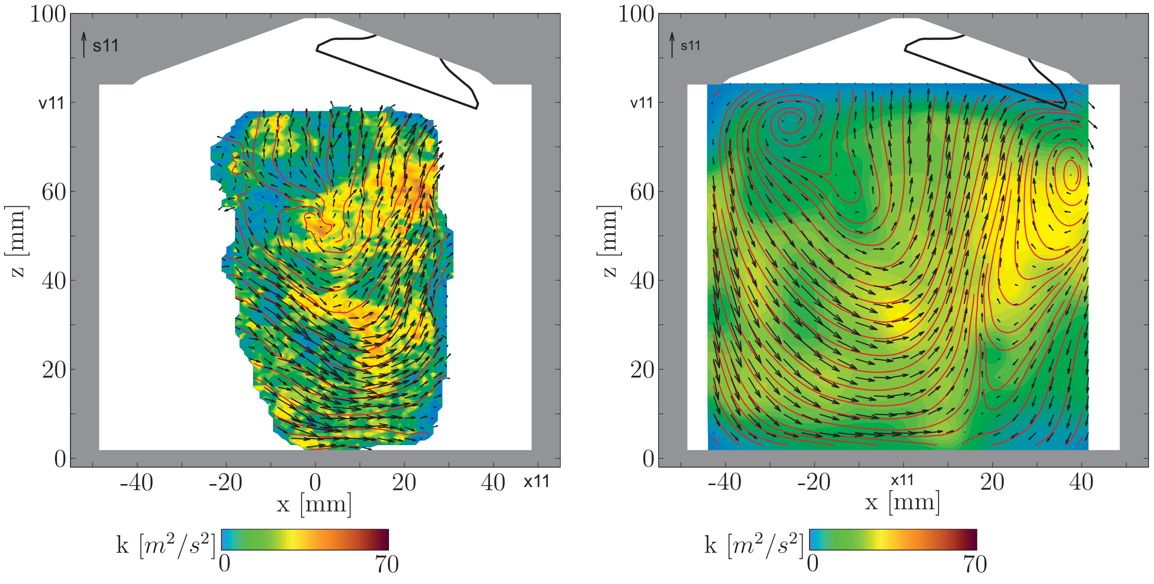

(c) y = 20 mm, HPIV

(d) y = 20 mm, 2C/2D-PIV

Figure 6.8 – Velocity vectors (every 3rd arrow), streamlines (red lines), and TKE (color code) at 160° atdc in two x-z-planes for HPIV measurements (left) and 2C/2D-PIV measurements performed by Dannemann et al. [30](right).

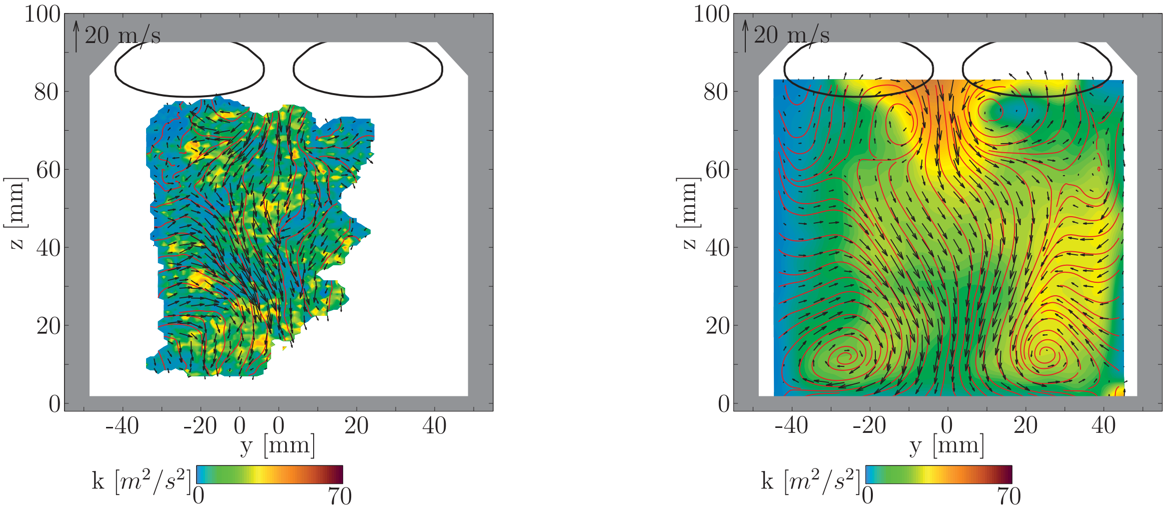

(a) x = -20 mm, HPIV

(b) x = -20 mm, 2C/2D-PIV

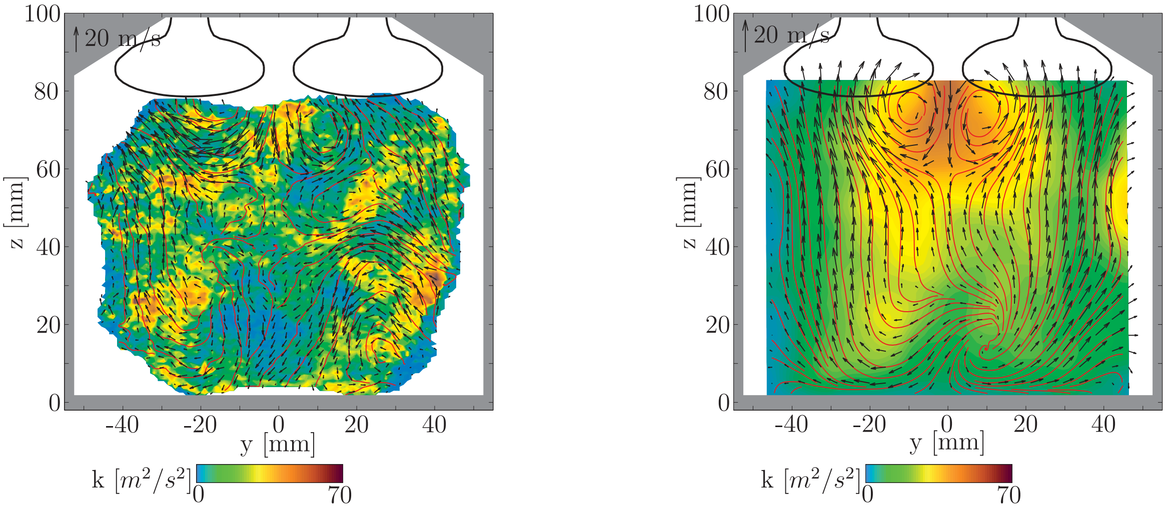

(c) x = 0 mm, HPIV

(d) x = 0 mm, 2C/2D-PIV

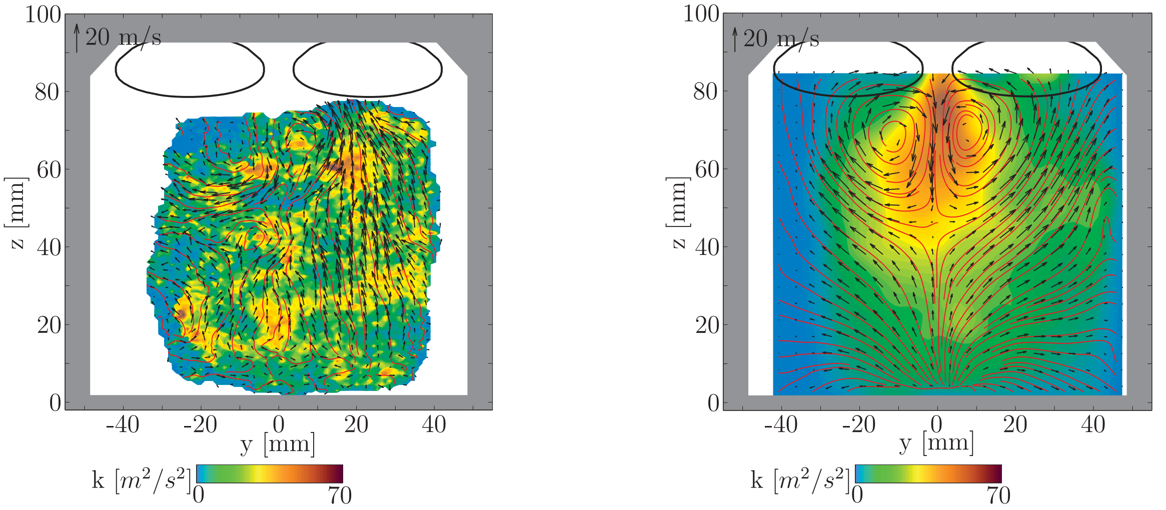

(e) x = 20 mm, HPIV

(f) x = 20 mm, 2C/2D-PIV

Figure 6.9 – Velocity vectors (every 3rd arrow), streamlines (red lines), and TKE (color code) at 160° atdc in three y-z-planes for HPIV measurements (left) and 2C/2D-PIV measurements performed by Dannemann et al. [30] (right).

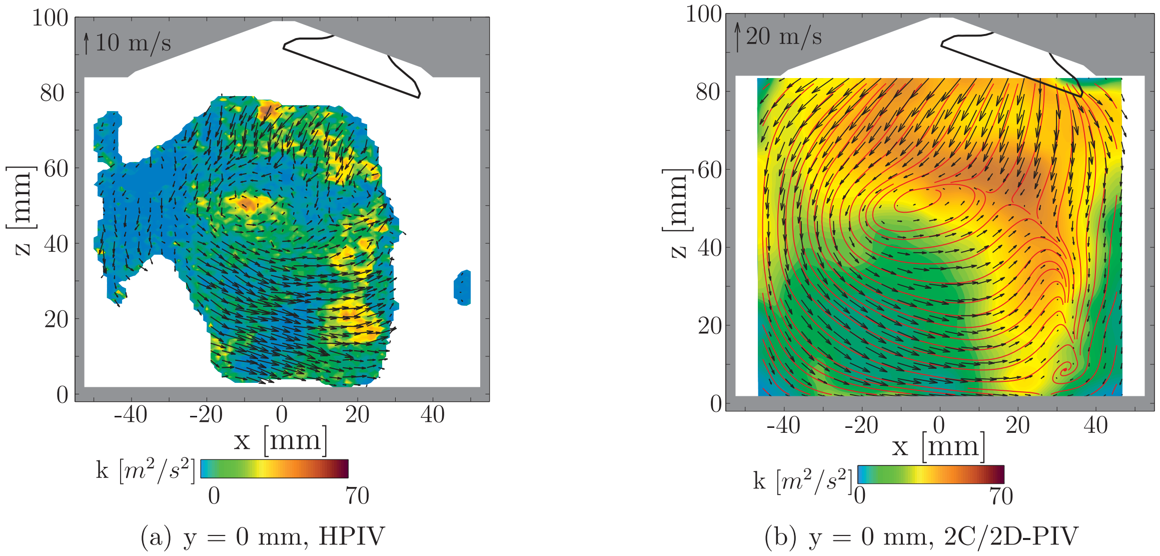

(a) y = 0 mm, HPIV

(b) y = 0 mm, 2C/2D-PIV

Figure 6.10 – Velocity vectors (every 3rd arrow) and TKE (color code) calculated from in-plane velocity components at 160° atdc for HPIV measurements (left) and 2C/2D-PIV measurements performed by Dannemann et al. [30] (right) in the tumble plane.

the flow and the low sampling rate. The absolute value is, for the HPIV measurements, somewhat lower than that of the 2C/2D-PIV measurements. This quantitative discrepancy is caused by the low sampling rate of the turbulent kinetic energy in the HPIV measurements. Nevertheless, the qualitative agreement of the turbulent kinetic energy as well as the overall flow structure, described in the paragraphs before, indicates that HPIV is capable of recording the flow field inside the cylinder at satisfactory accuracy and spatial resolution. The overall flow structure, described in the paragraphs before, shows that HPIV is capable of recording the flow field inside the cylinder at satisfactory accuracy and spatial resolution.

Three-dimensional distributions

In the previous subsection, the flow field was visualized in planes to juxtapose HPIV and 2C/2D-PIV data. This comparison showed the feasibility of HPIV to measure in-cylinder flow fields. In this subsection, fully three-dimensional distributions will be presented to visualize complete volumetric flow structure. Figure 6.11 shows the three-dimensional flow field at 160° atdc using streamlines color-coded by the absolute velocity. The flow enters the combustion chamber through the intake valves and forms two counter-rotating vortical structures below them that turn into a big rotating vortical structure, the so called tumble vortex. The counter-rotating vortical structures below the intake valves are part of the two ring vortices already mentioned by Dannemann et al. [30] and Bücker et al. [20]. In this region the jet-like flow through the gap between the intake valves as well as the flow in the lower part of the cylinder possess the highest absolute velocity.

Figure 6.11 – Three-dimensional distribution of streamlines at 160° atdc color-coded by the absolute velocity v_{abs}. The red arrows show the propagation of the tumble vortex.

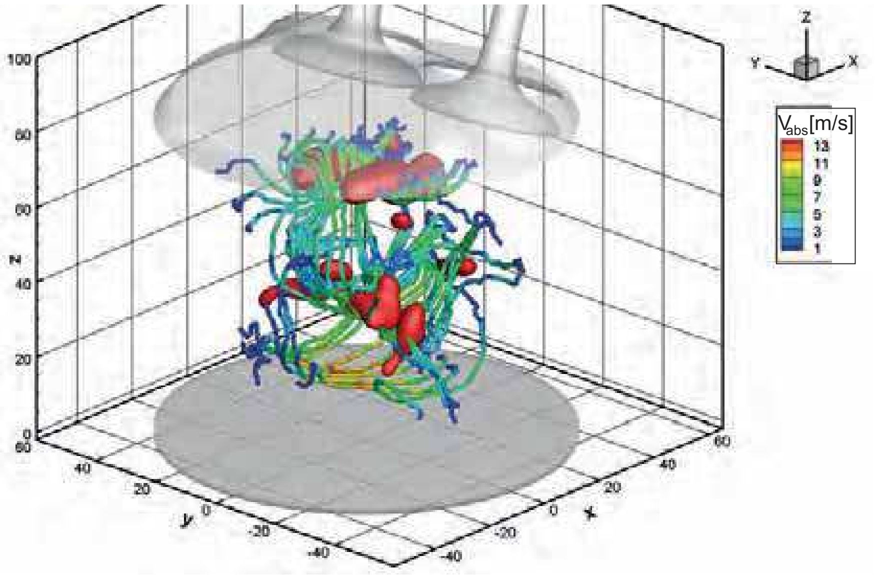

Figure 6.12 – Three-dimensional visualization of the engine flow at 160° atdc. Streamlines color-coded by the absolute velocity v_{abs} and λ_2-contours (red) are shown.

To emphasize the vortical structures and especially the vortex cores of the different vortices fig. 6.12 shows the same flow field by streamlines as well as λ_2-contours. Note that to calculate the λ_2-contours the velocity was low-pass filtered in the frequency domain to remove the small-scale fluctuations and enhance the visualization of the large-scale flow structures. The two elongated contours belong to the ring vortices below the intake valves. The propagation of parts of the ring vortex suggests that the ring vortex is somewhat elliptic, rather than circular. This can be explained through the locality of the high speed jet through the gap between the intake valves. Furthermore, the spatial propagation of the tumble vortex can clearly be seen. The tumble vortex possesses a U-shaped form, which was also shown by Bücker et al. [20] in a similar test engine.

6.2.2 Tomo-PIV Results

In the following, the in-cylinder flow fields are analyzed. In the first subsection the ensemble averaged velocity fields of the three measured crank angles are described in detail. The three-dimensional flow field is visualized to give an overview of the propagation of the large-scale vortical structures and the turbulent kinetic energy in the measurement volume. Then, the discussion focuses on the three-dimensional distribution of the main vortical structure, the tumble vortex, at one crank angle. Additionally, several planes inside the measurement volume are analyzed concerning the turbulent kinetic energy and the velocity field to gain a deeper understanding of the turbulent mixing process.

6.2.3 Three-Dimensional Flow Results

Figs. 6.14 - 6.16 show ensemble-averaged flow fields in one x-z plane (y = 0 mm) and two y-z planes (x = 29.5 mm and x = -8.5 mm) for all three measured crank angles. The measurement planes are color-coded with the turbulent kinetic energy k. Furthermore, two-dimensional surface lines on the x-z plane (black) and crank-angle based streamlines of the three-dimensional flow (red) are shown to illustrate the flow structures. Additionally, contours of the Γ_1 vortex identification function (blue) calculated from the ensemble averaged velocity fields evidence vortex cores. To keep the focus on the main flow details, only one half of the flow field is shown, since it is nearly symmetric with respect to the tumble plane. Furthermore, the three-dimensional streamlines are only plotted around the intake vortices. The tumble vortex at 240° atdc misses the symmetry with respect to the tumble plane. This observation will be investigated in the section (Multi-plane visualization) in higher detail. To gain a better understanding of the global averaged flow structures of the three-dimensional flow field, fig. 6.13 shows schematics of the main flow features of the in-cylinder flow at 80°, 160°, and 240° atdc.

The flow field at 80° atdc, fig. 6.14, shows a strong jet-like flow structure between the intake valves. Furthermore, the turbulent kinetic energy shows high values in the upper region of the cylinder between the intake valves. The blue isocontour visualizes one half of the elliptical vortex ring that forms in the upper part of the cylinder. This also is schematically evidenced in fig. 6.13(a). At this crank angle the vortex ring is not fully developed, yet. It forms due to the flow around the valves and the resulting shear layer. The tumble vortex that is typical for this engine is not yet formed since the intake ports are not specifically designed to promote tumbling flow at this crank angle (Boree and Miles [16]). Measurements from Dannemann et al. [30] evidenced that the tumble will start to form at about 100° atdc.

Figure 6.15 shows the fully developed ring vortex at 160° atdc illustrated by the Γ_1-contour. Furthermore, the streamlines illustrate the velocity field and indicate the development of the vortical structures. Due to the fact that the intake valves are still open, the flow possesses a strong downward velocity component, resulting in a fully developed tumble vortex. This vortex can be identified by the surface lines (black) in the x-z plane. Compared to the flow field at 80° atdc, the absolute peak value of the turbulent kinetic energy decreases by a factor of 6.5. The highest values of the turbulent kinetic energy produced by the pronounced shear stress distribution still occur in the upper part of the cylinder between the intake valves and low values occur in the center region of the tumble vortex. That is, the tumble conserves energy such that turbulent fluctuations around the tumble vortex decrease [20, 61]. The second Γ_1-contour in the lower part also evidences to the tumble vortex. It possesses a U-shaped form that is sketched in fig. 6.13(b). Its three-dimensional propagation is discussed at length in the next section.

Figure 6.16 shows the flow field at 240° atdc. At this crank angle, the ring vortex begins to collapse, i.e., no new energy is transferred into the rotational energy of the vortex due to the now missing intake jets. The broadening of the vortex ring is visualized by the streamlines around the Γ_1-contour. The tumble vortex is in the center plane and is evidenced by the surface lines in the lower left part of the x-z plane. The lower part of the flow field possesses an upward flow component resulting from the piston movement. At this higher crank angle the turbulent kinetic energy has been further diminished.

6.2.4 Three-Dimensional Distribution of the Tumble Vortex

Figures 6.17 and 6.18 are used to analyze the three-dimensional distribution of the tumble vortex. In the sub-figures, only one plane inside the measurement volume is shown. The tumble and the elliptical ring vortex are visualized by streamlines and the Γ_1-contour. The plane is rotated in $\Delta\theta = 5°$ steps with respect to the z-axis. Note that this illustration and as such the spatial analysis are only possible through the volumetric velocity data provided by the tomographic PIV measurements. In the center on the left of fig. 6.17(a) the vortex core of the tumble is evident. Furthermore, the ring vortex is visible in the upper right corner of the measurement plane. In the subsequent sub-figures the tumble vortex core is shifted to the center of the measurement volume. At fig. 6.18(d) this shift decreases and this part of the tumble vortex keeps its position. Another part of the tumble appears in the lower right corner of the plane which bends upwards such that both parts of the vortex core are finally nearly symmetric in the last figure (fig. 6.18(i)).
The three-dimensional shape of the tumble is driven by the contour of the cylinder. The vortex core has to follow the geometric boundary leading to the U-shaped form of its vortex core. The center of the ring vortex is shifted from the upper right corner to the upper center of the sub-figures at increasing θ. Through the rotation of the viewing plane, the second part of the ring vortex is visualized in the upper left corner of fig. 6.17(c) and occurs at increasing θ near the upper center of the subsequent viewing planes. In figure 6.18(i) both parts of the ring vortex are symmetric with respect to the center of the plane. As already mentioned, the ring vortex is generated due to the flow around the intake valves and the resulting shear layer.

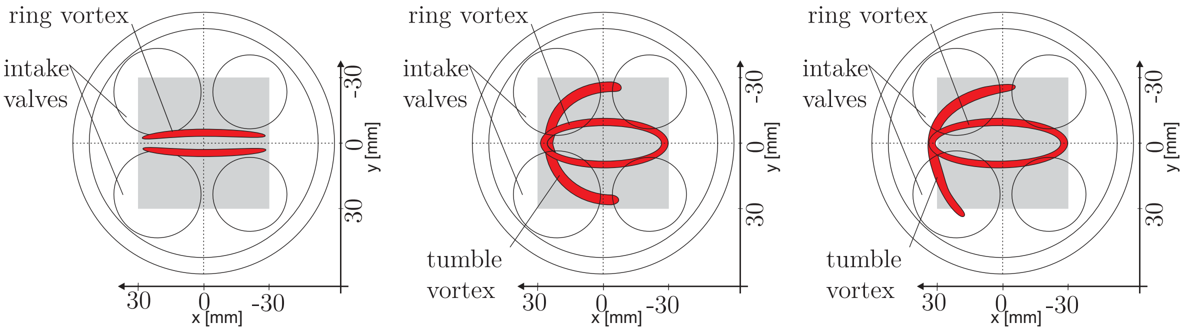

(a) 80° atdc. (b) 160° atdc. (c) 240° atdc.

Figure 6.13 – Schematic visualization of the vortex propagation of the helical intake vortex and the tumble vortex for 80°, 160°, and 240° atdc.

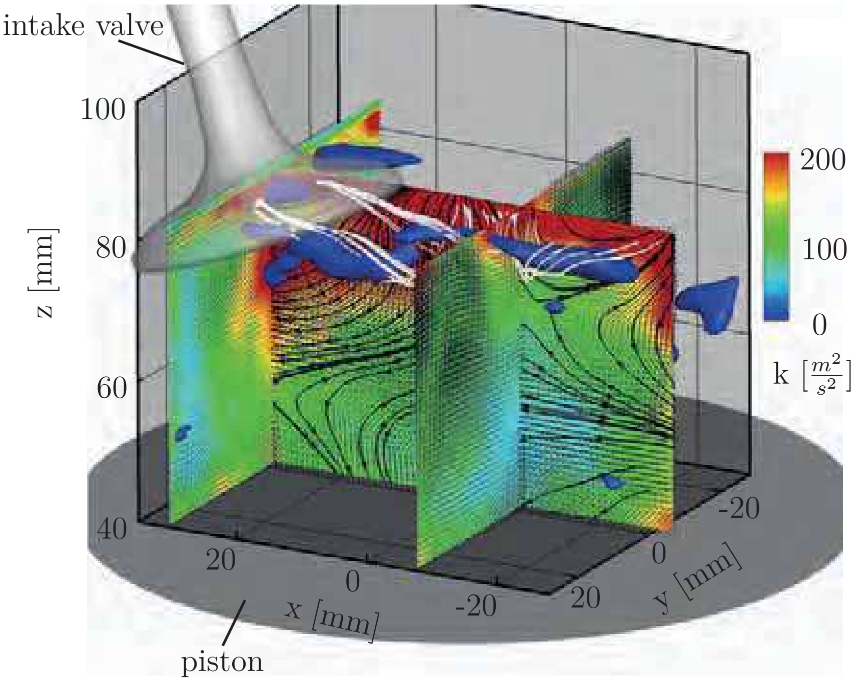

Figure 6.14 – Three-dimensional visualization of the engine flow at 80° atdc: streamlines (white), surface lines (black), contours of $\Gamma_{1,x}$ criterion (blue), and turbulent kinetic energy (color code).

6.2.5 Multi-Plane Visualization

To investigate the temporal development of the flow field, figs. 6.19, 6.20, and 6.21 show five y-z planes for all three crank angles. Each row corresponds to a fixed x-position, each column to one of the three measured crank angles. For clarity, only every 3rd measured vector of the in-plane velocity components (black arrows) is plotted. Furthermore, crank-angle based streamlines (red lines) and the contours of the turbulent kinetic energy (color code) are shown. Note that the figures are based on the fully three-dimensional measurements, i.e., the velocity vectors, the streamlines, and the turbulent kinetic energy represent a planar map of the volumetric flow field. It is evident that at 80° atdc and 160° atdc the flow is nearly symmetric with respect to the center line (y = 0 mm), whereas the flow at 240° atdc shows an asymmetric behavior.

The flow field at 80° atdc is dominated by two vortical structures in the upper part of the cylinder, i.e., the elliptical ring vortex, and a jet generated by the flow through the intake valves. This jet points in the downward direction for both positive x-planes and is then deflected towards the cylinder sidewalls. Furthermore, high values of turbulent kinetic energy quantify the turbulent character of the flow field. For negative x-values, the z-component of the velocity field in the center of the planes points in the positive z-direction. This is due to the roll up around the valve edge that leads to the elliptical ring vortex mentioned above. This vortex directs the flow to the outer region to the pent roof. Furthermore, a part of a second symmetric vortex pair can be observed at the border of the measurement volume at $z = 50$ mm for $x = 10$ mm and $x = 0$ mm.

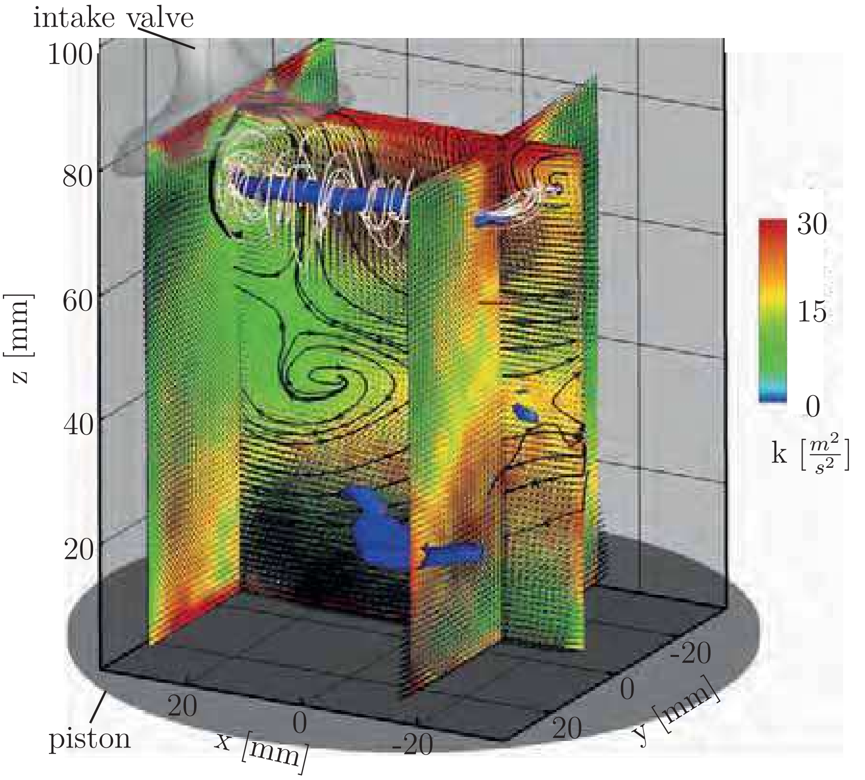

Figure 6.15 – Three-dimensional visualization of the engine flow at 160° atdc: streamlines (white), surface lines (black), contours of $\Gamma_{1,x}$ criterion (blue), and turbulent kinetic energy (color code).

These vortices were also investigated by Dannemann et al. [30]. The symmetric vortex structure in the lower part is formed by the interaction of the high speed jet and the elliptical ring vortex.
At 160° atdc, the intake valves are not fully closed. Therefore, the jet between the intake valves is still visible and has the highest value of turbulence for this crank angle. The elliptical ring vortex in the upper part of the cylinder is fully developed as indicated by the two symmetrical vortices in the upper part of the cylinder. The two vortical structures in the lower part correspond to the U-shaped tumble vortex. Compared to 80° atdc the turbulent kinetic energy decreases, due to an energy conservation in the large-scale structures, i.e., tumble vortex and ring vortex and an overall decreasing velocity.
For 240° atdc only the upper part of the flow field shows a symmetric behavior. The elliptical ring vortex still exists near the pent roof of the engine. In the lower part, only one vortex is visible at $y = -20$ corresponding to the tumble vortex. The region with positive y-values misses the part of the tumble vortex. In fact, this part of the flow is dominated by a flow directed to the cylinder wall. This suggests that the large-scale structures that are responsible for the symmetric behavior start to dissipate. This agrees with the findings by Voisine et al. [105] who state that the mean tumbling

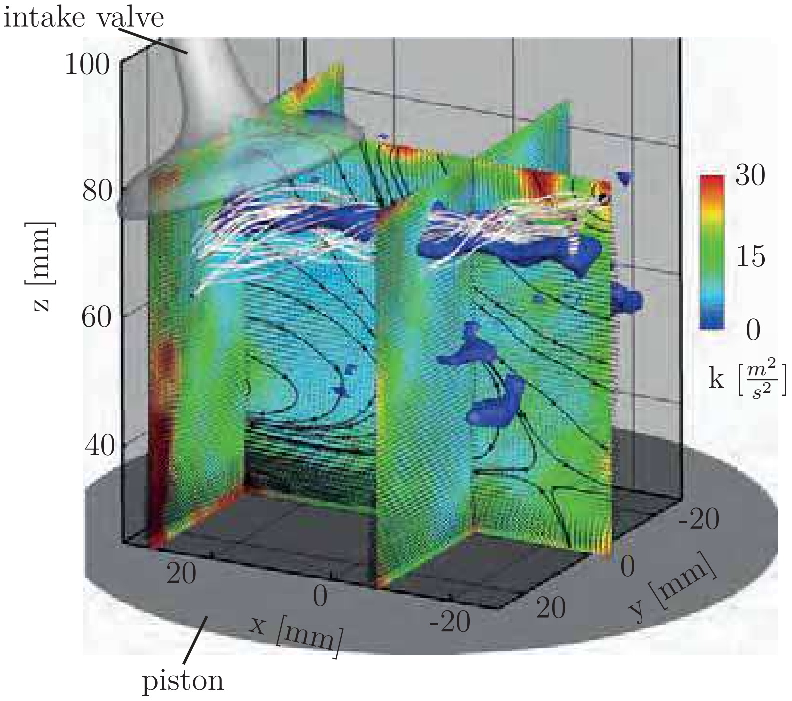

Figure 6.16 – Three-dimensional visualization of the engine flow at 240° atdc: streamlines (white), surface lines (black), contours of $\Gamma_{1,x}$ criterion (blue), and turbulent kinetic energy (color code).

motion is not symmetric at all with respect to the cross tumble plane. The region near the piston is dominated by a high positive velocity distribution in the z-direction due to the upward moving piston. Furthermore, a decreasing turbulent kinetic energy is evident.

To investigate the tumble planes in greater detail, figs. 6.22, 6.23, and 6.24 show five y-z planes for all measured crank angles. Analogous to figs. 6.19, 6.20, and 6.21, each row corresponds to a fixed y-position and each column to a fixed crank angle. The flow fields for 80° and 160° atdc are nearly symmetric with respect to the $y = 0$ plane. For the center plane of 80° atdc the upper part of the flow points in the negative z-direction. This is due to the flow through the intake valves. Furthermore, the generation of the elliptical ring vortex at $[x, z] = (-20, 80)$ is evidenced. A second vortical structure can be seen at $[x, z] = (-30, 65)$. Both vortices redirect the inflow to the left cylinder wall. Then, the flow is again redirected in the positive x-direction nearly parallel to the piston. The planes outside of the center of the cylinder show a positive velocity component in the z-direction. The aforementioned ring vortex generates a flow directed to the pent roof which is then redirected to the cylinder walls. Furthermore, in the $y = -20$ mm and $y = 20$ mm plane a vortical structure at $[x, z] = (20, 50)$ can be observed. These two vortices seem to indicate the initialization of the tumble vortex that is fully evident at 160° atdc. At this crank angle, the flow is dominated by this vortex. Its position is shown in the center plane at $[x, z] = (15, 40)$ and the vortex core has a U-shaped form that was already schematically shown in fig. 6.13(b). Furthermore, two parts of the elliptical ring vortex are clearly visible through the two

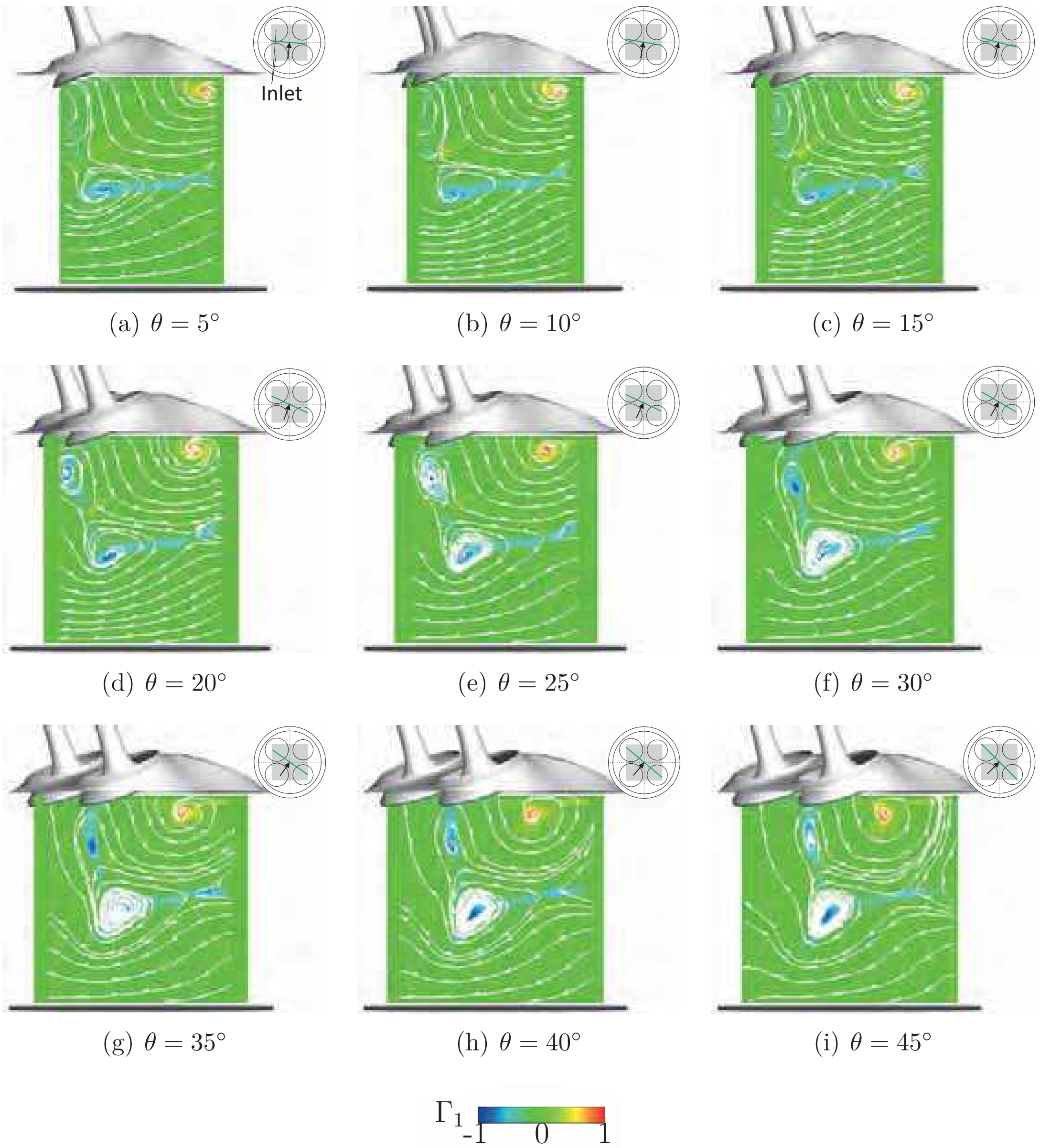

(a) $\theta = 5°$ (b) $\theta = 10°$ (c) $\theta = 15°$

(d) $\theta = 20°$ (e) $\theta = 25°$ (f) $\theta = 30°$

(g) $\theta = 35°$ (h) $\theta = 40°$ (i) $\theta = 45°$

(j)

Figure 6.17 – Spatial distribution of the tumble-vortex for 160° atdc shown through normalized Γ_1-contour (color code) and streamlines (white). Tumble plane was rotated in 5° steps around the z-axis within the range $5° \leq \theta \leq 45°$.

(a) $\theta = 50°$ (b) $\theta = 55°$ (c) $\theta = 60°$

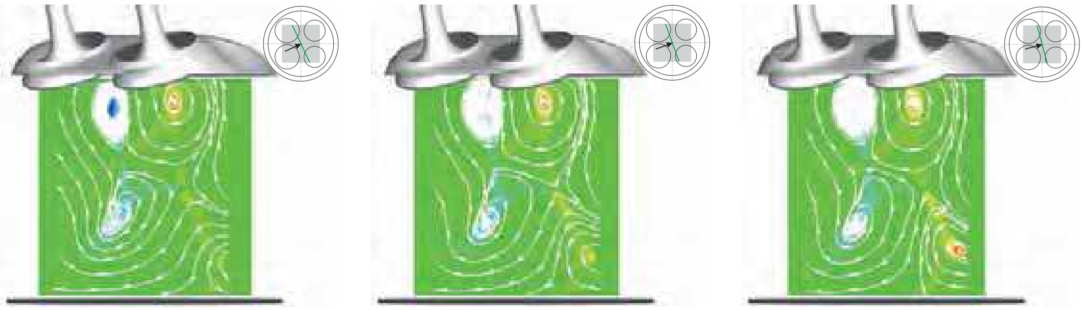

(d) $\theta = 65°$ (e) $\theta = 70°$ (f) $\theta = 75°$

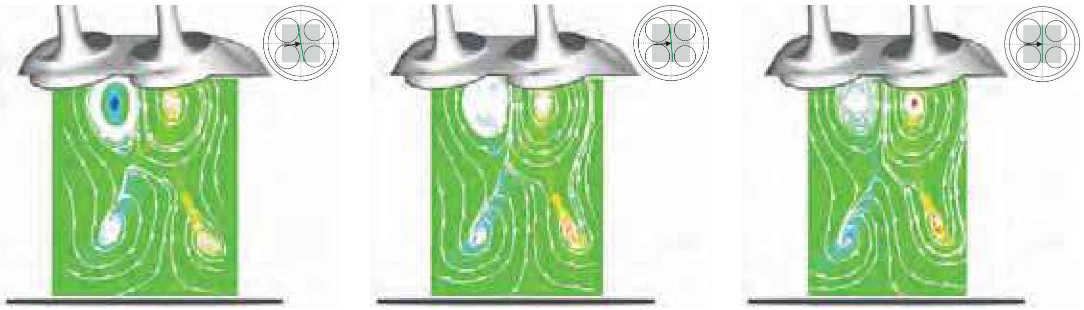

(g) $\theta = 80°$ (h) $\theta = 85°$ (i) $\theta = 90°$

(j)

Figure 6.18 – Spatial distribution of the tumble-vortex for 160° atdc shown through normalized Γ_1-contour (color code) and streamlines (white). Tumble plane was rotated in 5° steps around the z-axis within the range $50° \leq \theta \leq 90°$.

vortex cores at $[x, z] = (-25, 75)$ and $[x, z] = (30, 70)$. The ring vortex directs the flow to the pent roof where it is deflected to the cylinder wall and then to the piston. The outer planes show mostly a positive z-component of the flow that was already presented in figs. 6.19, 6.20, and 6.21.

At 240° atdc the asymmetry of the tumble is clearly visible by investigating the vortex core in each plane. For positive y-values the vortex core is clearly visible whereas for the $y = -20$ mm plane no clear vortex core can be identified. This is due to the curved form of the vortex core trajectory in this part of the cylinder. A schematic of the resulting vortex propagation is shown in fig. 6.13(c). Furthermore, the high velocity region near the piston, resulting from its upward movement is clearly illustrated. The high values of turbulent kinetic energy in the tumble vortex core compared the flow field at this crank angle are caused either by its breakup, since the large-scale structures dissipate into smaller turbulent structures, or by an increased cyclic variability of the tumble core.

6.2.6 Influence of Internal Exhaust Gas Recirculation

In the following, the results from the Tomo-PIV measurement with exhaust gas recirculation are presented. As the effect of intermediate compression shortly before tdc exhaust, causes condensation of air humidity during the intake stroke, the measurable crank angles are restricted to the compression stroke. Therefore, only measurements at 240° atdc have been conducted. To compare the flow field of the different valve timings the ensemble averaged velocity fields in three selected x-z planes and three selected y-z planes out of the measured volume are juxtaposed as to the general structure of the flow field and the turbulent kinetic energy k.

Figure 6.25 shows three y-z planes for the standard valve timing (left) and EGR (right). One can clearly see that the turbulent kinetic energy is higher for all EGR planes compared to the standard valve timing. Moreover, the position of the upper counter-rotating vortices is somewhat shifted for the EGR case. In the lower region of the flow field, no vortical structures, referencing to the tumble vortex, can be seen. This leads to a more symmetric flow field in the lower part of the combustion chamber compared to the standard valve timing. Additionally, higher velocities especially in the lower part of the cylinder can be visualized for the EGR case. The upward movement of the piston without tumble movement leads to a more upward directed flow movement. Fig. 6.26 shows three x-z planes for the standard valve timing (left) and EGR (right). Again, the turbulent kinetic energy as well as the velocities in the lower part of the cylinder are higher for EGR. Furthermore, the tumble vortex that can be seen in fig. 6.26(c) at about [x,z]=(25 mm, 40 mm) is not visible for EGR. The lower momentum of the flow, caused by lower valve lift and shorter intake valve opening times reduces the tumble ratio such that the tumble vortex is not present at compression. Instead, more small-scale vortical structures are present, visualized through turbulent kinetic energy. However, a clockwise rotating vortical structure can be detected below the exhaust valves for the y = -20 mm and the y = 0 mm plane. This vortex is assumed to belong to the ring vortex pair below the valves that forms below the intake valves

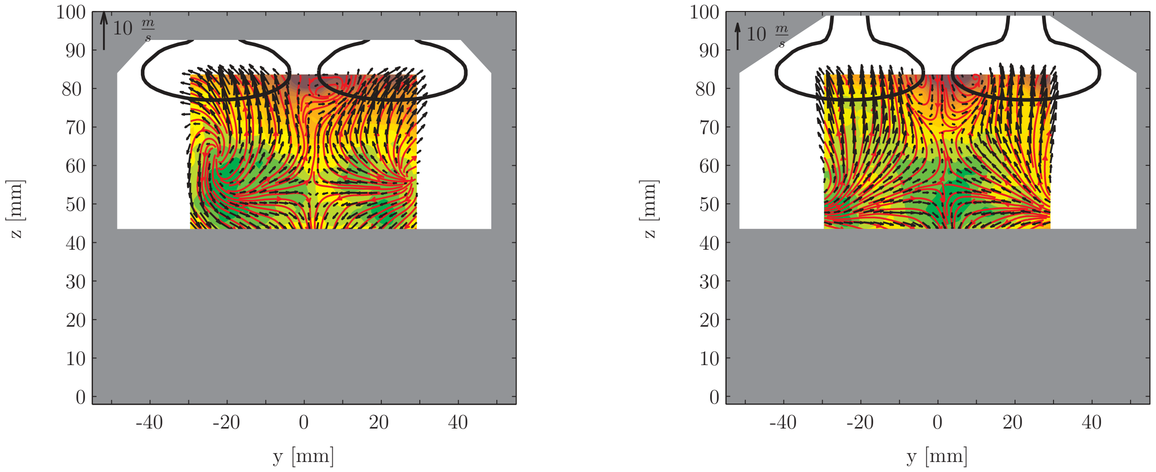

(a) x=-20 mm, 80° atdc (b) x=-10 mm, 80° atdc

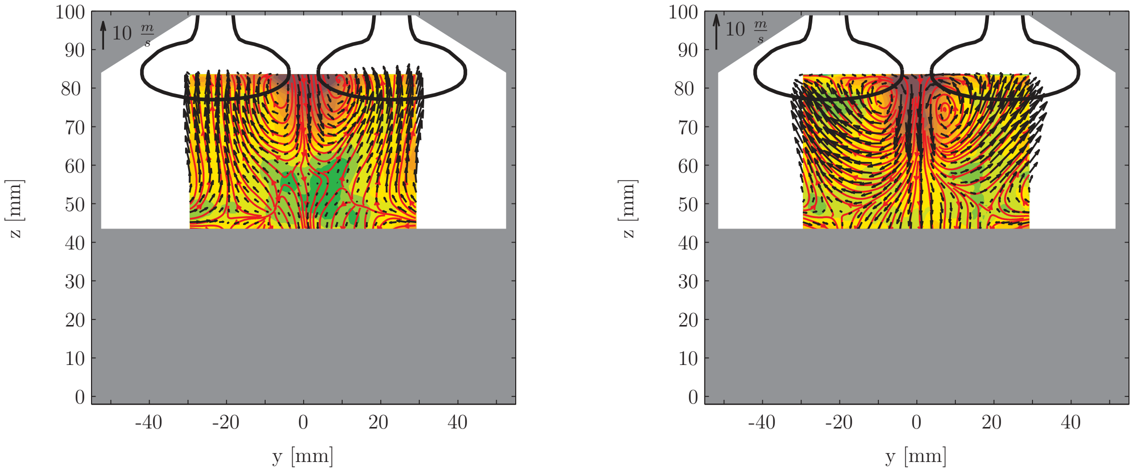

(c) x= 0 mm, 80° atdc (d) x=10 mm, 80° atdc

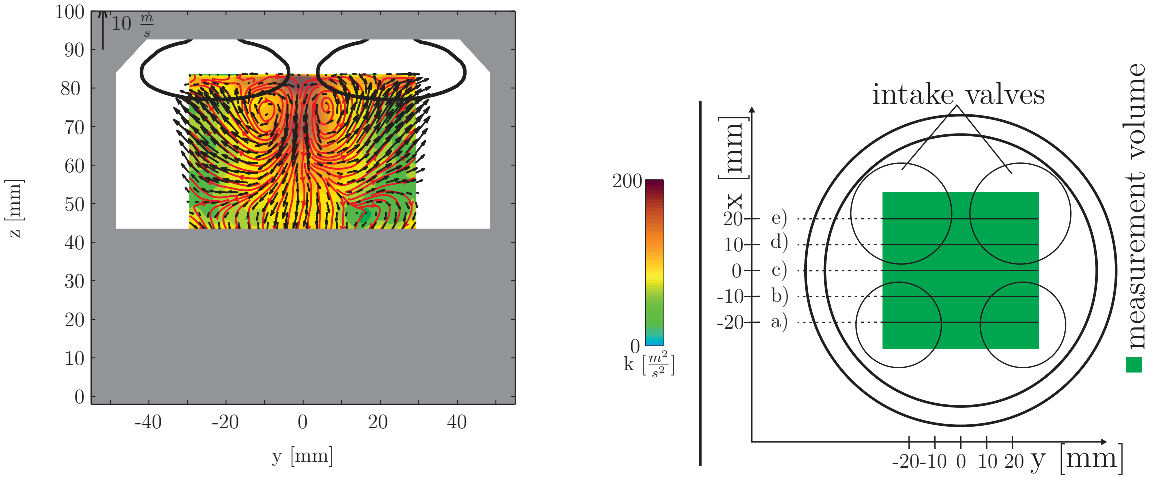

(e) x=20 mm, 80° atdc (f) Position of the displayed planes and legend for fig. 6.19 (a)-(e).

Figure 6.19 – Velocity vectors (every 3rd arrow), streamlines (red lines), and turbulent kinetic energy (color code) at 80° in 5 yz-planes, from x = -20 mm to x = 20 mm (as marked in subfigure f)).

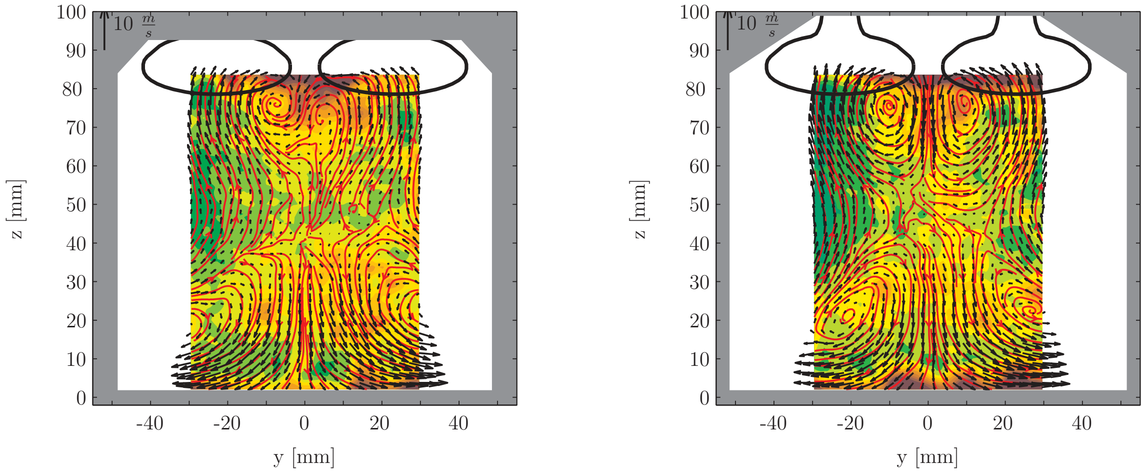

(a) x=-20 mm, 160° atdc

(b) x=-10 mm, 160° atdc

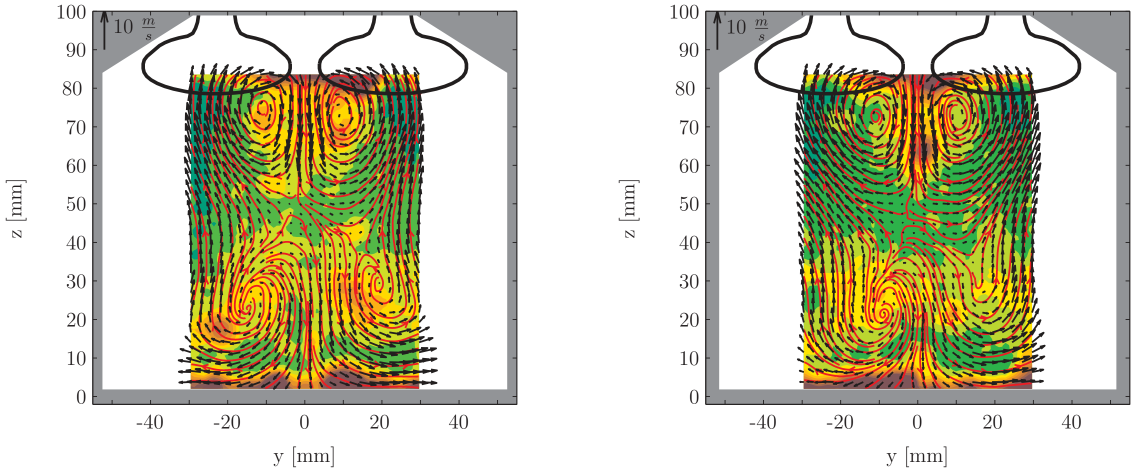

(c) x= 0 mm, 160° atdc

(d) x=10 mm, 160° atdc

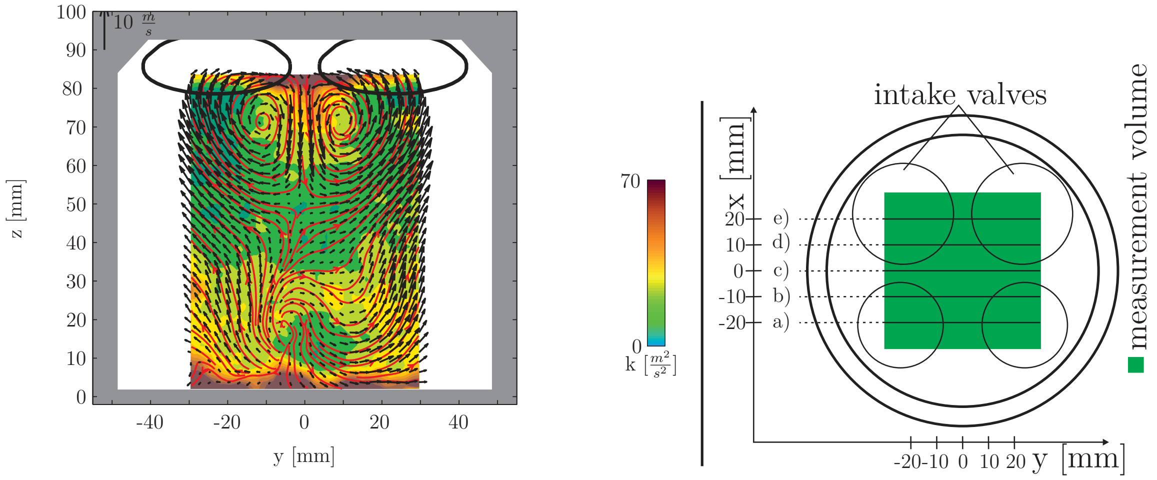

(e) x=20 mm, 160° atdc

(f) Position of the displayed planes and legend for fig. 6.20 (a)-(e).

Figure 6.20 – Velocity vectors (every 3rd arrow), streamlines (red lines), and turbulent kinetic energy (color code) at 160° in 5 yz-planes, from x = -20 mm to x = 20 mm (as marked in subfigure f).

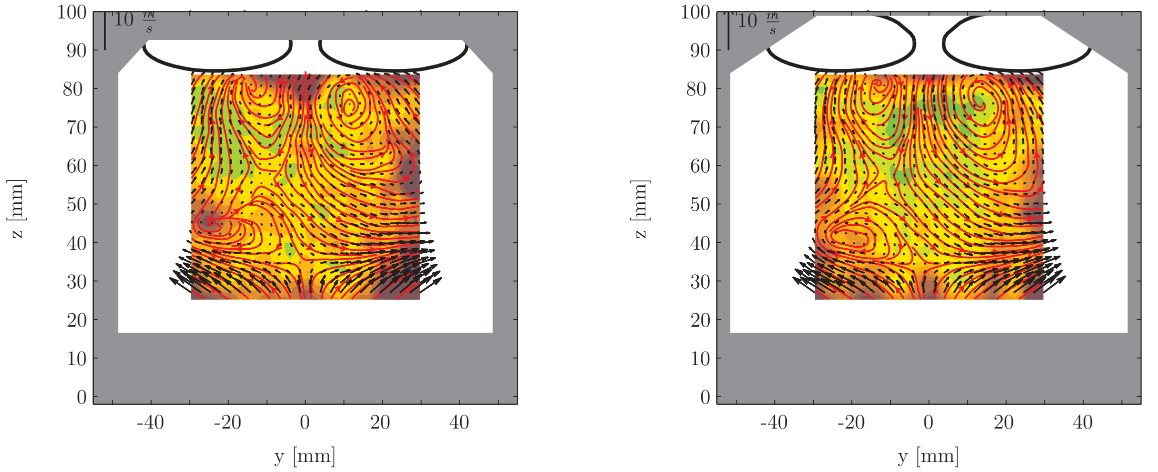

(a) x=-20 mm, 240° atdc

(b) x=-10 mm, 240° atdc

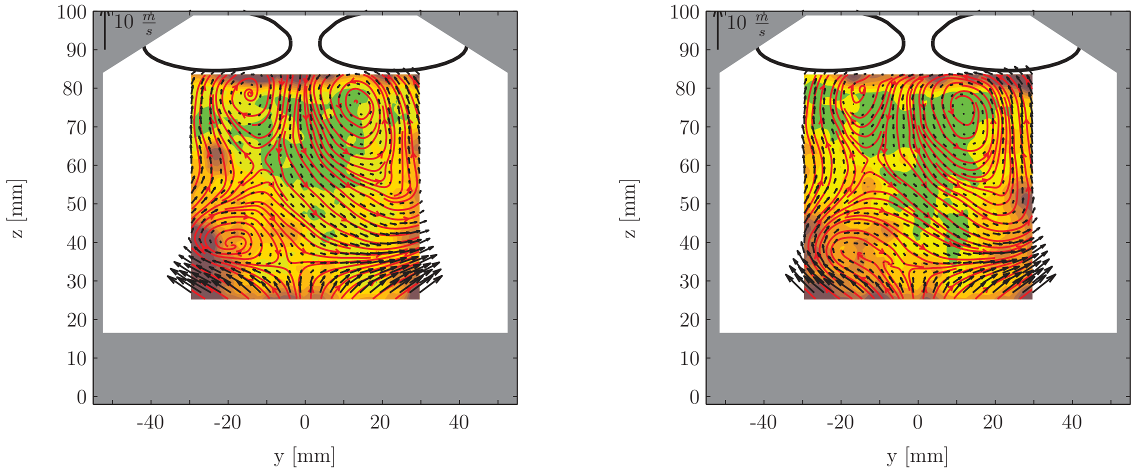

(c) x= 0 mm, 240° atdc

(d) x=10 mm, 240° atdc

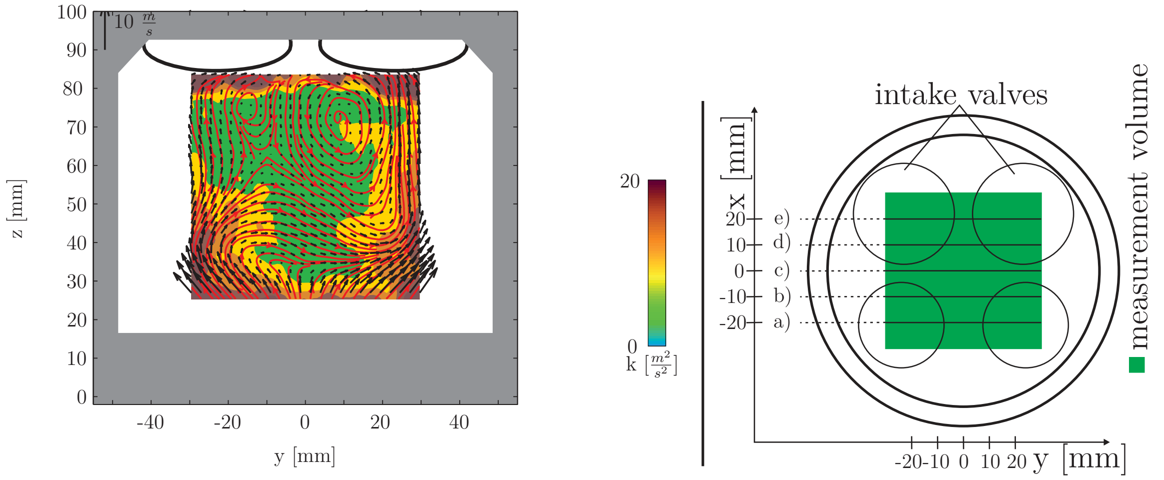

(e) x=20 mm, 240° atdc

(f) Position of the displayed planes and legend for fig. 6.21 (a)-(e).

Figure 6.21 – Velocity vectors (every 3rd arrow), streamlines (red lines), and turbulent kinetic energy (color code) at 240° (right) in 5 yz-planes, from x = -20 mm to x = 20 mm (as marked in subfigure f).

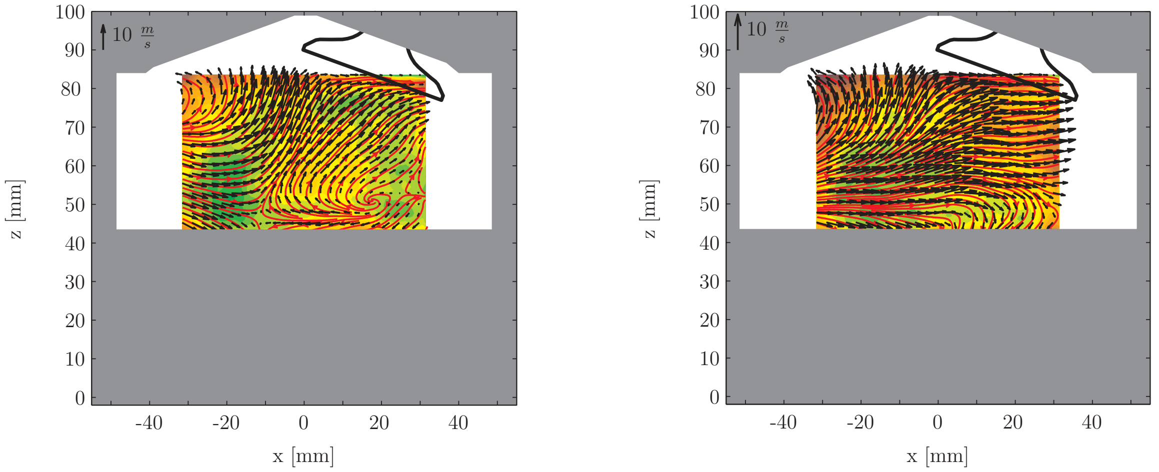

(a) y=-20 mm, 80° atdc

(b) y=-10 mm, 80° atdc

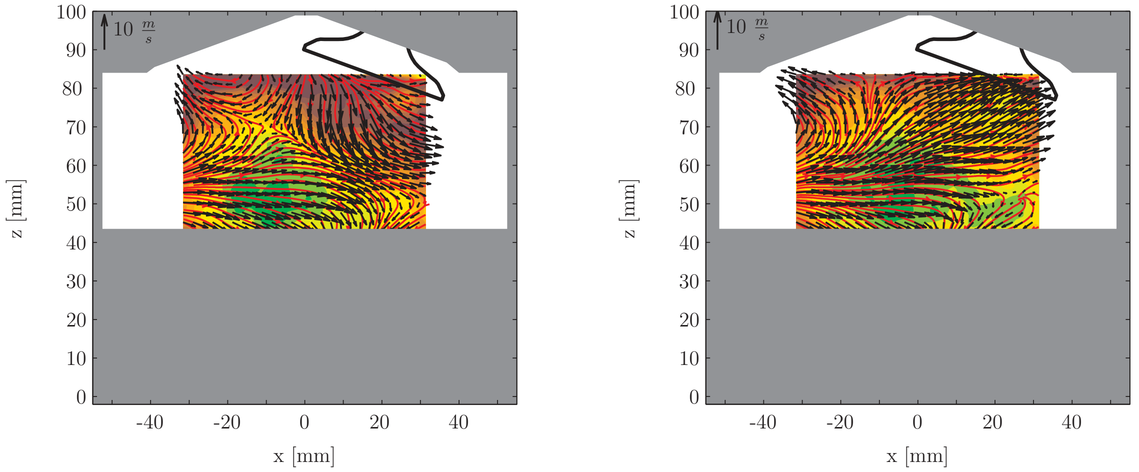

(c) y= 0 mm, 80° atdc

(d) y=10 mm, 80° atdc

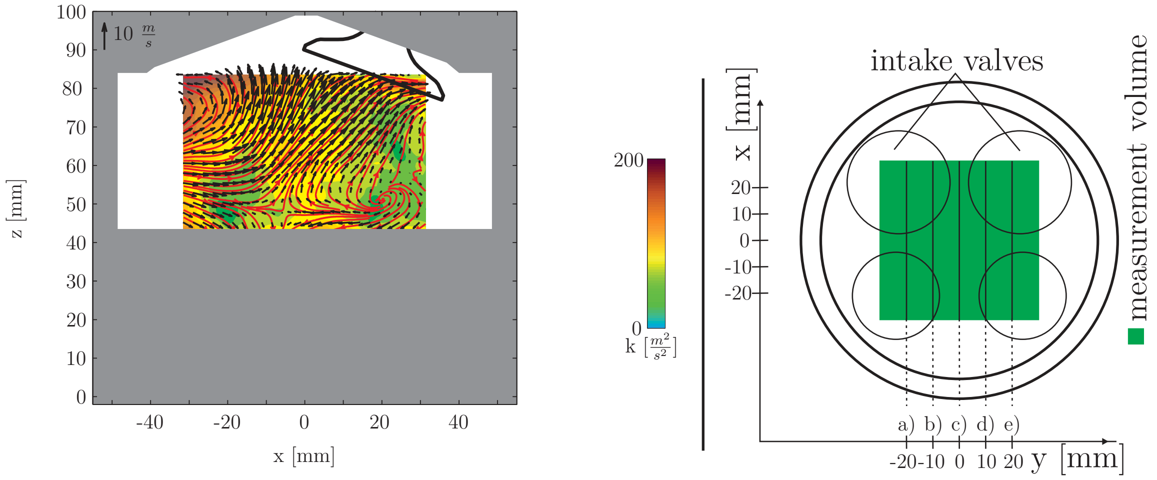

(e) y=20 mm 80° atdc

(f) Position of the displayed planes and legend for fig. 6.22 (a)-(e).

Figure 6.22 – Velocity vectors (every 3rd arrow), streamlines (red lines), and turbulent kinetic energy (color code) at 80° in 5 xz-planes, from y = -20 mm to = 20 mm (as marked in subfigure f).

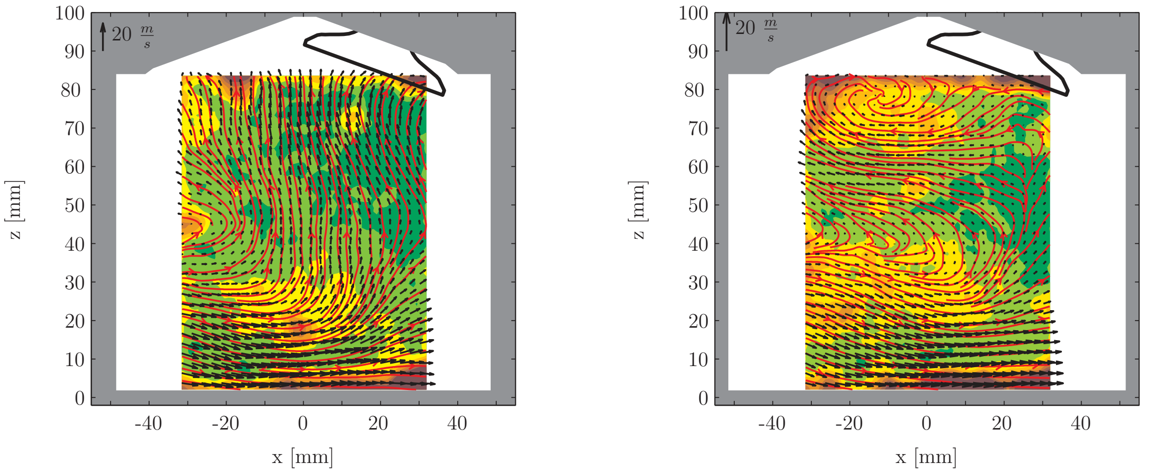

(a) y=-20 mm, 160° atdc

(b) y=-10 mm, 160° atdc

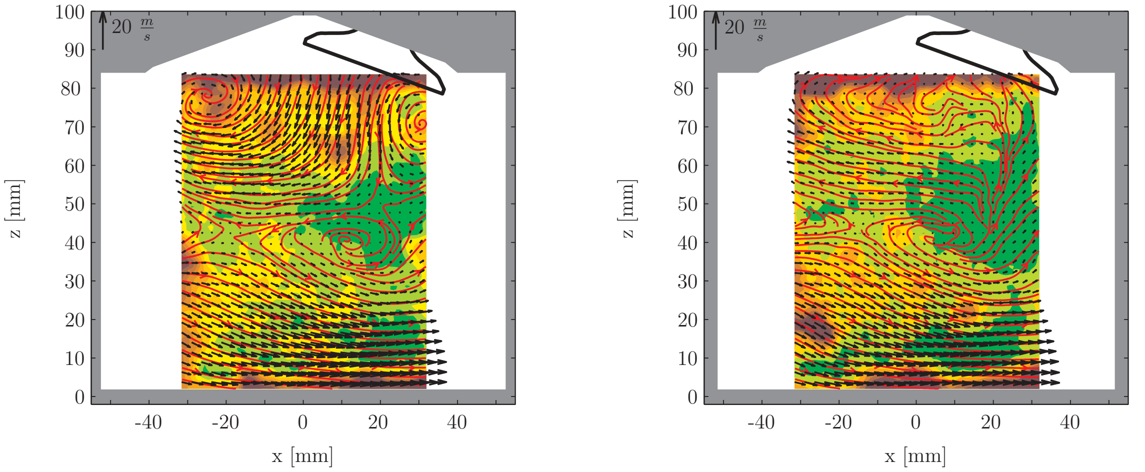

(c) y= 0 mm, 160° atdc

(d) y=10 mm, 160° atdc

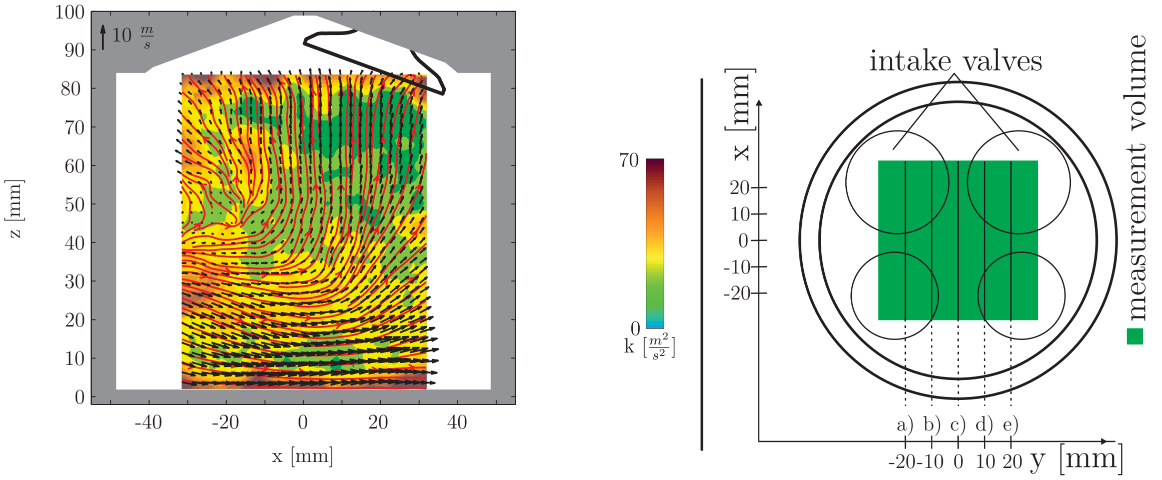

(e) y=20 mm, 160° atdc

(f) Position of the displayed planes and legend for fig. 6.23 (a)-(e).

Figure 6.23 – Velocity vectors (every 3rd arrow), streamlines (red lines), and turbulent kinetic energy (color code) at 160° (center) in 5 xz-planes, from y = -20 mm to = 20 mm (as marked in subfigure f).

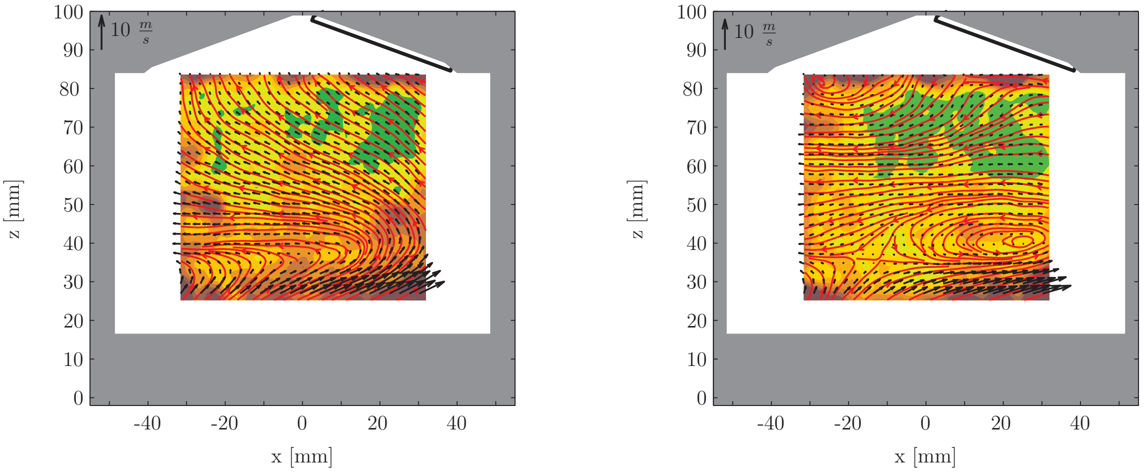

(a) y=-20 mm, 240° atdc

(b) y=-10 mm, 240° atdc

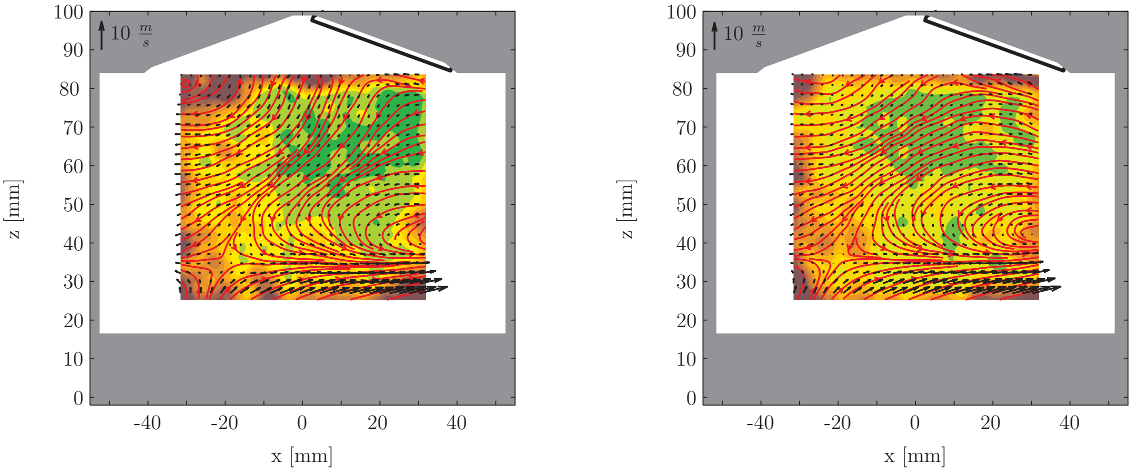

(c) y= 0 mm, 240° atdc

(d) y=10 mm, 240° atdc

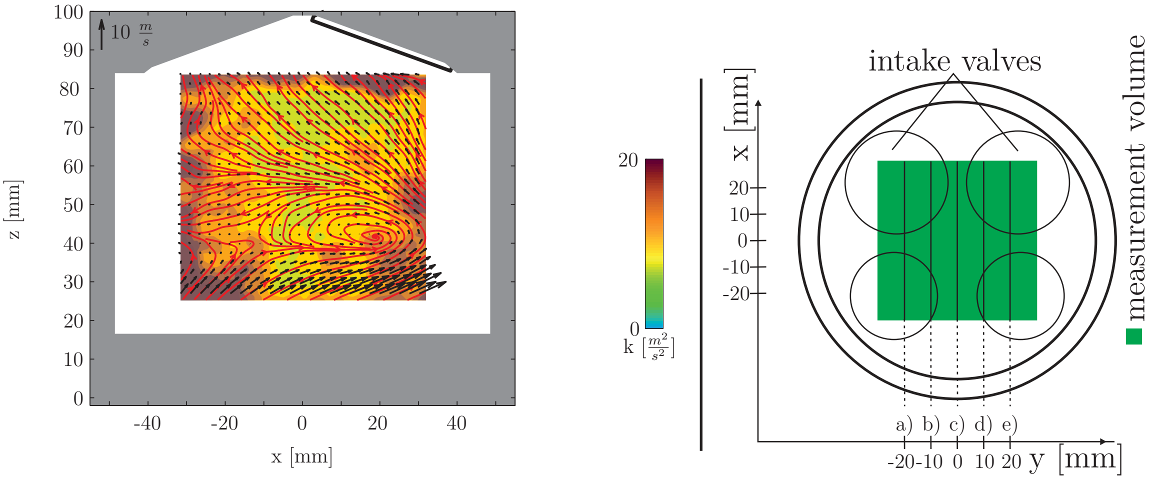

(e) y=20 mm, 240° atdc

(f) Position of the displayed planes and legend for fig. 6.24 (a)-(e).

Figure 6.24 – Velocity vectors (every 3rd arrow), streamlines (red lines), and turbulent kinetic energy (color code) at 240° (right) in 5 xz-planes, from y = -20 mm to = 20 mm (as marked in subfigure f).

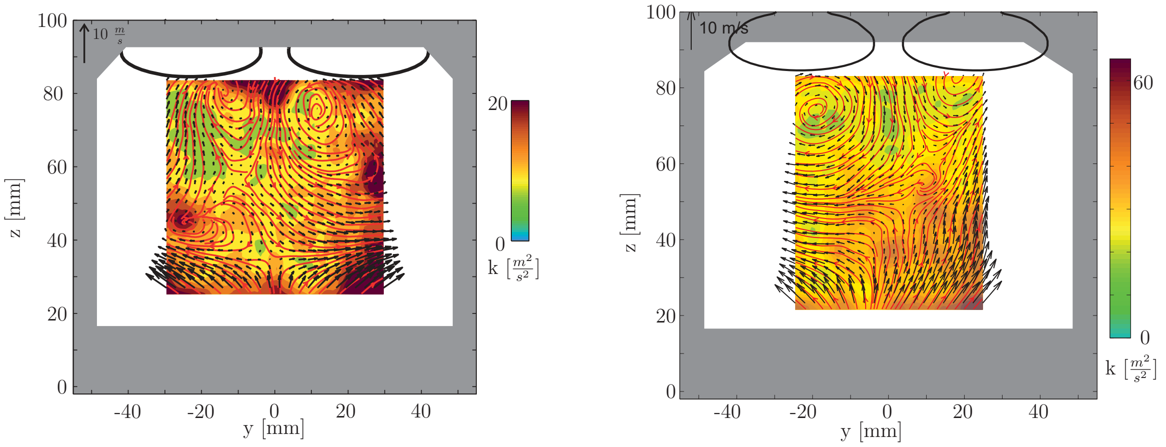

(a) x=-20 mm, standard valve timing (b) x=-20 mm, EGR valve timing

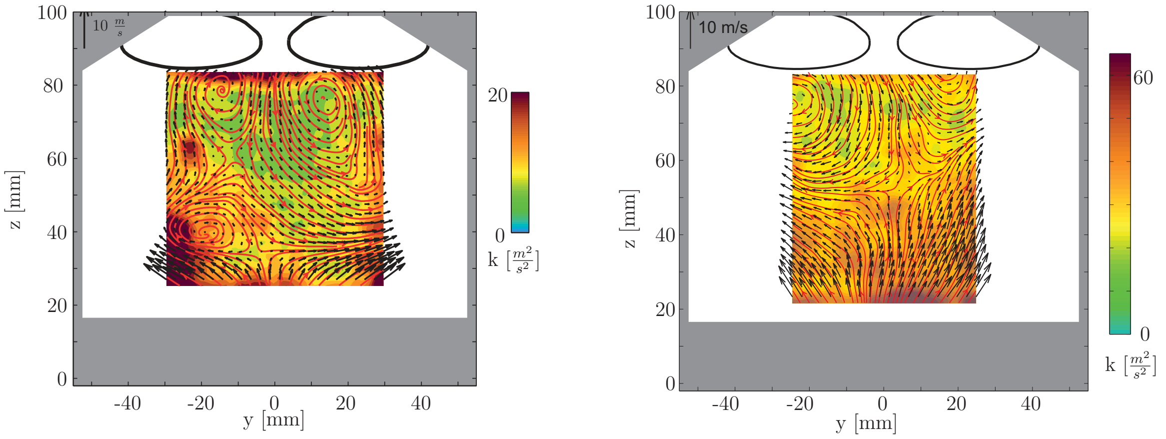

(c) x=0 mm, standard valve timing (d) x=0 mm, EGR valve timing

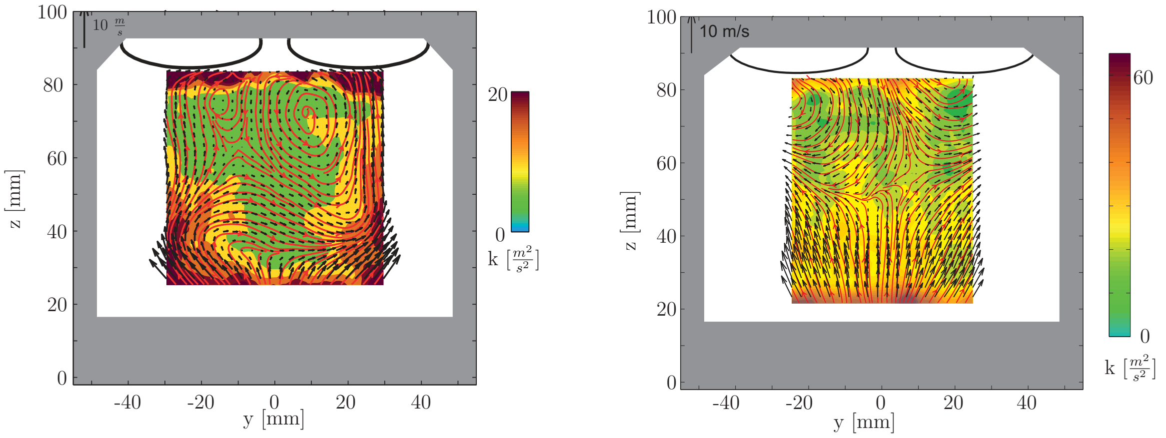

(e) x=20 mm, standard valve timing (f) x=20 mm, EGR valve timing

Figure 6.25 – Velocity vectors (every 3rd arrow), streamlines (red lines), and turbulent kinetic energy (color code) at 240° in 5 yz-planes, from x = -20 mm to x = 20 mm (from top to bottom) for standard valve timing and EGR.

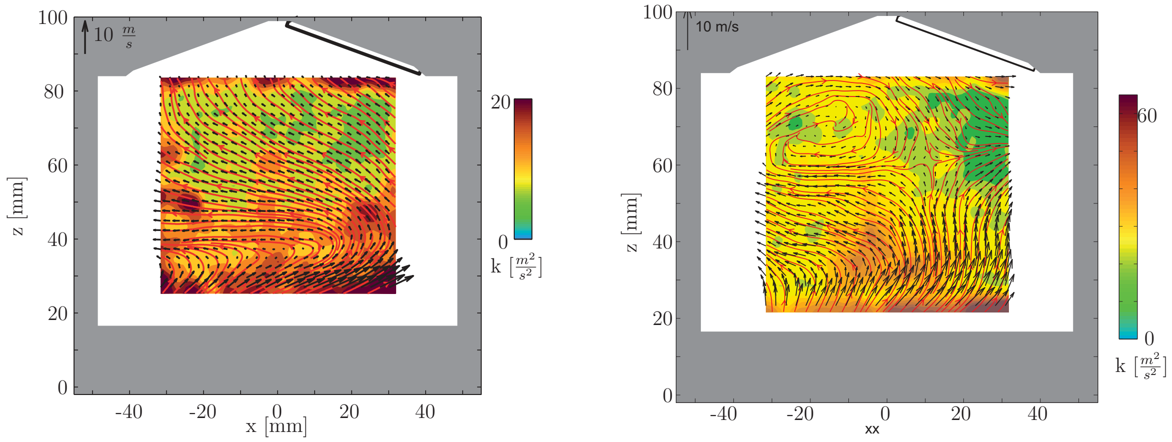

(a) y=-20 mm, standard valve timing (b) y=-20 mm, EGR valve timing

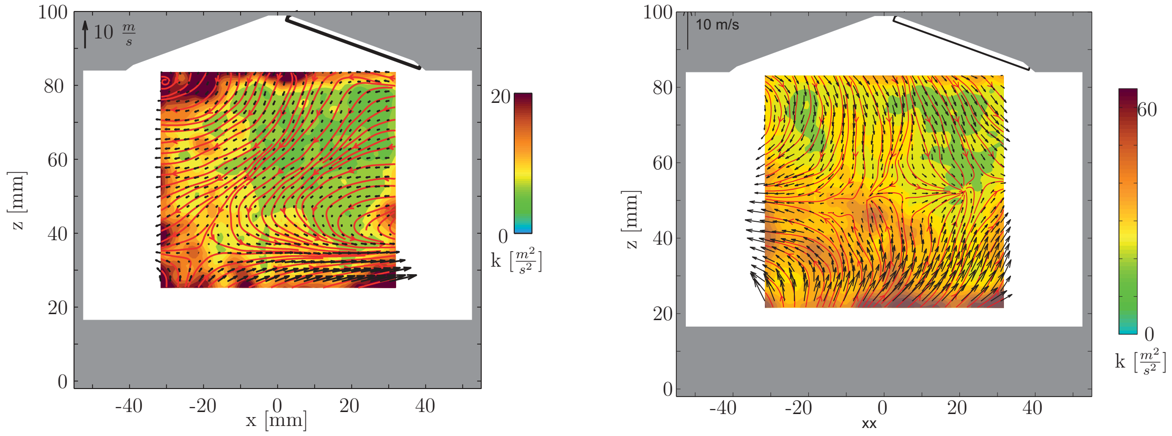

(c) y=0 mm, standard valve timing (d) y=0 mm, EGR valve timing

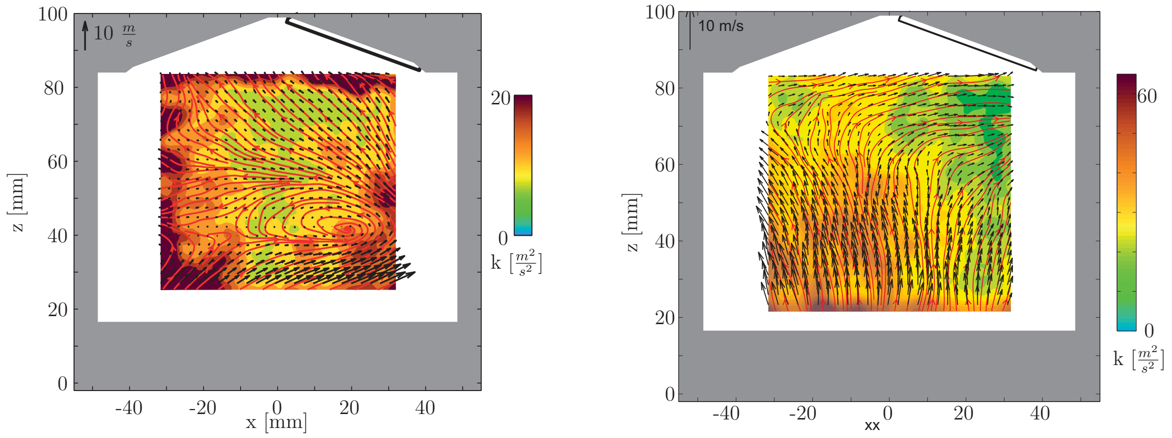

(e) y=20 mm, standard valve timing (f) y=20 mm, EGR valve timing

Figure 6.26 – Velocity vectors (every 3rd arrow), streamlines (red lines), and turbulent kinetic energy (color code) at 240° in 5 xz-planes, from x = -20 mm to x = 20 mm (from top to bottom) for standard valve timing and EGR.

and that has been explained in sec. 6.2.3 in detail.
Summarizing, one can say that internal EGR leads to a lower tumble ratio through lower valve lifts and lower mass flux inside the engine. This promotes the break up of the tumble at earlier crank angles. Through this, turbulent kinetic energy levels rise above the values, known from standard valve timing, which increases the mixing of fuel and air at late compression.

6.2.7 Mie Scattering Analysis of Fuel Injection

In the following, the analysis of the injection behavior for ethanol and methyl ethyl ketone (MEK) is presented. For ethanol, four different injection pressures (50 bar, 100 bar, 150 bar, and 200 bar) at three different crank angles (60° atdc, 277°, and 297°) with three different injection durations (500 μs, 1000 μs, and 2000 μs) at 2,000 rpm have been investigated. Furthermore, the injection measurements at 60° atdc with an injection duration of 500 μs have been repeated for 1,500 rpm. The longer injection durations have been performed to provide data for comparison with experiments conducted in a pressure chamber without flow. For MEK, the same injection pressures at the same crank angles have been investigated. However, as long injection durations higher than 500 μs are not of high interest for real engines, the MEK measurements have been restricted to an injection duration of 500 μs. Both fuels are investigated concerning their vertical penetration.

Results of the injection of Ethanol

The penetration of ethanol as a function of the crank angle is shown in figs. 6.27 - 6.29. For early injection at 60° atdc, it is evident that the vertical penetration increases with larger injection pressure, which is caused by the higher exit velocities at the nozzle tip. Furthermore, the influence of increasing engine speed can clearly be seen by comparing figs. 6.27(a) - 6.27(b) and figs. 6.27(c) - 6.27(d). On the intake side, the spray reaches the piston at earlier crank angles. At 1,500 rpm, the engine speed as well as the general flow velocity is lower. Therefore, the influence of the tumble movement on the spray is reduced. For the exhaust side, two distinct changes in the slope can be clearly seen for the injection at 1,500 rpm. The first change at about 65° atdc is caused by the interaction of the spray with the liner wall. The second variation at about 70° atdc could be caused by the interaction of the spray and the tumble. Karhoff [49] showed for the same engine and engine speed that the tumble forms between 60° and 80° atdc. The tumble movement accelerates the atomized spray. This can not be seen for the measurements at 2,000 rpm. The higher engine speed causes the tumble to form at earlier crank angles. This, and a higher piston and flow velocity results in a smoother propagation of the spray as it is injected into an already formed tumble.
Comparing the injection behavior at 2,000 rpm (figure 6.27(c) - 6.27(h)) for different injection durations no pronounced differences can be observed. Obviously, the longer injection duration causes the combustion chamber to be filled with more fuel. However, the maximum vertical penetration is restricted by the piston movement. Therefore, it

is comparable for all injection durations. A distinct change of the slope is evident for all measurement at about 67° atdc, which is caused by the impingement of the spray on the liner wall.
Figure 6.28 shows the vertical penetration for a SOI at 277° atdc. It is obvious that large differences occur for the spray on the intake and exhaust side. On the exhaust side, the spray behavior is comparable to the injection at 60° atdc. For injection pressures of 100 - 200 bar the spray exits the nozzle with high velocities, until a change of the slope at about 284° atdc indicates the interaction of spray and liner wall. Then, the decelerated spray is directed to the piston. The spray wets the piston at about 300° atdc. At injection pressures of about 50 bar, the interaction of the liner and the spray can be observed for later crank angles of about 287° atdc. Subsequently, the spray is redirected until it wets the piston at about 303° atdc. With increasing injection duration, no real change in penetration behavior is evident. The general slope of all curves is nearly the same.
On the intake side, the spray is not comparable to the injection at 60° atdc. After a fast first spray propagation until about 285° atdc, the spray is redirected to the pent roof. This is due to the tumble movement. The momentum of the in-cylinder flow field causes the fuel to be redirected. Therefore, neither liner nor piston wetting occur on the intake side as the spray droplets are trapped inside the tumble vortex. Only for an injection pressure of 200 bar, the spray interacts with the piston at late crank angles. To highlight this, figure 6.30 shows the raw Mie scattering images for one exemplary cycle for an injection pressure of p= 200 bar and an injection duration of 500 μs. It can be seen that the tumble causes a redirection of the fuel spray on the intake side and the formation of a vortical structure below the intake valves. For higher injection durations, the spray is also redirected through the tumble movement. However, the oscillating amplitude of the vertical penetration decreases, compared to the measurements with an injection duration of 500 μs.
Figure 6.29 shows the vertical penetration for an SOI at 297° atdc. Again, the exhaust side shows a progressing behavior of the spray penetration. However, the change in the slope is not as distinct as for an SOI at 60° atdc and 277° atdc. The increased pressure inside the combustion chamber as well as the restricted area combined with the tumble movement cause the spray to not interact with the liner wall. Instead, it wets the piston about 15° after SOI for all cases. Again, an increase in the injection duration does not change the penetration. The slopes on the exhaust side are comparable for all injection durations.
On the intake side, again the interaction of spray and tumble is evident. The redirection of the spray to the pent roof through the tumble vortex can clearly be seen. However, due to the restricted area at later crank angles, the amplitude of the oscillating penetration is not as distinct as at 277° atdc. Nevertheless, the interaction of spray and tumble movement causes the spray to wet the piston at late crank angles of about 325° for an injection duration of 500 μs. With increasing injection duration, the piston wetting occurs at earlier crank angles. This is due to the increased fuel mass inside the combustion chamber and therefore the higher influence on the momentum of the tumble vortex. This trend can also be observed for an injection duration of 2000 μs.

Results of the injection of methyl-ethyl ketone (MEK)

Figure 6.31 shows the penetration for MEK at 60° atdc, 277° atdc, and 297° atdc for the intake and exhaust side at an engine speed of 2,000 rpm. At a SOI of 60° atdc, the vertical penetration increases with increasing injection pressure. This is caused by the higher exit velocities at the nozzle tip as already explained for the ethanol case. On the exhaust side, the spray shows a slower penetration velocity compared to the intake side. Furthermore, the spray seems to accelerate at about 65° atdc. This could be caused by the interaction of tumble and spray and can also be partially observed for the ethanol injection. The injection with 50 bar shows a slow propagation of the vertical penetration with late interaction of spray and piston. A change in the slope to lower penetration velocities can be observed at about 69° atdc. This suggests an interaction of liner and spray. On the intake side, the spray impinges upon the piston at about 67° atdc. Note that for ethanol piston wetting was reported at about 75° atdc. No direct change in the slope can be observed, which is a sign for missing liner wetting, whereas liner wetting occurred for all ethanol injection cases.

The injection with a SOI at 277° atdc is comparable to the ethanol injection. On the intake side, the vertical penetration is determined by the interaction of spray and tumble. The tumble vortex forces the spray upwards at about 285° atdc depending on the injection pressure. An interaction of spray and piston can only be observed for an injection pressure of 200 bar. For all other cases, no direct piston wetting is visible. However, the interaction of spray and flow field is not as strong as for the ethanol case since the change in penetration is not as high as for ethanol. This could be caused by bigger fuel droplets of MEK and therefore a higher inertia of the fuel spray indicated by the lower Ohnesorge number of the MEK spray. On the exhaust side, the change in the slope at about 285° atdc indicates an interaction of liner and spray. This was already reported for the ethanol injection. The spray impinges upon the piston at about 300° atdc, which is again comparable to the ethanol injection. However, the penetration for an injection pressure of 50 bar is closer to the penetration of the other injection pressures compared to the ethanol injection. Again, this could be a result from a higher inertia of the spray and therefore a lower impact of the flow field on the MEK spray.

For late injection at 297° atdc, again the injection behavior is comparable to ethanol. On the intake side, the interaction of tumble and spray is clearly visible such that the tumble prevents the spray to impinge upon the piston. Especially for an injection pressure of 50 bar, the vertical penetration is almost suppressed. For all injection pressures a piston wetting at about 323° atdc can be reported. However, the strong interaction of spray and tumble prevents the spray to impinge upon the liner.

Comparing the general behavior of ethanol and MEK, it is evident that MEK impinges on the piston earlier for all starting times of injection. This is mainly caused by the higher nozzle Reynolds number and higher exit velocities, which are caused by the lower viscosity. This results in lower friction losses inside the injector. Furthermore, the change in the direction of the spray for the injection at 277°atdc and 297° atdc at the intake side are not as distinct as for ethanol. This suggests larger larger MEK

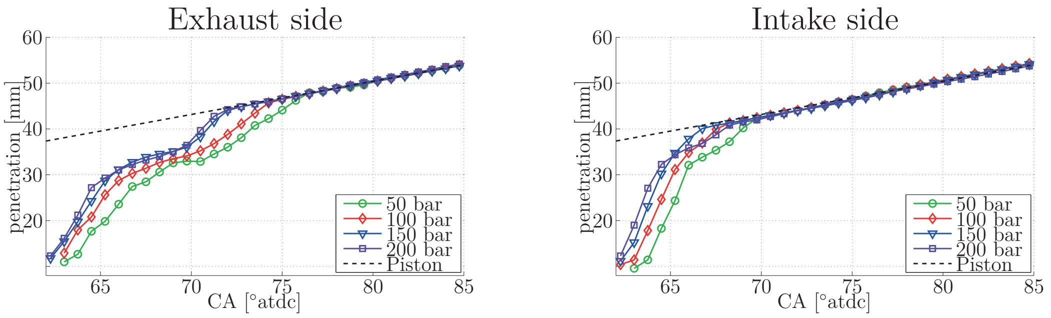

(a) DOI: 500 μs, 1500 rpm (b) DOI: 500 μs, 1500 rpm

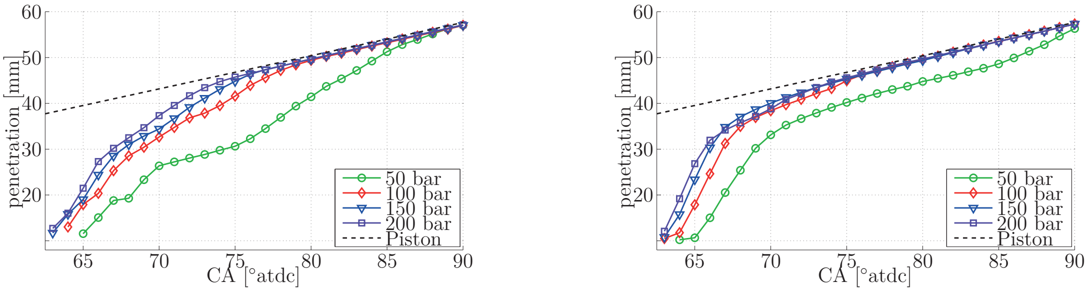

(c) DOI: 500 μs, 2000 rpm (d) DOI: 500 μs, 2000 rpm

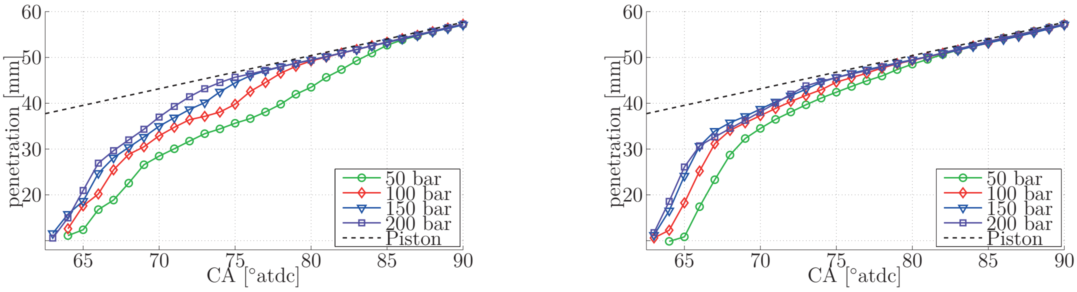

(e) DOI: 1000 μs, 2000 rpm (f) DOI: 1000 μs, 2000 rpm

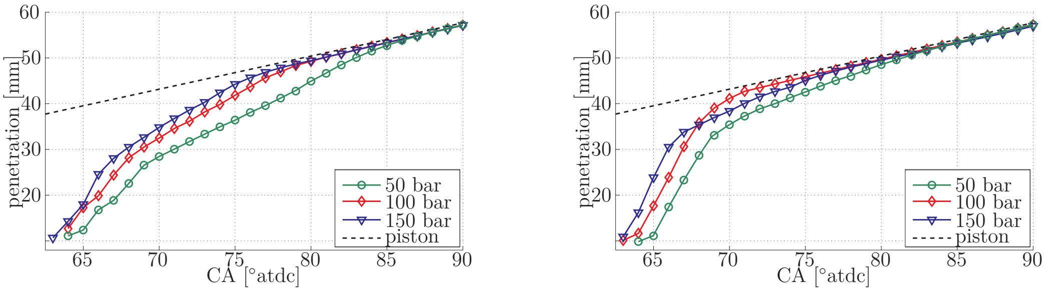

(g) DOI: 2000 μs, 2000 rpm (h) DOI: 2000 μs, 2000 rpm

Figure 6.27 – penetration for exhaust (left) and intake (right) side with a SOI at 60° atdc and an injection duration of 500μs (top), 1000 μs (middle), and 2000 μs (bottom). The dashed line shows the piston position.

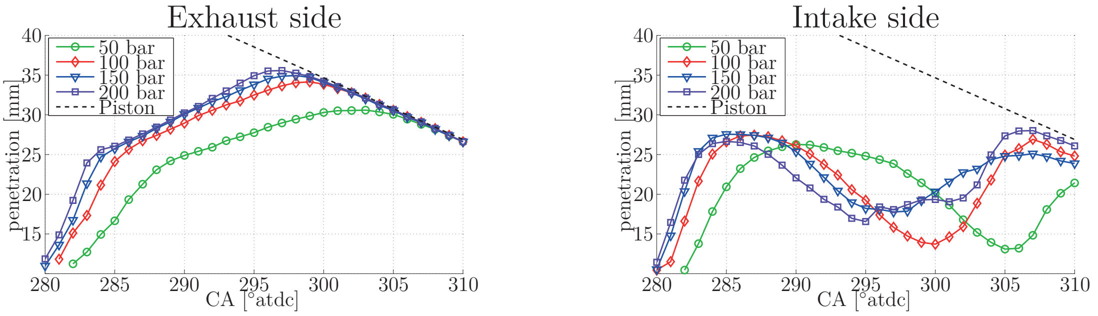

(a) DOI: 500 μs, 2000 rpm (b) DOI: 500 μs, 2000 rpm

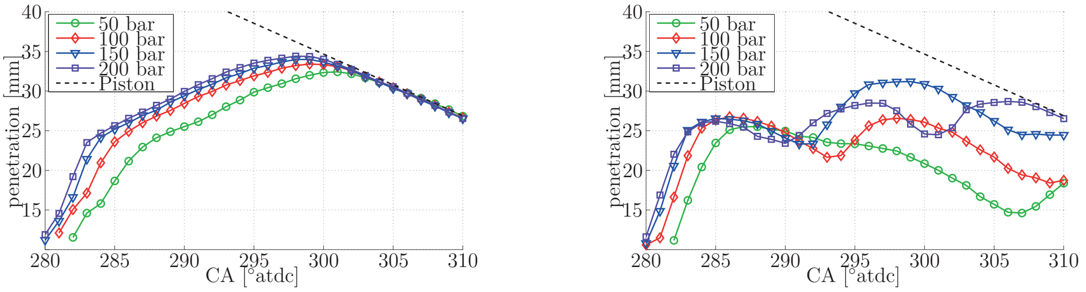

(c) DOI: 1000 μs, 2000 rpm (d) DOI: 1000 μs, 2000 rpm

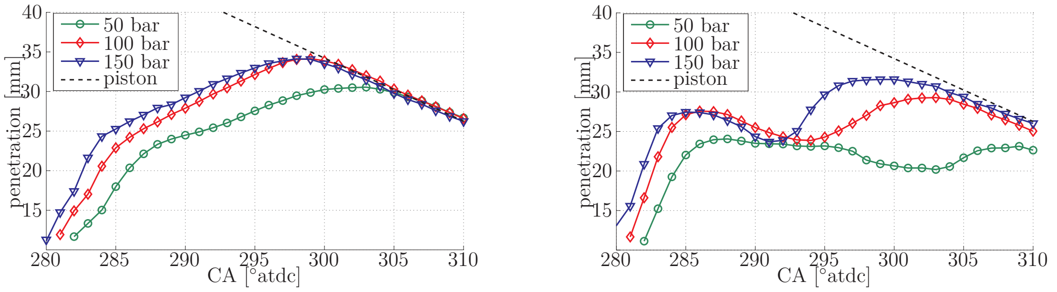

(e) DOI: 2000 μs, 2000 rpm (f) DOI: 2000 μs, 2000 rpm

Figure 6.28 – penetration for exhaust (left) and intake (right) side with a SOI at 277° atdc and an injection duration of 500μs (top), 1000 μs (middle), and 2000 μs (bottom). The dashed line shows the piston position.

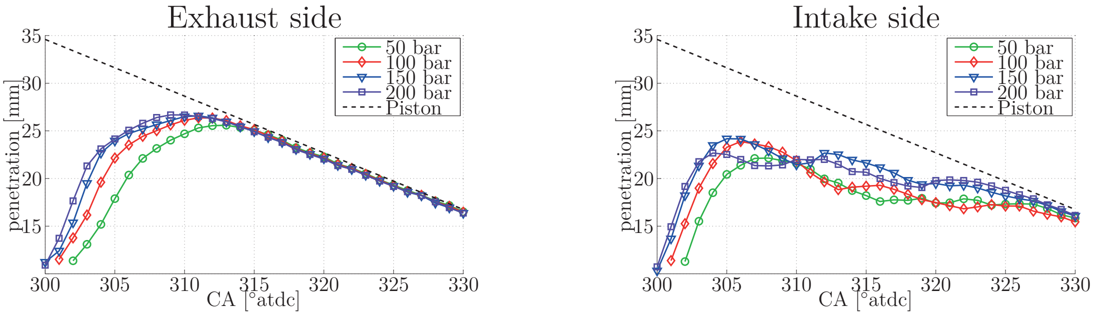

(a) DOI: 500 μs, 2000 rpm (b) DOI: 500 μs, 2000 rpm

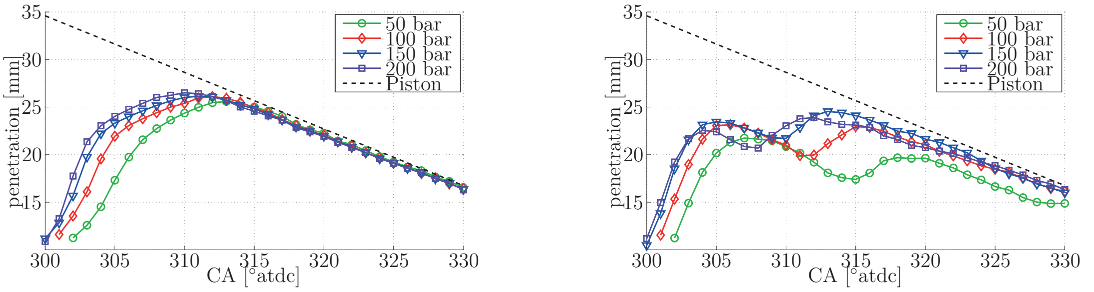

(c) DOI: 1000 μs, 2000 rpm (d) DOI: 1000 μs, 2000 rpm

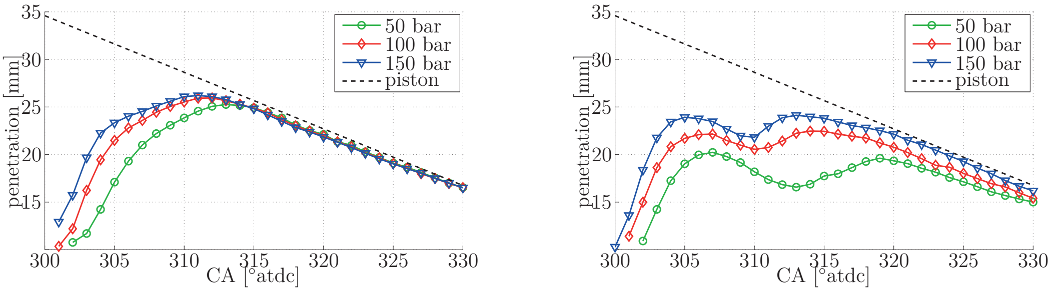

(e) DOI: 2000 μs, 2000 rpm (f) DOI: 2000 μs, 2000 rpm

Figure 6.29 – penetration for exhaust (left) and intake (right) side with a SOI at 297° atdc and an injection duration of 500μs (top), 1000 μs (middle), and 2000 μs (bottom). The dashed line shows the piston position.

droplets, which do not follow the flow as well.

Comparison of the Injection Angle for Ethanol and methyl-ethyl ketone (MEK)

Table 6.4 shows the injection angle to the injector axis for ethanol and MEK for different injection pressures and starting points of injection. For ethanol at a start of injection of 60° atdc and 1,500 rpm it is evident that the injection angle is higher than expected from the geometric design half angle of 47°. Investigations performed by Mathieu [62] in a pressure chamber without flow field showed that the injected half cone angle coincides with the design half cone angle. On the exhaust side, the flow field causes the spray cone angle to expand as the intake jet pushes the spray cone to bigger angles. On the intake side, the interaction of the early tumble vortex and the spray also causes an increase in injection cone angle. With increasing injection pressure, a small decrease of injection angle is visible. The higher nozzle exit velocity stabilizes the spray cone and reduces the influence of the flow field on the injection.

At an engine speed of 2,000 rpm, this effect is partly diminished. This can be explained by a slightly different flow field due to the higher piston velocity, which causes a different tumble movement. For both measurements, the higher injection pressure reduces the half cone angle. The higher nozzle exit velocity stabilizes the spray cone and decreases the influence of the flow field on the injection.

At a starting time of injection of 277° and 297° atdc, the exhaust half cone angle is comparable to the early injection at 60° atdc. The counter-clockwise rotating tumble vortex increases the spray cone angle. It is similar to the intake jet at early injection. However, the spray angle on the intake side differs from the angle at early injection. For a starting point of injection at 277° atdc, it is close to the design half cone angle of 47°. However, for a starting point of injection of 297° atdc, a further reduction of the spray angle on the intake side is evident, which is again caused by the interaction of tumble and spray. The center of the tumble vortex moves in the direction of the intake valves (Bücker et al. [21]) and causes a redirection of the spray to the center of the combustion chamber. However, an increase of the spray cone angles is visible for higher injection pressures since the higher fuel velocities stabilize the spray immediately after start of injection.

For MEK at a start of injection of 60° atdc, the spray cone angle is close to the design cone angle of 47° on both sides. This is caused by the higher spray Reynolds number and flow velocity as well as larger droplets with MEK. Only a small deviation in the injection angle is visible that is in the range of the measurement accuracy.

At 277° atdc the MEK spray is partly influenced by the tumble vortex. On the exhaust side, slightly higher half cone angles occur compared to early injection. The momentum of the tumble pushes the fuel spray in the direction of the liner. Again, the intake side shows injection angles close to the design cone angle with a small increase for higher injection pressures. This means that the the flow field does not affect the spray strongly at these injection Reynolds and Ohnesorge numbers.

For late injection at 297° atdc of the MEK fuel, the influence of the tumble vortex on the half cone angle on the exhaust side is pronounced. The spray is redirected

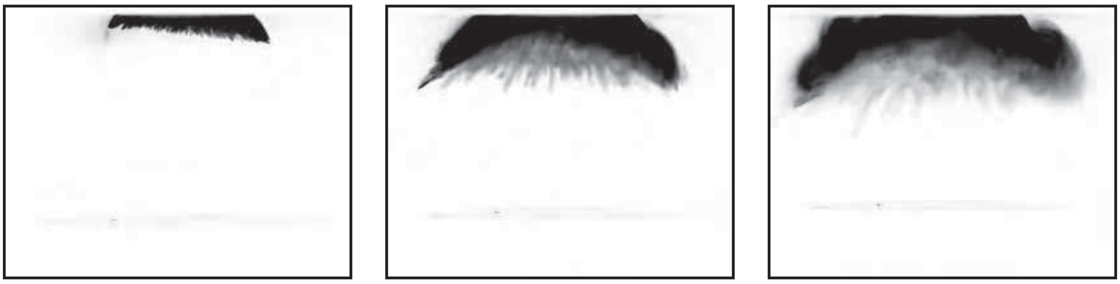

(a) CA=282° atdc (b) CA=284° atdc (c) CA=286° atdc

(d) CA=288° atdc (e) CA=290° atdc (f) CA=292° atdc

(g) CA=294° atdc (h) CA=296° atdc (i) CA=298° atdc

(j) CA=300° atdc (k) CA=302° atdc (l) CA=304° atdc

(m) CA=306° atdc (n) CA=308° atdc (o) CA=310° atdc

Figure 6.30 – Exemplary inverted Mie scattering images of the injection of ethanol at a start of injection (SOI) at 277° atdc and injection duration of 500 μs with an injection pressure of 200 bar.

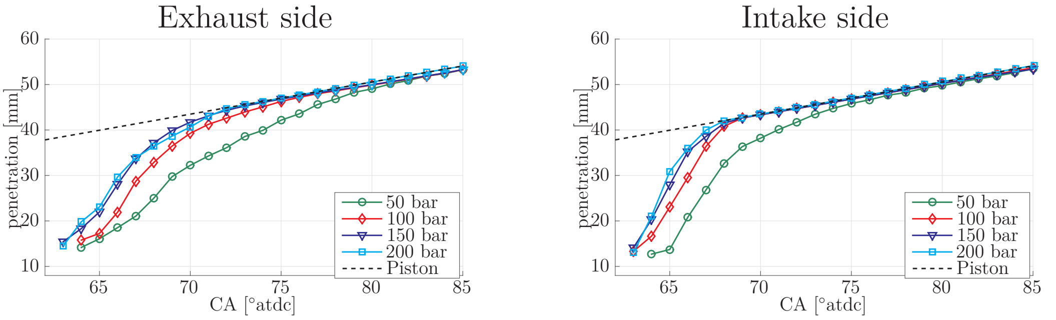

(a) SOI: 60° atdc, 2000 rpm (b) SOI: 60° atdc, 2000 rpm

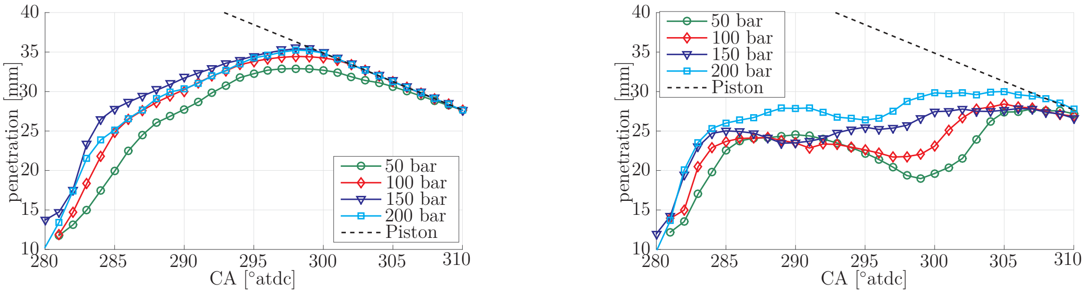

(c) SOI: 277° atdc, 2000 rpm (d) SOI: 277° atdc, 2000 rpm

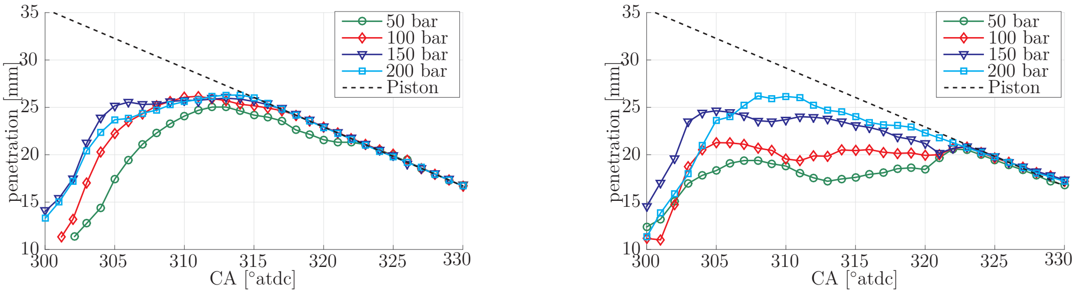

(e) SOI: 297° atdc, 2000 rpm (f) SOI: 297° atdc, 2000 rpm

Figure 6.31 – penetration for exhaust (left) and intake (right) side with a SOI at 60° atdc (top), 277° atdc (middle), and 297° atdc (bottom), and an injection duration of 500μs (top) for MEK. The dashed line shows the piston position.

to the wall of the cylinder such that higher injection angles than expected from the design injection angle are determined. Again, the effect of increasing injection pressure and higher momentum of the spray is visible by a decreased spray cone angle. On the intake side, the spray cone angle is close to the design cone angle. Overall, the MEK spray is not as strongly affected by the flow field than the ethanol spray. The higher nozzle-exit velocities and spray droplets, shown through the higher Reynolds and Ohnesorge numbers cause the MEK spray to be determined by the design angle through higher droplet momentum and reduce the influence of the flow field on the spray at early injection. This is consistent with the findings from the horizontal penetration that also show a decreased interaction between flow field and spray compared to the measurements for ethanol injection.

Table 6.4 – Spray angle to the injector axis on the intake (α_{in}) and exhaust side (α_{ex}) shortly after start of injection (SOI) for ethanol and MEK and several injection pressures

	50 bar		100 bar		150 bar		200 bar	
Ethanol	α_{ex}	α_{in}	α_{ex}	α_{in}	α_{ex}	α_{in}	α_{ex}	α_{in}
SOI = 60° atdc, 1500 rpm	54°	53°	53°	53°	52°	52°	50°	52°
SOI = 60° atdc, 2000 rpm	52°	52°	52°	52°	52°	51°	50°	51°
SOI = 277° atdc, 2000 rpm	53°	48°	53°	48°	52°	47°	52°	46°
SOI = 297° atdc, 2000 rpm	53°	43°	53°	44°	52°	44°	51°	44°
MEK								
SOI = 60° atdc, 2000 rpm	47°	47°	47°	47°	47°	48°	47°	48°
SOI = 277° atdc, 2000 rpm	48°	47°	48°	47°	47°	48°	47°	48°
SOI = 297° atdc, 2000 rpm	52°	47°	51°	48°	50°	48°	50°	49°

6.2.8 Stereo-PIV Results

In the following, the stereoscopic PIV measurements of the interaction of the ethanol injection and the in-cylinder flow field will be analyzed. First, the temporal evolution of the ensemble-averaged flow field and the turbulent kinetic energy at 1,500 rpm are compared to measurements without fuel injection performed by Karhoff [49] from 100° atdc to 300° atdc in 40° steps. Then, the ensemble-averaged tumble movement at the four injection pressures will be compared to measurements performed by Karhoff [49] using the Γ_1 vortex identification criterion and the ensemble and spatial-averaged normalized vorticity Ω. Finally, an analysis concerning the ensemble-averaged turbulent kinetic energy, k, is given. Furthermore, a comparison of the tumble movement, the ensemble and spatial averaged normalized vorticity, and the turbulent kinetic energy for 1,500 and 2,000 rpm will be performed.

Comparison of the in-cylinder flow field without and with injection

Figures 6.32 - 6.37 show the ensemble-averaged temporal evolution of the in-cylinder flow field without and with injection. The top images, i.e., figs. 6.32(a) - 6.37(a), always

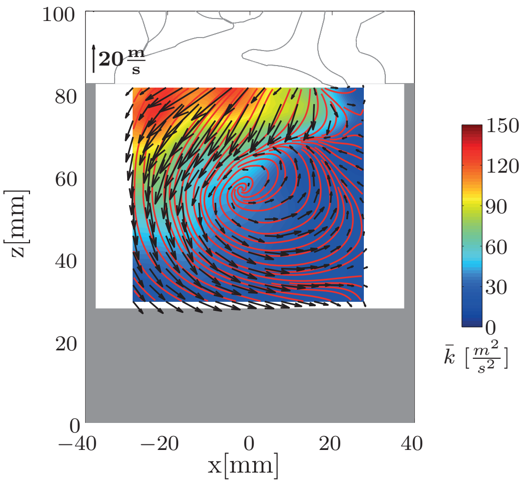

(a) Reference measurements without fuel injection [49]

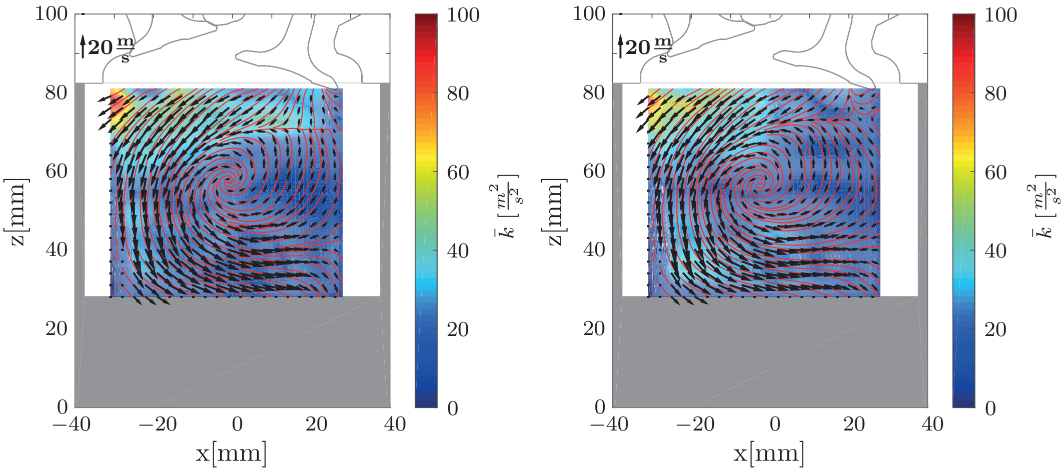

(b) $p_{inj} = 50\ bar$

(c) $p_{inj} = 100\ bar$

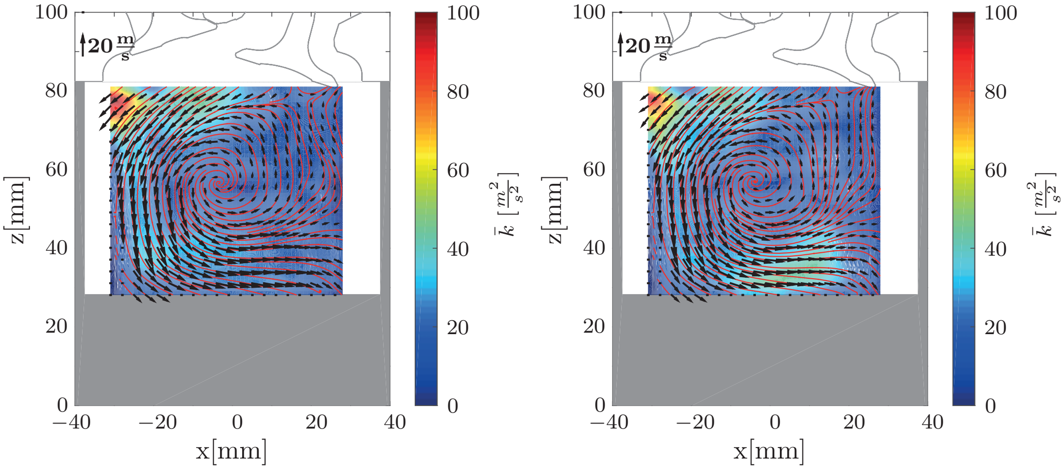

(d) $p_{inj} = 150\ bar$

(e) $p_{inj} = 200\ bar$

Figure 6.32 – Ensemble-averaged velocity vectors (arrows), streamlines (red lines), and turbulent kinetic energy (color map) of the symmetry plane at 100° atdc for N = 1,500 rpm, SOI=60° atdc, t_{inj} = 500 μs

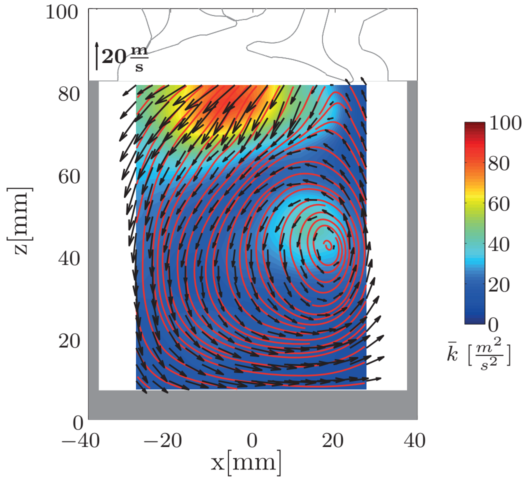

(a) Reference measurements without fuel injection [49]

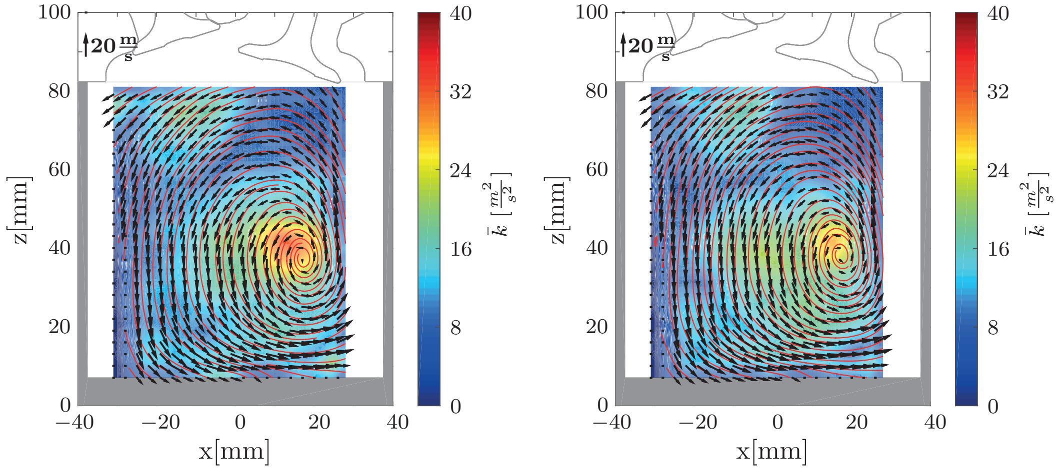

(b) $p_{inj} = 50\ bar$ (c) $p_{inj} = 100\ bar$

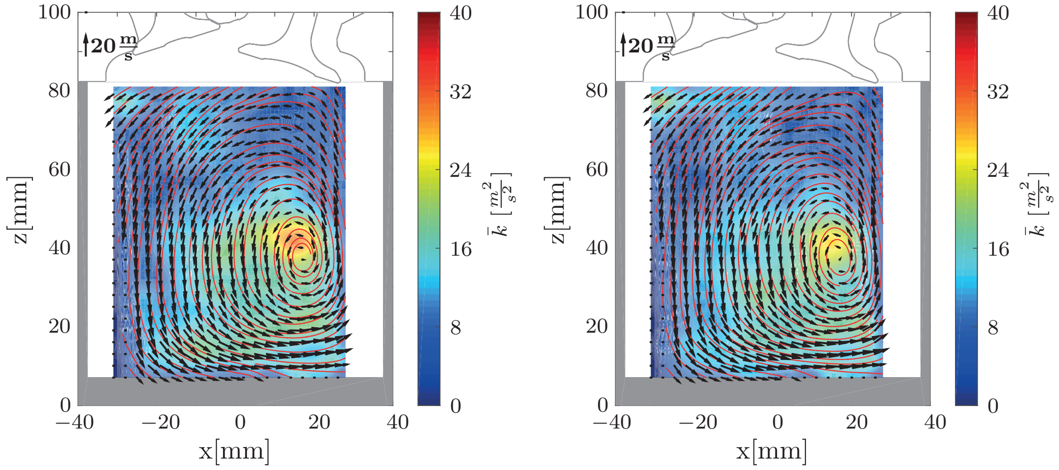

(d) $p_{inj} = 150\ bar$ (e) $p_{inj} = 200\ bar$

Figure 6.33 – Ensemble-averaged velocity vectors (arrows), streamlines (red lines), and turbulent kinetic energy (color map) of the symmetry plane at 140° atdc for N = 1,500 rpm, SOI=60° atdc, $t_{inj} = 500\ \mu s$

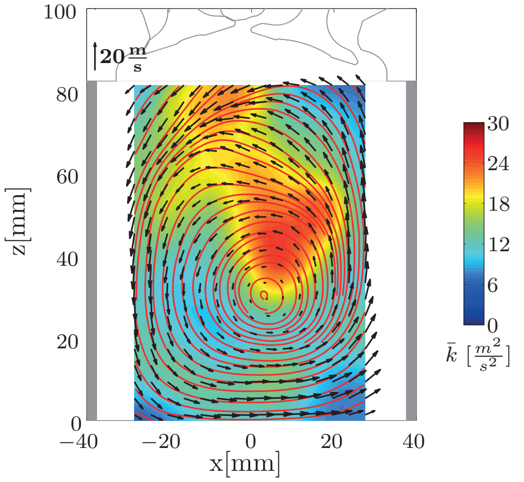

(a) Reference measurements without fuel injection [49]

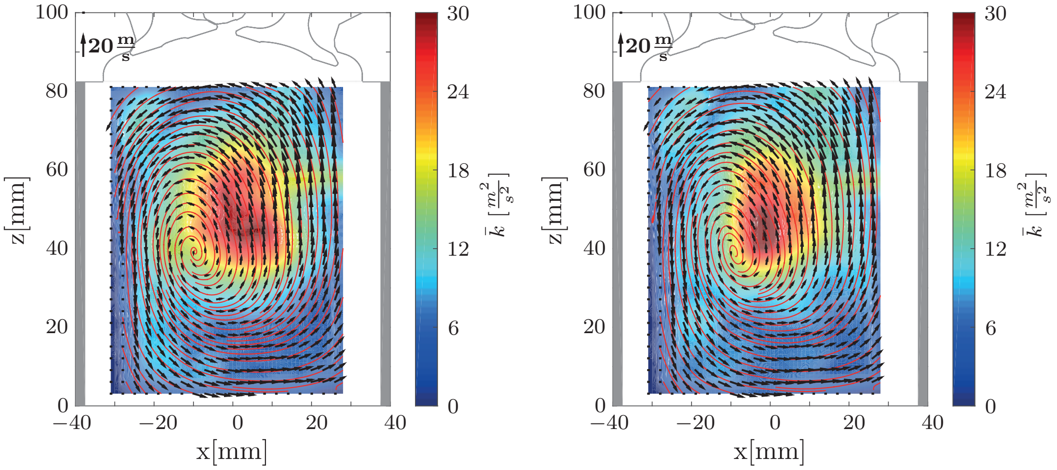

(b) $p_{inj} = 50\ bar$ (c) $p_{inj} = 100\ bar$

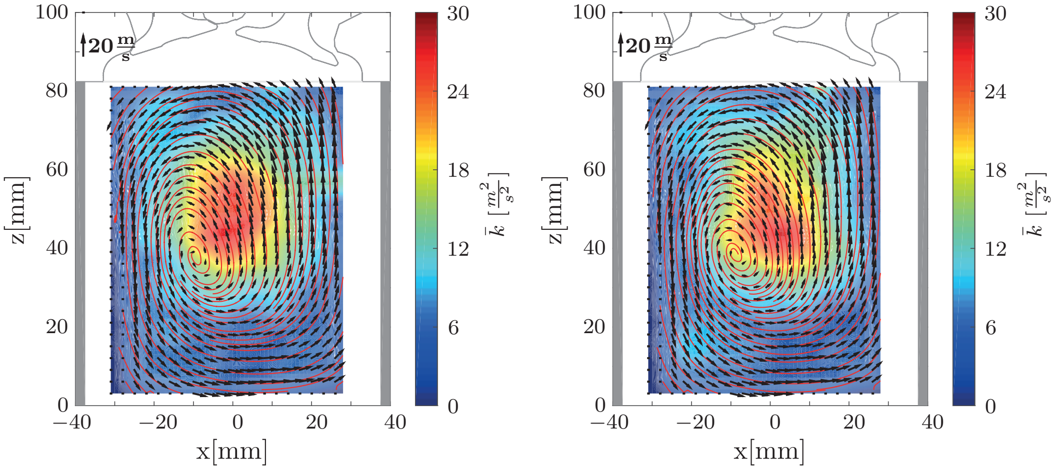

(d) $p_{inj} = 150\ bar$ (e) $p_{inj} = 200\ bar$

Figure 6.34 – Ensemble-averaged velocity vectors (arrows), streamlines (red lines), and turbulent kinetic energy (color map) of the symmetry plane at 180° atdc for N = 1,500 rpm, SOI=60° atdc, $t_{inj} = 500\ \mu s$

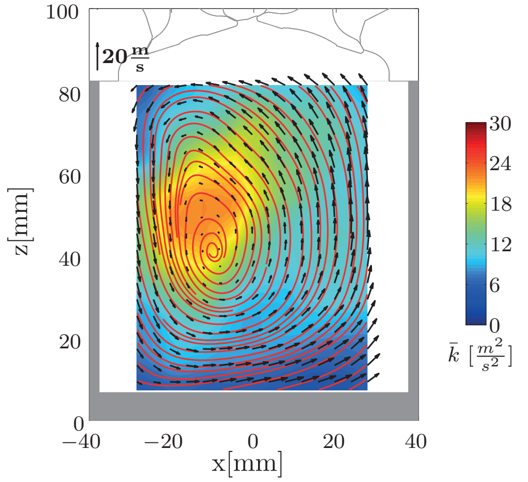

(a) Reference measurements without fuel injection [49]

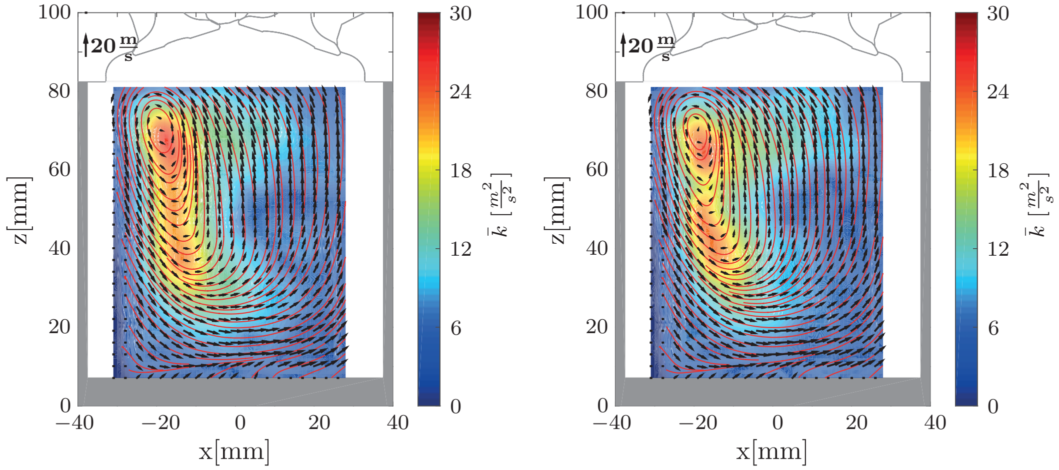

(b) $p_{inj} = 50\,bar$

(c) $p_{inj} = 100\,bar$

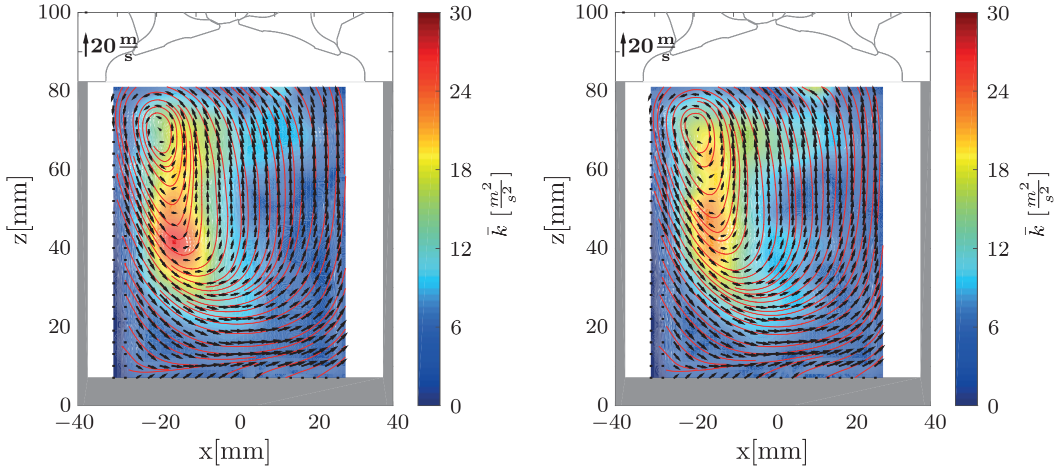

(d) $p_{inj} = 150\,bar$

(e) $p_{inj} = 200\,bar$

Figure 6.35 – Ensemble-averaged velocity vectors (arrows), streamlines (red lines), and turbulent kinetic energy (color map) of the symmetry plane at 220° atdc for N = 1,500 rpm, SOI=60° atdc, $t_{inj} = 500\ \mu s$

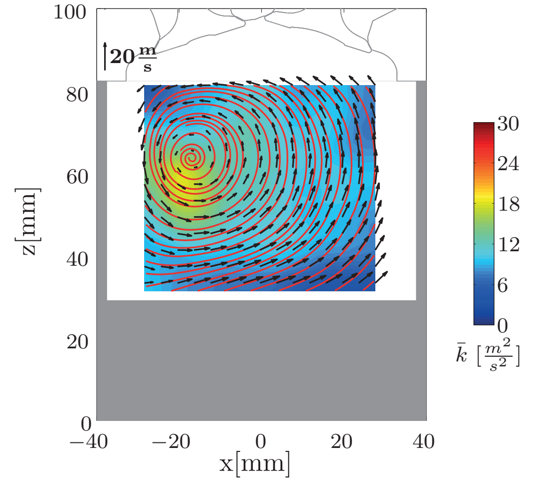

(a) Reference measurements without fuel injection

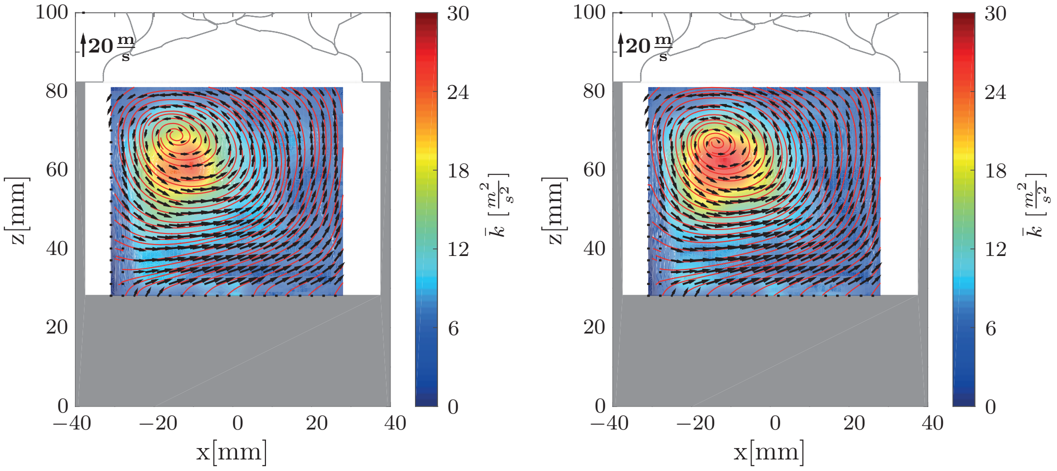

(b) $p_{inj} = 50\ bar$

(c) $p_{inj} = 100\ bar$

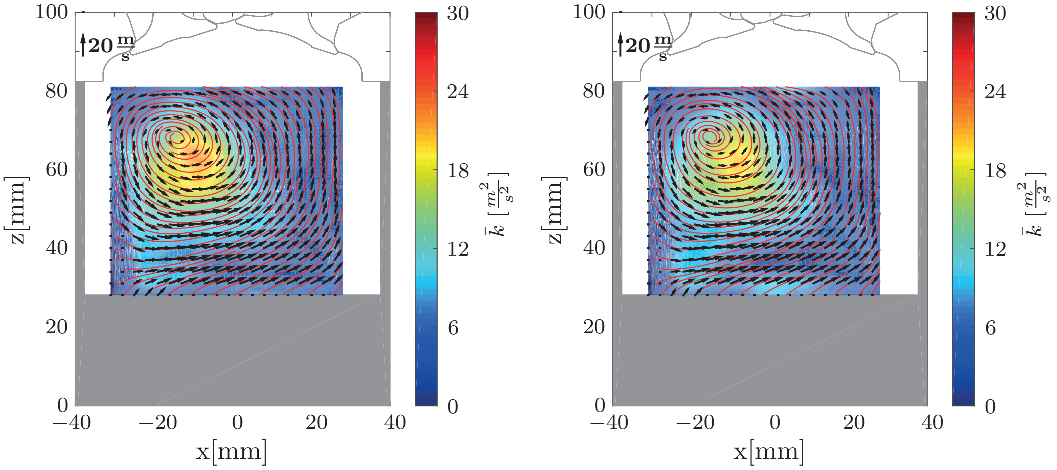

(d) $p_{inj} = 150\ bar$

(e) $p_{inj} = 200\ bar$

Figure 6.36 – Ensemble-averaged velocity vectors (arrows), streamlines (red lines), and turbulent kinetic energy (color map) of the symmetry plane at 260° atdc for N = 1,500 rpm, SOI=60° atdc, $t_{inj} = 500\ \mu$s

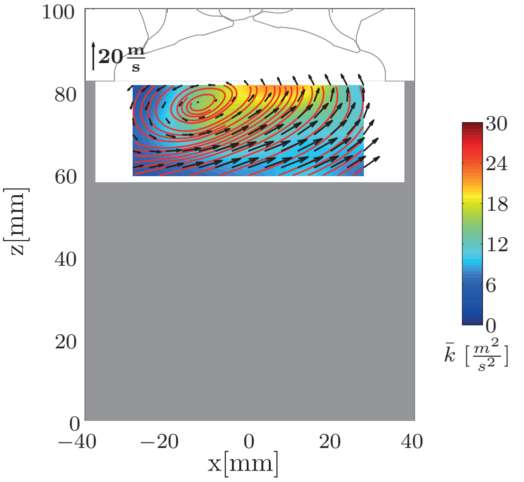

(a) Reference measurements without fuel injection [49]

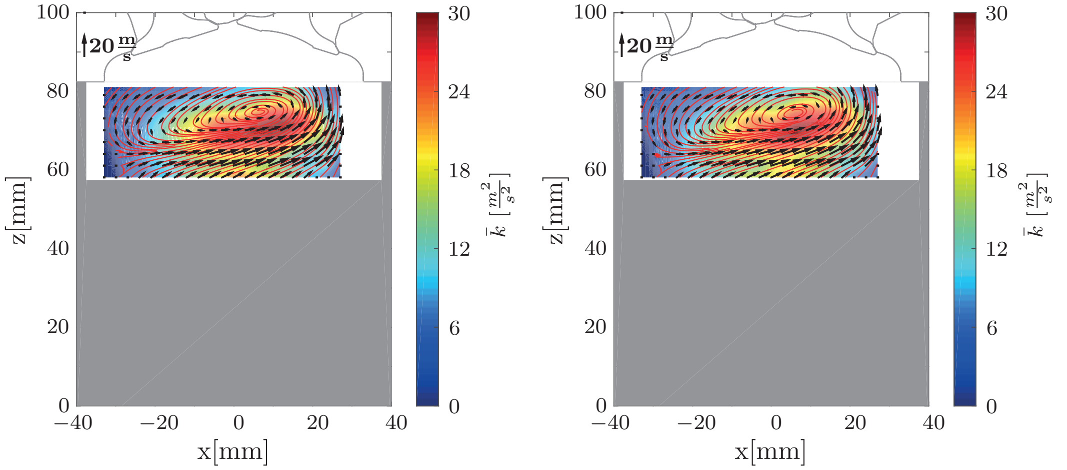

(b) $p_{inj} = 50\ bar$

(c) $p_{inj} = 100\ bar$

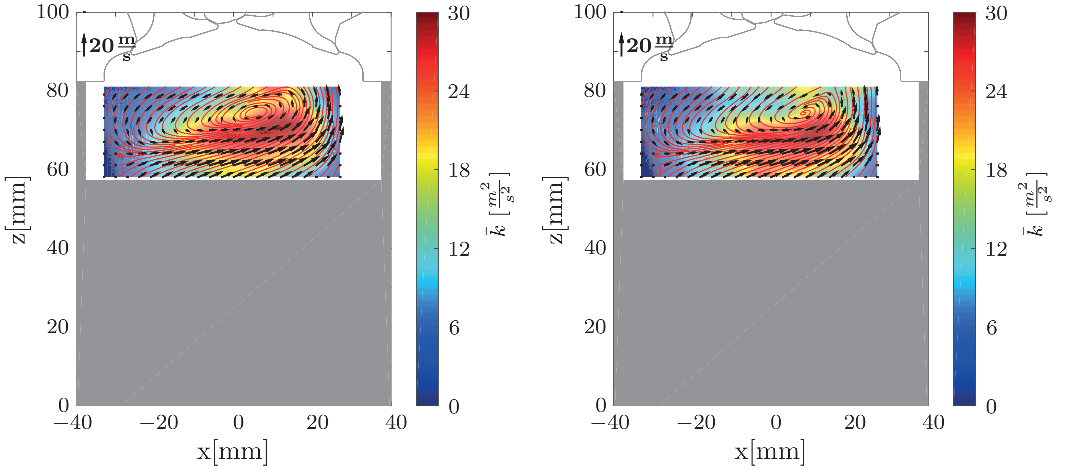

(d) $p_{inj} = 150\ bar$

(e) $p_{inj} = 200\ bar$

Figure 6.37 – Ensemble-averaged velocity vectors (arrows), streamlines (red lines), and turbulent kinetic energy (color map) of the symmetry plane at 300° atdc for N = 1,500 rpm, SOI=60° atdc, $t_{inj} = 500\ \mu s$

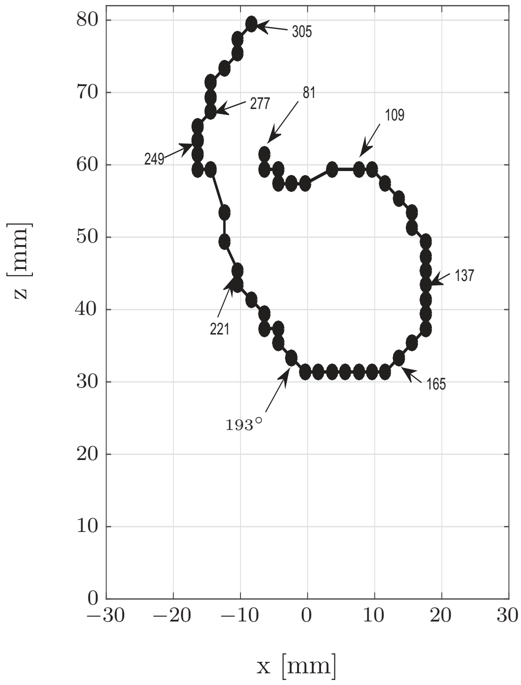

(a) Reference measurements without fuel injection [49]

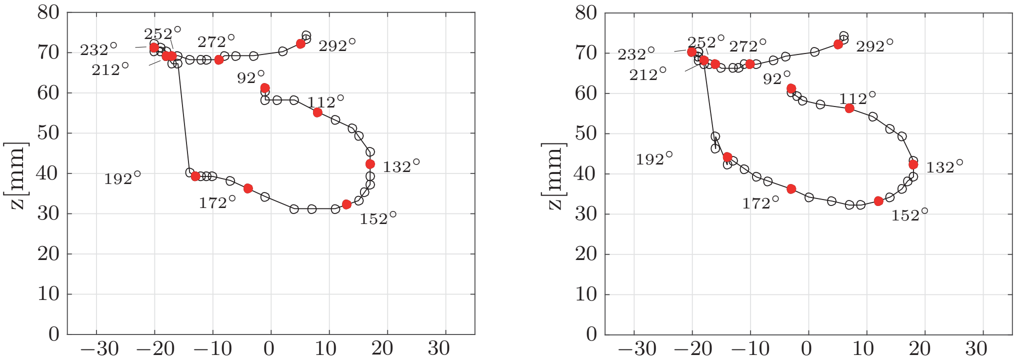

(b) $p_{inj} = 50\,bar$

(c) $p_{inj} = 100\,bar$

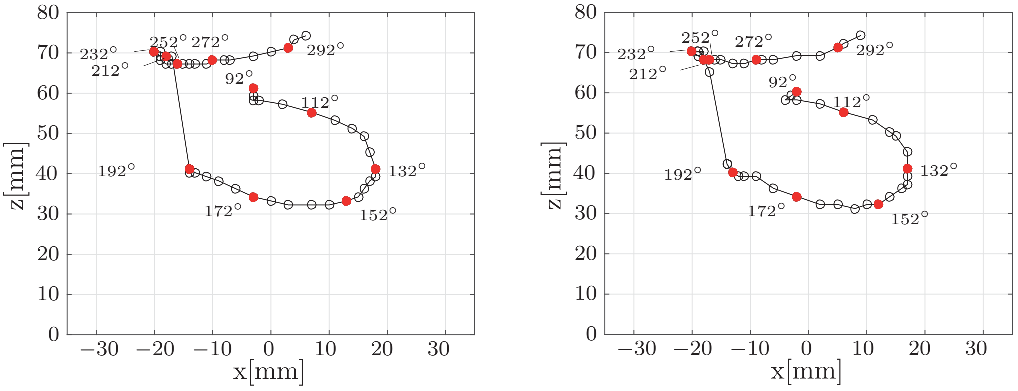

(d) $p_{inj} = 150\,bar$

(e) $p_{inj} = 200\,bar$

Figure 6.38 – Ensemble-averaged path of the tumble vortex core for N = 1,500 rpm, SOI=60° atdc, t_{Inj}=500μs

show the reference flow field without injection, whereas the remaining images illustrate the flow field for increasing injection pressure.

At 100° atdc, i.e., figure 6.32 the general flow structure between the reference case and the injection cases is comparable. The injection cases have somewhat lower intake velocities. Note that due to the injection, light reflected from the pent roof can influence the velocity calculation in this area. The position of the tumble vortex is at about $[x, z] \approx [-5\ \text{mm}, 60\ \text{mm}]$ for all cases. The maximum turbulent kinetic energy is about 50% higher for the reference case compared to the injection measurements. For the injection measurements, the highest values can be found near the pent roof below the exhaust valves. Furthermore, a C-shaped area of higher turbulent kinetic energy extends down to the piston. Additionally, the spray seems to cause higher fluctuations near the piston since the spray cone impinges upon the piston crown.

At 140° atdc in figure 6.33 the reference case still shows high values of turbulent kinetic energy at the upper part of the cylinder of up to 100 m^2/s^2. The injection measurements show significantly lower values of about 30 m^2/s^2. The highest values can be found in the tumble vortex core, which suggests a somewhat unstable behavior of the tumble due to the spray propagation. Furthermore, the injection seems to decrease the turbulent kinetic energy with increasing injection pressure. The tumble vortex core is somewhat shifted for the injection cases compared to the reference case. It is located at about $[x, z] \approx [18\ \text{mm}, 38\ \text{mm}]$ compared to the reference position of about $[x, z] \approx [18\ \text{mm}, 42\ \text{mm}]$.

Figure 6.34 evidences that at 180° atdc the turbulent kinetic energy level significantly drops for the reference case with highest values near the tumble core and the intake jet. For the injection measurements, the highest turbulent kinetic energy values can still be found near the tumble vortex core with decreasing values for increasing injection pressures. The area near the intake jet still possesses low values of turbulent kinetic energy compared to the reference case. The tumble vortex core is located at about $[x, z] \approx [2\ \text{mm}, 35\ \text{mm}]$ for the reference case, whereas its location for the injection cases is at about $[x, z] \approx [-10\ \text{mm}, 40\ \text{mm}]$. Again, no pronounced difference between the different injection cases can be seen.

At 220° atdc in figure 6.35 a further reduction of the turbulent kinetic energy is visible for the reference case and all injection cases. The highest turbulent kinetic energy occurs in the tumble vortex core with an elongated band of higher turbulent kinetic energy below the exhaust valves with maximum values of about 30 m^2/s^2 for the reference and the injection case. Again, the general tumble position differs significantly between the injection and the reference case. The tumble is located at about $[x, z] \approx [-12\ \text{mm}, 40\ \text{mm}]$ for the reference case and at about $[x, z] \approx [-20\ \text{mm}, 70\ \text{mm}]$ for the injection cases. Comparing the structure of the flow field for the four injection cases reveals hardly any differences.

Figure 6.36 shows that at 260° the maximum turbulent kinetic energy is found near the tumble vortex core for the reference case as well as the injection cases. This suggests an unstable behavior of the position of the tumble vortex core as already shown by Karhoff et al. [49]. The injection cases possess higher values of turbulent kinetic energy than the reference case. The highest values can be seen for an injection pressure of 100

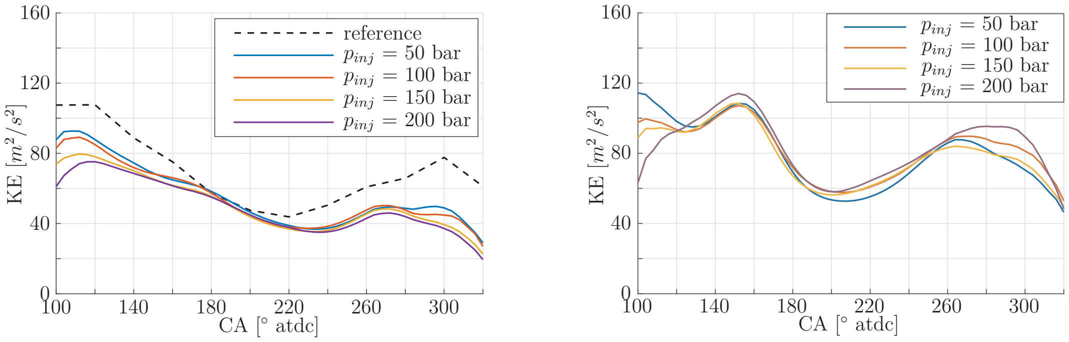

(a) 1,500 rpm

(b) 2,000 rpm

Figure 6.39 – Development of the kinetic energy in the symmetry plane for the reference case and four injection pressures at 1,500 rpm (a) and for four injection pressures at 2,000 rpm (b).

bar. The overall flow structure is comparable. Only a small deviation in the tumble vortex core position between the reference case ($[x, z] \approx [-20\ mm,\ 65\ mm]$) and the injection cases ($[x, z] \approx [-20\ mm,\ 70\ mm]$) is to be mentioned.

At 300° atdc in figure 6.37 the injection cases show about 25% higher values of turbulent kinetic energy compared to the reference case. The highest turbulent kinetic energy can be seen for an injection pressure of 100 bar with decreasing values for higher injection pressures. The tumble position differs between the reference case and the injection cases with the tumble position for the reference case being $[x, z] \approx [-18\ mm,\ 75\ mm]$ and for the injection cases $[x, z] \approx [5\text{ mm}, 75\text{ mm}]$.

To analyze the influence of the injection on the mean velocity fields figure 6.39(a) shows the temporal development of the spatially and ensemble averaged mean kinetic energy for the reference case and all four different injection pressures at 1,500 rpm. Mind that for calculating the kinetic energy, no adjustment concerning the additional mass of the fuel has been made. It can be clearly seen that the injection reduces the kinetic energy of the flow. As the kinetic energy is directly related to the flow velocity, this also indicates a general reduction of the speed of the flow field. This can be caused by the higher inertia of the fuel droplets and therefore a lower acceleration of the flow field. Furthermore, for early crank angles, a correlation between higher injection pressures and a reduced kinetic energy is evident. However, at about 140° atdc, the curves show nearly the same values. Small deviations are within the error of the experiment and therefore not statistically significant. However, the general progression of the kinetic energy is comparable between the reference case without injection and the fuel injection cases.

To better investigate the tumble movement, the Γ_1 vortex identification criterion has been used to track the tumble vortex core for all ensemble-averaged measurements. Figure 6.38 shows the trajectory of the tumble core movement for the reference case and all injection cases. It is evident that the fuel injection influences the tumble movement significantly. Especially during late compression, the tumble moves for all injection cases in the direction of the intake valves, whereas it stays below the exhaust valves for the reference case. However, no big variations between the different injection pressures can be seen. Thus, there is only a weak influence of the increasing injection pressure on the tumble vortex core trajectory.

To further investigate the influence of the injection on the tumble vortex, figure 6.42(a) shows the temporal development of the normalized out-of-plane vorticity component Ω at an engine speed of 1,500 rpm. The distributions show a divergence for the intake stroke and a general similarity between the reference case and the injection curves from the beginning of the compression stroke onwards. Furthermore, with increasing injection pressure, a decline of vorticity is evident. Hence, the momentum of the spray decreases the build-up of the tumble vortex.

Since differences in the turbulent kinetic energy were evident, the ensemble and spatial-averaged turbulent kinetic energy were calculated to investigate the general progression more thoroughly. Figure 6.40 shows the turbulent kinetic energy and the standard deviation of the turbulent kinetic energy for the reference case and the four injection pressures at N = 1,500 rpm. It can be clearly seen that the ensemble and spatial-averaged turbulent kinetic energy is twice as high for the reference case compared to the flow field with injection during the early intake stroke. One explanation could be an increase in inertia since the flow field has to move the fuel droplets. The higher inertia acts as a low-pass filter that dampens the small scale fluctuations that cause an increase in turbulent kinetic energy during the intake stroke. However, the general progression of the turbulent kinetic energy for the reference and the injection cases is similar as a decrease in the turbulent kinetic energy is evident for increasing crank angles. Furthermore, the increase in the turbulent kinetic energy at late compression is evident for all cases. The injection cases reach values in the range of the reference case. Similar to the vorticity distribution, a higher injection pressure leads to a decreased turbulent kinetic energy. However, the deviation is within the standard deviation of the measurements and therefore not statistically significant. In conclusion, the injection suppresses small scale fluctuations since the general turbulent kinetic energy drops to values well below the reference value during the early intake stroke. However, the increase near tdc combustion, which is also reported in Borée [16] and Bücker et al. [20]), ensures a good mixture formation since the tumble decays into small scale vortical structures, which can be seen by a general increase in the turbulent kinetic energy.

Influence of higher RPM

Next the measurements with an engine speed of 2,000 rpm are compared to the measurements with 1,500 rpm. Since the general flow structures are comparable, this section will focus on the tumble movement, the development of the spatially and ensemble averaged mean kinetic energy, and turbulent kinetic energy. Figure 6.39(b) shows the development of the spatially and ensemble averaged mean kinetic energy. Again, no strong influence of an increasing injection pressure on the kinetic energy is visible. The main influence can be seen at early crank angles. Higher injection pressures seem to decrease the kinetic energy of the flow field. The injection seems to counteract on the intake jet such that a decelerating of the flow is visible. However, at about 120° atdc the value of the mean kinetic energy are nearly at the same level. Small differences

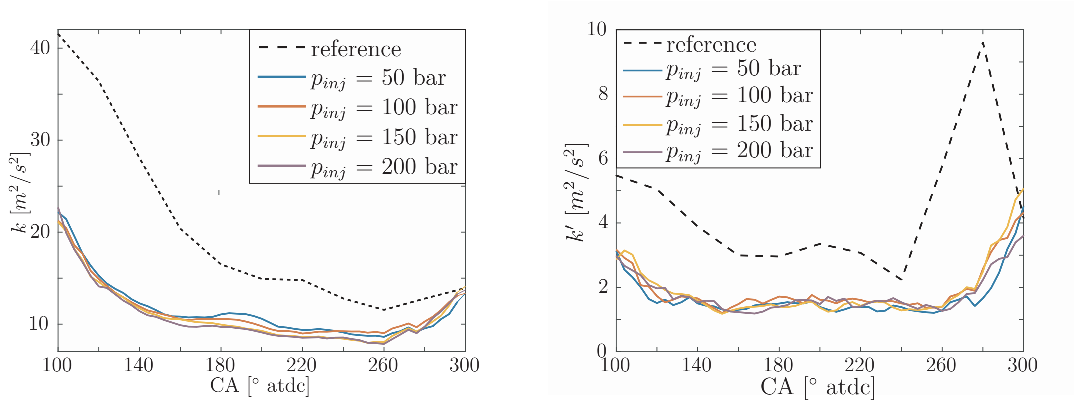

(a) turbulent kinetic energy k.

(b) standard deviation of k.

Figure 6.40 – Progress of plane- and ensemble- averaged turbulent kinetic energy (a) and standard deviation of turbulent kinetic energy (b) for N = 1,500 rpm, SOI=6° atdc, t_{Inj}=500 μs

between the different injection pressures are within the error of the experiment and therefore not statistically significant.

Figure 6.41 shows the trajectory of the tumble vortex for 1,500 rpm with an injection pressure of 200 bar and at 2,000 rpm for all four injection pressures. Note that it is evident from figure 6.38 that the tumble motion at 1,500 rpm hardly depends on the injection pressure. However, it is evident in figure 6.41 that the propagation of the tumble vortex core is strongly influenced by the higher rpm. At 100° atdc, the position of the tumble has already propagated below the intake valves at about $[x, z] \approx [15$ mm, 60 mm], whereas the tumble position for 1,500 rpm is at about $[x, z] \approx [-5$ mm, 59 mm]. Furthermore, the semi-steady tumble position in the middle of the compression stroke at about $[x, z] \approx [-20$ mm, 70 mm] cannot be observed for the cases at an engine speed of 2,000 rpm. Additionally, the tumble position at the end of the compression stroke differs strongly from that at 1,500 rpm. The end position is at about $[x, z] \approx [0$ mm, 80 mm] for the 2,000 rpm cases and at $[x, z] \approx [10$ mm, 80 mm] for the 1,500 rpm case. Only the case with an injection pressure of 200 bar shows a difference in the end position and is close to the 1,500 rpm case. However, from the normalized mean vorticity in figure 6.42(b) it is evident that hardly any influence of the higher engine speed can be observed. Since the vorticity has been normalized by the engine angular velocity, the total vorticity is higher, which causes a more stable tumble. Furthermore, the general trajectory is closer to the reference case without injection. The saddle point in figure 6.42(a) between 140° and 160° atdc has vanished. Additionally, the small decrease in vorticity with increasing injection pressure cannot be observed anymore. This suggests that at higher engine speeds the spray is no longer able to strongly disturb the tumble movement.

The variation of the spatially and ensemble averaged turbulent kinetic energy for an engine speed of 2,000 rpm is shown in figure 6.43. The maximum turbulent kinetic energy of $k = 33$ m^2/s^2 can be found for the case with an injection pressure of 200 bar at 100° atdc. All other cases show values in the range of $k = 23$ m^2/s^2, which is

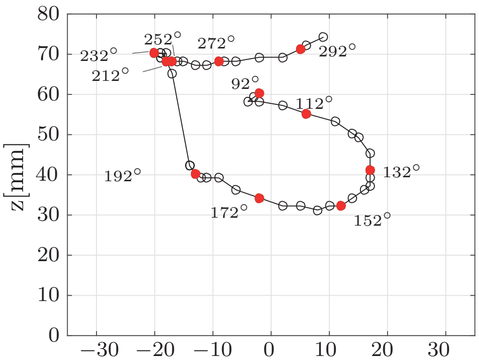

(a) $p_{inj} = 200\,bar$, 1,500 rpm

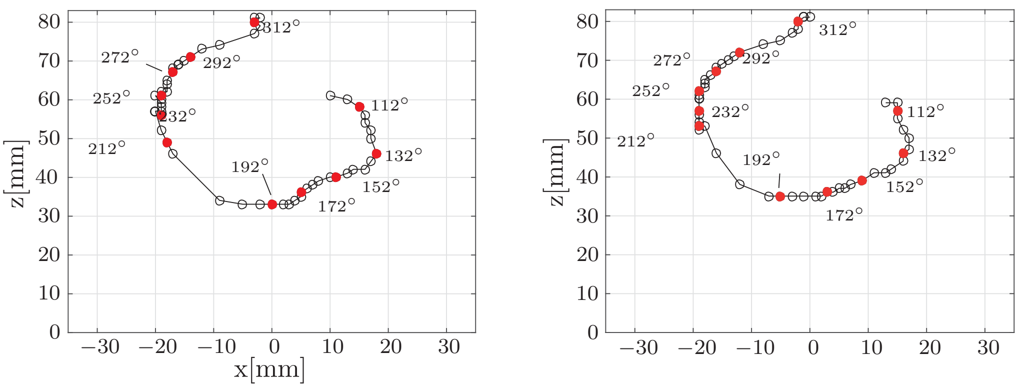

(b) $p_{inj} = 50\,bar$, 2000 rpm

(c) $p_{inj} = 100\,bar$, 2,000 rpm

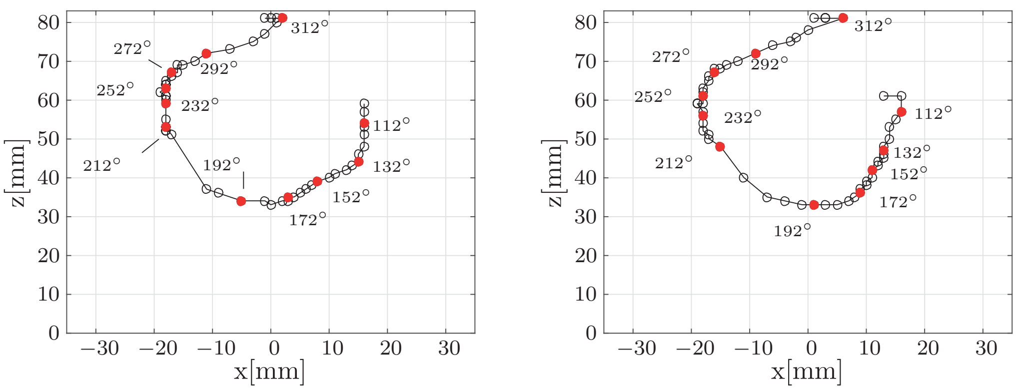

(d) $p_{inj} = 150\,bar$, 2,000 rpm

(e) $p_{inj} = 200\,bar$, 2,000 rpm

Figure 6.41 – Comparison of the ensemble-averaged path of the tumble vortex core for N = 1,500 rpm (top), and N = 2,000 rpm (center, bottom), SOI=60° atdc, t_{Inj}=500μs.

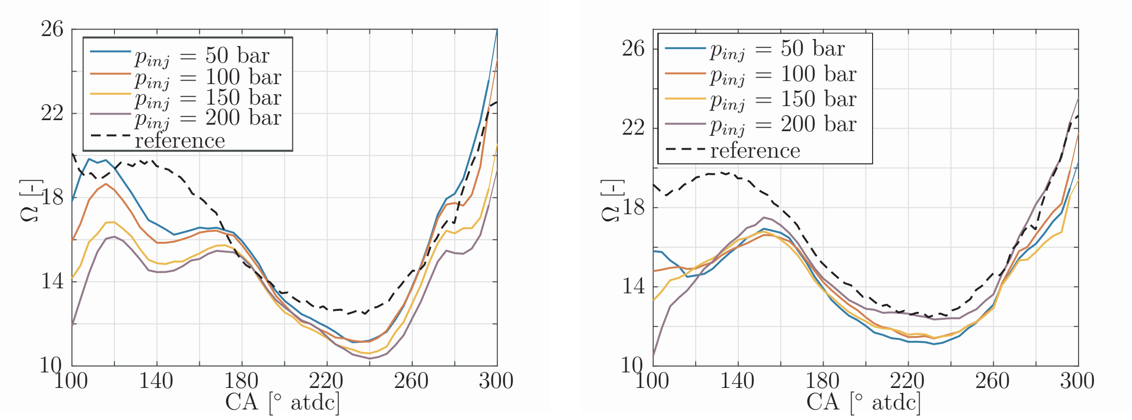

(a) 1,500 rpm (b) 2,000 rpm

Figure 6.42 – Development of the out-of-plane vorticity component in the symmetry plane for the reference case and four injection pressures at 1,500 rpm (a) and for four injection pressures at 2,000 rpm (b).

comparable to the cases with an engine speed of 1,500 rpm. However, the general slope of the turbulent kinetic energy progression is somewhat flatter such that the lowest values are about $k = 14\ m^2/s^2$ at 250° atdc compared to $k = 8\ m^2/s^2$ at 260° atdc for an engine speed of 1,500 rpm. Hence, the turbulent kinetic energy also shows higher values near the end of the compression stroke which can leads to a better mixture formation and therefore a more efficient combustion.

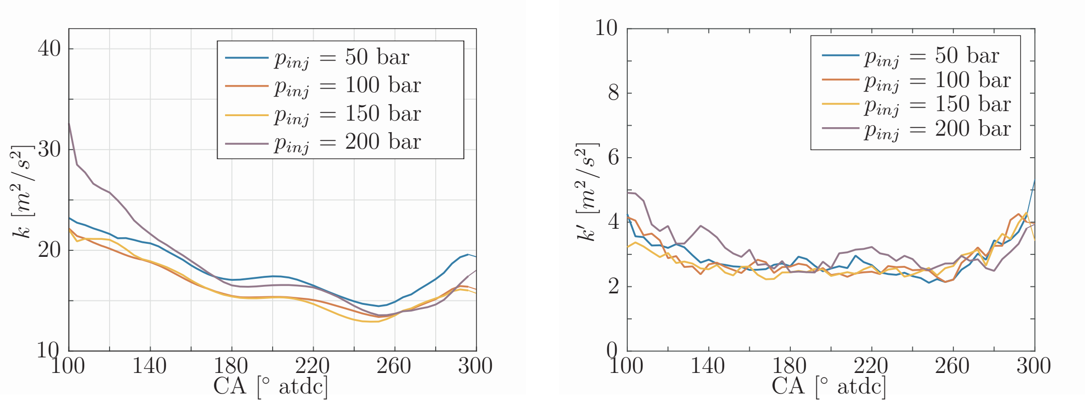

(a) turbulent kinetic energy k. (b) standard deviation of k.

Figure 6.43 – Progress of plane- and ensemble-averaged turbulent kinetic energy (a) and standard deviation of turbulent kinetic energy (b) for N = 2000 rpm, SOI=6° atdc, t_{Inj}=500 μs

7

Conclusion

In this thesis, the volumetric, three-dimensional flow behavior of the large-scale vortical structures of an internal combustion engine and the mixture formation during intake and compression stroke for two bio-fuels have been investigated. To this end, two volumetric measurement techniques, namely holographic particle-image velocimetry and tomographic particle image velocimetry, have been introduced. Furthermore, stereoscopic particle-image velocimetry and Mie scattering imaging have been introduced to analyze the interaction of fuel injection and in-cylinder flow field.

The volumetric measurement techniques have been used to analyze the propagation of the large-scale vortical structures, namely the tumble vortex and the ring vortex below the intake valves, and the small-scale structures by means of turbulent kinetic energy. For the first time, it was possible to resolve nearly the whole combustion chamber with sufficient resolution such that a volume with a diameter of about 60 mm and a height of approximately 80 mm could be resolved with a spatial resolution of 0.75 mm for a crank angle of 160° atdc and an engine speed of 1,500 rpm.
This results in about 600,000 velocity vectors that could be resolved. A comparison with monoscopic particle-image velocimetry data shows the technique to be feasible to analyze the flow field inside an internal combustion engine. Furthermore, the measurements have shown a U-shaped profile of the tumble vortex core. As the analogue nature of holographic PIV restricts the number of measurements such that statistically reliable analyses are not possible tomographic particle-image velocimetry has been applied to the engine to analyze the flow field at 80° atdc, 160° atdc, and 240° atdc for an engine speed of 1,500 rpm to investigate the large-scale flow structures and the turbulent kinetic energy in higher detail. With this, 300 statistically independent velocity volumes for every investigated crank angle could be analyzed. The resolved measurement volume has a size of about 60 x 60 x 80 mm^3 for the measurements at 160° atdc whose axial extent decreases for the other crank angles. A spatial resolution of 3.4 mm^3 and a vector spacing of 0.85 mm leads to approximately 450,000 vectors for the measurements at 160° atdc. Based on the volumetric flow field, a method combining coordinate transformation and the Γ_1 vortex identification criterion, has been applied to track the three-dimensional propagation of the tumble vortex throughout the combustion chamber. The tumble vortex is created through the interaction of the

intake jet and the curved cylinder walls. Furthermore, it was possible to show a ring vortex below the pent roof, which is driven by the shear layer at the intake valves. Both, tumble and ring vortex are stable throughout intake and compression stroke. The analysis of the turbulent kinetic energy evidenced that the high in-flow velocity and the resulting shear layer at 80° atdc and 160° atdc increase the mixing between the intake valves. Additionally, during compression, at 240° atdc the breakup or an increased cyclic variability of the tumble vortex was evidenced through an increased turbulent kinetic energy in its core region. The analysis of the internal exhaust gas recirculation shows a decrease in tumble strength and therefore an early break-up of the tumble. Through this higher levels of turbulent kinetic energy could be observed. This suggests a higher mixture inside the flow field at earlier crank angles and therefore an increase in the mixing of fuel and air in mid compression.

After that, Mie Scattering Imaging has been performed to investigate the interaction of ethanol fuel spray and internal combustion flow field in the tumble symmetry plane for three starting times of injection, namely 60° atdc, 277° atdc, and 297° atdc, corresponding to an in-cylinder pressure of 1, 2, and 3 bar. The measurements have been performed for an injection pressure of 50, 100, 150, and 200 bar, an engine speed of 1,500 and 2,000 rpm, and injection durations of 0.5, 1, and 2 milliseconds. Furthermore, the injection behavior of methyl ethyl ketone has been analyzed for the aforementioned starting times of injection and injection pressures at an engine speed of 2,000 rpm with an injection duration of 0.5 milliseconds. The results show the flow field to strongly influence the injection behavior. For early injection at 60° atdc the spray on the exhaust side is redirected through the tumble movement such that a slowdown in vertical penetration length could be observed. Furthermore, liner and piston wetting was observed for all cases of ethanol injection. Higher engine speeds increase the vorticity of the tumble and therefore increase the manipulation of the spray behavior. Where injection timing was started later, the importance of the tumble movement is evident. On the intake side, the spray is heavily redirected through the tumble movement such that piston wetting only occurred for an injection pressure of about 200 bar at a start of injection at 277° atdc. However, on the exhaust side, the spray is trapped inside the tumble such that liner and piston wetting occur for this side. Even for the latest injection time, piston and liner wetting is strongly reduced on the intake side. The behavior of MEK is comparable to the behavior of ethanol. However, the lower dynamic viscosity leads to higher spray Reynolds numbers. Furthermore, the nozzle exhaust velocity is increased. This leads to higher penetration length depending on crank angle compared to ethanol. Furthermore, the results show lower piston wetting as well as reduced liner wetting. The change in penetration direction on the intake side for a start of injection at 277° atdc and 297° atdc is not as distinct. This suggest bigger fuel droplets for MEK and therefore worse flow following behavior through higher inertia forces.

Finally, stereoscopic particle-image velocimetry measurements have been performed to investigate the interaction of flow field and ethanol fuel spray. For this, the aforementioned injection pressures at a start of injection at 60° atdc have been analyzed for an injection duration of 0.5 milliseconds and an engine speed of 1,500 and 2,000 rpm with a temporal resolution of 4° CA. The results confirm the findings from the Mie scattering Imaging such that a strong interaction of tumble movement and spray behavior is evident. The movement of the tumble vortex core is changed through the injection process. Especially shortly after injection, the normalized vorticity of the tumble vortex is significantly reduced for both investigated engine velocities with a higher influence at 2,000 rpm. However, higher engines speeds lead to a more stable tumble vortex for later crank angles. Furthermore, the injection causes a reduction of turbulent kinetic energy during intake and compression stroke. However, at the end of the compression stroke, the tumble starts to decompose and creates values of turbulent kinetic energy comparable to the flow field case without injection. This increases the turbulence level and improves the final mixture formation shortly before the power stroke.

The findings show the flow field and the interaction between flow field and spray to be highly complex. However, the general flow structure of the large- and small-scale vortical structures is mostly understood. Therefore, future work has to focus on the interaction of spray and flow field in more detail. As the results showed, an increase in engine speed stabilizes the tumble and therefore the mixture formation. This is mostly due to the higher kinetic energy of the flow. Another approach is the supercharging of the intake air, which leads to higher intake velocities and therefore higher vorticity rates of the tumble vortex. This process has to be investigated in greater detail to fully understand the relationship between supercharging, flow field and mixture formation. Furthermore, the influence of different valve timings on the spray behavior has to be analyzed. Especially the so-called Miller cycle is of high interest for the combustion of Tailor-Made Fuels from Biomass, as higher compression ratios and therefore higher engine efficiencies are possible. All this will help to reduce the pollutant emissions, increase the combustion efficiency, and reduce the fuel consumption of modern combustion engines.

References

[1] Abd-Alla, G.: Using exhaust gas recirculation in internal combustion engines: a review. EnergyConversion and Management **43**, 1027 – 1042 (2002)

[2] Abdelfattah, A.: Numerische Simulation von Strömungen in 2- und 4- Ventil Motoren. Ph.D. thesis, RWTH Aachen (1998)

[3] Adomeit, P., Brunn, A., Ewald, J., Budde, M., Jakob, M., Pischinger, S.: Effect of Intake Port Design on the Flow Field Stability of a Gasoline DI Engine. SAE Technical Paper (2011-01-1284)

[4] Adomeit, P., Sehr, A., Weinowski, R., Stapf, K.G., Seebach, D., Pischinger, S., Hoffmann, K., Abel, D., Fricke, F., Kleeberg, H., Tomazic, D.: Operation strategies for Controlled Auto Ignition CAI Engines. In: SAE World Congress. Detroit, MI, USA (2009). SAE Paper No. 2009-01-0300

[5] Adrian, R.J.: Twenty years of particle image velocimetry. Exp Fluids **39**, 159 – 169 (2005)

[6] Albin, T., Drews, P., Hesseler, F.J., Ivanescu, A., Seidl, T., Abel, D.: A hybrid control approach for low temperature combustion engine control. In: 50th IEEE Conference on Decision and Control and European Control Conference (2011)

[7] Arroyo, M.P., Greated, C.A.: Stereoscopic particle image velocimetry. Meas Sci Technol **2**, 1181 – 1186 (1991)

[8] Atkinson, C.: An Experimental Technique for the Investigation of the Three-Dimensional Structure of Wall-Bounded Turbulence. Ph.D. thesis, LTRAC, Monash University, Melbourne (2011)

[9] Atkinson, C., Soria, J.: An efficient simultaneous reconstruction technique for tomographic particle image velocimetry. Exp Fluids **47**, 553 – 568 (2009)

[10] Bardi, M., Payri, R., Malbec, L., Bruneaux, G., Pickett, L., Manin, J., Bazyn, T., Genzale, C.: Engine Combustion Network: Comparison of spray development, vaporization, and combustion in different combustion vessels. Atomization and Sprays **22**, 807 – 842 (2012)

[11] Barnhart, D.: Whole-Field Holographic Measurements of Three-Dimensional Displacement in Solid and Fluid Mechanics. Ph.D. thesis, Loughborough University (2001)

[12] Barnhart, D.H., Adrian, R.J., Papen, G.C.: Phase-conjugate holographic system for high-resolution particle-image velocimetry. Applied Optics **33**, 7159– 7170 (1994)

[13] Basset, A.B.: A treatise on hydrodynamics, vol. 2. Deighton, Bell and Co. (1888)

[14] Baum, E., Peterson, B., Surmann, C., Michaelis, D., Böhm, B., Dreizler, A.: Tomographic PIV measurements in an IC engine. In: 16th Int Symp on Applications of Laser Techniques to Fluid Mechanics, Lisbon, Portugal, (2012)

[15] Bhave, A., Kraft, M., Mauss, F., Oakley, A., Zhao, H.: Evaluating the EGR-AFR Operating Range of a HCCI Engine. In: SP-1963 Homogeneous Charge Compression Ignition (HCCI) Combustion 2005 (2005)

[16] Boree, J., Miles, P.C.: In-Cylinder Flow. In: Encyclopedia of Automotive Engineering. John Wiley & Sons, Ltd. (2013)

[17] Bracewell, R.N.: Strip integration in radio astronomy. Australian Journal of Physics **9**, 198 – 217 (1956)

[18] Bücker, I.: Experimental Investigation of the In-Cylinder Flow of an internal Combustion Engine. Ph.D. thesis, RWTH Aachen, University, (2013)

[19] Bücker, I., Karhoff, D., Dannemann, J., Pielhop, K., Klaas, M., Schröder, W.: Comparison of PIV Measured Flow Structures in Two Four-Valve Piston Engines. Notes on Numerical Fluid Mechanics and Multidisciplinary Design **121**, 633–640 (2013)

[20] Bücker, I., Karhoff, D., Klaas, M., Schröder, W.: Stereoscopic Multi-Planar PIV Measurements of In-Cylinder Tumbling Flow. Exp. Fluids **53**, 1993 – 2009 (2012)

[21] Bücker, I., Karhoff, D., Klaas, M., Schröder, W.: Engine In-Cylinder Flow Control via Variable Intake Valve Timing. SAE Int. J. Engines **2013-24-0055** (2013)

[22] Buschbeck, M., Bittneer, N., Halfmann, T., Arndt, S.: Dependence of combustion dynamics in a gasoline engine upon the in-cylinder flow field, determinde by high-speed PIV. Exp Fluids **53**, 1701 – 1712 (2012). DOI DOI 10.1007/s00348-012-1384-3

[23] Caulfield, H.J. (ed.): Handbook of Optical Holography. Academic Press, Inc. (1979)

[24] Chan, V.S.S., Koek, W.D., Barnhart, D.H., Juchem, T., Hampp, N.A., Coupland, J.M., Halliwell, N.A.: Application of holography to fluid flow measurements using bacteriorhodopsin (bR). Meas. Sci. Technol. **15**, 647–655 (2004)

[25] Chan, V.S.S., Koek, W.D., Barnhart, D.H., Poelma, C., A., O.T., Bhattacharya, N., Braat, J.J.M., Westerweel, J.: HPIV using Polarization Multiplexing Holography in Bacteriorhodopsin (bR). In: 13th International Symposium on Applications of Laser Techniques to Fluid Mechanics. Lisbon, Portugal (2004)

[26] Chao, B.T.: Turbulent transport behaviour of small particles in a turbulent fluid. "Osterreichisches Ingenieur-Archiev **18:7** (1964)

[27] Collier, R., Burckhardt, C., Lin, L.: Optical Holography. Academic Press, Inc. (1971)

[28] Coudert, S., Schon, J.P.: Back-projection algorithm with misalignment corrections for 2D3C stereoscopic PIV. Meas Sci Technol **12**, 1371 – 1381 (2001)

[29] Dannemann, J.: Multidimensional Measurements of the In-Cylinder Flow of a Four-Valve Internal Combustion Engine. PhD thesis, RWTH Aachen University (2012)

[30] Dannemann, J., Pielhop, K., Klaas, M., Schröder, W.: Cycle resolved multi-planar flow measurements in a four-valve combustion engine. Exp Fluids **50**, 961 – 976 (2010). DOI 10.1007/s00348-010-0963-4. Online First

[31] Daubert, T., Danner, R.: "Physical and thermodynamic properties of pure chemicals". Hemisphere Pub. Corp. New York. (2000)

[32] Demptröder, W.: Experimentalphysik 2 Elektrizität und Optik. Springer Berlin Heidelberg (2006)

[33] Deshmukh, A., Bode, M., Pitsch, H., Kirsch, V., Reddemann, M., Palmer, J., Kneer, R., van Overbrüggen, T., Schröder, W., Liebergesell, B., Bardow, A., Ottenwälder, T., Pischinger, S.: Spray breakup and mixture formation of novel biofuels. In: 3rd TMFB International Conference, Aachen, Germany (2015)

[34] van Doorne, C.W.H., Westerweel, J.: Measurement of laminar, transitional and turbulent pipe flow using Stereoscopic-PIV. Exp Fluids **42**, 259–279 (2007)

[35] Elsinga, G., Scarano, F., Wieneke, B., van Oudheusden, B.: Tomographic particle image velocimetry. Exp. Fluids **41**, 933–947 (2006). URL http://dx.doi.org/10.1007/s00348-006-0212-z. 10.1007/s00348-006-0212-z

[36] Garbor, D.: A new microscopic principle. Nature **161.4098**, 777–778 (1948)

[37] Gaydon, C., Raffel, M., Willert, C., Rosengarten, J., Kompenhans, J.: Hybrid stereoscopic particle image velocimetry. Exp Fluids **23**, 331–334 (1997)

[38] Graftieaux, L., Michard, M., Grosjean, N.: Combining PIV, POD and vortex identification algorithms for the study of unsteady turbulent swirling flows. Meas. Sci. Technol. **12**, 1422–1429 (2001)

[39] Haertig, J.: Introductory lecture on particle behaviour. In: ISL/AGARD Workshop on Laser Anemometry (Institut Saint Louis) (1976)

[40] Hecht, E.: Optik. Oldenbourg, München (2009)

[41] Heflinger, L., Stewart, G., Booth, C.: Holographic motion pictures of microscopic plankton. Applied Optics **17**(6), 951–954 (1978)

[42] Hermann, G., Lent, A.: Iterative reconstruction algorithms. Comput Biol Med **6**, 273 – 294 (1976)

[43] Herrmann, S.F.: Three-dimensional optical flow measurements with short coherence holography. Ph.D. thesis, Universität Oldenburg, Uhlhornsweg 49-55, 26129 Oldenburg (2006)

[44] Heywood, J.B.: Internal combustion engine fundamentals. McGraw-Hill (1988)

[45] Hjelmfelt, A.T., Mockros, L.F.: Motion of discrete particles in a turbulent fluid. Applied Scientific Research **16**, 149–161 (1966)

[46] Hong, C.W., Tarng, S.D.: In-Cylinder Tumble Flow Field Measurements and Predictions. Journal of Engineering for Gas Turbines and Power **123**, 139–145 (2001)

[47] Jeong, J., Hussain, F.: On the identification of a vortex. Journal of Fluid Mechanics **285**, 69–94 (1995)

[48] Karhoff, D., Bücker, I., Dannemann, J., Pielhop, K., Klaas, M., Schröder, W.: Experimental analysis of three-dimensional flow structures in two four-valve combustion engines. SAE Technical Paper **24** (2011)

[49] Karhoff, D.C.: Experimental Analysis of Flow Phenomena in Internal Combustion Engines. Ph.D. thesis, Institute of Aerodynamics and Chair of Fluid Mechanics, RWTH Aachen, University (2014)

[50] Konrath, R.: Strömungsanalyse im Zylinder eines 4-Ventil-Motors mit der holographischen Particle-Image Velocimetry. PhD thesis, RWTH Aachen University (2003)

[51] Konrath, R., Schröder, W., Limberg, W.: Holographic particle-image velocimetry applied to the flow within the cylinder of a four-valve internal combustion engine. Exp. Fluids **33**, 781–793 (2002)

[52] Kreis, T.: Handbook of Holographic Interferometry: Optical and Digital Methods. Wiley-VCH (2005)

[53] Kulick, J.D., Fessler, J.R., Eaton, J.K.: Particle response and turbulence modification in fully developed channel flow. J. Fluid Mech. **277**, 109 – 134 (1994)

[54] Lang, O., Salber, W., Hahn, J., Pischinger, S., Hortmann, K., Buecker, C.: Thermodynamical and Mechanical Approach Towards a Variable Valve Train for the Controlled Auto Ignition Combustion Process. SAE Paper **01-0762** (2005)

[55] Lauterborn, W.: Kohärente Optik. Springer Berlin / Heidelberg (1993)

[56] Leick, P.: Quantitative Untersuchungen zum Einfluss von Düsengeometrie und Gasdichte auf den Primärzerfallsbereich von Dieselsprays. Ph.D. thesis, TU Darmstadt (2008)

[57] Lourenco, L., Krothapalli, A.: On the accuracy of velocity and vorticiy measurements with PIV. Exp Fluids **18**, 421 – 428 (1995)

[58] Lumley, J.: Engines: An Introduction. Cambridge University Press, United Kingdom (1999)

[59] Ma, T., Zhao, H., Li, J., Ladommatos, N.: Experimental Investigation of Controlled Auto-ignition (CAI) Combustion in a 4-stroke Multi-Cylinder Gasoline Engine And Drive Cycle Simulations. In: A new Generation of Engine Combustion Processes for the Future pp. 115–124 (2001)

[60] Maas, H., Westfield, P., Putze, T., Boetkjaer, N., Kitzhofer, J., Brücker, C.: Photogrammetric techniques in multi-camera tomographic PIV. In: In proceedings of PIV09, Melbourne, Australia (2009)

[61] Mahmood, Z., Chen, A., Yianneskis, M.: On the Structure of Steady Flow Through Dual-Intake Engine Ports. Int. J. Numer. Meth. Fl. **23**, 1085 – 1109 (1996)

[62] Mathieu, F.: Laseroptische Untersuchungen des Einflusses alternativer Bio-Kraftstoffe auf die ottomotorische Gemischbildung. Ph.D. thesis, RWTH Aachen, University (2015)

[63] Melling, A.: Tracer particles and seeding for particle image velocimetry. Measurement Science and Technology **8**, 1406–1416 (1997)

[64] Michaelis, D., Novara, M., Scarano, F., Wieneke, B.: Comparison of volume reconstruction techniques at different particle densities. In: 15th Int Symp on Applications of Laser Techniques to Fluid Mechanics Lisbon, Portugal, 05-08 July (2010)

[65] Mishra, D., Muralidhar, K., Munshi, P.: A robust MART algorithm for tomographic applications. Numerical Heat Transfer, Part B: Fundamentals: An International Journal of Computation and Methodology **35**, 485 – 506 (1999)

[66] von Ohnesorge, W.: Die Bildung von Tropfen an Düsen und die Auflösung flüssiger Strahlen. ZAMM - Zeitschrift für Angewandte Mathematik und Mechanik **16**, 355 – 358 (1936)

[67] Oldendorf, W.H.: Solated flying spot detection of radiodensity discontinuities-displaying internal structural pattern of complex object. Bio-Medical Electronics, IRE Transactions on **8**(1), 68 – 72 (1961)

[68] Organisation, W.H.: Global Health Risks: Mortality and Burden of Deisease Attributable to Selected Major Risks. Tech. rep., Geneva: World Health Organisation (2009)

[69] Ortmann, R.: Untersuchung der Strömung im Zylinder eines 4-Ventil-Serienmotors mit der Particle-Image-Velocimetry. Ph.D. thesis, Institute of Aerodynamics and Chair of Fluid Mechanics, RWTH Aachen, University (1997)

[70] van Overbrüggen, T., Bahl, B., Dierksheide, U., Klaas, M., Schröder, W.: Tomographic particle-image velocimetry in an IC engine. In: 10th international Symposium on Particle Image Velocimetry - PIV13 Delft, The Netherlands, July 1-3 (2013)

[71] van Overbrüggen, T., Braun, M., Klaas, M., Schröder, W.: Experimental Analysis of the Impact of Injected Biofuels on In-Cylinder Flow Structures. SAE Int. J. Engines **9**(2) (2016)

[72] van Overbrüggen, T., Bücker, I., Dannemann, J., Karhoff, D.C., Klaas, M., Schröder, W.: Planar, Stereoscopic, and Holographic PIV-Measurements of the In-Cylinder Flow of Combustion Engines. In: M. Klaas, S. Pischinger, W. Schröder (eds.) Fuels From Biomass: An Interdisciplinary Approach, Notes on Numerical Fluid Mechanics and Multidisciplinary Design, vol. 129, pp. 155–191. Springer Berlin Heidelberg (2015)

[73] van Overbrüggen, T., Dannemann, J., Klaas, M., Schröder, W.: Holographic particle-image velocimetry measurements in a four-valve combustion engine. In: 16th Int Symp on Applications of Laser Techniques to Fluid Mechanics, Lisbon, Portugal (2012)

[74] van Overbrüggen, T., Dannemann, J., Klaas, M., Schröder, W.: Holographic particle-image velocimetry measurements in a four-valve combustion engine. Exp. Fluids **55** (2014)

[75] van Overbrüggen, T., Klaas, M., Bahl, B., Schröder, W.: Tomographic Particle-Image Velocimetry Analysis of In-Cylinder Flows. SAE Int. J. Engines **8** (2015). DOI 10.4271/2015-01-9042

[76] van Overbrüggen, T., Klaas, M., Soria, J., Schröder, W.: Experimental analysis of particle sizes for PIV measurement. In: 11th international Symposium on Particle Image Velocimetry - PIV15 Santa Barbara, California, September 14-16, 2015 (2015)

[77] van Overbrüggen, T., Schröder, F., Klaas, M., Schröder, W.: A particle-image velocimetry tracer generating technique for liquid flows. Meas Sci Technol **25**, 087,001 (2014)

[78] Palmer, J., Ramesh, M., Kirsch, V., Reddemann, M.e.a.: Spray analysis of c8h18o fuel blends using high-speed schlieren imaging and mie scattering. SAE Technical Paper **2015-24-2478** (2015). DOI doi:10.4271/2015-24-2478

[79] Petersen, B., Ghandhi, J.: High-resolution turbulent scalar field measurement in an optically accessible internal combustion engine. Exp. Fluids **51**, 1695–1708 (2011)

[80] Pickett, L., Manin, J., Genzale, C., Siebers, D.e.a.: Relationship between diesel fuel spray vapor penetration/dispersion and local fuel mixture fraction. SAE Int. J. Engines **4(1)**, 764 – 799 (2011)

[81] Pope, S.B.: Turbulent Flows. Cambridge University Press (2001)

[82] Prasad, A.K.: Stereoscopic Particle Image Velocimetry. Exp Fluids **29**, 103–116 (2000)

[83] Prasad, A.K., Adrian, R.: Stereoscopic particle image velocimetry applied to liquid flows. Exp Fluids **15**, 49–60 (1993)

[84] Prasad, A.K., Jensen, K.: Scheimpflug stereocamera for particle image velocimetry in liquid flows. Appl Opt **34**, 7092–7099 (1995)

[85] Raffel, M., Willert, C., Wereley, S., Kompenhans, J.: Particle Image Velocimetry: A Practical Guide, 2nd edn. Springer (2007)

[86] Reddemann, M.: Mikroskopische Analyse des Zerfalls motorischer Sprühstrahlen. Ph.D. thesis, RWTH Aachen, University (2015)

[87] Reuss, D., Megerle, M., Sick, V.: Particle-image velocimetry measurement errors when imaging through a transparent engine cylinder. Meas. Sci. Technol. **13**, 1029 – 1035 (2002)

[88] Ruck, B.: Einfluß der Tracerteilchengröße auf die Signalinformation in der Laser-Doppler-Anemometrie. Technisches Messen **57**, 284 – 295 (1990)

[89] Scarano, F., Poelma, C.: Three-dimensional vorticity patterns of cylinder wakes. Exp. Fluids **47**, 69 – 83 (2009)

[90] Siebers, D.L.: Scaling liquid-phase fuel penetration in diesel sprays based on mixing-limited vaporization. SAE Technical Paper (1999-01-0528)

[91] Soloff, S.M., Adrian, R., Liu, Z.C.: Distortion Compensation for Generalized Stereoscopic Particle Image Velocimetry. Meas Sci Technol **8**, 1441 – 1454 (1997)

[92] Soria, J., Atkinson, C.: Towards 3C-3D digital holographic fluid velocity vector field measurement - tomographic digital holographic PIV (Tomo-HPIV). Meas. Sci. Technol. **19**, 074,002 (2008)

[93] Sperling, D., Claussen, E.: Motorizing the Developing World. ACCESS Magazine **24**, 10 – 15 (2004)

[94] Stansfield, P., Wigley, G., Justham, T., Catto, J., Pitcher, G.: PIV analysis of in-cylinder flow structures over a range of realistic engine speeds. Exp. Fluids **43**, 135 – 146 (2007)

[95] Stapf, K., Seebach, D., Fricke, F., Pischinger, S., Hoffmann, K., Abel, D.: CAI-Engines: Modern combustion system to face future challenges. In: SIA Int. Conference - The Spark Ignition Engine of the Future. Strasbourg (2007)

[96] Stein, T., Grande, P., Kayser, H., Sibilla, F., Leitner, W., de Dominguez, M.: From biomass to feedstock: one-step fractionation of lignocellulose components by the selective organic acid-catalyzed depolymerization of hemicellulose in a biphasic system. Green Chem. **13**, 1772 – 1777 (2011)

[97] Tchen, C.M.: Mean value and correlation problems connected with the motion of small particles suspended in a turbulent fluid. Ph.D. thesis, Delft University (1947)

[98] Tennekes, H., Lumley, J.: A First Course in Turbulence. MIT Press, Cambridge (1972)

[99] Townsend, A.: The Structure of Turbulent Shear Flow. Cambridge University Press (1976)

[100] Tropea, C., Yarin, A., Foss, J.: Handbook of Experimental Fluid Mechanics. Springer, Berlin (2007)

[101] Tsai, R.Y.: An efficient and accurate camera calibration technique for 3D macmach vision. In: Proceedings of IEEE conference on computer vision and pattern recognition, Miami Beach (1986)

[102] Urushihara, T., Hiraya, K., Kakuhou, A., Itoh, T.: Expansion of HCCI Operation Region by the Combination of Direct Fuel Injection, Negative Valve Overlap and Internal Fuel Reformation. SAE Transactions **112**, 1092 – 1100 (2003)

[103] Verhoeven, D.: Limited-data computed tomograpy algoritms for the physical sciences. Appl Opt **32**, 3736 – 3754 (1993)

[104] Vikram, C.: Holoraphic recording of moving objects. Nouvelle Revue d'Optique Appliquee **3**, 305 – 308 (1972)

[105] Voisine, M., Thomas, L., Boree, J., Rey, P.: Spatio-temporal structure and cycle to cycle variations of an in-cylinder tumbling flow. Exp. Fluids **50**, 1393 – 1407 (2010)

[106] Westerweel, J., Scarano, F.: Universal outlier detection for PIV data. Exp Fluids **39**, 1096 – 1100 (2005)

[107] Wieneke, B.: Stereo-PIV using seif-calibration on particle images. Exp Fluids **39**, 267 – 280 (2005)

[108] Wieneke, B.: Volume self-calibration for 3D particle image velocimetry. Exp Fluids **45**, 549 – 556 (2008)

[109] Willert, C.: Stereoscopic digital particle image velocimetry for application in wind tunnel flows. Meas Sci Technol **8**, 1465 – 1479 (1997)

[110] Zhang, J., Tao, B., Katz, J.: Turbulent flow measurement in a square duct with hybrid holographic PIV. Exp. Fluids **23**, 373 – 381 (1997)

Appendix A

Hologram development and bleaching

Table A.1 – SM-6 developer

chemical	formula	amount
sodium hydroxide	$NaOH$	12 g
Phenidone	$C_9H_10N_2O$	6 g
ascorbic acid	$C_6H_8O_6$	18 g
sodium phosphate dibasic anhydrous	Na_2HPO_4	28.4 g
water	H_2O	1 l

Table A.2 – PBU-Amidol Bleach

chemical	formula	amount
potassium peroxodisulfate	$K_2S_2O_8$	10 g
citric acid anhydrous	$C_6H_8O_7$	50 g
copper(II) bromide	$CuBr_2$	1 g
potassium bromide	KBr	20 g
Amidol	$C_6H_10Cl_2N_2O$	1 g
water	H_2O	1 l

Table A.3 – Process of hologram development

step	reactant	time
Development	SM-6	2 min
Wash	water	1-2 min
Bleach	PBU-Amidol	until clear (2-3 min)
Wash	water	5 min
Final Wash	water with wetting agent (Agepon)	1 min
Drying	slow air	until dry

Appendix B

Test rig for particle analysis

Figure B.1 shows the experimental setup for the in-depth analysis of the particle response to an oscillating flow. This flow is generated in an octagonal tank with transparent glass walls. Inside the tank a piston is driven by a 2 phase stepper motor (Rorze Automation) and creates an oscillating flow field. The motor has a resolution of 1.8° per step resulting in 200 pulses per revolution. To achieve a sinusoidal velocity profile, two vertical and one horizontal bearing guide the piston movement. The piston plate has a diameter of 80 mm, the stroke is 20 mm. The PIV-setup consists of a Quantronix Darvin-Duo double-pulsed Nd:YLF laser, whose beam is expanded through a four-lens light sheet optic to illuminate the flow field, a PCO Dimax camera with a Zeiss lens with a focal length of 100 mm and $f/2.0$, and a delay generator that synchronizes piston movement, laser pulse, and camera acquisition. The setup leads to a measurement area of 15.6 x 35.9 mm^2. To analyze a wide range of Stokes numbers, the measurements are performed for 3 frequencies at 10, 15, and 20 Hz and two particles. To resolve the

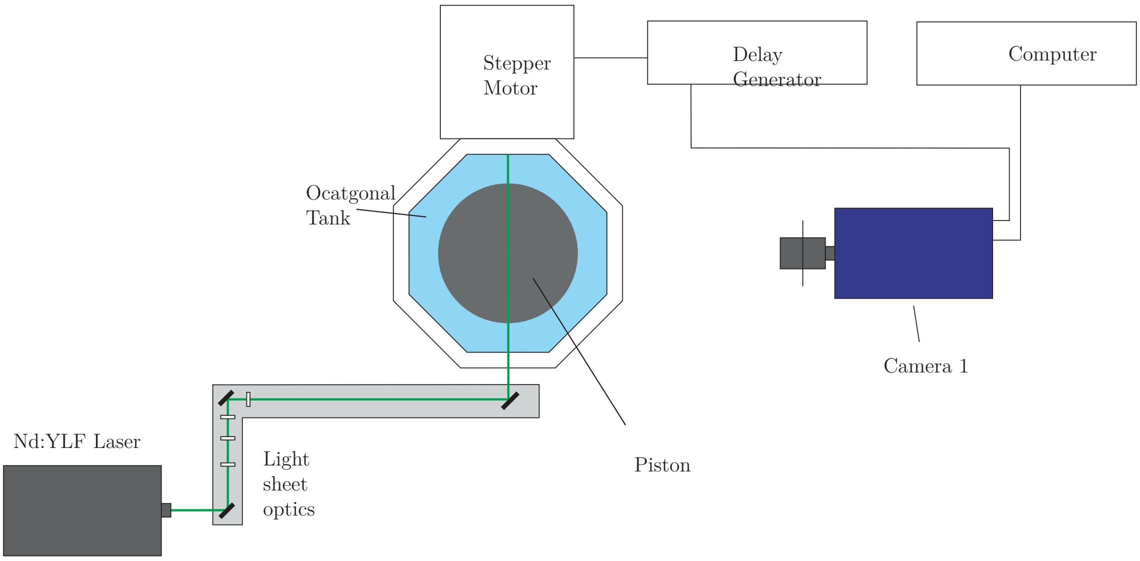

Figure B.1 – Experimental Setup.

.

movement of the particles with respect to the piston, the flow field has been recorded with a frequency of 1800 Hz for the 10 Hz and 20 Hz case and a frequency of 2700 Hz for the 15 Hz case. The particle properties are listed in tab. B.1.

Table B.1 – Particle properties

particle	$d_m [\mu m]$	ρ_p $[kg/m^3]$	St(10 Hz) St_1 / St_2	St(15 Hz) St_1 / St_2	St(20 Hz) St_1 / St_2
SH400S33	14	1700	0.87 / 0.019	1.59 / 0.023	2.45 / 0.027
Vestosint 2161	26	1016	2.16 / 0.038	3.97 / 0.046	6.12 / 0.054

The quantity d_m is the mean particle diameter, ρ_p the particle density, and St the Stokes number calculated by eq. 4.16. The particle size distribution, provided by the particle manufacturer is shown in fig. B.2.

SH400S33 (Potters Industries) are spherical silver coated hollow glass spheres. Vestosint 2161 (Evonik Industries) are spherical polyamide particles. Both particles

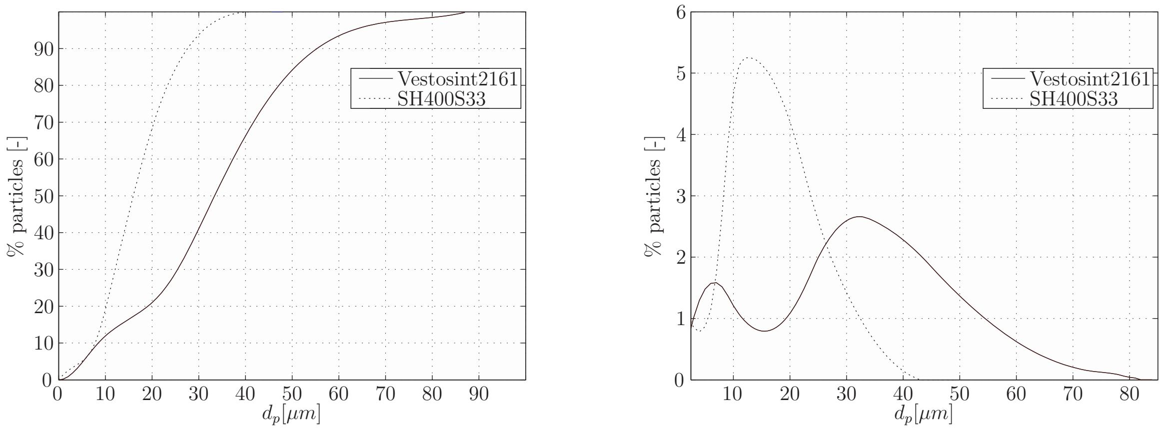

(a) particle size distribution (b) Differential particle size distribution.

Figure B.2 – Particle volume size distribution (a) and differential particle volume size distribution (b) for Vestosint 2161 (solid line) and SH400S33 (dotted line).

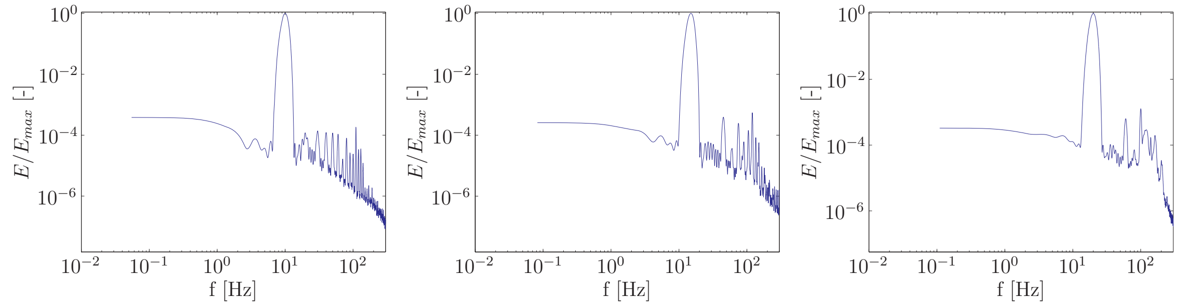

(a) 10 Hz (b) 15 Hz (c) 20 Hz

Figure B.3 – Normalized energy spectra of stepper motor movement.

are normally used for seeding in water. They have purposely been chosen to achieve high Stokes numbers as normal seeding for air possesses nearly perfect flow following behavior for the frequencies, achievable with the stepper motor.
Figure B.3 shows the energy spectra of the piston movement. These spectra have been measured using an accelerometer (DeltaTron Accelerometer Type 4507 B, Brüel &Kjær). Apart from the main frequency, every spectrum shows higher order peaks in the range of $30-300$ Hz. These peaks are caused by the discrete movement of the stepper motor with a resolution of 1.8°.

Appendix C

Author-related pre-published papers and theses

Previously Published

The author of this dissertation has authored or co-authored the following scientific publications. Excerpts of these publications are used in the present thesis:

- van Overbrüggen et al.: Holographic particle-image velocimetry measurements in a four-valve combustion engine. [73].
- van Overbrüggen et al.: Tomographic particle-image velocimetry in an IC engine. [70].
- van Overbrüggen et al.: Holographic particle-image velocimetry measurements in a four-valve combustion engine. [74].
- van Overbrüggen et al.: A particle-image velocimetry tracer generating technique for liquid flows. [77]
- van Overbrüggen et al.: Tomographic Particle-Image Velocimetry Analysis of In-Cylinder Flows. [75].
- van Overbrüggen et al.: Experimental analysis of particle sizes for PIV measurement. [76].
- van Overbrüggen et al.: Planar, Stereoscopic, and Holographic PIV-Measurements of the In-Cylinder Flow of Combustion Engines. [72].
- Deshmukh et al..: Spray breakup and mixture formation of novel biofuels. [33].
- van Overbrüggen et al.: Experimental Analysis of the Impact of Injected Biofuels on In-Cylinder Flow Structures. [71]

Student Theses

The following student theses have been written within the research project of this dissertation. Figures of these theses may also appear in this dissertation:

- G. Schulze Forsthövel and B. Bahl: Versuchstandsoptimierung und Messung der Motorinnenströmung mit Hilfe der holographischen Particle-Image Velocimetry, project thesis, 2011
- G. Geulen and D. Willms: Ausbau und Inbetriebnahme eines PIV-Demonstrators. project thesis, 2012.
- B. Bahl: Cycle-resolved tomographic particle-image velocimetry measurements of a four-valve combustion engine, master thesis, 2013
- J. Miao: Untersuchung des Einflusses verschiedener Ventilsteuerzeiten auf die Strömung in einem 4-Ventil-Ottomotor mittels tomografischer Particle-Image Velocimetry, bachelor thesis, 2013
- M. Braun: Machbarkeitsstudie zur Verwendung der holographisch tomographischen Interferometrie zur Dichtemessung im Brennraum eines fremdgetriebenen Viertaktmotors, bachelor thesis, 2014
- M. Braun: Experimental Investigation of the Interaction between Fuel Injection and the Flow Field of a single Cylinder Combustion Engine , master thesis, 2015